USES OF THE SYNCHROTRON X-RAY LAUE TECHNIQUE AND INVESTIGATION OF MICROGRAVITY CRYSTAL GROWTH

A THESIS SUBMITTED TO THE UNIVERSITY OF MANCHESTER
FOR THE DEGREE OF DOCTOR OF PHILOSOPHY
IN THE FACULTY OF SCIENCE

By

E. H. Snell

Department of Chemistry

November 1995

Contents

List of Figures 9

List of Tables 17

Abstract 19

Declaration 22

Copyright & Ownership 23

The Author 24

Acknowledgements 25

Abbreviations and Symbols Used 27

I Uses of the Synchrotron Laue Technique 29

1 Introduction to the Laue Method and Synchrotron Radiation 30

1.1 Historical Background (X-rays and the Laue method) 30

1.2 Synchrotron Radiation 36

1.3 Previous Laue Work 39

2 Laue Theory and Practice 55

2.1 Introduction 55

2.2 Reciprocal Space Sampling: Energy Overlap and Wavelength Bandpass 57

2.3 Spatial Overlap 59

2.4 The "Low Resolution Hole" 60

2.5 Wavelength Normalisation 61

2.6 Multiple Deconvolution 63

2.7 Correction for f' and f'' variation 65

2.8 Crystal Perfection 66

3 Image Plate Small Crystal Study 69

3.1 Introduction 69

3.2 Image Plate and Film as Area Detectors 70

3.3 Nickel Aluminophosphate Small 'Test' Crystal 74

3.4 Data Collection 74

3.5 Image to Intensities 79

3.6 Intensities to Structure 82

3.7 Comparison of Data Processing Strategies 88

3.8 The NiAPO Structure 90

3.9 Comparison with Monochromatic Studies 92

3.10 Future Work 93

3.11 Summary 98

4 A Protein Study - Filling the "Low Resolution Hole" in Laue Data 100

4.1 Introduction 100

4.2 Lysozyme 101

4.3 Crystallisation 102

4.4 Laue Data Collection 104

4.5 Laue Data Processing 104

4.6 Structure Refinement and Modelling 109

4.7 Electron Density Maps 111

4.8 Quality of final models 126

4.9 Summary 128

5 ESRF CCD detector calibration with the Laue method 129

5.1 Introduction 129

5.2 "Image Mapping" Corrections and Calibrations 130

5.3 Equipment 130

5.4 Experimental 132

5.5 Data Processing 133

5.6 Results 137

5.7 Discussion and Concluding Remarks 138

6 Future Development of the Synchrotron Laue Method 146

6.1 Discussion and Conclusions 146

6.2 Future Work: Overview 147

II Microgravity Crystallization and Application 149

7 Microgravity in Crystallization 150

7.1 Introduction 150

7.2 Eliminating Convection 152

7.3 X-ray Characterisation of Crystals 154

7.4 Previous Microgravity-Grown Crystal Analysis 161

8 Crystallization of Lysozyme in Microgravity 166

8.1 Introduction 166

8.2 Apparatus for Crystallization in Microgravity 167

8.3 Previous Work on Lysozyme Crystal Perfection: The Spacehab-1 Mission 171

8.4 The IML-2 mission 174

8.5 Results 176

8.6 Discussion 183

8.7 Summary and Main Findings 192

9 Diffraction Characterisation of (IML-2) Microgravity Grown Crystals 193

9.1 Introduction 193

9.2 Evaluation of Crystal Perfection with the Laue Method on ESRF BL-3 194

9.3 Evaluation of Crystal Perfection by Monochromatic Methods . . . 196

9.4 Discussion 205

9.5 Summary of Main Findings 210

10 Mosaic Block Structure of Microgravity-Grown Crystals and X-ray Topography Studies **211**

10.1 Introduction 211

10.2 Experimental 212

10.3 Results 213

10.4 Extinction Effects 216

10.5 Discussion 220

10.6 Summary 222

11 Interferometer Concentration Measurements **223**

11.1 Introduction 223

11.2 Equipment 225

11.3 Theory 227

11.4 Calibration 228

11.5 Experimental 231

11.6 Results 235

11.7 Limitations and Overcoming Them 243

11.8 Discussion 245

11.9 Main Findings and Future Work 246

12 Discussion, Conclusions and Future Work for Microgravity and Protein Crystal Growth **247**

12.1 Discussion 247

12.2 Conclusions 249

12.3 Future Work 250

References **254**

Publications **287**

List of Figures

1.1 Setup of the first Laue experiment apparatus (Friedrich, Knipping and von Laue (1912)[103]) 33

1.2 Universal spectral distribution of synchrotron radiation 39

2.1 Ewald representation of the region of accessible space with the Laue method 58

2.2 Example of the diffraction geometry for a Laue doublet for two different crystal orientations 64

2.3 Explanation of mosaicity, η_{hkl}, of a crystal 67

2.4 Schematic diagram of an ideally imperfect "mosaic" crystal 68

3.1 MAR image plate used for data collection on station 9.5 of the SRS 75

3.2 NiAPO Laue data recorded on (a) image plate and (b) film 76

3.3 Film holder and camera used on station 9.5 of the SRS 77

3.4 Contour plot for the intensity of an average spot from (a) an image plate, and (b) a photographic film exposure 78

3.5 Flowchart showing image to reflection intensity processing 80

3.6 Root mean square deviations between predicted and observed patterns using monochromatic cell parameters and refined cell parameters from Laue data 82

3.7 Flowchart showing reflection intensities to crystal structure determination 84

3.8 Wavelength normalisation curve produced from NiAPO data . . . 85

3.9 Absorption correction surface produced for NiAPO 89

3.10 The NiAPO molecular structure 91

3.11 Single Image Plate diffraction images from NiAPO 94

3.12 A simulated "MILD" image from 9 separate NiAPO Laue images 95

3.13 Schematic representation of the rotating crystal method 97

4.1 Ribbon diagram of lysozyme 103

4.2 Normalisation curves for 2, 4, 10 and 30° angular interval lysozyme Laue data 105

4.3 Percentage completeness against resolution for Laue data from tetragonal lysozyme crystals 107

4.4 2Fo-Fc Laue electron density maps showing the Arg 5 residue in tetragonal lysozyme 112

4.5 2Fo-Fc Laue electron density maps showing the His 15 residue in tetragonal lysozyme 113

4.6 2Fo-Fc Laue electron density maps showing the Phe 38 residue in tetragonal lysozyme 114

4.7 2Fo-Fc Laue electron density maps showing the Asp 52 residue in tetragonal lysozyme 115

4.8 2Fo-Fc Laue electron density maps showing the Tyr 53 residue in tetragonal lysozyme 116

4.9 2Fo-Fc Laue electron density maps showing the Pro 70 residue in tetragonal lysozyme 117

4.10 2Fo-Fc Laue electron density maps showing the Trp 108 residue in tetragonal lysozyme 118

4.11 2Fo-Fc Laue electron density maps showing the disulphide bridge between the Cys 6 and Cys 127 residues in tetragonal lysozyme . 119

4.12 2Fo-Fc Laue electron density maps showing the disulphide bridge between the Cys 30 and Cys 115 residues in tetragonal lysozyme . 120

4.13 2Fo-Fc Laue electron density maps showing the disulphide bridge between the Cys 64 and Cys 80 residues in tetragonal lysozyme . 121

4.14 2Fo-Fc Laue electron density maps showing the disulphide bridge between the Cys 76 and Cys 94 residues in tetragonal lysozyme . 122

4.15 Cα trace of the lysozyme structure coloured according to the R-factor of the residues (red = 0.43, blue = 0.26) for data collected with (a) 2° angular steps, (b) 4° angular steps, (c) 10° angular steps, and (d) 30° angular steps 124

4.16 The Real-Space R-factors are shown on a per-residue basis, for the 2, 4, 10 and 30° angular interval Laue data 125

4.17 Ramachandran plots for 2, 4, 10 and 30° angular step data refinement of tetragonal lysozyme 127

5.1 Image intensifying CCD detector installed on ESRF beamline 3 (seen without electrostatic shielding) 131

5.2 ESRF CCD images recorded from lysozyme (a) uncorrected and (b) with distortion correction applied 132

5.3 Histogram of normalised intensities against (a) wavelength and (b) resolution for determination of λ_{min} and d_{min} soft limits 134

5.4 Deviation from the mean for the twist, tilt and bulge refinement parameters with ESRF CCD collected Laue data 135

5.5 Wavelength normalisation curve produced from ESRF CCD collected lysozyme crystal data 136

5.6 ESRF Laue data (a) recorded photographically from tetragonal lysozyme and (b) the corresponding detector response function . . 138

5.7 Intensity response surfaces for ESRF Beamline 3 CCD detector for spindle axis settings of (a) 0°, (b) 1°, (c) 2° and (d) 3° 139

5.8 Intensity response surfaces for ESRF Beamline 3 CCD detector for spindle axis settings of (a) 4°, (b) 5°, (c) 6° and (d) 7° 140

5.9 Intensity response surfaces for ESRF Beamline 3 CCD detector for spindle axis settings of (a) 8°, (b) 16°, (c) 24° and (d) 32° 141

5.10 Intensity response surfaces for ESRF Beamline 3 CCD detector for spindle axis settings of (a) 40°, (b) 48°, (c) 56° and (d) 64° 142

5.11 Intensity response surfaces for ESRF Beamline 3 CCD detector for spindle axis settings of (a) 72° and (b) 80° 143

5.12 Deviation of peak intensity response across CCD detector 143

5.13 R_{factor} (on Intensity) plotted against (a) d_{min} and (b) intensity for both intensity corrected (via. LAUESCALE and monochromatic data) and uncorrected data 144

8.1 Schematic diagram of ESA's APCF dialysis reactor 169

8.2 Photograph of the dialysis reactor 169

8.3 Photograph of APCF with the process chamber open 171

8.4 Video images of tetragonal lysozyme in microgravity reactor from the point of first crystal formation in the IML-2 mission 177

8.5 Video images of tetragonal lysozyme in microgravity reactor until the end of the IML-2 mission 178

8.6 Photograph of typical tetragonal crystal produced on the IML-2 mission 179

8.7 Plot of the growth of the (110) face over time (length and width) under microgravity conditions 180

8.8 Illustration of the (110) and (101) faces of tetragonal lysozyme . . 181

8.9 Plot of the growth rate over time under microgravity conditions . 182

8.10 A photograph of the reactor at the end of the IML-2 mission . . . 184

8.11 Clumps of microgravity grown orthorhombic crystals 185

8.12 Needle shaped microgravity-grown orthorhombic crystal extruding from tetragonal crystal 186

9.1 ψ circle diffractometer used for data collection 197

9.2 Rocking widths of microgravity-grown lysozyme crystals mounted in *quartz* and *glass* capillaries 203

9.3 Rocking widths of microgravity-grown and earth-grown lysozyme crystals 204

9.4 Distribution of microgravity-grown and earth-grown lysozyme crystal rocking widths 205

9.5 Reflection 0 0 8 from earth-grown and microgravity-grown crystal 206

9.6 Reflection 7 7 6 from earth-grown and microgravity-grown crystal 207

9.7 Typical intensities of microgravity and earth-grown reflections . . 208

9.8 Reflection (32 57 0) recorded at 1.2Å resolution for a microgravity-grown crystal 209

10.1 X-ray topograph recorded from a microgravity-grown lysozyme crystal for two different reflections 214

10.2 X-ray topograph recorded from a microgravity grown lysozyme crystal 215

10.3 X-ray topograph recorded from an earth-grown lysozyme crystal at two different reflections 217

11.1 Photograph of the Mach-Zehnder interferometer 225

11.2 Schematic diagram of the Mach-Zehnder interferometer 226

11.3 Plot of the Cauchy function for water, buffer, salt and protein solutions over a wavelength range, 400 nm to 800 nm 232

11.4 Example of fringes recorded by the video camera with wide field of view optics 234

11.5 Images recorded from interferometer between 00:06 hours and 02:29 hours 236

11.6 Images recorded from interferometer between 08:59 hours and 42:12 hours 237

11.7 Plot of averaged grey level recorded during interferometer monitoring of ground growth tests 239

11.8 Cumulative total number of fringe peaks plotted against time . . 240

11.9 Protein chamber image at end of experiment. 241

11.10 Spatial concentration measurements through the protein chamber 243

List of tables

1.1 Historical survey of small molecule crystal Laue (largely synchrotron) data collection and processing results (where available) 40

1.2 Historical survey of protein crystal synchrotron Laue data collection and processing results 47

3.1 NiAPO R_{factor} (on F) results for different data treatments 88

3.2 Effect of $f'f''$ corrections applied after absorption correction to both $f'f''$ initially corrected, and uncorrected data 89

3.3 NiAPO cell parameters for monochromatic and Laue data sets . . 92

4.1 Reflections used and normalised by LAUENORM 106

4.2 Table of AGROVATA output for lysozyme Laue data 106

4.3 Completeness of data for protein crystal Laue collection at different angular steps 107

4.4 Low resolution cutoffs at 50% completeness for protein crystal Laue data 108

4.5 Results for X-PLOR refinement and FRODO modelling of lysozyme 110

4.6 Water structure found for the different angular data sets 110

4.7 Lysozyme residues present in most favoured and additionally allowed regions of the Ramachadran plot 126

9.1 List of earth-grown crystal reflections comprising rocking width data (composites excluded) 199

9.2 List of earth-grown control crystal (composite reflection) rocking width data 200

9.3 List of microgravity-grown crystal reflections comprising rocking width data using a *glass* capillary for mounting 201

9.4 List of microgravity-grown crystal reflections comprising rocking width data (crystal mounted in *quartz* capillary). 202

11.1 Refractive index differences of solutions 230

11.2 Refractive indices of solutions 231

Abstract

UNIVERSITY OF MANCHESTER

ABSTRACT OF THESIS submitted by **E. H. Snell** for the Ph.D. Degree entitled **Uses of the Synchrotron X-ray Laue Technique and Investigation of Microgravity Crystal Growth**

Month and Year of Submission: November 1995

The work presented here is divided into two parts. The first deals with three separate developments of the synchrotron Laue method. The second part describes the use of microgravity to produce more perfect protein crystals, X-ray topography to examine them and the use of the Mach-Zehnder interferometer as a diagnostic tool in crystallography.

Part I: The Laue method was used for a structural solution of a small inorganic test crystal, NiAPO (Snell *et al.* 1995, J. Synchrotron Rad.).[219] An image plate

was used for the data collection and comparison made with the use of photographic film. Synchrotron data collection was completed in less than one hour and a structure produced with an R-factor on F of 5.11% for $I > 3\sigma(I)$ comparing well with monochromatic studies on the same crystal. Secondly the problem of completeness of data at low resolution, "the low resolution hole", was tackled for the protein lysozyme via a strategy involving small angular interval data collection. From a data set of 31 images recorded at 2° intervals a subset of 4°, 10° and 30° intervals (16, 6 and 3 images respectively) were compared in terms of completeness and electron density maps. The 2° data gave the best completeness of 86.1% for d_{min}-∞, 88.1% for d_{min}-$2d_{min}$ and 68.6% for $2d_{min}$-∞ and an overall improved electron density. The study documents the progressive deterioration of completeness and map quality as coarser angular intervals are employed. Thirdly the Laue method is used to examine the performance of the European Synchrotron Radiation Facility's (ESRF) Image intensifying Charge Coupled Device (CCD) X-ray detector, with a view to helping to realise optimal detector calibration and use.

Part II: Firstly, lysozyme crystals have been grown using the European Space Agency's (ESA) Advanced Protein Crystallization Facility (APCF) on-board the NASA STS-65 International Microgravity Laboratory-2 (IML-2) Space Shuttle mission. Exceptionally large, well defined morphology, tetragonal crystals were produced. The crystals had a 1.8 mm average length (2.5 mm maximum) along the longest dimension as opposed to 0.6 mm average (0.8 mm maximum) for the ground-control crystals grown under identical conditions (but *not* within an APCF). An unusual presence of orthorhombic 'needle shaped' crystals was also observed in the microgravity-grown case. Rocking width measurements were

made at the ESRF, with a high resolution diffractometer, of a microgravity-grown and an earth-grown control, tetragonal crystal. The microgravity-grown crystal displayed mosaic spreads as low as 0.0019° compared to the lowest value of 0.0067° for the earth-grown control crystal. The reduction in mosaic spread results in a corresponding increase in peak intensity for the reflections giving improved signal to noise for microgravity-grown crystal X-ray data (Snell *et al.* 1995, Acta Cryst. D).[220] It was also readily possible to measure diffraction at 1.2 Å for the microgravity-grown crystal. Secondly, a topographic study of the microgravity-grown crystals was conducted at the National Synchrotron Light Source (NSLS). Images of mosaic blocks in the crystals were obtained, the first direct evidence for these ever obtained as far as we know. The sizes of the blocks correlates well with the IML-2 grown ESRF rocking width measurements. Thirdly, a potential diagnostic tool, the Mach-Zehnder interferometer (implemented in the engineering model of the Advanced Protein Crystallization Facility) has been investigated with lysozyme as the test sample. This allowed the time-dependence of the lysozyme crystal growth process to be monitored, via the refractive index changes in the solution.

Discussions and future work are presented for both parts of the thesis.

Declaration

No portion of the work referred to in this thesis has been submitted in support of an application for another degree or qualification of this or any other university or other institution of learning.

Edward H. Snell, Manchester, November 1995.

Copyright & Ownership

1. Copyright for the text of this thesis rests with the Author. Copies (by any process) either in full, or of extracts, may be made **only** in accordance with instructions given by the Author and lodged in the John Rylands University Library of Manchester. Details may be obtained from the Librarian. This page must form part of any such copies made. Further copies (by any process) of copies made in accordance with such instructions may not be made without the permission (in writing) of the Author.

2. The ownership of any intellectual property rights which may be described in this thesis is vested in the University of Manchester, subject to any prior agreement to the contrary, and may not be made available for use by third parties without the written permission of the University, which will prescribe the terms and conditions of any such agreement.

   Further information on the conditions under which disclosures and exploitation may take place is available from the Head of Department of Chemistry.

The Author

The author graduated from Liverpool Polytechnic with a 1st class honours degree in Applied Physics. During his undergraduate time he worked with the Royal Armament Research and Development Establishment as part of a "Proof of Future Concepts Team" which also involved participation in a two month British Army exercise in Northern Germany where he was in charge of trial instrumentation on three main battle tanks. He also has experience of parallel processing (transputer) communication over long distances and development and implementation of such techniques.

His postgraduate studies have involved him in both monochromatic and Laue data collection from synchrotrons in England, France (ESRF, the European machine) and the USA, on both small and macro-molecule crystals. Crystallization experiments have been carried out on the NASA Space Shuttle and microgravity work has involved him working in the Dornier Research Labs in Southern Germany and as a consultant to the Universities Space Research Association in the USA.

Acknowledgements

Many people have been involved in helping me with my research but above all I have to thank my supervisor, Professor John Helliwell. Through him I have had to chance to dip my feet in the truly international world of crystallography, his guidance, support and help have been invaluable. My colleagues in the Structural Chemistry group are thanked for producing such a good atmosphere in which to work. In particular I have to thank Dr. William Hunter, Dr. Steve Harrop, Dr. Gordon Leonard, Dr. Susanne Weisgerber, Charlie Bond and Serena Cooper for answering my many questions and offering various pearls of wisdom. Dr. Mark Vincent is thanked for the disk space and putting up with my LaTeXing on his machines.

Further afield I am indebted to Andy Thompson for introducing me to a "hands on" approach to synchrotrons, Dr. Vivian Stojanoff for her experience and help with X-ray topography and Dr. Edgar Weckert for letting me use his diffractometer. Dr. Klaus Furhmann, Rodger Bosch, Dr. Luthor Potthast, Dr. Paul Lautenschlager and the members of the ESA working group on microgravity crystallization are thanked for making me most welcome in my travels through Germany and Belgium. I also thank the staff and members of the HERCULES

93 course in France for the introduction to red wine and for putting up with my Franglais.

The final group I must thank are those responsible for pointing me in the right direction and keeping me going. Professor Colin Reynolds, Dr. Fritjoff Körber, Dr. Steve Prince, Richard Carter and Tracy Chapman are thanked for introducing me to crystallography and brain-storming throughout my undergraduate studies. J.W.T., S.F., J.S. and J.R. are thanked for their input into my practical training and for two important rules. Finally my sister, my mother and father (who still hasn't forgiven me for being in the wrong branch of crystallography) and the spell checker, without whose support none of this would have been possible, are thanked.

I can only hope that some time in the future I can repay the enormous amount of gratitude I have for the many people who have helped me throughout the years.

Abbreviations and Symbols Used

Å	Ångstrom (10^{-10}m)
APCF	Advanced Protein Crystallization Facility
CCD	Charge Coupled Device
CCP4	Collaborative Computational Project no. 4
CHESS	Cornell High Energy Synchrotron Radiation Source
ESA	European Space Agency
ESRF	European Synchrotron Radiation Facility
FWHM	Full Width at Half Maximum
IML	International Microgravity Laboratory
IRF	Instrument Resolution Function
LED	Light Emitting Diode
LOT	Large-angle Oscillation Technique
LURE	Laboratorie Utilisation Rayonnement Electromagnetique
NASA	National Aeronautics and Space Administration
NSLS	National Synchrotron Light Source (Brookhaven)
PDB	Protein Data Bank
rms	root mean square
SRS	Synchrotron Radiation Source (Daresbury)

"Nature uses only the longest threads to weave her patterns, so each small piece of fabric reveals the organisation of the entire tapestry"

Richard Feynman (1918-1988)

Part I

Uses of the Synchrotron Laue Technique

Chapter 1

Introduction to the Laue Method and Synchrotron Radiation

1.1 Historical Background (X-rays and the Laue method)

In the old Bavarian university town of Würzburg, Wilhelm Conrad Röntgen, Professor of Physics, had assembled equipment to investigate the hotly contested subject of cathode rays. Included in his apparatus was a fairly large induction coil and suitable discharge tubes. Röntgen never divulged what measurements he intended to make nor what discharge tube he was using when, on the 8th of November 1895, he noticed the effect of X-rays (as he called the rays for the sake of brevity).[92] A barium platino cyanide screen lying on the table at a considerable distance from the tube showed a flash of fluorescence every time a discharge of the induction coil went through the tube. Already knowing that cathode rays (e^-) were absorbed by the glass of the tube and the outside air he concluded that the fluorescence was caused by something, the unknown X, that

travelled in a straight line from the spot where the cathode ray in the tube hit the glass wall. The unknown agent was absorbed by metals and these cast a shadow on the fluorescent area of the screen. He therefore spoke of X-rays and showed that these rays were exponentially absorbed in matter with an exponent roughly proportional to the mass traversed. Röntgen was well aware he had found something fundamentally new and in a breathless but comprehensive period of work he wrote his first communication in December 1895 for the local Würzburg Scientific Society.[199] The paper was quickly set and Röntgen sent out proofs as New Years Greetings to a number of his scientific friends. A translation of his paper appeared later in Nature.[200]

In 1900 Röntgen was appointed to the chair of experimental physics at Munich University. In 1912 at the same University Paul P. Ewald was preparing his doctor's dissertation under Arnold Sommerfeld, who held the Chair of Theoretical Physics. Max von Laue had joined Sommerfeld's group from a post doctoral position with Max Planck in the Autumn of 1909. Ewald was analysing, theoretically, the passage of light waves through a crystalline arrangement of scattering atoms and he consulted Laue, a Privat-Dozent (lecturer), about his treatment of the phenomenon.

Ewald described to Laue the idea that crystals were thought to have an internal regularity with distances between atoms of 1/500 to 1/1000 the wavelength of light. Laue suggested that if the atoms really formed a lattice then irradiation with shorter waves, ie. X-rays, should produce interference phenomena similar to light interferences in optical gratings. Various work had suggested that X-rays had a wavelength of the order of 1 Å. Laue discussed his idea of X-ray diffraction with Sommerfeld whilst on a skiing holiday in the Alps. He also discussed it

at the Café Lutz physics table (in Munich) - this was the general rallying point for physicists after lunch for a cup of coffee and problem solving, making use of pencil drawn diagrams and equations on the smooth white marble tops of the Cafés tables. There was strong disbelief in the idea of any diffraction due to the assumption that thermal motion of the atoms would impair the lattice effect. Sommerfeld allowed his newly appointed experimental assistant, Walter Friedrich (who had just finished his doctoral thesis on the theory of X-ray scattering under Röntgen) with assistance from Paul Knipping, also from Röntgen's institute, to try Laue's idea. Friedrich was hitherto to study the directional distribution of the X-rays emanating from the anode so it was an easy matter to set up the experiment as the X-ray tube and induction coil were already in place.

The experiment on transmission of X-rays through crystals began around Easter 1912 with the apparatus shown in figure 1.1 (*a little behind the backs of the particular bosses)*[133].

Guided by exposure times from experiments on double scattering Friedrich knew that exposures of several hours would be needed. He constructed a lead box to contain the crystal and photographic plate, screening them from spurious X-rays from the glass wall of the tube and irradiated air. To further protect the experiment a lead screen was used with windows to limit the X-ray beam to approximately 1 mm in width. Photographic plates were distributed around the crystal to catch any diffracted rays.

The first sample used for the experiment was a crystal of copper sulphate found in the laboratory. This was attached to a holder by means of wax in a random orientation. Initially the photographic plate was placed between the X-ray tube

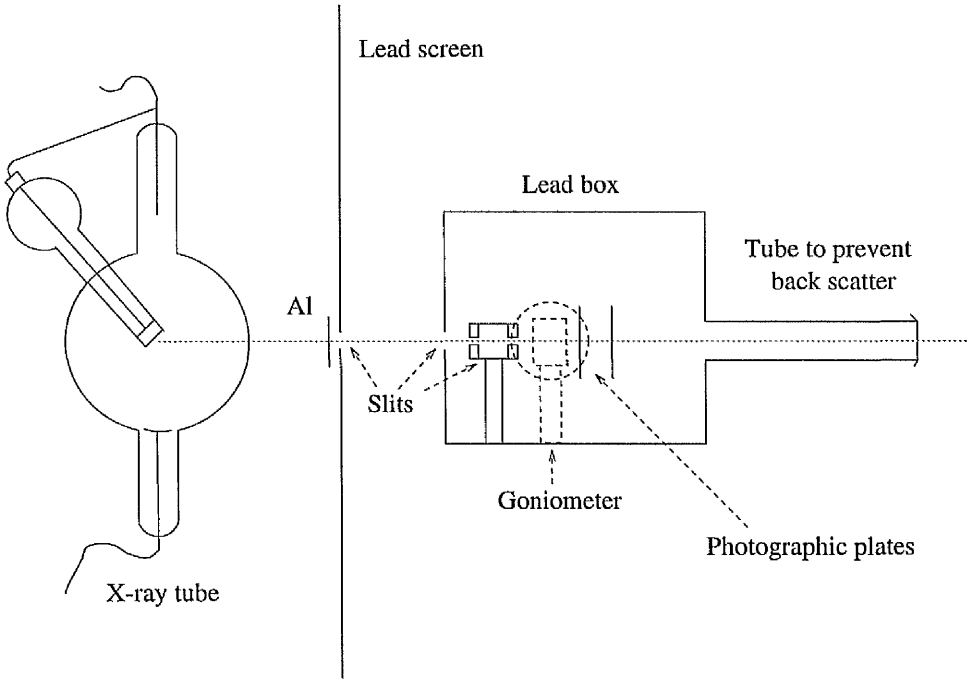

Figure 1.1: Setup of the first Laue experiment apparatus (translated from Friedrich, Knipping and von Laue (1912)[103])

and the crystal on the assumption that the crystal would act as a reflection grating. This proved incorrect so a second attempt was made with the plate behind the crystal. The total exposure to X-rays of a few hours took a day and a night with the frequent halts to let the X-ray tube cool down. On developing the plate, surrounding the direct beam spot there were rings of fuzzy spots seen. Further exposures were taken with varying crystal to plate distances showing the reflected rays to be travelling in straight lines. On tilting the crystal the spots shifted their positions and altered in intensity - they behaved to all intents and purposes as would be expected if they were caused by diffraction. As a final check the crystal was ground up and the pattern of spots disappeared.

Laue, Friedrich and Knipping's research was communicated to the Bavarian

Academy of Sciences on the 8th June and 6th July 1912 and published in the Proceedings (Sitzungsberichte) of the Academy.[103] Laue developed the theory to go with the experiment and since then the use of a white (polychromatic) X-ray beam incident on a stationary crystal has become known as the Laue method.

On 11th November 1912 four months after first hearing about von Laue's results William Lawrence Bragg read a paper to the Cambridge Philosophical Society with the correct interpretation of the results.[37] Lawrence Bragg had noticed that spots, which were round when his photographic plate was close to the crystal, became elliptical as the plate moved further away. Von Laue's treatment assumed that only a few definite wavelengths are present in the incident radiation and his equations were satisfied approximately. Bragg found Laue's explanation unsatisfactory and reformulated von Laue's conditions assuming a continuous spectrum over a wide range of wavelength and a different point of view to the action of the crystal as a diffraction grating. This led to some simplification and gave Bragg's law;

$$\lambda = 2d\cos\theta$$

where λ is the wavelength of the incident radiation, d is the shortest distance between successive planes in the crystal, and θ is the angle of incidence of the primary rays to the normal of the reflecting plane. In a later paper[38] he redefined the angle θ to be the glancing angle or angle of diffraction giving Bragg's law as it is known today;

$$n\lambda = 2d\sin\theta \tag{1.1}$$

where n represents the "order" of the reflection. Bragg subsequently went on to use monochromatic X-rays due to perceived limitations of the Laue method. Experimentally the limitation was the weakness of the available X-ray source. In particular characteristic monochromatic radiation was over four orders of magnitude higher in intensity than the polychromatic Bremsstrahlung radiation. Three other problems also limited the Laue method; multiplicity or overlapping orders, wavelength normalisation, and the lack of absolute cell parameters.

When the polychromatic beam is incident on the crystal ($\lambda_{min} \leq \lambda \leq \lambda_{max}$), each reflecting plane, described by the Miller indices hkl extracts from the white beam that particular component that satisfies Bragg's law. If two particular wavelengths λ and $\frac{\lambda}{2}$, are both present in the incident band pass, they will give rise to diffraction by the planes $d_{h,k,l}$ and $d_{2h,2k,2l}$ at exactly the same angle. The resulting spot is therefore a superposition of these two reflections (termed a doublet). This problem can also occur for more than two such interrelated reflecting planes and wavelengths leading to triplets, quadruplets and higher order multiplets. In W.L. Bragg's own words[40];

> X-ray analysis started with the Laue photograph. It is too hard to attach a quantative significance to the intensity of the spots which are due to the superposition of diffracted beams of several orders selected from a range of white radiation.

This then is the so called multiplicity problem (see also Amorós, Buerger & Amorós (1975)).[8] The wavelength normalisation problem can also be described in Bragg's own words[39];

> The deduction of the crystal structure from the appearance of the Laue photographs is a complicated process because the intensities of the spots do not depend on structure alone. They depend also upon the strength of the components in the continuous range of the original beam to which they are respectively due, and each spot may be composed of several orders superimposed. They are also influenced by the different blackening effect of radiation of different wavelengths and complications arise here owing to the absorption of X-rays by the silver and bromine in the photographic plate.

The Laue method was, in essence, revived on the utilisation of synchrotron radiation sources where its full advantage could be exploited, namely the rapid speed of data collection over monochromatic methods due to full use of the available continuous bandpass. Indeed the synchrotron emission (universal curve, see figure 1.2) is obviously quite distinct from the case of X-ray tube emission, referred to earlier (of a few emission lines superimposed on a weak continuous 'background' spectrum). However the introduction of undulators as insertion devices for quasi monochromatic synchrotron radiation production reopens the question of which type of source to use.

1.2 Synchrotron Radiation

Synchrotron radiation came about as a nuisance by-product from particle accelerators developed for high energy physics experiments. It was a nuisance in that

this was the primary energy loss (electricity cost) of going to ever higher energies. Fortunately, for a great many areas of science, the usefulness of synchrotron radiation was speedily recognised and the first dedicated synchrotron radiation sources (eg. the Daresbury Synchrotron Radiation Source (SRS) (1981)) were born.

A synchrotron accelerates ~~of~~ charged particles to relativistic velocities, with the particles confined within a closed orbit by the use of magnets. The particles (electrons or positrons) emit photons tangentially along their path. Because the speed of the particles is close to that of light, relativistic effects produce extreme collimation, which gives synchrotron radiation some of its useful properties.[158]

The properties of synchrotron radiation which make it a useful experimental tool for X-ray crystallography are;

- High flux, brightness and brilliance
- Tunable over a wide wavelength range
- Defined Time Structure
- Calculable spectra
- Polarized

Flux, brightness and brilliance are related. Flux (*integrated* over the vertical opening angle) is defined as the number of photons per second per mrad horizontal per 0.1 % relative bandwidth ($\delta\lambda/\lambda$); brightness as flux per unit solid angle; brilliance, in the European definition,[90] as brightness per unit source area. Synchrotron X-radiation has intrinsically a high brilliance; in the most optimal

use of the ESRF undulator, 20 mm gap, 6 GeV and 100 mA, the brilliance is greater than 10^{18} photons per second per mm^2 per $mrad^2$ over 0.1 % bandwidth ($\delta\lambda/\lambda$).

A synchrotron has a spectral distribution of photons as illustrated in figure 1.2. As can be seen there are no characteristic peaks in the spectrum but is a continuous curve which is known as the universal curve because it is applicable to all synchrotron radiation sources (with the exception of undulators). Insertion devices within the synchrotron storage ring can be used to 'tailor' the spectrum; wigglers shift the universal curve towards shorter wavelengths and undulators allow the synchrotron radiation to undergo constructive interference causing peaks in the universal curve spectrum. These undulator peaks are tunable in wavelength by altering the magnetic field (gap) in the insertion device.

The synchrotron radiation beam is produced in bursts corresponding to the groups of bunched electrons in the storage ring. The circumference length of the machine can accommodate a certain maximum number of bunches, the harmonic number. This mode of operation is known as "multibunch". Moffat, Bilderback and Schildkamp[165] have suggested that single bunch mode can be used for time-resolved experiments[168] with the exposures being taken with a time scale of one orbit of the ring. The time resolution is then the bunch width (eg. 50 psec at the ESRF). A remarkably beautiful advantage of such a machine. Preliminary experiments to investigate this have been carried out with Laue X-ray data being collected with time resolutions of 120 psec (at the Cornell High Energy Synchrotron Source (CHESS))[232] and now 50 psec at ESRF[256] on beamline 3.

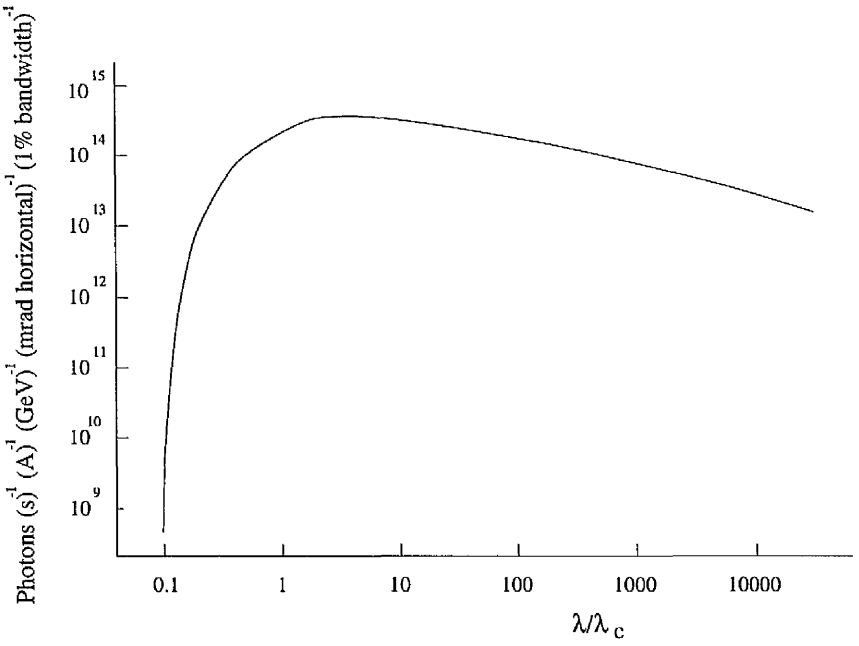

Figure 1.2: Universal spectral distribution of synchrotron radiation, from Helliwell, 1992,[126] where λ_c is the critical wavelength of the source

1.3 Previous Laue Work

The Laue method has been used to investigate many structures. Tables 1.1 and 1.2 summarise the development and results of the method with small molecules and biological macromolecules respectively. Initial work involved small molecules with sealed tube sources and X-ray sensitive film as the detector. The use of the Laue method with protein crystals has had to use synchrotron radiation due to the weak scattering nature of the crystals.

With macromolecule work considerable interest, and criticism, has been shown in the data completeness. Overall completeness between $d_{min} - 2d_{min}$, $d_{min} - \infty$ and $2d_{min} - \infty$ are tabulated.

Table 1.1: Historical survey of small molecule crystal Laue (largely synchrotron) data collection and processing results (where available)

Project	Publication year	Spacegroup & Cell	d_{min} Å	λ_{min} Å	λ_{max} Å	$\Delta\phi$	N_{exp}	Exposure time (s)	$\theta_{coverage}$	R_{factor}
$CuSO_4.5H_2O$ (beerstein)[103]	1912									
Rock Salt (NaCl)[38] Iron Pyrite (FeS_2) Spinel	1913									
And many others by L. Pauling, R.W.G. Wykcoff, R. Dickinson, etc. in the 1920's to 1930's The remaining work tabulated (with one exception) has used synchrotron radiation										
continued on next page										

continued from previous page

Project	Publication year	Spacegroup & Cell	d_{min} Å	λ_{min} Å	λ_{max} Å	$\Delta\phi$	N_{exp}	Exposure time (s)	$\theta_{coverage}$	R_{factor}
ZnS [225]					4.0			10 -20		
α-$AlPO_4$ (berlinite)[253]	1983	$P3_121$								19%
(2-tert-butyloxycarbonyl)-9-0xa-1-azabicyclo[5.2.O]nonane [190] (bremsstrahlung study)	1987	$P2_12_12_1$ a=15.25Å b=5.91Å c=14.63Å								6.5%

continued on next page

continued from previous page

Project	Publication year	Spacegroup & Cell	d_{min} Å	λ_{min} Å	λ_{max} Å	$\Delta\phi$	N_{exp}	Exposure time (s)	$\theta_{coverage}$	R_{factor}
$[FeRhCl(CO)_5$ $Ph_2PCH(=CH_2)PPh_2]$ [119]	1988	$P2_1$ a=8.26Å b=19.81Å c=15.837Å β=111.3°	-	0.58	1.55	18	10	6		12.0%
$C_{10}H_{11}ClFNO$ [106]	1989	$P2_12_12_1$ a=5.418Å b=12.030Å c=15.837Å	0.9	0.2	2.6	8	13		96	8.7%
$C_{25}H_{20}N_2O_2$ [132]	1989	$P2_12_12_1$ a=11.879Å b=17.178Å c=9.711Å	0.9	0.35	1.1	10	10	0.2 Film	90	5.29% (on F)

continued on next page

continued from previous page

Project	Publication year	Spacegroup & Cell	d_{min} Å	λ_{min} Å	λ_{max} Å	$\Delta\phi$	N_{exp}	Exposure time (s)	$\theta_{coverage}$	R_{factor}
$C_{10}H_9N_4OBr.H_2O$ [107]	1990	P1 a=13.50Å b=6.84Å c=13.55Å α=96.76° β=72.32° γ=96.92°	0.9	0.35	0.9	10	19	0.25 Film	180	14.0%
$La_3C_{36}H_52N_{13}O_{21}$ [53]	1993	Pbca a=22.74Å b=21.130Å c=23.245Å	1.0	0.4	1.4			1.2		3.6%

continued on next page

continued from previous page

Project	Publication year	Spacegroup & Cell	d_{min} Å	λ_{min} Å	λ_{max} Å	$\Delta\phi$	N_{exp}	Exposure time (s)	$\theta_{coverage}$	R_{factor}
$C_{13}H_{12}N_3^+0.5(SO_4^{2-})$ [53]	1993	$P2_1/c$ a=12.703Å b=19.940Å c=21.487Å β=92.24°	0.95	0.3	1.4			80		7.7%
$AuO_{53}P_3C_{52}O_8$ [53] * Arbitary scale	1993	$C2/c$ a=36.643Å b=9.701Å c=35.008Å	0.32*	0.12*	0.45*			60		9.2%
$[Mo_5S_2O_{23}]\cdot\frac{1}{2}N(C_2H_4)]_4$ $.C_6H_5CN$ [157]	1993	$P2_1/n$ a=12.712Å b=30.38Å c=14.745Å β=88.02°	1.05	0.25	1.05					10.7%

continued on next page

continued from previous page

Project	Publication year	Spacegroup & Cell	d_{min} Å	λ_{min} Å	λ_{max} Å	$\Delta\phi$	N_{exp}	Exposure time (s)	$\theta_{coverage}$	R_{factor}
$[AuOS_3H(CO_8)\{PH_2PCH_2P(Ph)$-$C_6H_4\}(PPh_3)]$[78]	1994	C2/c a=37.46Å b=9.645Å c=34.86Å β=104.6°	0.65	0.24	1.80	60 10	5	14 Film	140	7.8%
$Ru(C_12H_10O_4)(C_8H_1P)_2$ $(CO)_2$[78]	1994	C2/c a=9.637Å b=13.689Å c=23.042Å	0.65	0.28	1.50	20 60	8	0.2 Film	140	7.5%

continued on next page

continued from previous page

Project	Publication year	Spacegroup & Cell	d_{min} Å	λ_{min} Å	λ_{max} Å	$\Delta\phi$	N_{exp}	Exposure time (s)	$\theta_{coverage}$	R_{factor}
$(Mg_90Fe_10)_2SiO_4$ [91]	1994	a=4.76Å b=10.21Å c=6.00 Å	0.5	0.2	2.6	25 10	5	0.05 un- processed		
NiAPO [219]	1995	$P2_1/n$ a=10.02Å b=15.73Å c=14.13Å β=101.31°	0.95	0.36	1.50	10	20 This thesis	0.3	190	7.9%

The term $\Delta\phi$ is the angular step (in degrees) between exposures. N_{exp} is the number of exposures and $\theta_{coverage}$ is the angular range of data collected. The R_{factor}, referred to in the last column of the table, is defined by $R_{factor} = \frac{\sum_{hkl} ||F_{obs}| - k|F_{calc}||}{\sum_{hkl} |F_{obs}|}$ where F_{obs} is the observed structure factor amplitude, F_{calc}, the structure factor amplitude calculated from the structure model and k a scaling factor

Table 1.2: Historical survey of protein crystal synchrotron Laue data collection and processing results

Project	Spacegroup & Cell	d_{min} Å	λ_{min} Å	λ_{max} Å	$\Delta\phi$	N_{exp}	Time sec	θ_{cover}	Completeness			R (I)
									d_{min} -∞	d_{min} -$2d_{min}$	$2d_{min}$ -∞	
Myoglobin[166, 169]	- - - -	-	-	-	-				-	-	-	
Pea Lectin[122, 123, 128]	$P2_12_12_1$ a= 50.73Å b= 61.16Å c= 136.59Å	2.6	0.4	2.5	15° or 30°	6		90°	-	-	-	

continued on next page

continued from previous page

Project	Spacegroup & Cell	d_{min} Å	λ_{min} Å	λ_{max} Å	$\Delta\phi$	N_{exp}	Time sec	θ_{cover}	Completeness			R (I)
									d_{min} -∞	d_{min} -$2d_{min}$	$2d_{min}$ -∞	
Glycogen phosphorylase b [115]	$P4_32_12$ a=b=128.8Å c=116.2Å	2.4	0.2	2.1	11.25°	3	-	22.5°	38%	-	-	
Xylose isomerase [94]	I222 a=98.7Å b=93.9Å c=87.7Å	2.5	0.2	2.5	45°	3	1-2	90°	-	-	-	
Bovine pancreatic β trypsin [19]	$P2_12_12_1$ a=54.8Å b=58.4Å c=67.6Å	1.8	0.6	2.0	5°	19	1-30	90°	35%	-	-	

continued on next page

continued from previous page

Project	Spacegroup & Cell	d_{min} Å	λ_{min} Å	λ_{max} Å	$\Delta\phi$	N_{exp}	Time sec	θ_{cover}	Completeness d_{min} -∞	Completeness d_{min} -$2d_{min}$	Completeness $2d_{min}$ -∞	R (I)
Tomato bushy stunt virus [49]	I23 a=b=c=383Å	3.5	0.38	2.1	-	1	24	-	90%	-	-	
Ha-Ras p21 [208, 209, 210]	$P3_221$ a=b=41.0Å c=164.8Å	2.8	0.7	2.0	-	3	10-15	15°	50%	-	-	
γ chymotrypsin [226]		2.5							25%	-	-	
Turkey egg white lysozyme [137]	$P6_522$ a=b=70.89Å c=84.6Å	2.5 (2.5)	0.2 (0.65)	2.1 (1.9)	-	1 (2) Film	2		67% (73%)	-	-	7.4% 8.4%

continued on next page

continued from previous page

Project	Spacegroup & Cell	d_{min} Å	λ_{min} Å	λ_{max} Å	$\Delta\phi$	N_{exp}	Time sec	θ_{cover}	Completeness d_{min} -∞	Completeness d_{min} -$2d_{min}$	Completeness $2d_{min}$ -∞	R (I)
Bovine pancreatic trypsin [18]	$P2_12_12_1$ a=63.6Å b=63.5Å c=67.8Å	1.5	0.68	1.6	-	9	0.1-0.5	-	40%	-	-	10.9%
Human carbonic anhydrase II [154]	$P2_1$ a=42.7Å b=41.7Å											
(HSO_3^- derivative)	c=73.0Å	2.2	0.4	2.3	10°	16	3		67%	81%	16%	9.4%
(pH6 derivative)	$\beta = 104.6^\circ$	"	"	"	"	7	20		55%	66%	16%	7.5%

continued on next page

continued from previous page

Project	Spacegroup & Cell	d_{min} Å	λ_{min} Å	λ_{max} Å	$\Delta\phi$	N_{exp}	Time sec	θ_{cover}	Completeness d_{min} -∞	Completeness d_{min} -$2d_{min}$	Completeness $2d_{min}$ -∞	R (I)
Glycogen phosphorylase b [80, 81]	$P4_32_12$ a=b=128.5Å c=116.3Å	2.5	0.5	2	11.5°	3	0.8	23°				
(Dark)									40%	-	-	9.8%
(3 min illumin.)									38%			14.1%
(15 min illumin.)									32%			10.6%
(1 hour illumin.)									29%			10.5%
Co concanavalin A [57] (Image Plate)	I222 a=88.7Å b=86.5Å c=62.5Å	2.0	0.5	0.9	7° and 10°	15	10	122°	76.5%	80.5%	51.6%	7.7%

continued on next page

continued from previous page

Project	Spacegroup & Cell	d_{min} Å	λ_{min} Å	λ_{max} Å	$\Delta\phi$	N_{exp}	Time sec	θ_{cover}	Completeness d_{min} -∞	Completeness d_{min} -$2d_{min}$	Completeness $2d_{min}$ -∞	R (I)
Myoglobin [47] (Deoxy)	$I2_1$ a=124.2Å b=42.5Å c=92.0Å β=92.0°	2.2	-	-	6°	24	10	-	72%	77%	39%	8.7%
(Carbonmonoxy)	a=124.6Å b=42.5Å c=92.1Å β=92.2°	2.1	-	-	6°	19	15	-	63%	67%	38%	11.1%

continued on next page

continued from previous page

Project	Spacegroup & Cell	d_{min} Å	λ_{min} Å	λ_{max} Å	$\Delta\phi$	N_{exp}	Time sec	θ_{cover}	Completeness			R (I)
									d_{min} -∞	d_{min} -$2d_{min}$	$2d_{min}$ -∞	
gGAPDH [239]	$P2_12_12$ a=135.5Å b=86.5Å c=62.5Å	3.2	0.54	1.84	25° and 15°	8	3.5-2.0	75°	52%			14.7%
Native concanavalin A [249] (Film)	I222 a=88.7Å b=86.5Å c=62.5Å	1.95	0.5	0.9	5° and 7.5°	20		120°	77.4%	82.6%	43.0% 45.5%	9.4% 9.9%
Chicken egg white lysozyme [50] (*with multiples)	$P4_32_12$ a=b=79.1Å c=37.9Å	2.5	0.488	1.9	15° and 25°	4	0.2-0.25	55°	58.4% 67.3%*	68.0% 73.3%	0.0% 31.0%	6.8% 8.1%

continued on next page

continued from previous page

Project	Spacegroup & Cell	d_{min} Å	λ_{min} Å	λ_{max} Å	$\Delta\phi$	N_{exp}	Time sec	θ_{cover}	Completeness d_{min} -∞	Completeness d_{min} -$2d_{min}$	Completeness $2d_{min}$ -∞	R (I)
Chicken egg white lysozyme (this thesis)	$P4_32_12$ a=b=79.1Å c=37.9Å	2.5	0.40	1.55	2°	31	0.5	60°	86.1%	88.1%	68.6%	8.9%
					4°	16		60°	84.8%	87.0%	64.7%	8.6%
					10°			60°				8.8%
					30°			60°				9.6%
Isocitrate dehydrogenase [33]	$P4_32_12$ a=b=105Å c=37.9Å	2.5	-	-	-	4	0.75	-				9.2%

In this case the R in the last column is termed the R_{merge} (or R_{factor} on I) and is given by $R_{merge} = \frac{\sum_{hkl}\sum_{j=1}^{N}|I_{hkl}-I_{hkl}i|}{\sum_{hkl}\sum_{i=1}^{N}I_{hkl}i}$ where $I_{hkl}i$ is the intensity of the ith measurement of reflection I_{hkl} and I_{hkl} is the mean intensity of the reflection

Chapter 2

Laue Theory and Practice

2.1 Introduction

This chapter describes the theory of Laue diffraction and the practice of how the problems, outlined in chapter 1, have been tackled. In essence the accuracy of the Laue technique is affected by a number of different possible sources of error. The main differences from monochromatic conditions that arise with Laue geometry are the dense population of reflections, the reduced signal to noise ratio due to the wider bandwidth (than monochromatic) of incident radiation, imperfect corrections for wavelength dependent effects and influence of crystal mosaicity (or perfection) on spot sizes. The acceptability of electron density maps calculated on the basis of Laue structure amplitudes is potentially further affected, unless particular care is exercised, by a systematic lack of completeness in the low resolution area of the data set. These problems are addressed in this chapter so as to define, in a pragmatic way, a compromise between speed of data acquisition and map quality.

The Laue method has two major advantages over monochromatic data collection.[26, 114, 129, 169, 194, 253] These are;

- Optimal harnessing of the intrinsic polychromatic nature of the synchrotron radiation emission to increase the flux intercepted by the (stationary) crystal.
- Direct production of integrated intensities with a stationary crystal ie. without the need to rotate the crystal over time, a fundamental requirement of monochromatic beam methods - excluding the convergent beam method.[257]

Much reduced exposure time over monochromatic methods result because of the use of the polychromatic beam. Many reciprocal lattice points are stimulated at once allowing the simultaneous recording of many reflections. The use of a stationary crystal also allows complete reflections to be recorded and removes problems with partials and crystal or beam decay during oscillation. These advantages make Laue techniques suited to rapid and time-resolved data collection.[113, 127, 167, 197] The method is only limited by the detector and the amount of photons that can be "instantaneously" applied to the crystal for a given exposure time.[63] Indeed it has been possible to produce a quantitative analysis of Laue patterns recorded in 120 ps.[232] From the outset of protein crystallography with synchrotron radiation sources dynamic possibilities have been a potential[121] as a natural extension of the earliest example of the use of synchrotron radiation in biological diffraction (from muscle fibres).[201] It is a very exciting but technically very challenging exercise which can lead to the direct visualization of a biological macromolecule as it functions.

2.2 Reciprocal Space Sampling: Energy Overlap and Wavelength Bandpass

In the Laue case the volume of reciprocal lattice that can be sampled in one image lies between Ewald spheres of radii $1/\lambda_{max}$ and $1/\lambda_{min}$, where λ_{max} and λ_{min} are the minimum and maximum incident wavelengths respectively, and the resolution sphere of radius $1/d_{min}$. This is illustrated in figure 2.1 adapted from Cruickshank *et al.*.[66] The shaded area shows the accessible region. Each Laue reflection will arise from the reciprocal points in the accessible region of reciprocal space. Reciprocal lattice points corresponding to the first and all higher orders lying on a central line passing through the origin of reciprocal space and can lead to a Laue spot being made up of several wavelength components. The Laue spots suffering from wavelength or energy overlap are termed multiplets, two wavelengths contributing to the spot give doublets, three, triplets etc. The multiplet problem was considered fundamental and thus prevented the use of the Laue method in quantitative crystal structure analysis. A full treatment of the multiplicity distribution of reflections[66] revealed that in the worst case of an infinite incident wavelength range 72.8% of the reciprocal lattice points were **in fact** stimulated by a single wavelength, 14.6% by two, 5.4% by three and 7.2% by higher multiplets.

When a finite wavelength range is used these figures improve such that with the widest wavelength range typically available experimentally ($0.3< \lambda < 2.6$ Å) the proportion of reciprocal lattice points stimulated by a single wavelength exceeds 83%.[66] Hence, the multiplicity problem caused by the relatively large volume of reciprocal space sampled (as opposed to monochromatic methods) in

one exposure is not as great a problem as had been initially thought. Until fairly recently, in modern Laue data processing multiples were discarded from the data set. Now however, continually improving and diverse computational techniques have been developed allowing them to be readily deconvoluted into their separate intensities.[51, 117, 195]

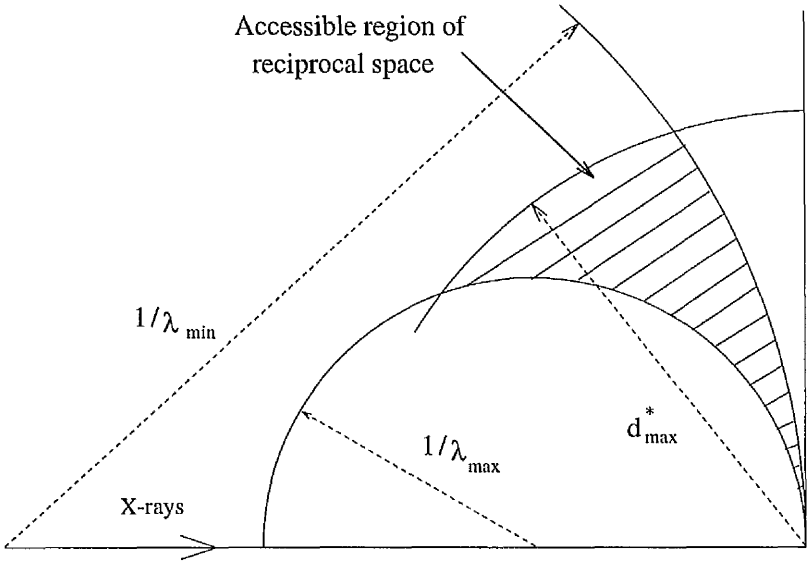

Figure 2.1: Ewald representation of the region of accessible space (cross-hatched) with the Laue method

An ideal wavelength range can be chosen by consideration of the signal to noise ratio.[231] The number of stimulated reflections is given by[166];

$$N_L = \frac{\frac{\pi}{4} d^{*4}}{V^*} (\lambda_{max} - \lambda_{min}) \tag{2.1}$$

where d^* is the limiting resolution of the crystal (assuming $d^* < 2/\lambda_{max}$) and V^* is the volume of the reciprocal unit cell. Longer wavelengths will produce a larger number of reflections though greater absorption and crystal damage will

result. Specimen absorption varies as λ^3 and somewhat lessens the effect of reduced scattering (λ^2 dependent) at shorter wavelengths.[11] Systematic errors in data owing to absorption become increasingly severe at longer wavelengths. An operational upper limit to the wavelength before these errors become unmanageable has been suggested by Sweet *et al.*,[231] as 1.5–1.6 Å. A practical example of the choice of wavelength range is given in Campbell *et al.*[50] where wavelength band pass of 0.5–2.2 Å was used for data collection with a band pass of 0.49–1.60 Å for processing. Reflections stimulated at shorter wavelengths are both weakly scattered and detected while spots stimulated at longer wavelengths also become weak due to absorption.

2.3 Spatial Overlap

The Laue diffraction spots themselves are of a finite size dependent on several factors such as crystal mosaic spread, beam divergence and collimator size.[9] A large number of spots are recorded, the minimum required separation between their centres for spot integration is determined by the finite size of the spots, crystal to detector distance, resolution of the crystal, wavelength range used and dimensions of the unit cell. Obviously for higher resolution and/or longer wavelength ranges more reciprocal lattice points are stimulated resulting in more spots. The closest spots tend to be at the high resolution limit of the data.[67] Decreasing the wavelength range and increasing the crystal to detector distance reduce the spatial overlap problem. New strategies using a 'toast-rack' form of detector[57, 125, 249] help alleviate this problem. In the Laue pattern there is a correlation of stimulating radiation wavelength with Bragg angle. The densest

parts of the pattern[67] occur at the Bragg angle of $\theta_d = \sin^{-1}(\lambda_{min}/2d_{min})$. By placing several films parallel to one another spaced some distance apart, the dense short wavelength parts of the pattern can penetrate to the rear of the film and so expand to fill the available area. Advances in producing more perfect crystals, chapter 8, will allow much larger crystal to detector distances to become feasible and reduce spatial overlap problems.

2.4 The "Low Resolution Hole"

At high resolution the completeness distribution for Laue and monochromatic structure factors are found to be similar but at lower resolution the Laue data are substantially less complete,[18, 66] a "low resolution hole"[62] occurs in the data. The volume of reciprocal space sampled in a Laue exposure narrows to a cusp toward the origin (see figure 2.1) ie. towards lowest resolution. Between exposures the crystal is rotated by an angle interval $\Delta\phi$ round the spindle axis. This angle will always be larger than the opening angle of the cusp which is effectively zero. Therefore, at the lowest resolutions, a proportion of reciprocal lattice points can not even come into the diffraction position at all. The resolution to which the reciprocal space is sampled incompletely, d_{all}, is given by[246];

$$d_{all} = \frac{\lambda_{min}\sqrt{1 + \frac{1}{k^2}}}{2} \tag{2.2}$$

where

$$k = \frac{\sin(\Delta\phi)}{\left(\frac{\lambda_{max}}{\lambda_{min}}\right) - \cos(\Delta\phi)} \tag{2.3}$$

By decreasing $\Delta\phi$, the difference in spindle angle between exposures, d_{all} can be increased, increasing the bandpass also increases d_{all}. Obviously to stimulate the unique region of reciprocal space a certain total angular coverage is required. To improve the completeness means that more exposures are needed within this overall angular coverage.

Low resolution diffraction spots are of higher average intensity than high resolution reflections. Exposure times are usually chosen to achieve as high a resolution for the dataset as possible. Therefore a significant proportion of the low resolution reflections may saturate the detector, especially with a detector of limited dynamic range. This can exacerbate the low resolution hole.

The lack of low resolution data can have several effects. Firstly, on the structural solution, atoms with high temperature factors may escape detection altogether with such truncated data. Secondly, electron density maps can become increasingly fragmented.[18, 80] Thirdly, partial data sets can cause problems in the interpretation of isomorphous difference Patterson maps.[113] Simply put poor completeness can plague the X-ray analysis. The use of too few exposures and too poor overall coverage will exacerbate things.

2.5 Wavelength Normalisation

Several factors affect the intensity of the measured Laue diffraction spot;

- The incident intensity of the synchrotron radiation spectrum.
- Long wavelengths are attenuated as the beam passes through beamline windows, air gaps etc.

- Sample absorption from crystal and capillary (if used).
- Short wavelengths are cut off by reflecting mirrors, if used.
- Detector response is wavelength dependent.
- There is a factor of λ^4 in the formula for integrated intensity

To correct for these factors wavelength normalisation can be achieved by the use of a wavelength normalisation curve f(λ) defined as;

$$f(\lambda) = (I_{Laue}/I_{mono}) \tag{2.4}$$

where I_{Laue} is the intensity of a reflection measured at a specific wavelength, λ, and I_{mono}, the relative intensity it would have if all reflection intensities were measured at one wavelength. The normalisation curve can however be found internally from the Laue data alone since the same reflection or symmetry equivalents are usually measured several times. These symmetry equivalents should have the same final intensity, in the absence of anomalous scattering, after wavelength normalisation. Hence it is possible in fact to put all the Laue data onto the same relative scale of intensity. Alternatively $f(\lambda)$ may be determined by comparing the Laue intensities with intensities measured by monochromatic methods for another crystal of the same substance. This normalization curve is applied to the collected intensities 'normalizing' to one wavelength for subsequent structure refinement. In this thesis some novel features are illustrated with the processing of image plate (rather than film) Laue data (chapter 3) and of European Synchrotron Radiation facility (ESRF) Laue data (shift of peak output to shorter wavelengths).

2.6 Multiple Deconvolution

Methods for the deconvolution of the separate intensities of the components of multiples have been developed.[51, 117, 259] The first method was dependent on the difference in energy absorption of a media for different wavelengths.[259] With X-ray sensitive film as a detector several films are usually used back to back in a film pack with the option of Al or foils or blank film as a separator between films. By analysing the intensity of a multiplet spot recorded on successive films the separate intensities of the individual reflections making up the multiplet can be evaluated by a least squares procedure. The procedure, it was found in practice, can be used for multiplets up to triplets but the accumulation of errors means that it cannot be extended beyond this.[259] The method is extendable to image plates in that it was shown that two image plates can be used placed one behind the other, in an analogous manner to the film packs.[125]

A second method is based on the same principles and assumptions as "direct methods" for phase determination.[117, 206] It is similar to the formula for extracting the relative contributions of overlapping reflections in powder diffraction[69] but has only been applied to small molecule Laue data at present.[117]

The method tested and applied further in this thesis is that of deconvolution using the wavelength normalization curve (section 2.5) with image plate data. This method is best illustrated by reference to figure 2.2. A doublet is shown in two different orientations using the Ewald sphere representation in reciprocal space.

In the first orientation the two components of the doublet arise from wavelengths

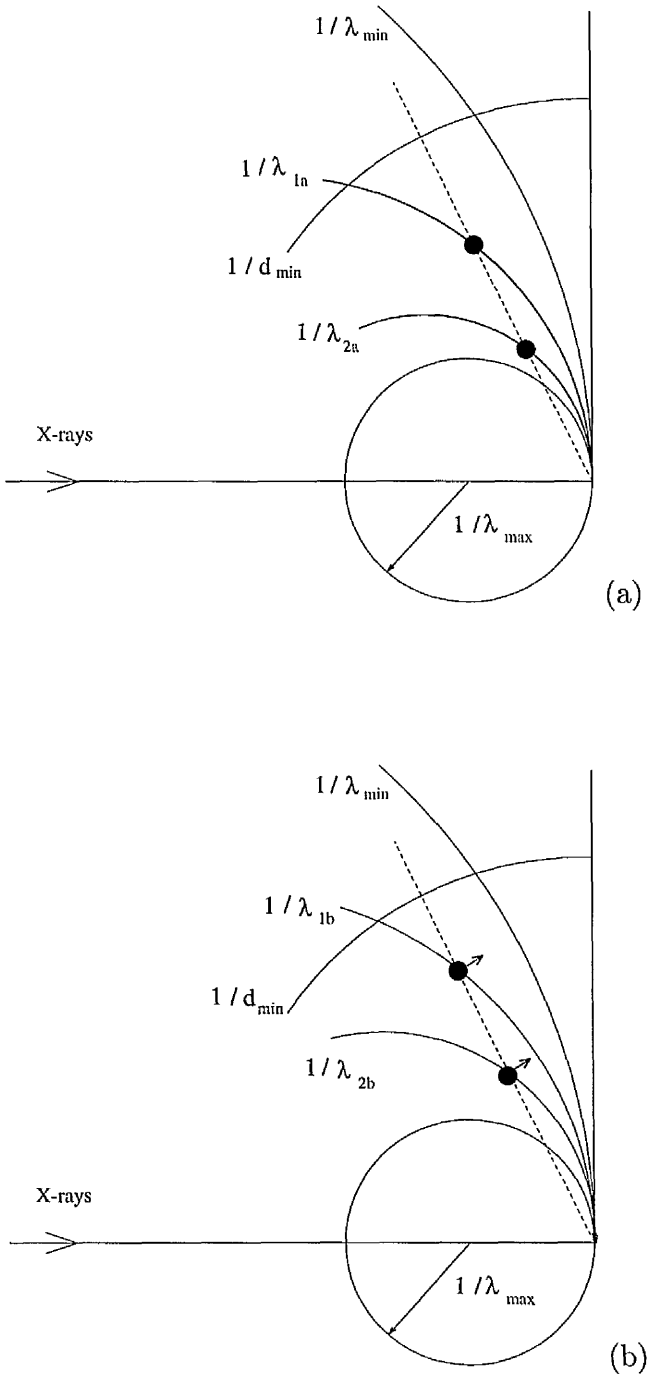

Figure 2.2: Example of the diffraction geometry for a Laue doublet for two different crystal orientations (a) and (b). For each case the Ewald spheres are shown for the two wavelength components of the double λ_{1a}, λ_{2a} in the first orientation and λ_{1b}, λ_{2b} in the second. The spheres marking the soft limits, λ_{min}, λ_{max} and d_{min} are also shown.

λ_{1a} and λ_{2a} where $\lambda_{2a} = 2\lambda_{1a}$. Similarly in the second orientation two components of the doublet arise from wavelengths λ_{1b} and λ_{2b}. Wavelength normalisation factors $f(\lambda)$ can be determined from singles data for each of the four wavelengths. If I_1 and I_2 are the normalized reflection intensity components of the double (ie. the desired values) and $I_{obs(a)}$ and $I_{obs(b)}$ the integrated intensities of the doublet spots then the following equations can be solved;

$$f(\lambda_{1a})I_1 + f(\lambda_{2a})I_2 = I_{obs(a)} \tag{2.5}$$

$$f(\lambda_{1b})I_1 + f(\lambda_{2b})I_2 = I_{obs(b)} \tag{2.6}$$

and the intensities of the component evaluated given there are two equations and two unknowns, provided $f(\lambda)$ is available. In general for an n component multiple spot at $(m \geq n)$ orientations we have;

$$\sum_{i=1}^{n} f(\lambda_{ij})I_j = I_{obs(j)} \quad (j = 1, 2, \ldots m) \tag{2.7}$$

In this way, to some extent (ie. up-to a certain multiplicity n and a certain statistical quality), intensities of multiples can be evaluated and used in the structure refinement.

2.7 Correction for f' and f'' variation

The scattering factors of atoms can change significantly over a wavelength range

due to anomalous scattering. This anomalous scattering has a phase change effect on the scattering factor for an atom. The scattering factor for the atom becomes 'complex' and f is given by;

$$f = f_o + f'(\lambda) + if''(\lambda) \tag{2.8}$$

where $f'(\lambda)$ and $if''(\lambda)$ vary with the wavelength of the incident radiation. This has to be taken into account with Laue data, which is obviously a polychromatic method.

2.8 Crystal Perfection

The Laue technique is more sensitive than monochromatic techniques to crystal disorder.[194] Crystal disorder is, in general, highest in protein crystals, characterised by a high solvent content (c.a. 30-80%)[159] and only few intermolecular contacts. Their internal ordering cannot therefore be expected to be perfect. In fact some protein crystals display very small angular rocking widths (eg. 0.015° for 2-Zn insulin[64]) whereas other small molecule crystals have a high mosaicity (eg. 2-3° for a small ($18 \times 8 \times 175 \mu m^3$) silicate crystal).[10] In the case of a perfect crystal all unit cells (10^{15} or so) would be perfectly aligned without any repetition errors. In such a case the angular rocking width (ie. the angle by which the crystal is rotated to fully record a diffraction spot) could be given by $\eta_{hkl} \approx (a/L)$ where a is the relevant unit cell edge and L either the length of the crystal or the extinction length, whichever is smaller (see chapter 10). Figure 2.3 shows an typical example with a cell edge of 50Å and crystal length of 0.5 mm.

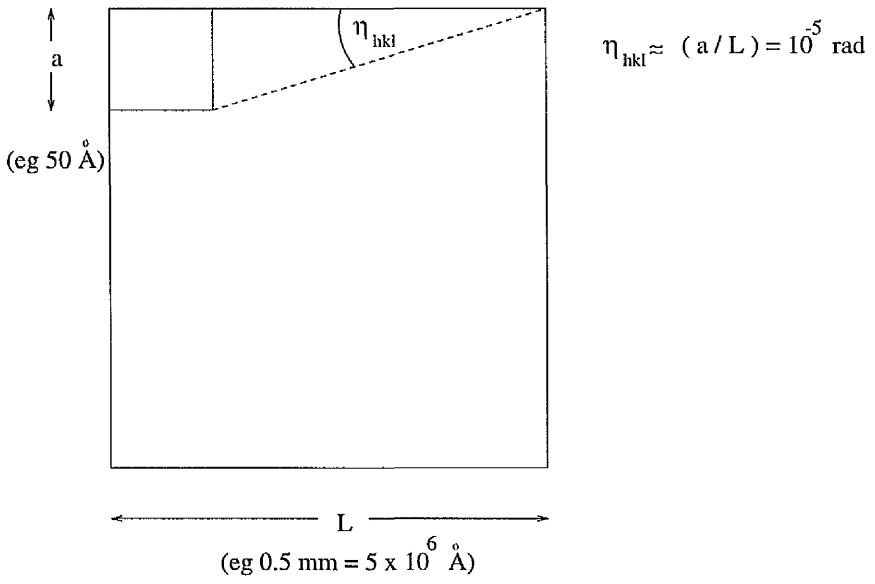

Figure 2.3: Explanation of mosaicity, η_{hkl}, of a crystal from Snell *et al.* (1995)[221]

In general, neither a or L are isotropic so it follows that η_{hkl} is, in the limit, anisotropic. A mosaic crystal is assumed to consist of blocks of perfect crystals which are misaligned to each other,[68] figure 2.4. Evidence for the mosaic block construction of a crystal has been indicated from high resolution diffractometer studies of tetragonal lysozyme crystals[221] and seen in X-ray topographs of the similar crystals (see chapter 10).[228]

The mosaic spread is then $\sqrt{\eta_{hkl}^2 + \eta^2}$ where η is the overall misalignment angles of the blocks of the sample. This is a good indication of crystal quality. Obviously reducing mosaic spread could be expected to produce improved crystals for X-ray data collection.

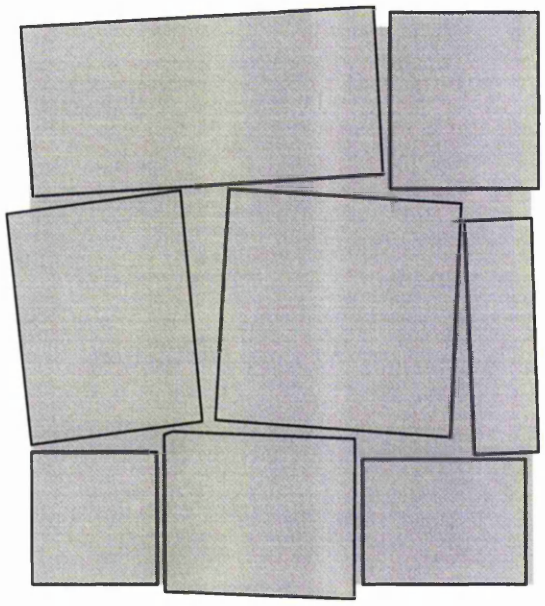

Figure 2.4: Schematic diagram of an ideally imperfect "mosaic" crystal, each bounded "mosaic" block can be considered as a perfect crystal. Several such blocks make up the crystal. From Snell *et al.* (1995)[221]

Chapter 3

Image Plate Small Crystal Study

3.1 Introduction

Image plates[5, 7, 6, 164] have had an important impact in X-ray crystallographic data collection both at the synchrotron and in the home laboratory. Also the advantageous speed of acquisition of area detector data in chemical crystallography, compared with diffractometry, can be critical. For example the number of reflections to be measured may be large whether due to a larger than average unit cell, a low symmetry space group or an interest in very high resolution data. Alternatively, a sample may be air sensitive and again speed of data collection may be critical.

The ease and speed of data collection at the synchrotron, ~~especially on time factors,~~ can benefit from the use of a large versatile area detector like the image plate. Although photographic film has been used effectively in a number of synchrotron studies of small molecules (examples from the Laue method are shown in table 1.1) the use of film with smaller and smaller crystals is ultimately beset by the problem of very small or very narrow (streaked) spots for which the pixel sampling of the

spot is too poor and/or the Wooster effect[254, 255] is a limitation. One aspect of this chapter is to show that image plates can readily be used with a small test crystal ($0.02 \times 0.05 \times 0.25$ mm^3) to provide data with good pixel sampling of the diffraction spots good enough for structure determination and refinement in contrast to the problems encountered with small spots and film as the detector. As the test case the crystal structure of a nickel containing aluminophosphate, whose structure has been solved using CuKα and MoKα monochromatic diffractometry,[131] is determined with the image plate data.

3.2 Image Plate and Film as Area Detectors

Image Plates

Image plates have advantages over photographic films which include wider dynamic range (1:10^5) (less chemical fog ie. noise), higher detector quantum efficiency, reduced exposure time (more sensitive) and large size. The detector quantum efficiency* of an image plate is better then 80% for 8-20 keV X-rays.[6] The plate consists of an amorphous layer (150 μm thick) of Barium-Europium halides (BaFBr:Eu^{2+}) with a protective layer (10 μm thick) and a support layer (250 μm thick) . Irradiation with X-rays creates so called colour or F centres which are meta-stable states of the trapped electrons in the phosphor. An excitation energy of 6 eV is required to create a colour centre. The phosphor has high absorption efficiency for X-rays and extremely low background (although

*Detector quantum efficiency, DQE, defined by $DQE = (S/N)_{out}/(S/N)_{in}$ where S is signal and N is noise.

not zero), 1/300 that of film[164] chemical fog. In addition there is no instantaneous count rate limitation and hence the image plate can make full use of the high flux of the synchrotron source. Upon absorption of a 2 eV photon of red He-Ne laser light (used to 'read' the image) the meta-stable electron returns to its ground state with subsequent emission of blue light. The intensity of this blue stimulated luminescence is proportional to the number of absorbed X-rays. A commonoly available image plate reader at synchrotron radiation sources is the MAR system. Its performance will be described as an example. The imaging plate is circular (180 mm in diameter) and its readout time is 70 seconds with an additional 20 seconds for erasure. The plate is read by rotating it under laser illumination with a photomultiplier scanning across the plate. In order to ensure that the readout time per pixel is constant over the circular plate the rotational speed is changed in proportion to the inverse radius of the scanner position to the centre of the plate. The number of pixels is proportional to the radius at any point. Due to the scan along a spiral curve the diffraction pattern is recorded in polar coordinates (R,θ), these are transformed into Cartesian (x,y) coordinates for further analysis and display. Uniformity response varies less than 1.6% over the active area and results are reproducible over a long period of repeated use unlike the processing of films which are each affected by slight changes in development conditions. Image plates still have a long readout time, of the order of minutes, and, for weak data have a lower signal to noise level than other detectors eg. multiwire gas proportional counters[152] and CCDs.

X-ray sensitive photographic film

Film has been commonly used as a X-ray detector. For X-ray photon energies greater than about 2KeV a single photon suffices to render a grain of the emulsion developable. The background density level (of developed grains) on photographic film amounts to 1000 X-ray photons compared to less than 3 per pixel per equivalent area for the image plate.[7] This background density represents the optical density for an un-exposed film developed in the standard way and includes contributions from the film base and emulsion chemical fog.[87] A high film background does not in itself reduce the accuracy of measurements but, since all density measurements are made superimposed upon this background, the dynamic range of a single piece of film is reduced. The detector quantum efficiency performance of film is affected in two ways. Firstly, incident quanta striking grains which have already been activated are wasted. Secondly, input photon noise is effectively amplified by the chemical fog, and, the fogged grains also contribute an additive noise to the signal.

The penetrating power of X-rays is such that it is practicable to use film bases which are coated with emulsion on both sides. Film has a very high spatial resolution, 12.5-25 μm (compared to image plate of 150 μm), but a low dynamic range. The dynamic range is determined by the differences in grey level that can be distinguished and the chemical fog due to developing. To extend the dynamic range several films can be used together in a film pack because the absorption efficiency of film for X-rays in the wavelength range between 0.6 and 1.8 Å lies between 20% and 70%. Photographic film contains silver bromide grains and therefore the absorption efficiency jumps at each absorption edge (0.92 Å Br K

edge, 0.49 Å Ag K edge). Data cannot be processed at wavelengths close to these absorption edges and has to be rejected.

Films are scanned with an optical densitometer, this has a resolution of 1 part in 256 repeatable grey level. The density is recorded by the microdesitometer via measuring the transmitted light through the film. It is related to the incident light intensity, I_o, and transmitted light intensity, I, by[254, 255];

$$D = log\left(\frac{I_o}{I}\right) \tag{3.1}$$

The X-ray intensity (density on the film) is therefore related in a logarithmic way to the intensity of the light transmitted through the film. Several important factors have to be considered when recording with film. This logarithmic variation causes the observed density to be too small in cases where the diffraction spot is small or streaked compared to the area scanned.[254, 255] This type of error, termed the Wooster effect, becomes worse as the diameter of the spots diminishes. X-ray films have relatively large grains of silver which are clearly visible with a microscope. The result of examining a small area is that the number of grains in the field of view varies considerably over an area that has been uniformly exposed to X-rays. What is gained in resolution in narrowing down the area examined is lost in reproducibility. For this reason, although films can be scanned with a 12.5 μm scan step, 50 μm is chosen to smooth out such variations. Hence to get both reproducibility and avoid Wooster effects with film decent sized spots are needed.

3.3 Nickel Aluminophosphate Small 'Test' Crystal

The Nickel Aluminophosphate (NiAPO) 'test' crystal used had dimensions of $0.02 \times 0.05 \times 0.25$ mm^3 (ie. needle shaped). The crystal itself was bright blue in colour and elongated along the [010] axis for data collection. It was supplied and mounted by Prof. V. Kaucic from the National Institute of Chemistry, Ljubljana, on to a thin glass fibre. Crystallization of NiAPO was carried out in a teflon lined autoclave under static conditions at 443K over 4 days.[191] The reaction gel used had the composition $0.4NiO{:}0.8Al_2O_3{:}1.0P_2O_5{:}1.5en{:}50H_2O$ where en=ethylenediamine. The source of the nickel was nickel acetate and the source of the aluminium was aluminium isopropoxide. The chemical formula for NiAPO is $NiAl_3P_4O_18C_4H_21N_4$ with a molecular weight of 676.77 and density of 2.06 gcm^{-3}. Four molecules are present in the unit cell, monoclinic space group $P2_1/n$. Cell parameters are a=10.02 Å, b=15.728(6) Å, c=14.134(6)Å and β=101.313(14)° with a volume of 2184.16 Å^3.

3.4 Data Collection

Station 9.5[41, 125, 235] of the Synchrotron Radiation Source (SRS) at the Daresbury Laboratory was used for data collection. The SRS was operating at 2 GeV with a current of 195 mA and wiggler at 5 T. A Mar Research Image Plate Scanner, diameter 180 mm was used as the detector, figure 3.1. Twenty images were recorded at 10° intervals each with an exposure time of 0.3 seconds. An example is shown in figure 3.2(a).

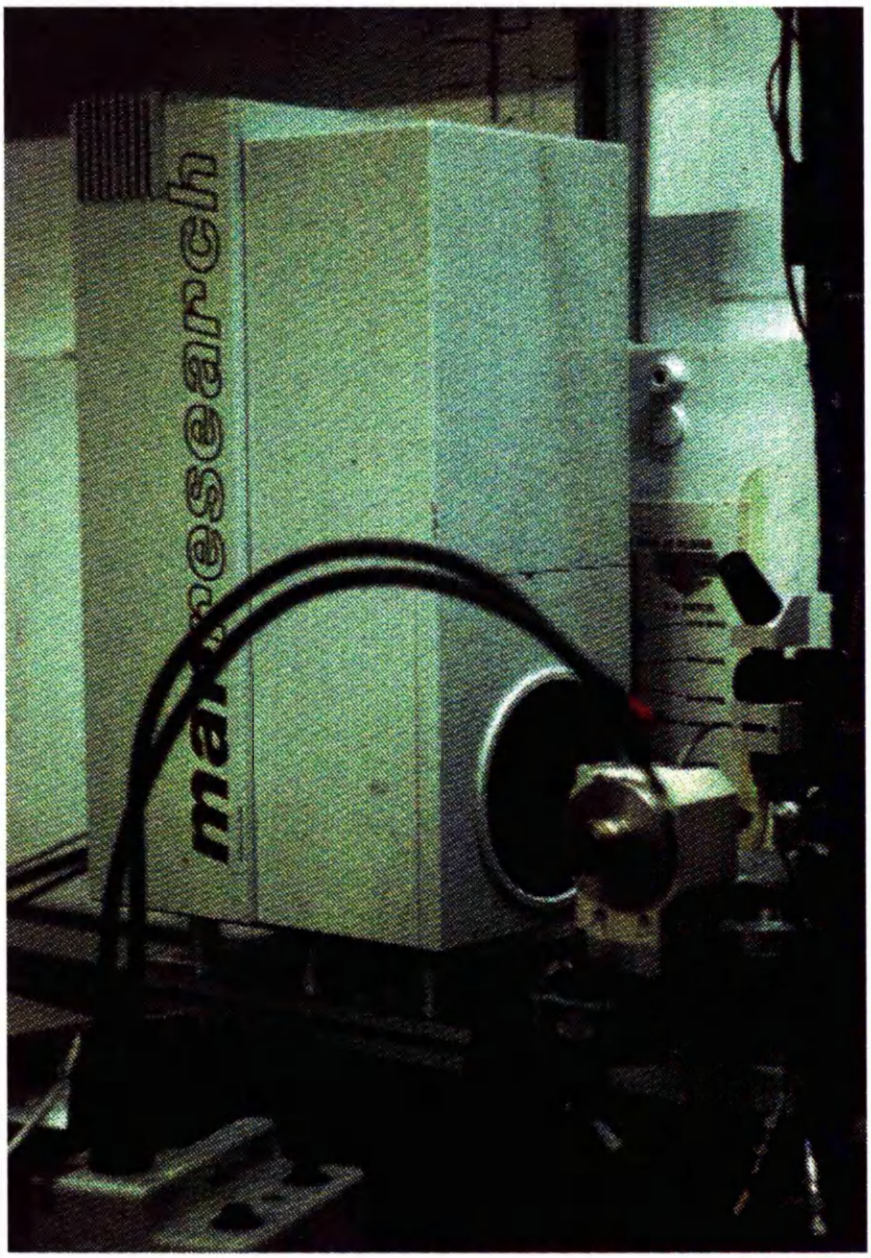

Figure 3.1: MAR image plate used for data collection on station 9.5 of the SRS

Indexing the Pattern

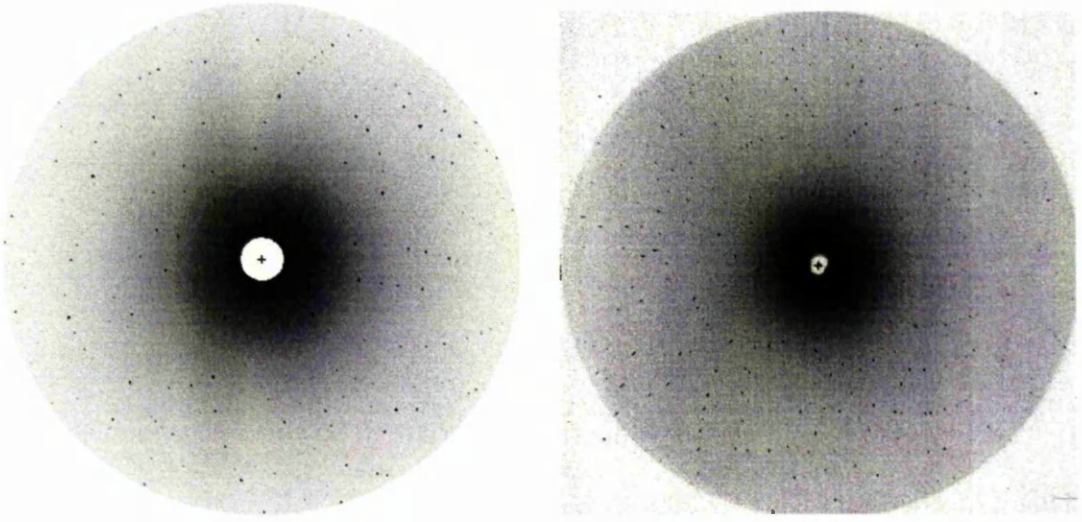

(a) (b)

Figure 3.2: NiAPO Laue data recorded on (a) image plate and (b) film at crystal to detector distances of 141 mm and 61 mm respectively. The effective aperture of the image plate is 32° and the film 44° so more of the diffraction pattern is seen recorded on the film. The image plate could not be moved any closer due to physical constraints.

The image plate has a duty-cycle of $2\frac{1}{2}$ minutes (ie. for scanning the image plate, writing the digitised image to disk and erasing the image plate). Hence the overall data collection time was dominated by this (compared to the crystal exposure time). The total elapsed time for the whole data collection was less than one hour. The illuminating white beam spectral range was $0.4 < \lambda < 2.0$ Å. Crystal to detector distance used was 141 mm. A 0.2 mm thick piece of aluminium foil was inserted into the upstream end of the collimator so as to reduce the X-ray background for attenuation of the longer wavelengths in the incident X-ray spectrum. To compare the image plate with X-ray sensitive film a single film exposure was also taken with an exposure time of 10 seconds, figure 3.2(b). The film was scanned by a Joyce-Loebl Ltd. microdesitometer using a tungsten

halide light source and 50 μm step size. Figure 3.3 shows the film plate holder and camera on station 9.5 of the SRS.

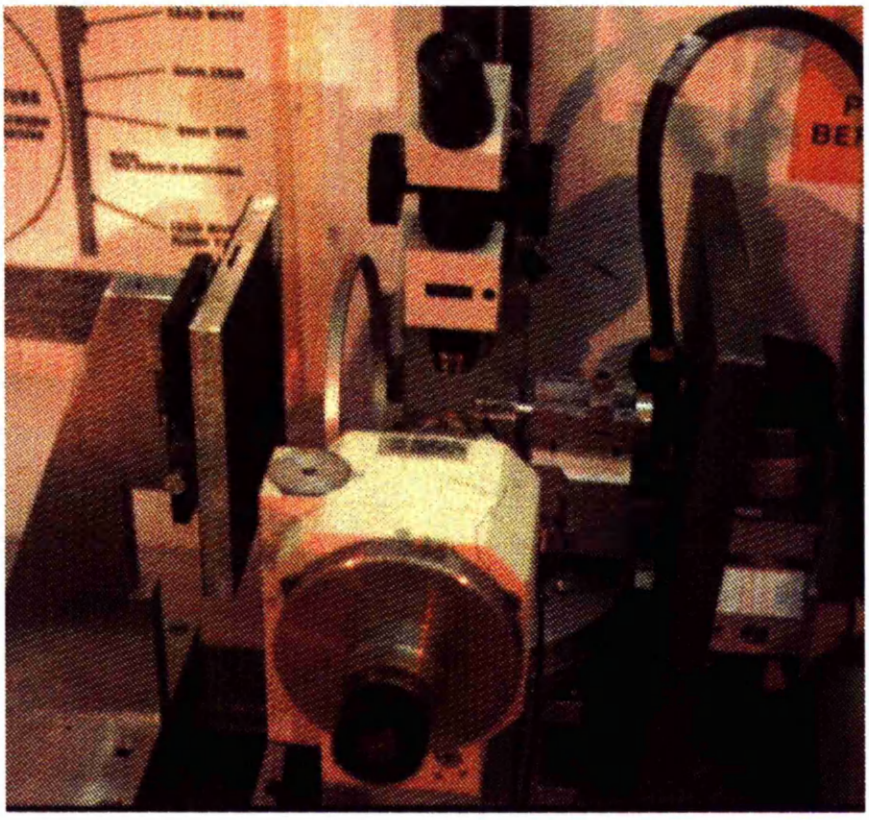

Figure 3.3: Film holder and camera used on station 9.5 of the SRS

An example of the average spot profile from one of the NiAPO image plate images is shown in figure 3.4(a). The pixel size is 150 μm square and it can be seen that the spots are circular with a full width at half maximum (FWHM) of 350 μm (ie. recorded over 3 pixels square). The spot image here is dominated by the image plate point spread function.

For comparison figure 3.4(b) shows the average spot profile from a Laue photograph with the crystal in the same orientation. The pixel size in this case is now

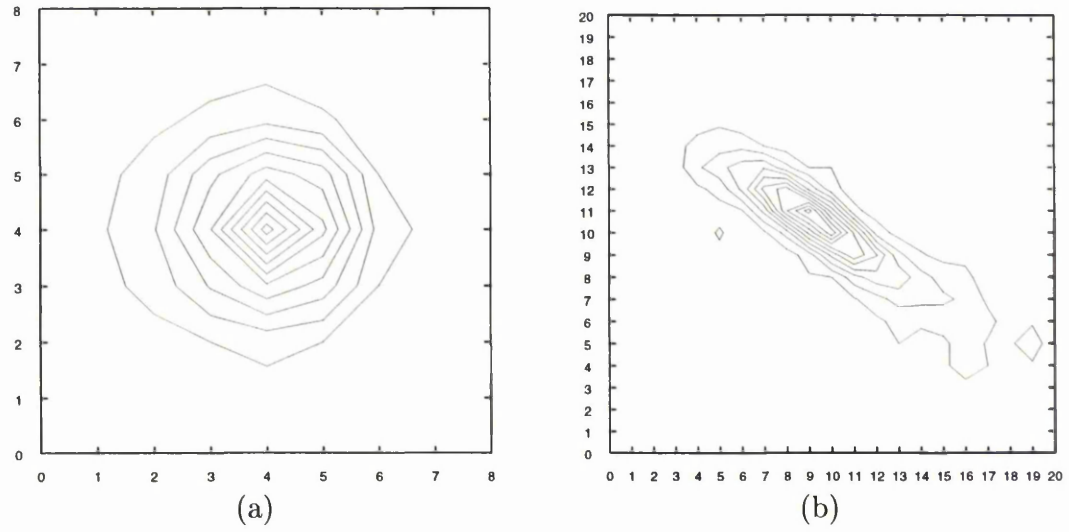

Figure 3.4: Contour plot for the intensity of an average spot from (a) an image plate exposure and (b) a photographic film exposure for identical crystal orientation. The maximum value of 100% (arbitrarily chosen) for the peak is in the centre with contour intervals of 10% from that. The coordinates refer to pixels, for the image plate 150 μm^2 and for the film 50 μm^2.

50 μ square. The spot is seen to be clearly streaked with a FWHM of 120 μm in width and 350 μm in length. The length is determined primarily by the mosaic spread of the sample.

Figure 3.4(b) then illustrates how the logarithmic sampling by a pixel of 50 μm across a sharp spot of 20 μm can be expected to lead to problems in intensity measurement. In this chapter it is not sought to reprove the Wooster effect. Instead it is sought to prove that with a crystal of this size good data can nevertheless be obtained with an image plate.

Following data collection on the image plate two distinct steps are carried out, calculation of intensities and translating these intensities into a structure, which will be described.

3.5 Image to Intensities

The process of analysing a recorded image and translating it to usable intensities are described in this section and summarised in the flow chart shown in figure 3.5. The Daresbury Laue software suite,[128] comprising of LAUEGEN, INTLAUE, LAUENORM and LAUESCALE, (suitably modified for the image plate digitized image format) was used here for processing the NiAPO image plate data. The orientation of the crystal and soft limits, λ_{max}, λ_{min} and d_{min}, are determined. Refinement of the crystal missetting angles, detector position etc. are carried out until convergence. The rms difference of the spots on the images from the predicted positions are examined. At the final stage the cell parameters were refined. All the parameters are then refined through an additional cycle. The diffraction spots are then integrated. These steps are described in detail below.

Indexing the Pattern

Using cell parameters derived from monochromatic work and a collected image displaying a large number of conics the program LAUEGEN produces a predicted pattern corresponding to the image. Initially a prediction is made by use of several nodal reflections (reflections at the intersection of two conics), a wider than estimated wavelength band and a better than estimated resolution limit.

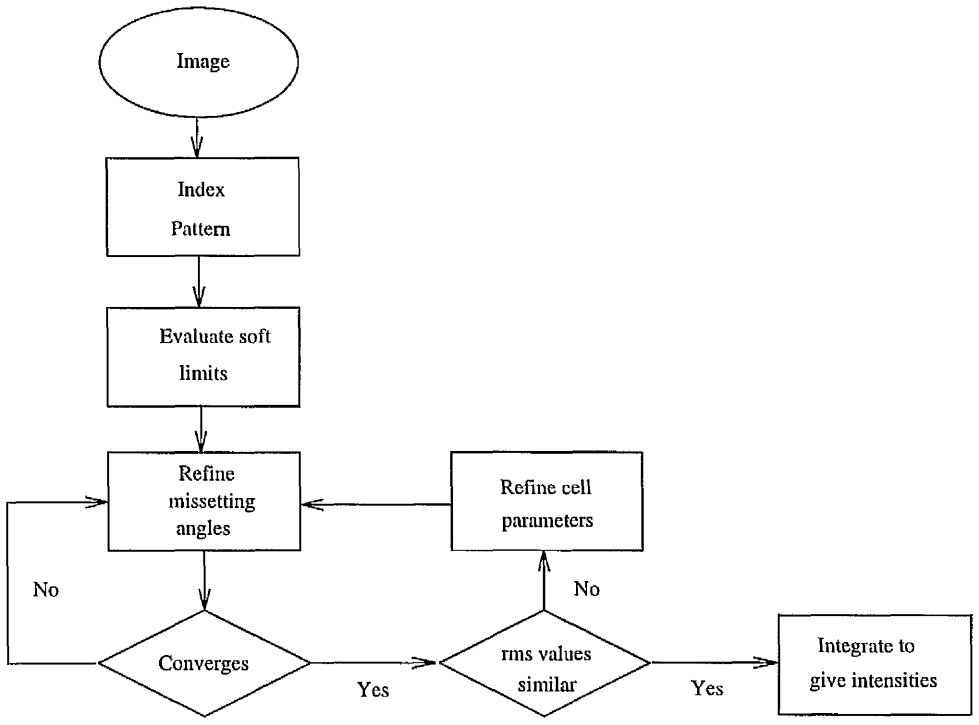

Figure 3.5: Flowchart showing image to reflection intensity processing

Evaluating Soft Limits

The soft-limits λ_{min}, λ_{max} and d_{min}, are evaluated by direct comparison with the recorded image and use of an interactive display of the prediction with sliding scales to alter the values of the soft limits. The values λ_{min}, λ_{max} and d_{min} were found to be 0.36 Å, 1.50 Å and 0.95 Å respectively.

Refine Missetting Angles

The resulting pattern prediction is then further optimised by refinement of the crystal missetting angles, crystal to detector distance and the beam centre. Distortion of the detector is also taken into account with refinement options of twist,

tilt, roff and toff. Twist and tilt are self-explanatory, roff and toff apply to the MAR image plate used in this case - they allow a radial and tangential offset correction due to the radial scanning of the image plate. Refinement is continued until the root mean square (rms) deviations of the predicted and observed spot centre of gravity values converge.

Refinement in this way for the NiAPO data produced rms deviations varying from 0.191 mm to 0.043 mm over the twenty images, illustrated with the top curve in figure 3.6. This variation was clearly worrying and could not be explained by misalignment of the crystal or inaccurate cell dimensions. The program LAUEGEN allows the refinement of cell parameters in the final stages of the refinement. By using this option and again carrying out the previous refinement with the updated cell parameters the rms deviations were substantially improved. In particular the unit cell parameters, b and c, (but with a fixed) were refined (see table 3.3, page 92). The rms deviations, figure 3.6 (lower curve), varied between 0.026 and 0.104 mm. The three higher than average values are due to two or three spots in the images concerned having individual high rms deviation which affected the overall value. The rms deviation between the predicted and observed spot positions was 0.031(6) mm calculated over all the images.

Once this refinement had been completed a series of data files containing the spot spatial positions on the detector was produced which is used in the intensity determination. There were no spatially overlapped spots for this size of unit cell.

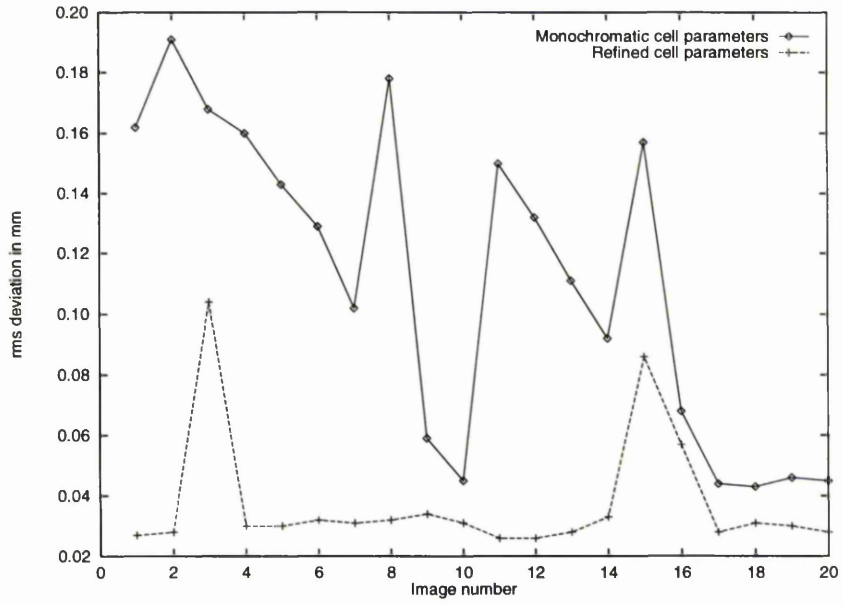

Figure 3.6: Root mean square deviations between predicted and observed patterns using monochromatic cell parameters and refined cell parameters from Laue data

Integrate Intensities

The program INTLAUE[128, 215] further refines the positional parameters of the spots from the LAUEGEN stage as it works with a much larger number of spots than at the LAUEGEN stage. It then determines an average spot profile and integrates the intensity within the profile.[110]

3.6 Intensities to Structure

The process of producing the structure from intensities is described in this section and summarised in figure 3.7. The intensities are normalised to a single wavelength then several choices are made about how the data will be processed.

If multiples are to be used their positions must be predicted with LAUEGEN, integrated, deconvoluted and then scaled into the singles data. The use of f' and f'' corrections (section 2.7) cannot be carried out with multiples as it requires scaled data with wavelength information still intact. Multiple deconvolution (section 2.6) evaluates the intensity of components but loses wavelength information. Direct methods or the Patterson function are used to locate initial atom positions followed by Fourier cycling to refine the structure to what is chemically realistic. Once the structure refinement has reached convergence it is possible to use the calculated structure to apply an absorption correction to the images. The normalisation and refinement are then repeated. Finally a structure is produced. These steps are described in detail below.

Normalising to a single λ

The program LAUENORM was used to produce a wavelength normalisation for all the images based on symmetry equivalent reflections measured at different wavelengths as described in section 2.5. The wavelength normalisation curve produced here is shown in figure 3.8 covering the wavelength range, (0.455 Å-1.180 Å). The curve is continuous peaking at 0.822 Å ie. no absorption edge jumps were evident (unlike film). A total of 6089 measured singles reflections were produced. Deconvolution of multiples resulted in 257 extra reflections.

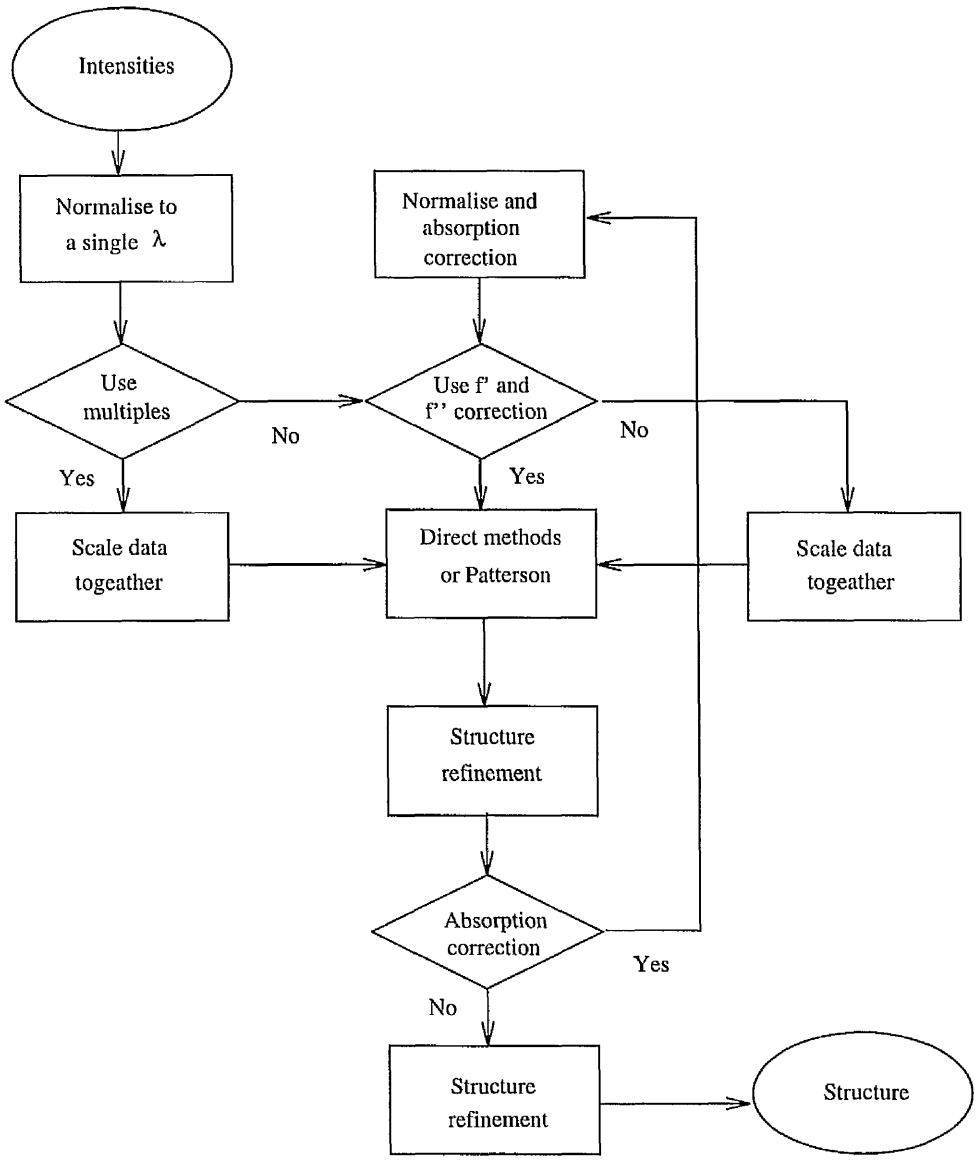

Figure 3.7: Flowchart showing reflection intensities to crystal structure determination

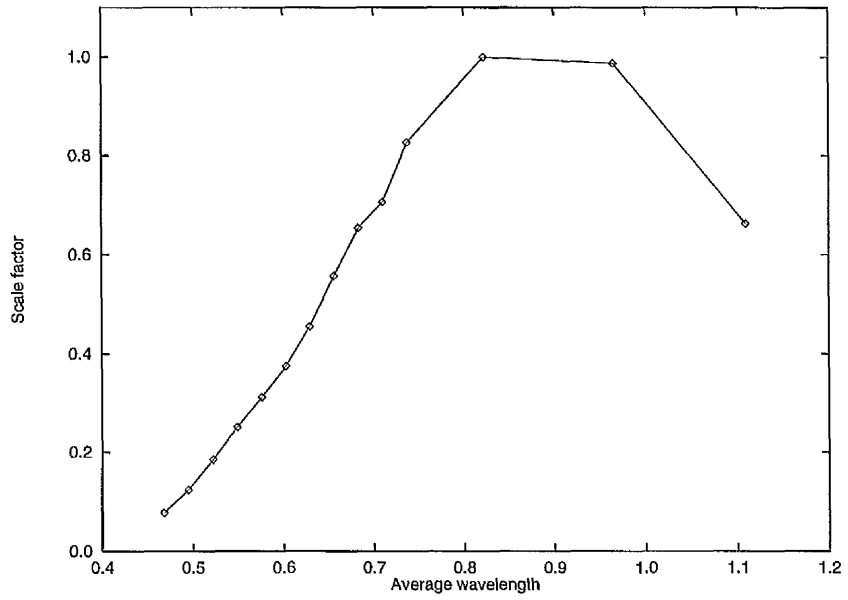

Figure 3.8: Wavelength normalisation curve produced from NiAPO data

Scaling Data Together

A unique set of data was produced by the CCP4[65] programs ROTAVATA (used for scaling all the images together) and AGROVATA (used for merging the data output from LAUENORM into a set of unique reflections. For singles only the merging R-factor (on I) was 10.6% for 6048 reflections (41 measurements rejected) giving 1896 unique reflections. The completeness of the data for $\infty - d_{min}$, $\infty - 2d_{min}$ and $2d_{min} - d_{min}$ was 67.6%, 55.7% and 68.8% respectively.

Patterson Search

The Patterson function[183, 184] allows the collected intensity data to be converted into a collection of inter-atomic vectors all taken to a common origin and the

position of heavy atoms determined.[21]

For the NiAPO molecule the expected approximate relative heights of typical peaks in the Patterson map are;

Ni-Ni	28 × 28	784	N-N	7 × 7	49
P-P	15 × 15	225	C-C	6 × 6	36
Al-Al	13 × 13	169	H-H	1 × 1	1
O-O	8 × 8	64			

Hence the nickel present will stand out being over three times greater peak height than the next highest peak. The Harker vectors,[120] in this case, are:

Position 1 to 1	$u = 0$	$v = 0$	$w = 0$
Position 2 to 1	$u = \frac{1}{2} - 2x$	$v = \frac{1}{2}$	$w = \frac{1}{2} - 2z$
Position 3 to 1	$u = 2x$	$v = 2y$	$w = 2z$
Position 4 to 1	$u = \frac{1}{2}$	$v = \frac{1}{2} - 2y$	$w = \frac{1}{2}$

The vector between any other positions is either identical to one of these or is related by a two-fold axis or by a centre of symmetry at the origin. Every Patterson map is centrosymmetric. The Patterson map calculated using SHELXL-93,[212, 211] for both singles only and combined singles and multiplet data, shows peaks at, among other positions:

Singles peak height			Combined peak height		
u=0.00	v=0.00	w=0.00	u=0.00	v=0.00	w=0.00
u=0.50	v=0.05	w=0.50	u=0.50	v=0.05	w=0.50
u=0.27	v=0.50	w=0.23	u=0.27	v=0.50	w=0.22

The highest peaks were selected as the nickel atom position.

Structure Refinement

Once the initial nickel position was found the rest of the structure was evaluated by Difference Fourier methods with the use of SHELX-93.[213] The results section describes the R_{factor}'s (see page 46) achieved after refinement converged for several combinations of techniques indicated in figure 3.7.

Correction for f' and f'' variation

The program SHELX-93[213] allows correction to be made for the contribution of f' and f'' when the wavelength of the reflections are known (consequently this cannot be applied to multiplet data). This may be necessary for establishment of structural detail as well as achieving a reasonable R_{factor}.[78] The tabulated values[204] of f' and f'' were used but did not show improvement in the refinement (tables 3.1 and 3.2).

Absorption Correction

In the refinement of the full structure (excluding H atoms) the thermal vibration parameters of the atoms were low with a minority even being negative. This can be caused by absorption effects reducing the measured intensity. An absorption correction procedure had proved to be effective in such cases before[157] and was applied here. The program SHELXL-93[213] produced a set of h, k, l and F_{calc} from

Multiples used	$f'f''$ correction applied	Absorption correction	Isotropic R factor	Anisotropic R factor
No	No	No	11.68	8.81
No	No	Yes	8.82	7.90
No	Yes	No	12.70	10.70
No	Yes	Yes	10.37	9.75
Yes	No	-	18.74	16.34

Table 3.1: NiAPO R_{factor} (on F, see page 46 for definition) results for different data treatments

the best isotropic refinement. LAUESCALE used these F_{calc} values to apply an absorption correction multiplication surface to the intensities from each image. This surface is unique for each orientation of the crystal. An example is shown in figure 3.9. From this a new set of $h, k, l, F, \sigma F$ and λ are produced. The merging R-factor (on I) for LAUESCALE with 6472 singlet measurements (greater than LAUENORMS's 6089 measurements due to a different acceptance procedure) was 10.9% producing 1979 unique measurements. The completeness of the data for $\infty - d_{min}$, $\infty - 2d_{min}$ and $2d_{min} - d_{min}$ was 70.6%, 56.5% and 72.0% respectively (see page 85 for earlier values). It is not possible to accurately derive multiplets from only one image using wavelength deconvolution so these cannot yet be used when an absorption correction is applied.

3.7 Comparison of Data Processing Strategies

All possible combinations of treatment of the data described in this chapter are now compared in tables 3.1 and 3.2.

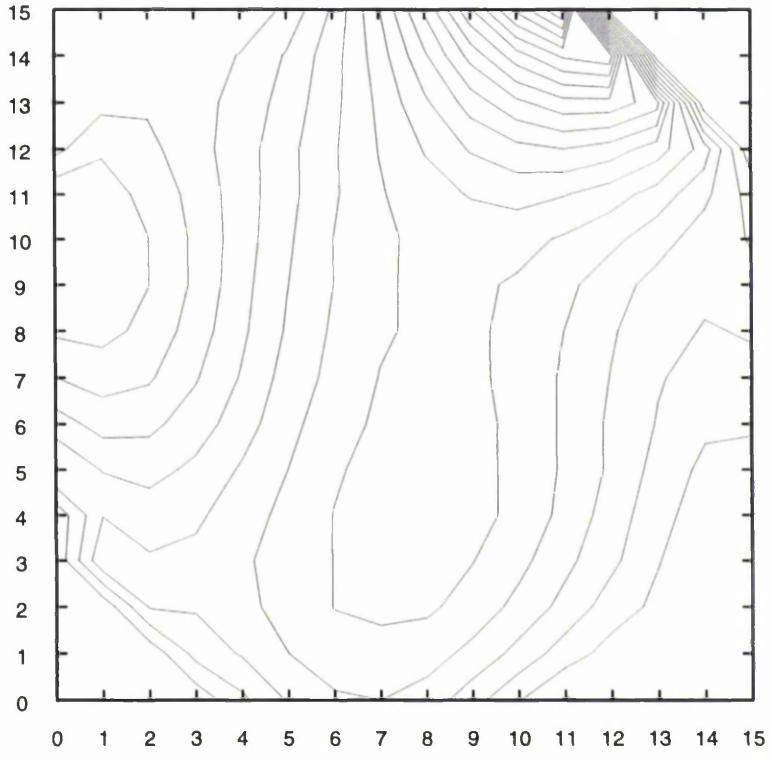

Figure 3.9: Absorption correction surface produced from one Laue image. Maximum correction applied is shown (100%) at the peak in the profile (shown as a plateau in the centre) with contour levels at 2.5% from that. The axis labelling is the relative positions on the recorded image

$f'f''$ corrected initial data	Absorption correction	$f'f''$ correction applied	Isotropic R factor	Anisotropic R factor
No	Yes	Yes	10.28	9.65
Yes	Yes	Yes	10.37	9.75

Table 3.2: Effect of $f'f''$ corrections applied after absorption correction to both $f'f''$ initially corrected, and uncorrected data

The best result is achieved with application of an absorption correction but without the use of multiples or taking into account f' and f'' variations (an R_{factor} (on F, see page 46) of 7.90% for all data (1934 unique reflections), 5.11% for $I > 3\sigma(I)$ (1397 unique reflections)). This had maximum and minimum differences in $F_o - F_c$ of 0.47 and -0.51 eÅ^{-3} with a mean of 0 and rms deviation from the mean of 0.11 eÅ^{-3}. For isotropic refinement (with all data) the number of parameters are 140 giving a data to parameter ratio of 13.8 and for anisotropic refinement the number of parameters are 310 giving a data to parameter ratio of 6.2.

3.8 The NiAPO Structure

The derived structure of NiAPO,[219] is shown in figure 3.10. Each nickel atom is six coordinated to three oxygen and three nitrogen atoms (2 ethylene diamine groups, one monodentate and the other bidentate) giving an octahedral form. The structure contains three aluminium atoms arranged in tetrahedral form to oxygen atoms. There are two water molecules, one connected to the nickel and the other which is free and linked to the structure by hydrogen bonds.

Lists of the structure factors and anisotropic thermal parameters have been deposited with the IUCr (Reference HI0010). Copies may be obtained through the Managing Editor, International Union of Crystallography, 5 Abbey Square, Chester, CH1 2HU, England.

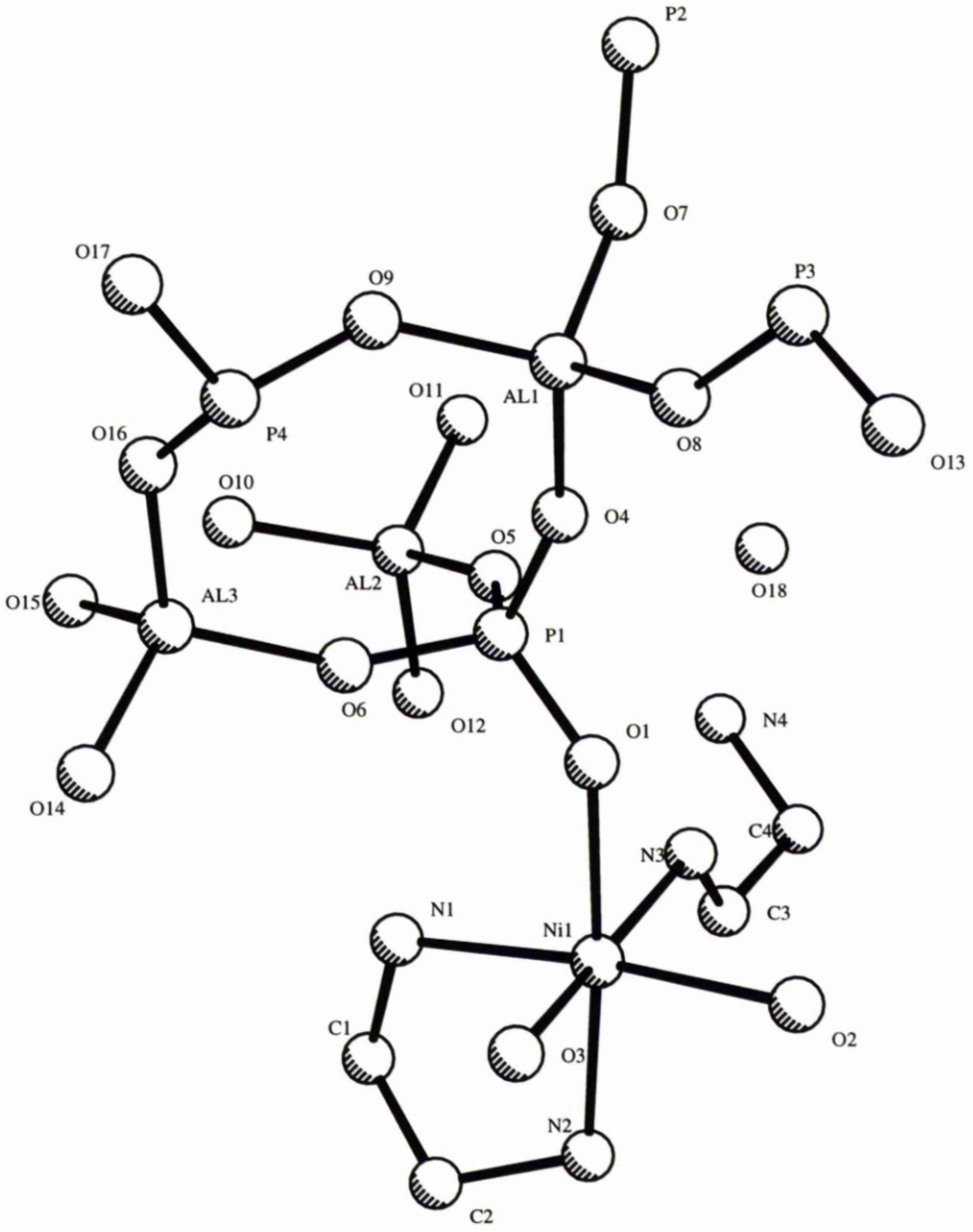

Figure 3.10: The NiAPO molecular structure

	a(Å)	b(Å)	c(Å)	β(°)	V(Å^3)
CuKα	10.0209(8)	15.661(1)	14.091(8)	101.216(5)	2169.3
MoKα	10.03(2)	15.67(2)	14.14(2)	101.3(1)	2180
Laue	10.02	15.728(6)	14.134(6)	101.313(14)	2184.16

Table 3.3: NiAPO cell parameters for monochromatic and Laue data sets

3.9 Comparison with Monochromatic Studies

The refined structure obtained here agrees well with that derived from earlier monochromatic studies[131] using CuKα and MoKα X-ray radiation. To illustrate this, the average value of bond distances from this study is given with the estimate from the earlier, monochromatic, study in brackets. The average Ni-O bond distance is 2.102 Å (2.097 Å) and Ni-N bond distance 2.097 Å (2.111 Å). The P-O bond linked to aluminium has a distance of 1.523 Å (1.541 Å) and the P-O linked to nickel has a bond distance of 1.477 Å (1.483 Å) respectively.

The refined structures from the Laue and monochromatic were overlapped with one another by a least squares determination of a rotation matrix and translation vector. The rms deviation in Å and maximum single atomic displacement (given in brackets) for the Laue:CuKα, Laue:MoKα and CuKα:MoKα cases (all atoms with the exception of hydrogens) were 0.030 (0.074), 0.034 (0.095) and 0.027 (0.060) respectively. The thermal parameters can be compared by taking the ratio B_{Laue}:$B_{CuK\alpha}$ which has the value of 0.64. This can be compared with the value $B_{MoK\alpha}$:$B_{CuK\alpha}$ of 0.86.[131] The cell parameters determined with monochromatic and Laue data are compared in table 3.3.

3.10 Future Work

A Multiple Image Laue Diffraction Technique

One of the striking aspects of small molecule data collection with the Laue method is the percentage of un-stimulated pixels on the detector. A method to utilise the un-stimulated area would be the use of one crystal but with multiple exposures on the same image at different spindle axis settings. The data collection time of this method, which I have termed Multiple Image Laue Diffraction (MILD), is limited only by the exposure time and the time taken to rotate the crystal to another orientation ie. it would be free of the duty cycle limitation of the image plate scanners. Its principal disadvantage is the addition of more background.

By making use of the NiAPO Laue data described in this chapter a MILD image has been simulated with a slightly modified version of the IPDISP program. The program has been altered such that multiple images can be added to together cumulatively instead of being pixel averaged. Figure 3.11 illustrates the large amount of blank space on four images and the result of combining nine images together is shown in figure 3.12.

Initial indexing can be carried out on the clearest set of nodal points using the knowledge that conics on the same exposure intersect at nodal points. If there are any problems with indexing then a separate single exposure image could be taken before or after a complete MILD data collection and used for indexing in the standard way. Once the index is found the image can be processed to produce a second set of intensities. This can be continued for each spindle orientation producing n separate data sets. It is possible to apply an absorption correction

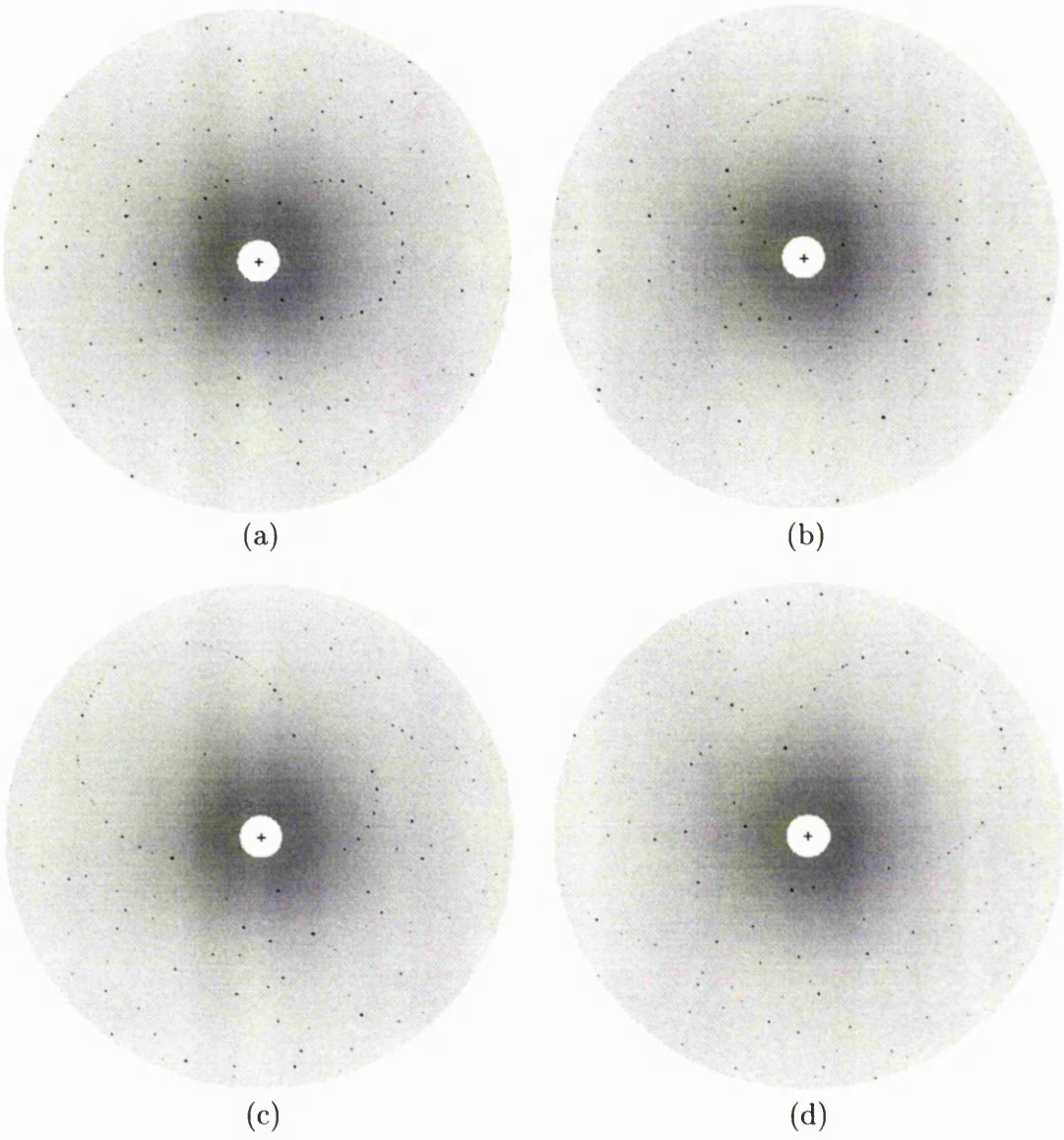

Figure 3.11: Single images (a-d) from Laue diffraction data of NiAPO

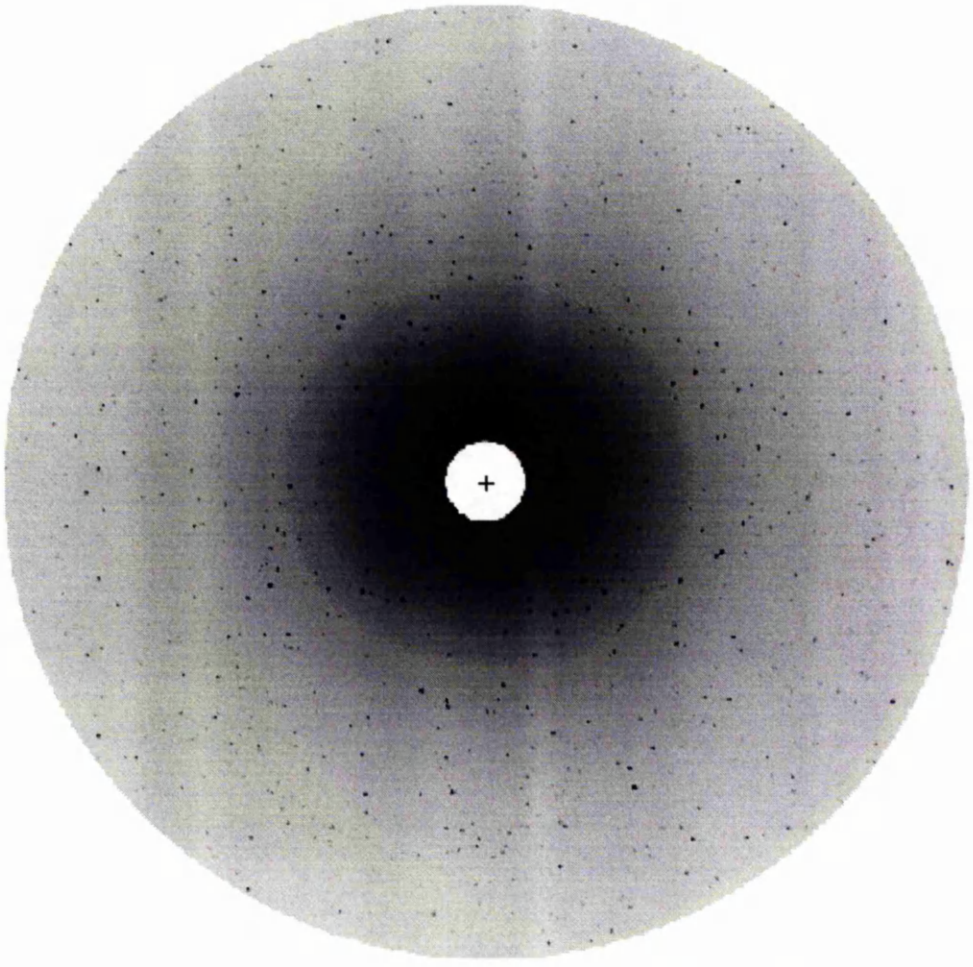

Figure 3.12: A simulated "MILD" image from 9 separate NiAPO Laue images. Total exposure time is 9 × 0.3 seconds. On top of this time, in practise, the time required to re-orient the crystal to different angular settings is needed.

to each separate data set as they are essentially individual images.

When images are merged in this way the background is considerably increased. In this case data was collected with little regard to background (because the crystal was strongly diffracting) so the simulation shown could be regarded as a worst case since precautions could in future be taken to reduce background (helium paths etc.). The idea of 'MILD' as a data collection method warrants further development since, in fact, figure 3.12 looks relatively clean, and with few spatial overlaps.

A Rotating Crystal Laue Method

If the crystal was continually rotating, a complete data set could be recorded in a time, T, given by;

$$T = nt \tag{3.2}$$

where n is the number of angular positions required and t the exposure time used ie. this has potential for very fast exposures, where now (compared with the figure 3.12 legend) one is left only with summation of exposure times.

Rotating the crystal with a polychromatic incident X-ray beam has, in fact, been the subject of a theoretical study[146] as a method to monitor time dependent changes on the time scale of synchrotron pulse widths. Initial discussion on this method has involved its use in observing the same reflection a number of times at slightly differing angular positions on the detector through a phase transition

in the sample. Computer simulations were carried out with the crystal rotating at 100000 rpm and exposures corresponding to the time scale of the synchrotron pulse, each 177 ns. This method poses high physical forces on the crystal and equipment and does not look likely to be realised at present.

However, here, by collecting images at different angular positions rather than looking at the same reflection over a small time period, as in the previous theoretical study,[146] synchrotron Laue data can be routinely collected from a rotating crystal. Figure 3.10 shows a representation of the method.

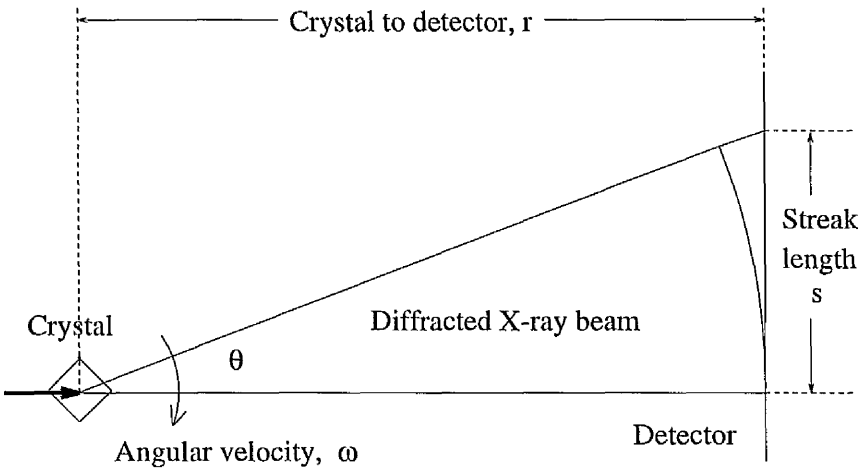

Figure 3.13: Schematic representation of the rotating crystal method

In figure 3.10 the fraction of spatially overlapped spots in the data will be governed by the spread of the diffraction spot, to a streak of length s. The term θ defines the angle through which the diffracted ray passes and r the crystal to detector distance. The angular velocity is given by;

$$\omega = \tan^{-1}\left(\frac{s}{r}\right)/t \tag{3.3}$$

Therefore, the faster the rotation of the crystal then the shorter exposure time used for a given acceptable streak.

An estimate for the rotational speed and exposure time can be made. For a small molecule with a crystal to detector distance of 100 mm, exposure time of 100 msec and a spot streak length of 0.05 mm allowed then the angular velocity of the crystal rotation would have to be no greater than 0.28 $^{\circ}s^{-1}$. A similar consideration can be made for protein data with large crystal to detector distances, eg. 2 m (to try and avoid spatial overlap problems) and the same conditions as described for the small molecule case. The angular velocity required is then no greater than 0.014 $^{\circ}s^{-1}$ for data collection from a protein crystal. Shorter exposure times would allow an increased rotational speed of the crystal. The angular velocity in both cases, protein and small molecule, is easily achieved with current systems.

3.11 Summary

With film, the measured intensities of spots can be underestimated where the diffraction spot is too small compared to the area scanned. This is not the case for the image plate where there is no Wooster effect. The use of the on-line image plate has proved to be very effective for the synchrotron Laue data collection and subsequent structural solution from a small ($0.02 \times 0.05 \times 0.25$ mm^3) test crystal. Moreover, data collection took place in less than one hour (although processing took much longer !) and produced results comparable in quality to monochromatic methods. The image plate offers rapid 'readout' times compared to film and now CCD's offer an improvement in terms of readout time

to image plates.

The MILD data scheme proposed in section 3.10 presents a possible very rapid means of obtaining a complete Laue data set for a small molecule making good use of the typical dead space on the detector (the un-stimulated regions as evidenced in figures 3.11). The rapid speed of data collection, especially with a rotating crystal and short exposure time, should reduce scaling problems between images due to intensity fluctuations etc. There will be an increased problem with background but this can be reduced to some extent by careful experimental design, good alignment of the beam stop and the use of helium paths. The method has not been assessed with macromolecules because of the high density of diffraction spots and the real possibility of spot overlap with two or more exposures on the same image. However with high perfection crystals, large detectors and large crystal to detector distances the method becomes feasible.

For the protein case, the spinning crystal technique has further application in time resolved work allowing a range of images to be recorded quickly with a suitable fast read out detector. The spinning crystal method may well have useful applications in time-resolved Laue crystallography as a rapid means for collecting several images at different orientations so as to provide as complete a data set as possible in a usefully short time.

Chapter 4

A Protein Study - Filling the "Low Resolution Hole" in Laue Data

4.1 Introduction

The low resolution hole can present problems of contrast in the electron density maps as has been discussed in section 2.4. By exploiting the speed of modern X-ray detectors small angular steps can be used to record a high completeness data set. The application of multiple deconvolution procedures can also help in filling the low resolution hole. The aim of this chapter is to explore the completeness that can be attained from small angular step data collection as a strategy and the consequent effect on the electron density maps. For this work lysozyme is used as a readily available, well studied, easily crystallizable test case.

4.2 Lysozyme

Lysozyme was discovered on November 21st 1921 by Alexander Fleming, a bacteriologist living in London. Fleming, having a cold and not being one to miss an experimental opportunity, diluted some of his own nasal mucus with saline, centrifuged it and then placed it on several streak cultures. Where the mucus had been placed there was no growth on the culture plate. To examine if this lytic activity (lysis in the sense of dissolution of cells or bacteria) was common in mucus, Fleming tested samples from many other people and found activity in them all. He also tested other fluids related to the mucus ie. tears, saliva, sputum, blood serum, plasma, peritoneal and pleural fluid. All showed the lytic activity. Widening the search further, on 12th January 1922, he found that egg white was a rich source of this lytic substance. Fleming's research was carried out in Almroth Wright's group at St Marys Hospital, London. It was to Wright he took his results in the form of a manuscript for publication.[98]

Lysozyme functions by dissolving the walls of certain bacteria by cleaving the polysaccharide component of the cell wall. The cell wall polysaccharide is made up of two kinds of sugars, N-acetylgucosamine (NAG) and N-acetylmuramate (NAM). In bacterial cell walls NAM and NAG are joined by glycosidic linkages between C-1 of one sugar and C-4 of the other. All of the glycosidic bonds of the cell wall polysaccharide have the oxygen below the plane of the sugar (β configuration). NAM and NAG alternate in sequence joined by β(1-4) glycosidic linkages to form the polysaccharide cell wall. Lysozyme hydrolises the glycosidic bond between C1 of NAM and C4 of NAG but not the C1 of NAG or C4 of NAM bond. The cell wall, now cleaved, loses its function of mechanical support and

the bacterial cell bursts.

The complete primary sequence of lysozyme was determined by protein ~~and DNA~~ sequencing.[140] The three dimensional structure was determined in 1962 at 6 Å resolution and later, in 1965, at 2 Å resolution by Phillips et al.[28, 30] The space group of tetragonal lysozyme is $P4_32_12$ with one protein molecule in the asymmetric unit. The molecule is roughly elliposoidal in shape with dimensions of about $45 \times 30 \times 30$ Å.

A deep crevice or cleft containing the active site divides the molecule into two domains,[230] one is almost entirely comprised of a β sheet structure encompassing residues 40 to 85. The other domain is comprised of the N and C terminal segments, residues 1 to 39 and 101 to 129, is more helical in nature. Three runs of α helices occur in this domain, residues 5 to 15, and 24 to 34. The two domains are linked by an α helix, residues 88 to 99. These are illustrated in figure 4.1 showing a ribbon[185] with the α helix in red and β sheet in green.

4.3 Crystallisation

The lysozyme crystals used for this study were, in fact, crystallized on Spacehab-1[248, 130, 221] flown by the STS-57 NASA Space Shuttle mission. Crystallization was carried out by the dialysis method with 15.8 mg of lysozyme (3 x crystallized, dialysed and lyophilized powder of chicken egg white lysozyme) dissolved in 188 μl 0.4 M acetate buffer (pH 4.7) and a precipitant of 1.350 M NaCl solution. Crystallization was carried out under microgravity conditions and at a constant temperature of 20 ± 0.1°C.

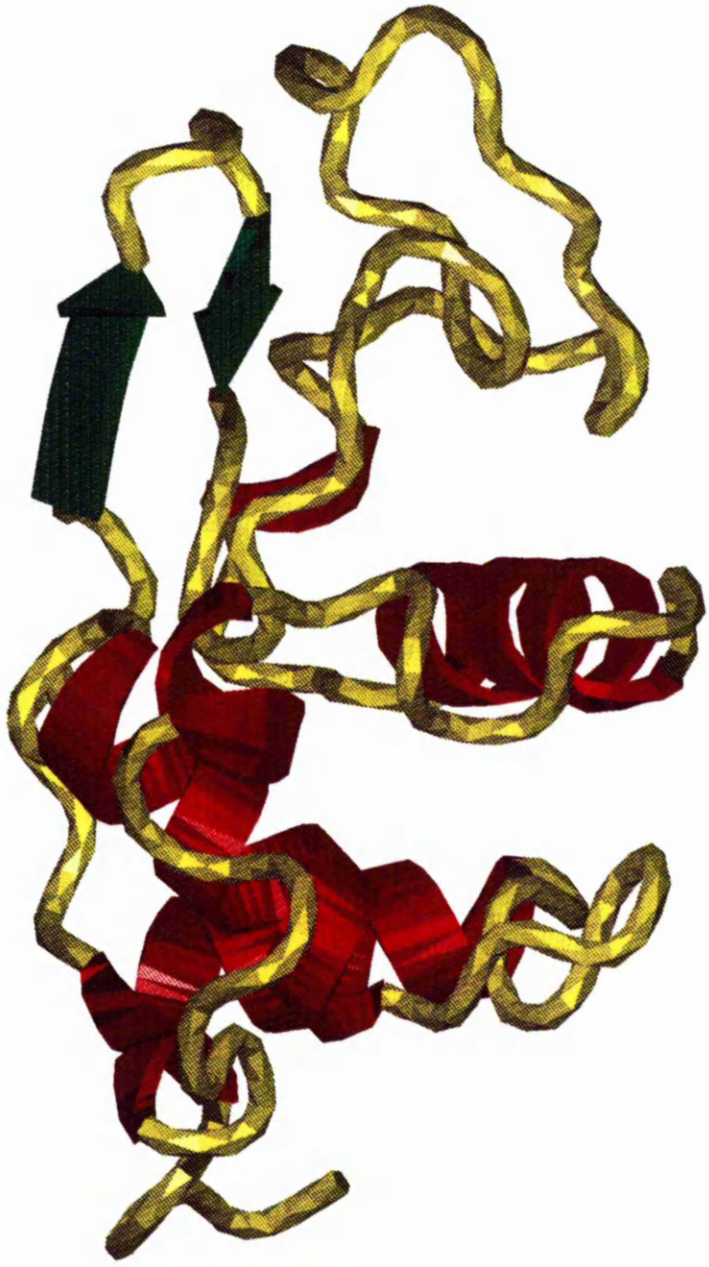

Figure 4.1: Ribbon diagram of lysozyme, α helix illustrated in red, β sheet in green.

4.4 Laue Data Collection

Utilising these crystals Laue data were collected on station 9.5 of the Daresbury Synchrotron Radiation Source.[41, 125, 235] A MAR image plate detector (see figure 3.1) was used to record 31 images from one of the microgravity-grown crystals at 2° intervals each with an exposure time of 500 ms. This detector uses on-line scanning of 1200 × 1200 0.150 mm^2 pixels. The outstanding nature of the data acquisition with this device (and even more so the CCD - see chapter 5) makes it practical to consider such fine angular interval data collection strategy. The synchrotron was operating at 2.0 GeV with an average current of 210 mA during the data collection run. To attenuate the longer wavelengths a 0.4 mm aluminium foil was used in the beam path (upstream of the (0.2 mm) collimator).

4.5 Laue Data Processing

The data were processed using the Daresbury Laue processing suite[128] (LAUEGEN[48] and INTLAUE) with soft limits λ_{min} of 0.40 Å, λ_{max} of 1.55 Å and d_{min} of 2.50 Å found as described in the small molecule case on page 3.2.To study the effects of data collection at different angular intervals several subsets of the data were examined; firstly, the complete data set of 31 images making up 60° in 2° intervals, secondly, 16 images making up 60° in 4° intervals, thirdly, 6 images making up 60° in 10° intervals and fourthly, 3 images with 30° degree intervals. The data were processed using firstly singlets only, and secondly, with multiplet deconvolution.[51] The normalisation curves for each set of singles data are shown in figure 4.2.

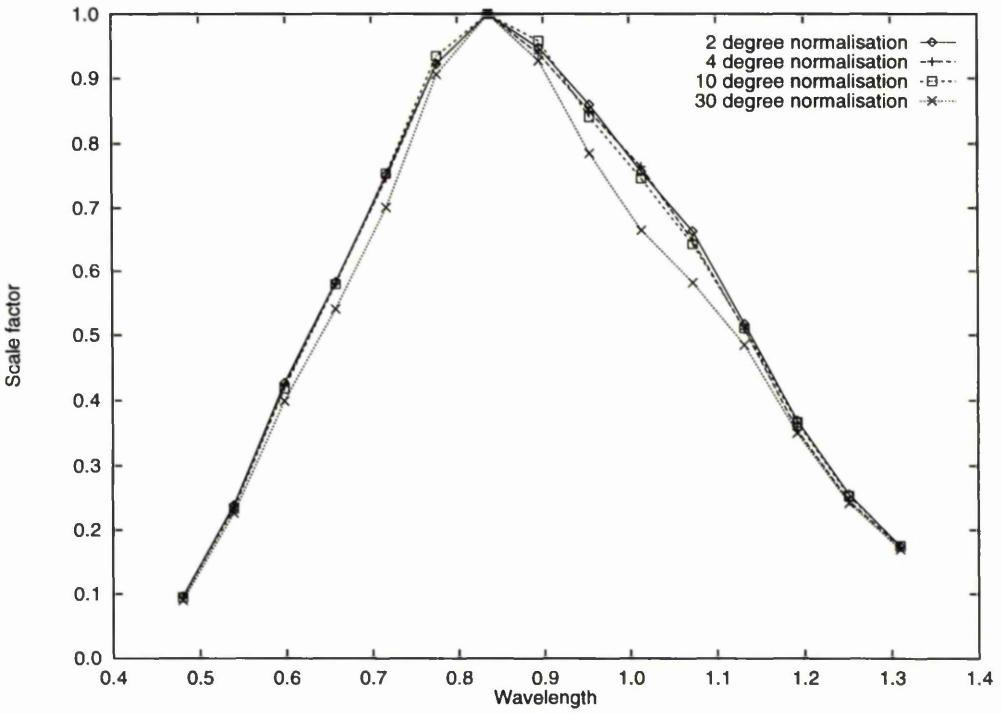

Figure 4.2: Normalisation curves for 2, 4, 10 and 30° angular interval lysozyme Laue data

The normalisation curves for each data set are identical except that it is noticeable that, the scaling factors are reduced slightly with the "30° interval" normalisation curve. Whilst it has been noted[194] that incomplete data at low resolution (with few images) may adversely affect the accuracy of the wavelength curve, we can see that this is true here only in the extreme case of 3 images separated by 30° which is, in any case, too coarse to be recommended.[57, 127]

The total number of reflections input and output from the normalisation process is shown in table 4.1. Reflections were rejected if they were outside the chosen wavelength limits, had negative intensities or negative sigma. Only reflections with intensities I greater than $3\sigma(I)$ were used for scaling. The merging R factors

Images in data set	Input reflections	Reflections for scaling	Normalised reflections	Multiples	R factor
31	94857	69643	75831	897	6.6 %
16	48925	35832	39026	798	6.1 %
6	21532	15448	17023	521	6.4 %
3	9249	6444	7264	218	7.1 %

Table 4.1: Reflections used and normalised by LAUENORM

Data	Rejected reflections	R factor on intensity	Overall multiplicity
2 degree combined	2.9 % (1784)	8.9 %	19.3
2 degree singles only	2.9 % (2230)	9.0 %	20.6
4 degree combined	1.5 % (596)	8.6 %	10.3
4 degree singles only	1.4 % (538)	8.7 %	10.9
10 degree combined	0.9 % (157)	8.8 %	4.8
10 degree singles only	0.7 % (127)	8.8 %	5.0
30 degree combined	0.5 % (39)	9.6 %	2.4
30 degree singles only	2.9 % (35)	9.3 %	2.5

Table 4.2: Table of AGROVATA output for lysozyme Laue data

are also those for measurements of the same sign with λ within 0.1 Å (the so called "R3" given in LAUENORM).

After normalisation the data is reduced to a unique data set using the CCP4 programs[65] ROTAVATA and AGROVATA. Table 4.2 lists the percentage of rejected reflections, overall R factor on intensity and data multiplicity.

The resulting completeness of the data sets in terms of $d_{min} - \infty$, $d_{min} - 2d_{min}$ and $2d_{min} - \infty$ are listed in table 4.3 whilst a plot against resolution is shown in figure 4.3.

It is useful to determine a low resolution cut off so as to quantify the impact of

	Singles only		
Data set	$d_{min} - \infty$	$d_{min} - 2d_{min}$	$2d_{min} - \infty$
2°	79.8%	82.2%	58.0%
4°	78.8%	81.2%	54.4%
10°	75.1%	78.8%	41.2%
30°	65.2%	69.6%	25.4%
	Multiplets included		
2°	86.1%	88.1%	68.6%
4°	84.8%	87.0%	64.7%
10°	80.2%	83.3%	52.2%
30°	68.3%	72.4%	32.0%

Table 4.3: Completeness of data for protein crystal Laue collection at different angular steps in terms of completeness from $d_{min} - \infty$, $d_{min} - 2d_{min}$ and $2d_{min} - \infty$ respectively

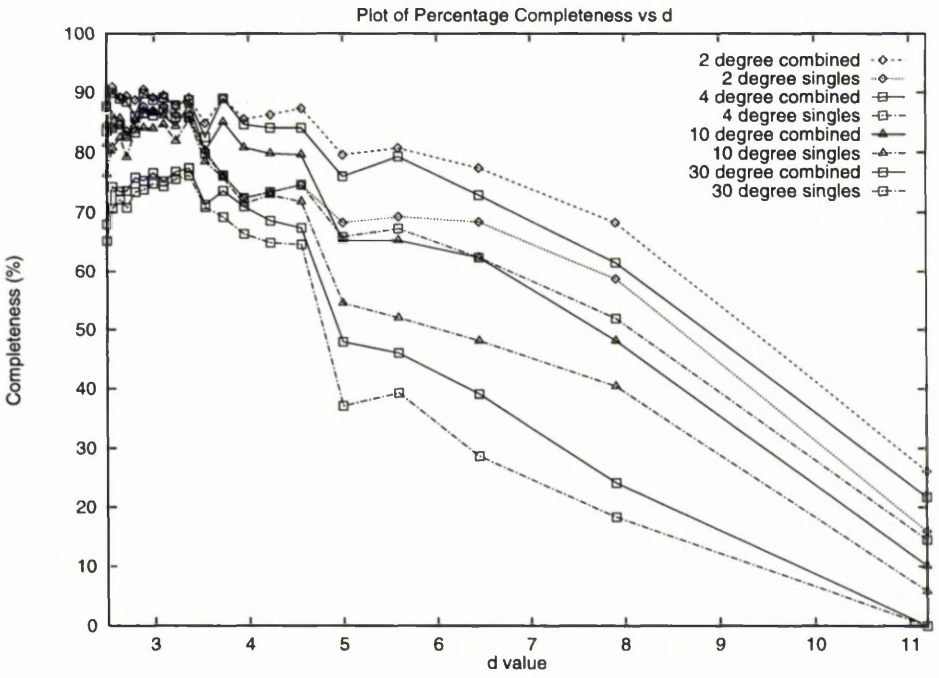

Figure 4.3: Percentage completeness vs d values for Laue data from tetragonal lysozyme crystals collected at station 9.5. The 4° and 30° data are represented by the same symbols, the 30° data obviously having the lower completeness values.

$\Delta\phi$	singles d_{max} Å	combined d_{max} Å
2°	8.6	9.3
4°	8.1	8.9
10°	6.0	7.8
30°	4.9	5.0

Table 4.4: Low resolution cutoffs at 50% completeness for protein crystal to illustrate the interest in low resolution LOT (Large-angle Oscillation Technique) data between $d_{max} < \lambda < \infty$ Å

the different strategies to fill the "low resolution hole". A breakdown in terms of the low resolution cutoffs at 50% completeness are listed in table 4.4 providing evidence especially of the usefulness of small angular steps, and, to a less extent, the use of multiple deconvolution. Table 4.4 also illustrates the interest in a low resolution data collection technique, the Large-angle Oscillation Technique (LOT)[249] to provide a way of filling the low resolution hole. In previous studies the deconvoluted multiplets, though marginal in terms of d_{max} improvements, do contribute to an improvement of map features for proteins[50] and have been used for structure refinement and modelling in this chapter. It can be expected then that a proportionally greater impact will arise from the use of fine angular steps. It should be noted, in contrast, that Ren & Moffat (1995)[195] have argued the opposite (that deconvoluted energy overlaps are more important).

With the diffraction data we can see readily how fine angular interval data collection, $\Delta\phi$, is better than multiples deconvolution (ie. in table 4.4 for 10° intervals, multiples increase d_{max} from 6.0 Å to 7.8 Å, but for the 4° interval case has d_{max} increase from 8.1 Å to 8.9 Å. We have not specifically separated the impact of these two approaches in terms of map quality ie. all the maps are shown for multiples included. However, the new parameter, d_{max}, is explicitly a low resolution

completeness (50% parameter) and will therefore be a very good indicator of map quality.

4.6 Structure Refinement and Modelling

The structure of lysozyme (coordinates deposited at the PDB,[22] (6LYZ),[77, 31] as starting model) was refined against each data set, ie. 2°, 4°, 10° and 30°. In each cycle the model structure was refined using the program X-PLOR[44] with 40 cycles of positional refinement followed by 20 cycles of temperature (B-factor) refinement. Subsequently electron density maps were calculated using the CCP4[65] software package and the model fitted to the maps manually using FRODO[143, 141, 142] and later O.[144] The refinement R-factor values[43] are illustrated in table 4.5. The model is already well refined so there is little difference in this case for the data sets.

The crystallographic R-factor is a measure of the match between the model and X-ray data whereas the quality of the geometry of the model can be checked through the rms deviations from ideality of the bond lengths, bond angles, dihedral angles and improper angles.

During the refinement, water molecules were added if a peak appeared above 3σ in the F_o-F_c map and within range 2.5-3.5 Å of a plausible hydrogen bonding position. Waters that had been chosen but did not reappear in the 1σ $2F_o$-F_c map were deleted. Table 4.6 gives the number of waters found using each set of data and the average, highest and lowest temperature factors seen in each case. The location of water molecules in the data set from 2° data was rapid with

	2°	4°	10°	30°
Unique reflections	3855	3794	3588	3055
Completeness	86.1%	84.8%	80.2%	68.3%
Single:Multiple	84.53	48.90	32.67	33.32
Initial				
R-factor	27.9	23.2	22.2	20.9
rms bond length	0.026	0.020	0.019	0.026
rms angles	3.589	2.923	2.588	2.758
rms dihedral angles	23.994	24.059	23.822	23.826
rms improper angles	3.160	2.285	1.872	2.179
Final				
R-factor	19.9	19.9	19.2	18.6
rms bond length	0.007	0.007	0.008	0.007
rms angles	1.817	1.792	1.945	1.818
rms dihedral angles	22.749	22.596	22.487	22.898
rms improper angles	1.117	1.216	1.161	1.183

Table 4.5: Results for X-PLOR refinement and FRODO modelling of lysozyme. The term *Single:Multiple* defines the ratio of singles to deconvoluted multiples

	2°	4°	10°	30°
Number of waters	56	49	48	38
Average temp. factor	34.57	36.52	33.01	27.14
Highest temp. factor	89.24	93.53	114.54	90.96

Table 4.6: Water structure found for the different angular data sets

difficulty increasing with the 4° to 30° data.

Several peaks near the surface of the protein are thought to represent Cl^- ions (these peaks being rather higher than the majority water molecules). There are known to be about 16 of these Cl^- ions in the crystal[31] but in this case (although some waters had low temperature factors) it was not possible to distinguish them.

4.7 Electron Density Maps

The effect of improved completeness at low resolution is indeed manifest in the respective "quality" of the electron density maps. Figures 4.4 to 4.10 show residues Arg 5, His 15, Phe 38, Asp 52, Tyr 53, Pro 70 and Trp 108 residues respectively. Figures 4.11 to 4.14 show the disulphide bridges between residues Cys 6 - Cys 127, Cys 30 - Cys 115, Cys 64 - Cys 80 and Cys 76 - Cys 94 respectively.

Arg 5, a basic residue, is the first residue in the α helix, 5 to 15, and occurs on the surface of the molecule. This is one of the more poorly ordered residues that can be found in the structure.[230] His 15 is also basic occurring on the surface of the molecule and ends the first α helix. Phe 38 occurs in the non β sheet domain. Asp 52 and Tyr 53 occur on the surface of the molecule in the β sheet domain as does Pro 70. Trp 108 is a hydrophobic residue situated on the surface of the cleft in the non β sheet domain. The four disulphide bridges can be identified as two groups, Cys 6 to Cys 127 and Cys 64 to Cys 80 are Similar as are Cys 30 to Cys 115 and Cys 76 to Cys 94. These residues have been chosen so the work can be directly compared with a study of singles alone and the effect of adding multiples by Campbell *et al.*.[50] Overall connectivity is clearly improved using the 2° data and quality decreases as the angular step sampling gets worse.

The collection of residues is effectively a broad ranging survey of residues in different locations of the protein and of different types. It gives little indication of the overall improvement in the data. Other indicators of map quality are the real space R-factors.[144] These are shown colour coded on a Cα trace in figure 4.15 and plotted per residue for each Laue data set in figure 4.16. There is little overall difference between the 2°, 4° and 10° data sets but the poor quality of the 30°

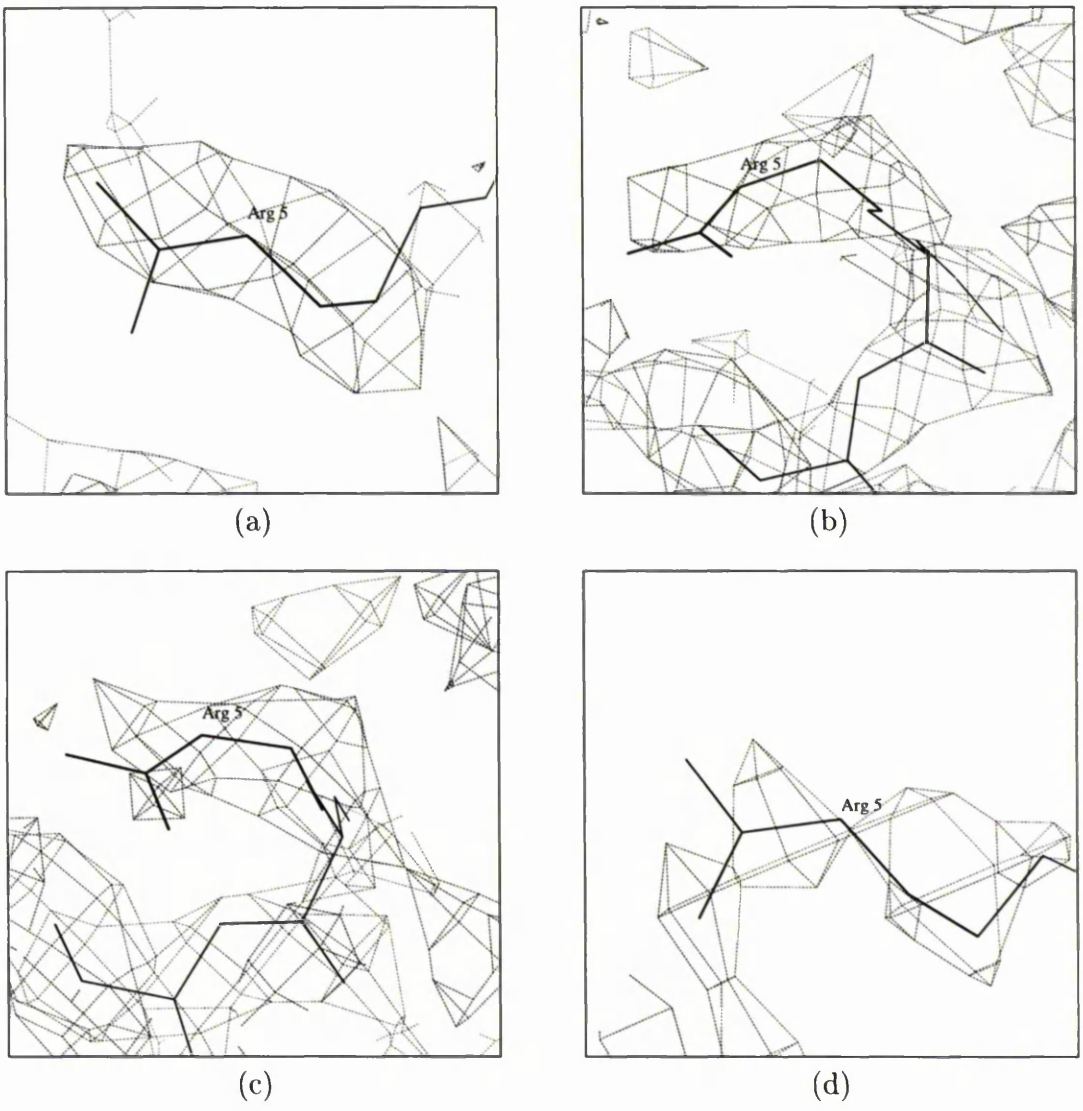

Figure 4.4: 2Fo-Fc Laue electron density maps at the 1σ level showing the Arg 5 residue for data collected with (a) 2° angular steps, (b) 4° angular steps, (c) 10° angular steps, and (d) 30° angular steps.

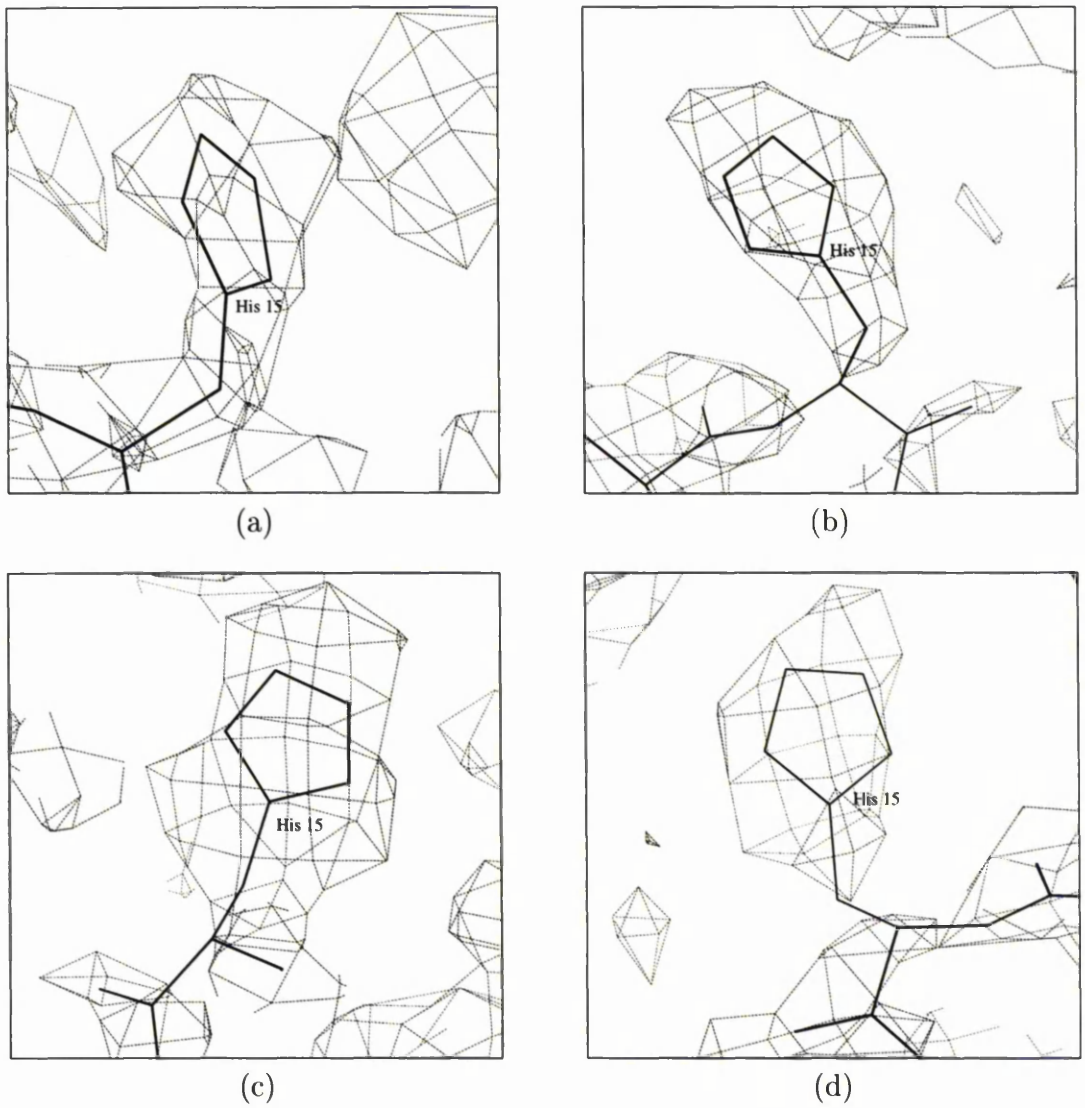

Figure 4.5: 2Fo-Fc Laue electron density maps at the 1σ level showing the His 15 residue for data collected with (a) 2° angular steps, (b) 4° angular steps, (c) 10° angular steps, and (d) 30° angular steps.

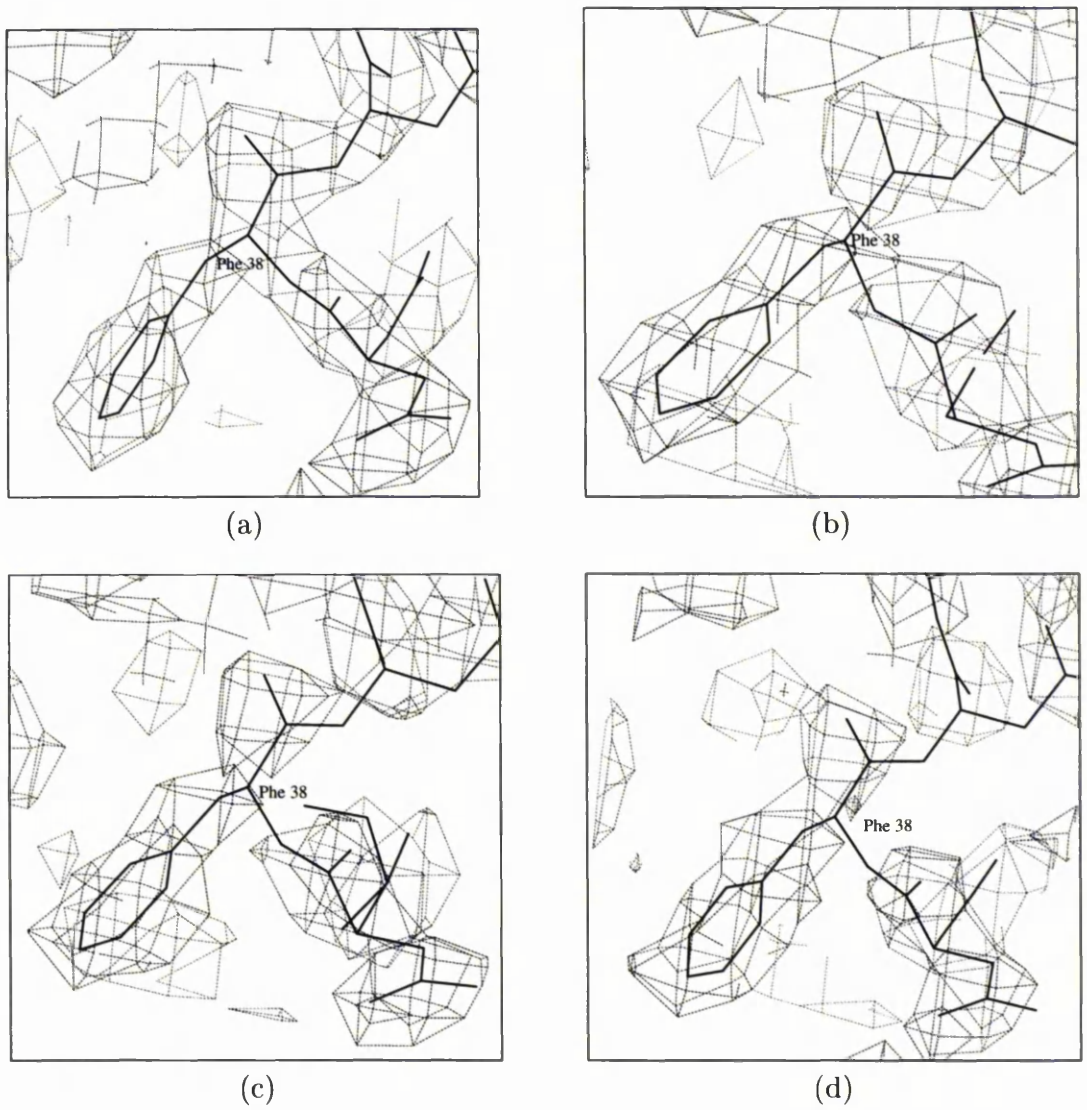

Figure 4.6: 2Fo-Fc Laue electron density maps at the 1σ level showing the Phe 38 residue for data collected with (a) 2° angular steps, (b) 4° angular steps, (c) 10° angular steps, and (d) 30° angular steps.

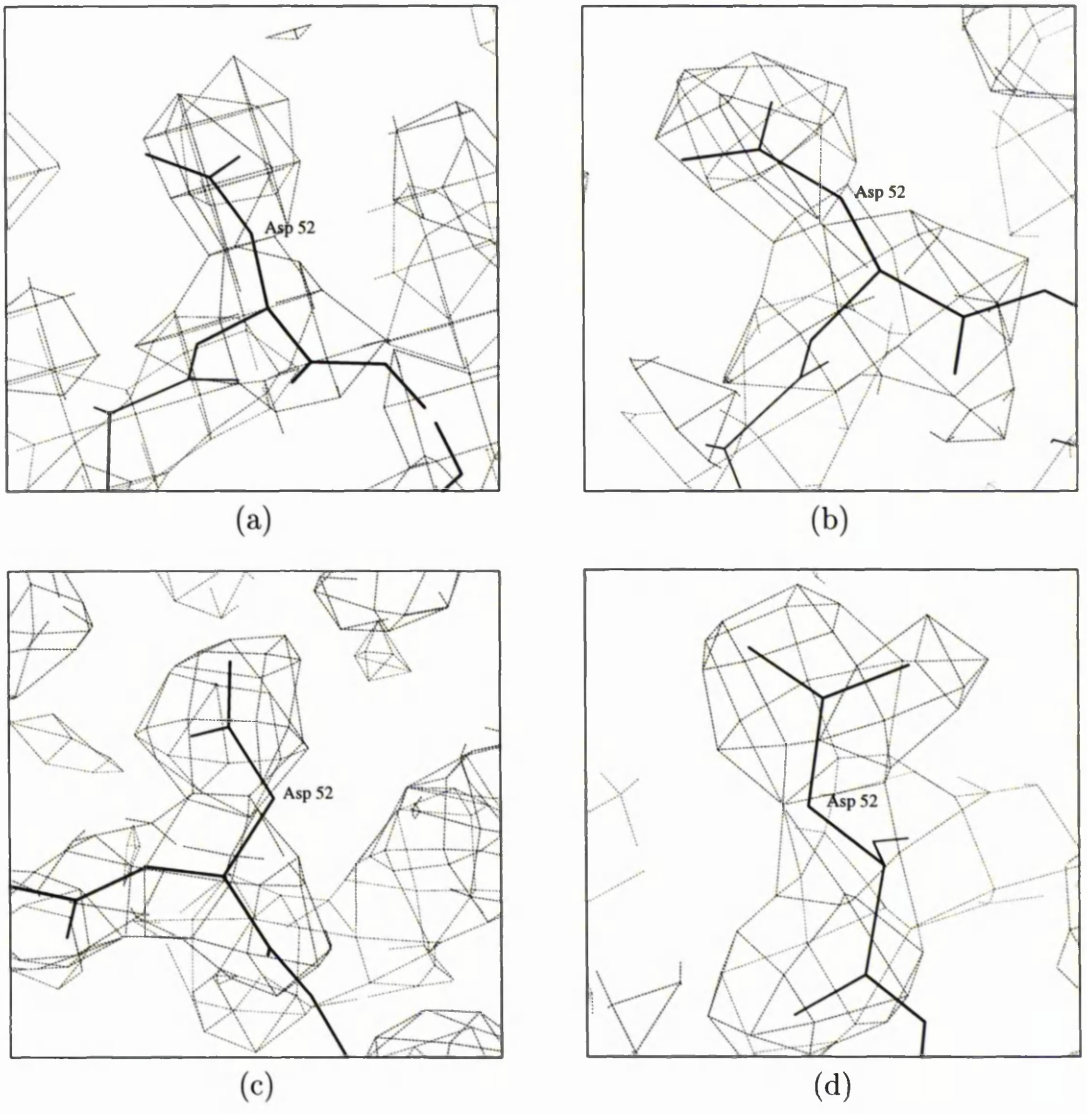

Figure 4.7: 2Fo-Fc Laue electron density maps at the 1σ level showing the Asp 52 residue for data collected with (a) 2° angular steps, (b) 4° angular steps, (c) 10° angular steps, and (d) 30° angular steps.

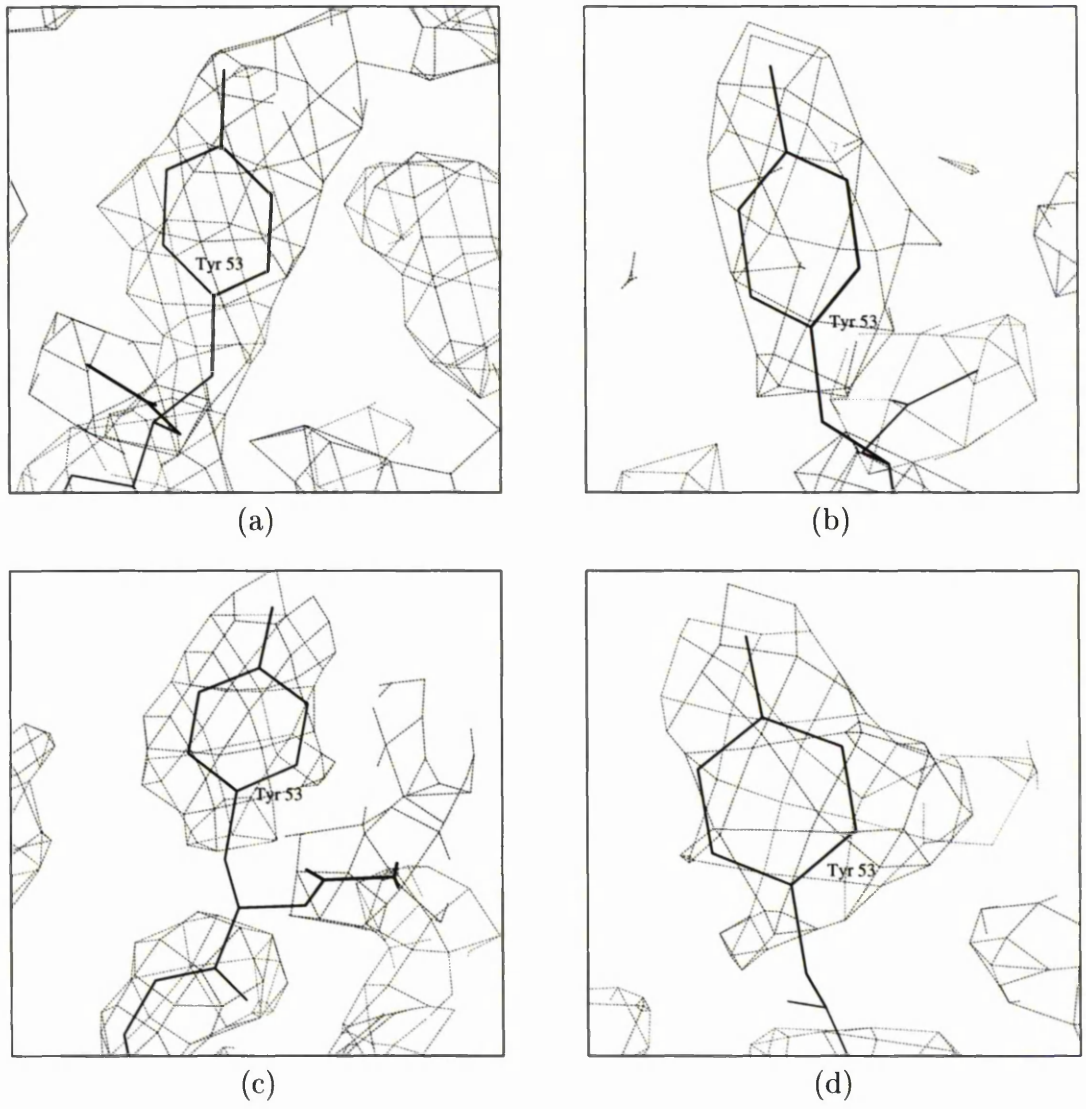

Figure 4.8: 2Fo-Fc Laue electron density maps at the 1σ level showing the Tyr 53 residue for data collected with (a) 2° angular steps, (b) 4° angular steps, (c) 10° angular steps, and (d) 30° angular steps.

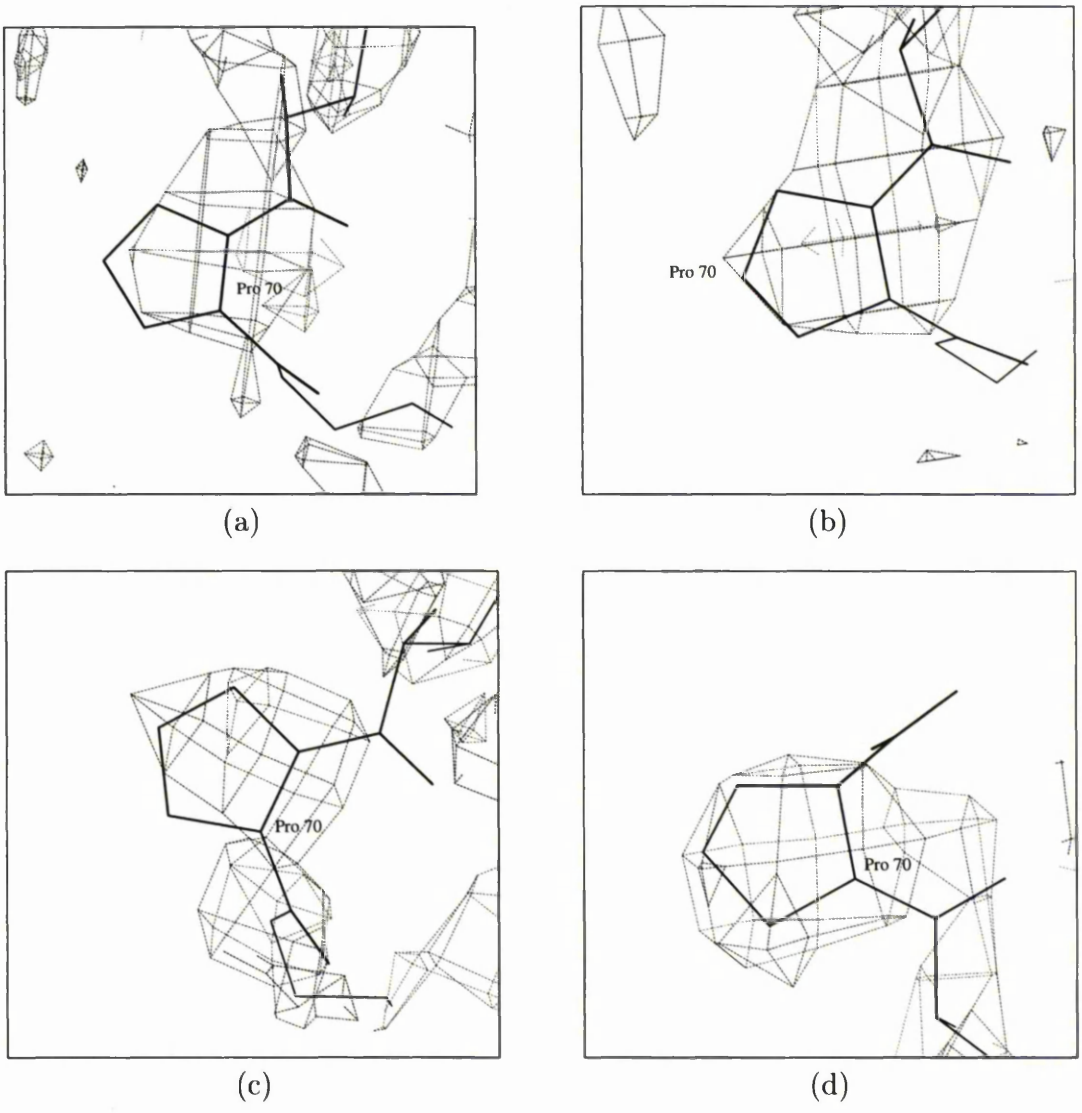

Figure 4.9: 2Fo-Fc Laue electron density maps at the 1σ level showing the Pro 70 residue for data collected with (a) 2° angular steps, (b) 4° angular steps, (c) 10° angular steps, and (d) 30° angular steps.

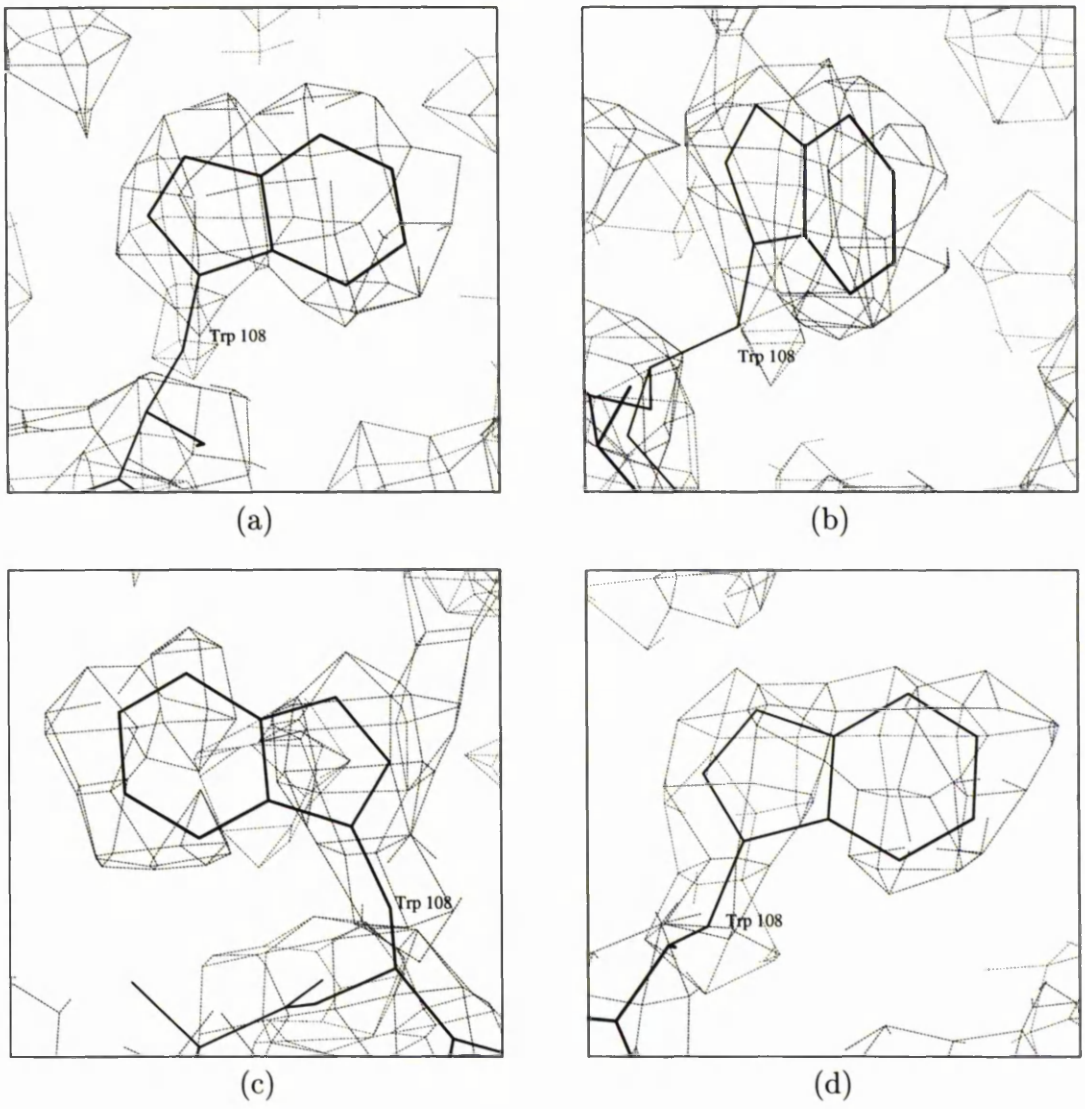

Figure 4.10: 2Fo-Fc Laue electron density maps at the 1σ level showing the Trp 108 residue for data collected with (a) 2° angular steps, (b) 4° angular steps, (c) 10° angular steps, and (d) 30° angular steps.

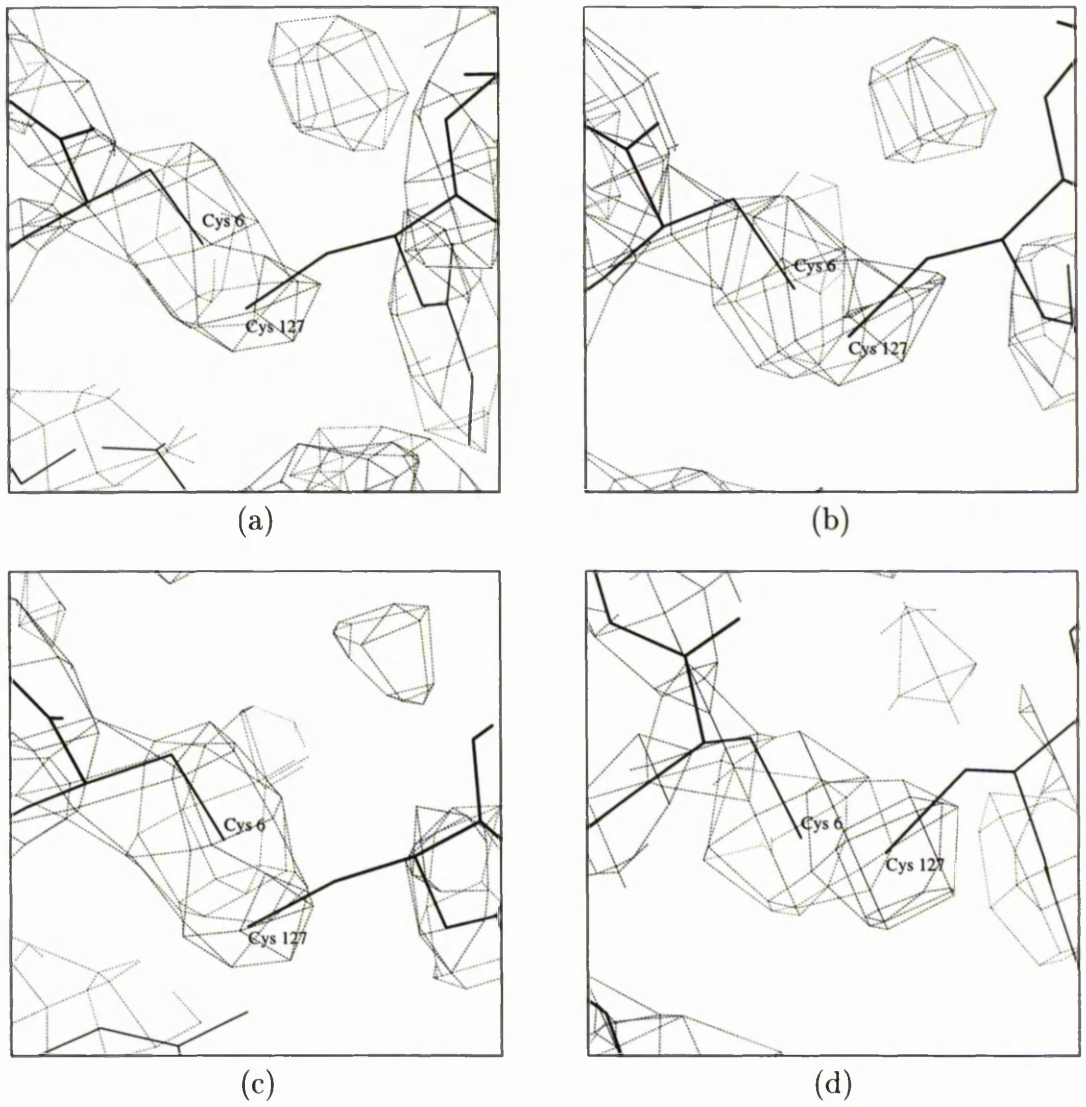

Figure 4.11: 2Fo-Fc Laue electron density maps at the 1σ level showing the disulphide bridge between the Cys 6 and Cys 127 residues for data collected with (a) 2° angular steps, (b) 4° angular steps, (c) 10° angular steps, and (d) 30° angular steps.

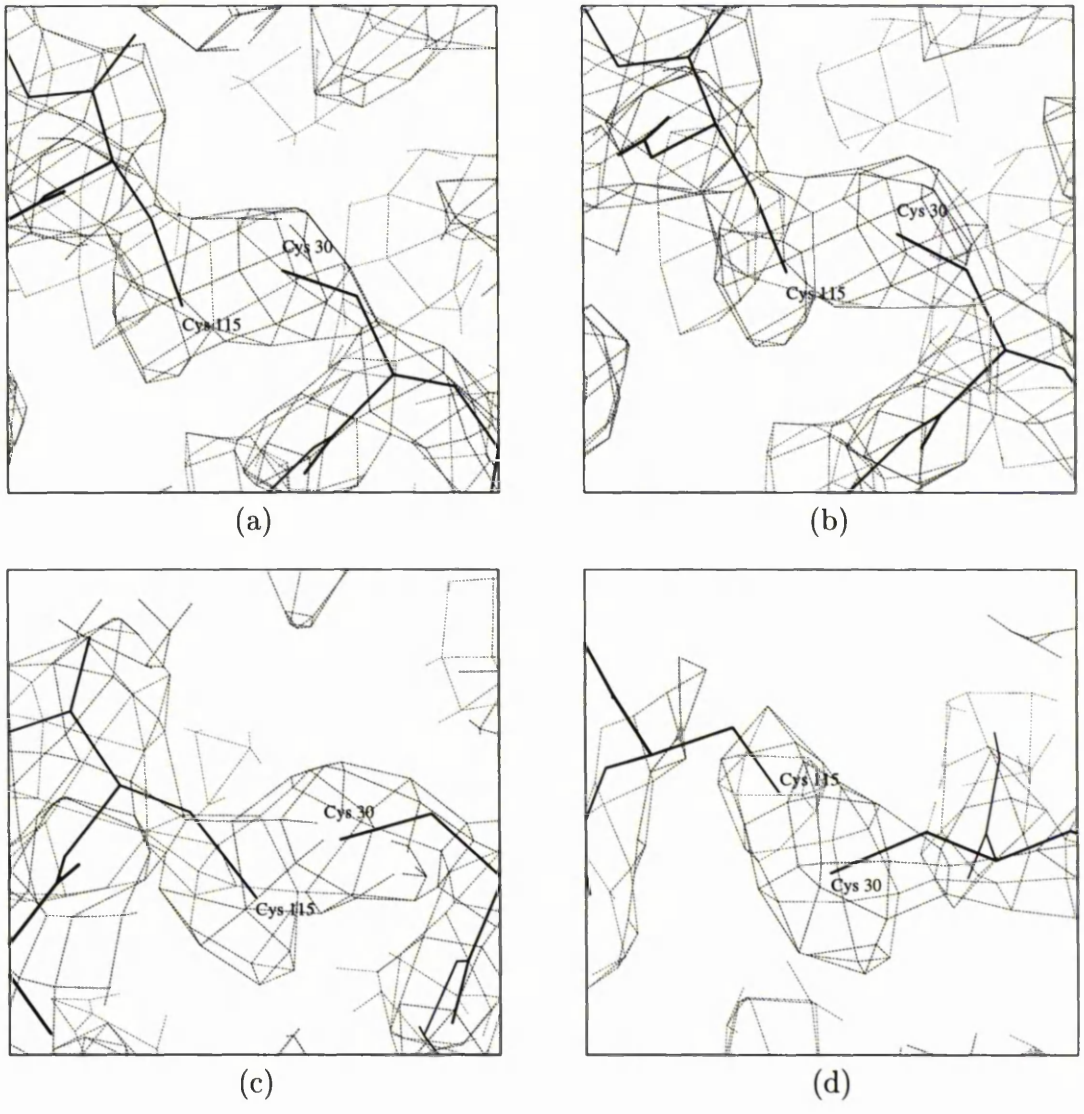

Figure 4.12: 2Fo-Fc Laue electron density maps at the 1σ level showing the disulphide bridge between the Cys 30 and Cys 115 residues for data collected with (a) 2° angular steps, (b) 4° angular steps, (c) 10° angular steps, and (d) 30° angular steps.

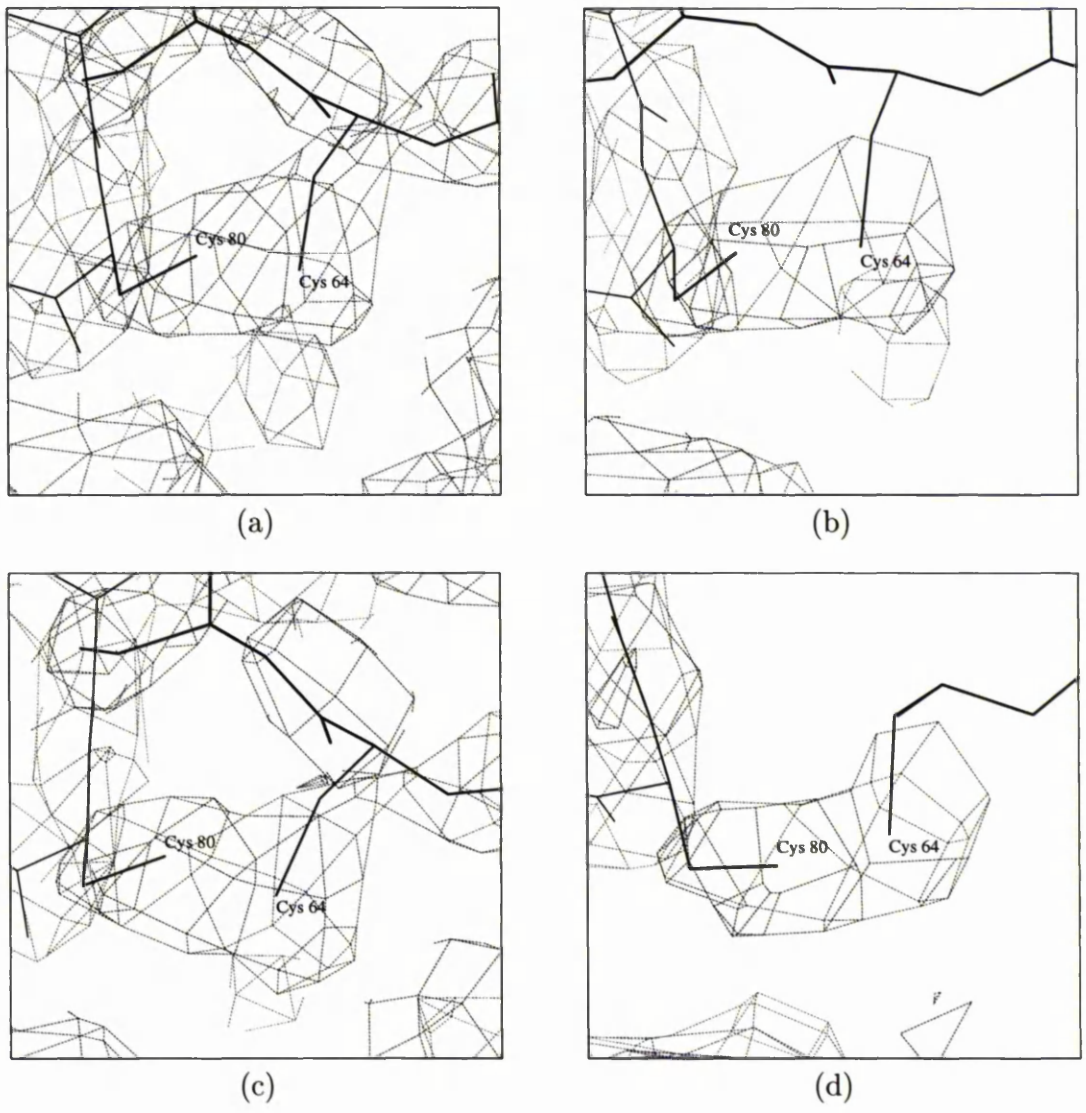

Figure 4.13: 2Fo-Fc Laue electron density maps at the 1σ level showing the disulphide bridge between the Cys 64 and Cys 80 residues for data collected with (a) 2° angular steps, (b) 4° angular steps, (c) 10° angular steps, and (d) 30° angular steps.

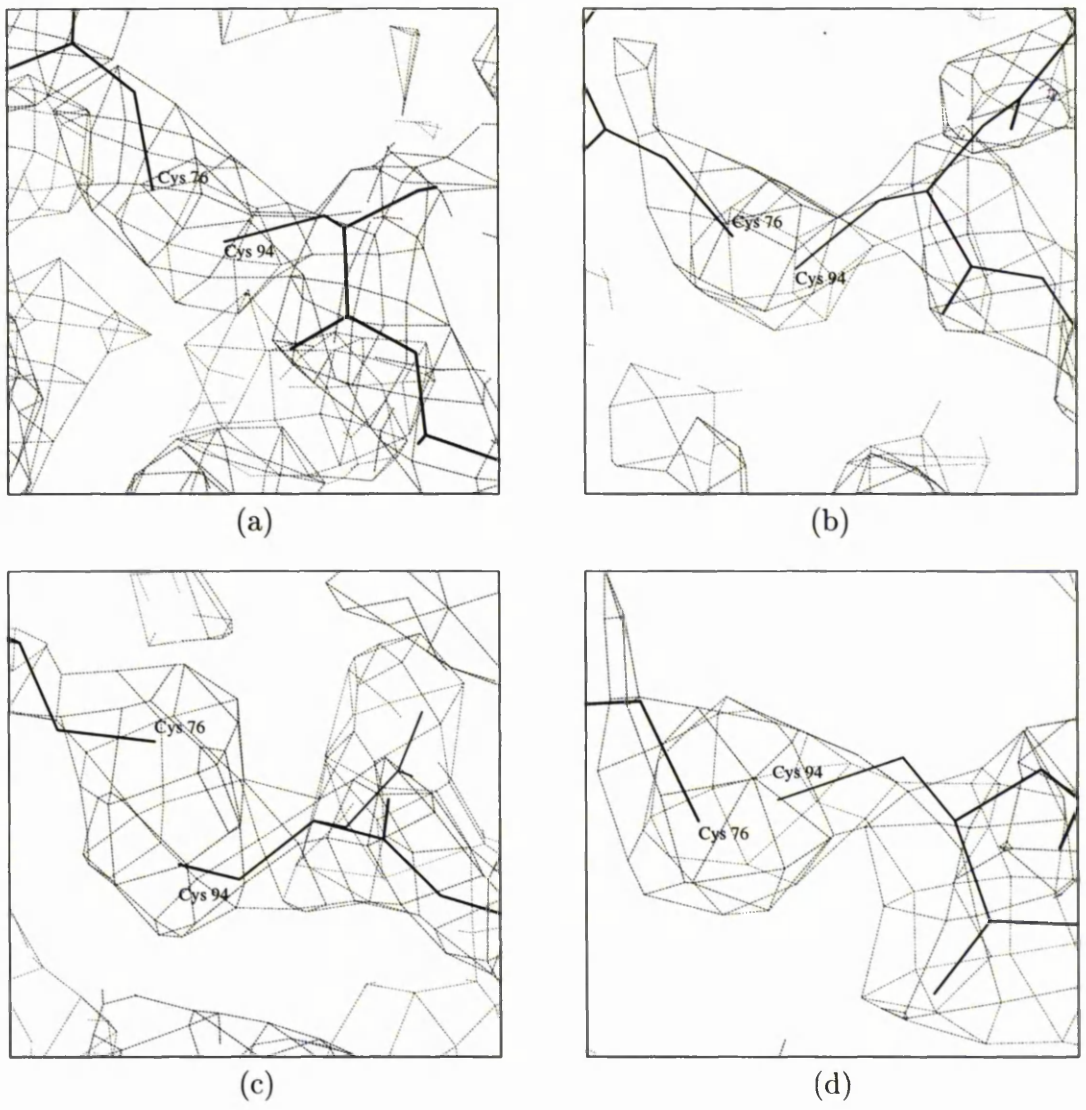

Figure 4.14: 2Fo-Fc Laue electron density maps at the 1σ level showing the disulphide bridge between the Cys 76 and Cys 94 residues for data collected with (a) 2° angular steps, (b) 4° angular steps, (c) 10° angular steps, and (d) 30° angular steps.

data set is well illustrated. The real space R-factor is given by

$$R_{res} = \sum |\rho_{obs} - \rho_{calc}| / \sum |\rho_{obs} + \rho_{calc}| \tag{4.1}$$

where ρ_{obs} is taken for the residue from the electron density map and ρ_{calc} from a calculated electron density assuming a Gaussian atom distribution. The function was primarily designed to identify where the protein sequence is out of register with the atom density but is useful in the case of methods development reported here.

It is evident that the increase of low resolution reflections contribute to the quality of the maps. The electron density around the four disulphide rings is good in each case as was also found in a study of the activity of lysozyme.[29] Overall connectivity of the main chain is much improved as is the side chain density with more data. Somewhat puzzling is that in a few regions lower completeness data seems to show a better electron density in terms of connectivity. Overall, however the expected trend is that indeed better completeness yields better connectivity.

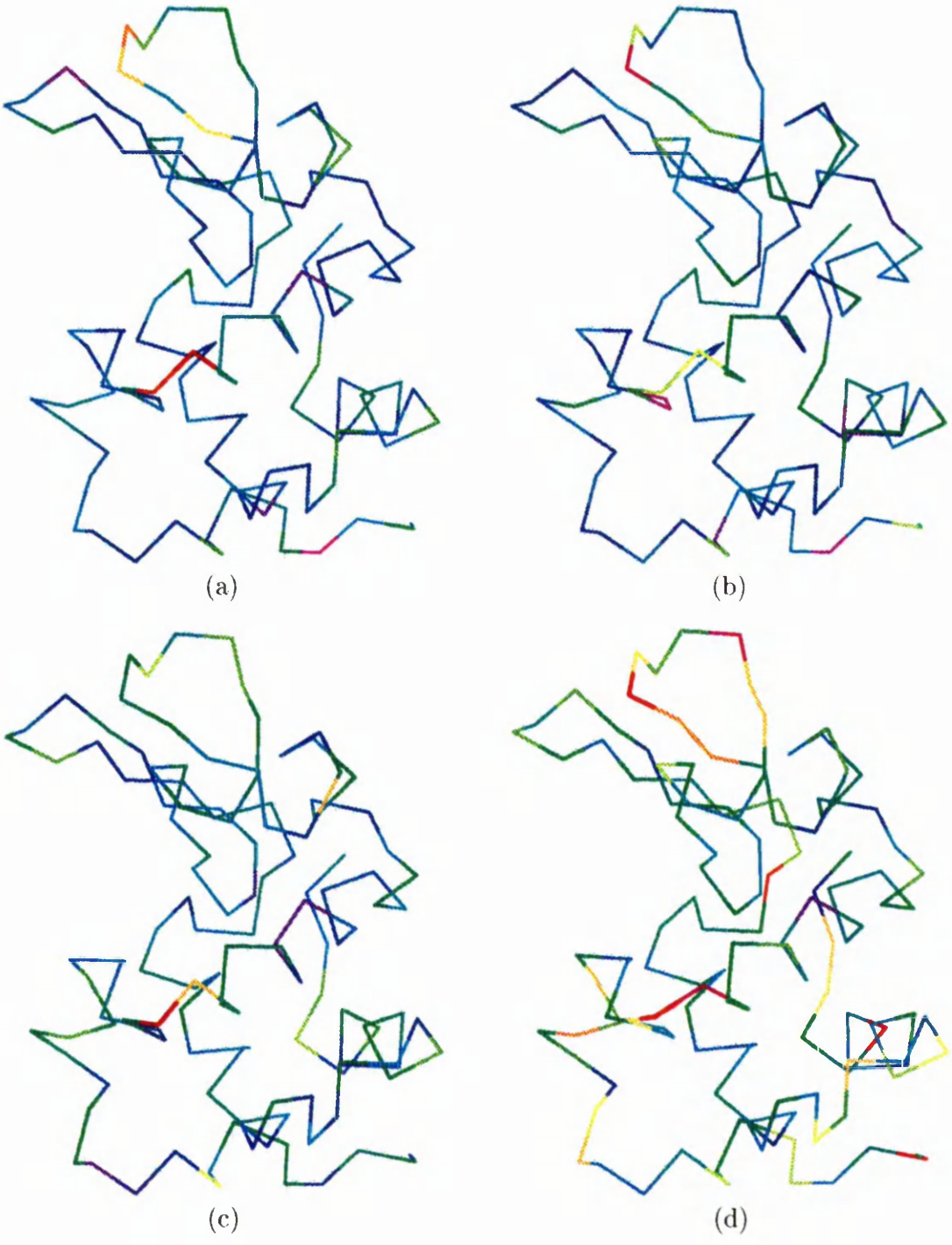

Figure 4.15: Cα trace of the lysozyme structure coloured according to the R-factor of the residues (red = 0.43, blue = 0.26) for data collected with (a) 2° angular steps, (b) 4° angular steps, (c) 10° angular steps, and (d) 30° angular steps

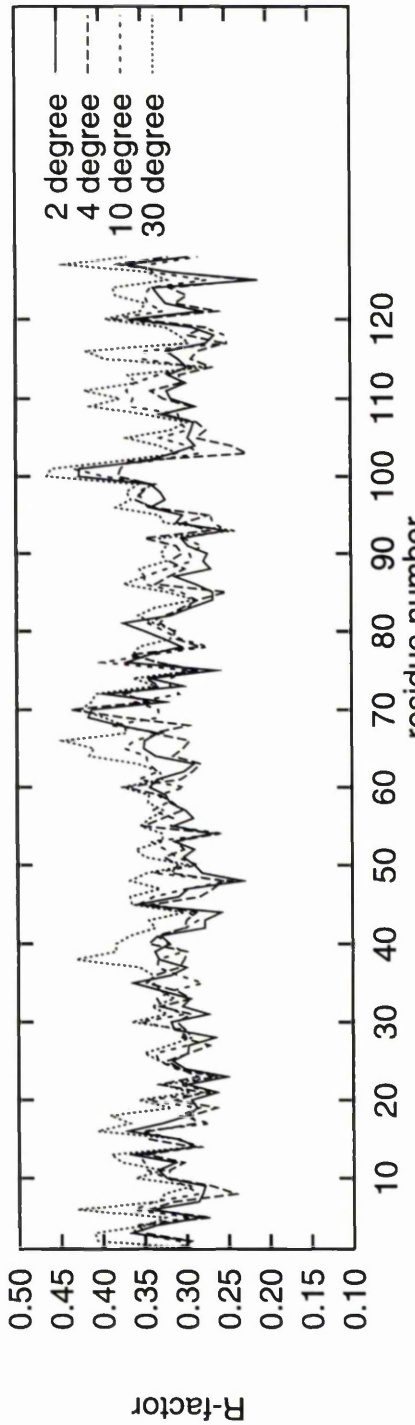

Figure 4.16: The Real-Space R-factors[144] are shown on a per-residue basis, for the 2°, 4°, 10° and 30° angular interval Laue data.

Residues	4°	10°	30°	6LYZ Model
In most favoured regions	87.6%	85.8%	84.1%	85.8%
In additionally disallowed regions	12.4%	14.2%	15.9%	14.2%

Table 4.7: Lysozyme residues present in most favoured and additionally allowed regions of the Ramachadran plot

4.8 Quality of final models

The Ramachadran[192] plots produced by PROCHECK[151] are shown in figure 4.17. The Ramachandran plot is a plot of the angle of rotation of the N-C_α bond (ϕ) against the angle of rotation of the C_α-C bond (ψ) from the same C_α atom of a particular part of the peptide chain of the protein. These two angles, ϕ and ψ, are the only degrees of freedom hence the conformation of the whole chain is completely determined when these are described. Most combinations of ϕ and ψ are not allowed because of steric collisions (either between atoms in different peptide groups or between a peptide unit and the side chain attached to the C_α). The residues in most favoured and additionally allowed regions are shown in table 4.7 along with the 6LYZ model details. There were no residues in generously allowed or disallowed regions. The Ramachandran plot displays allowed regions as shaded, glycine residues are marked as ▲ and non-glycine residues as ■. Glycine with only a hydrogen atom as a side chain can adopt a much wider range of conformations than the other residues. The most favoured regions are (A,B,L) are denoted by dark grey shading, additional regions (a,b,l,p), generously disallowed regions (~a,~b,~l,~p) and disallowed regions progressively lighter.

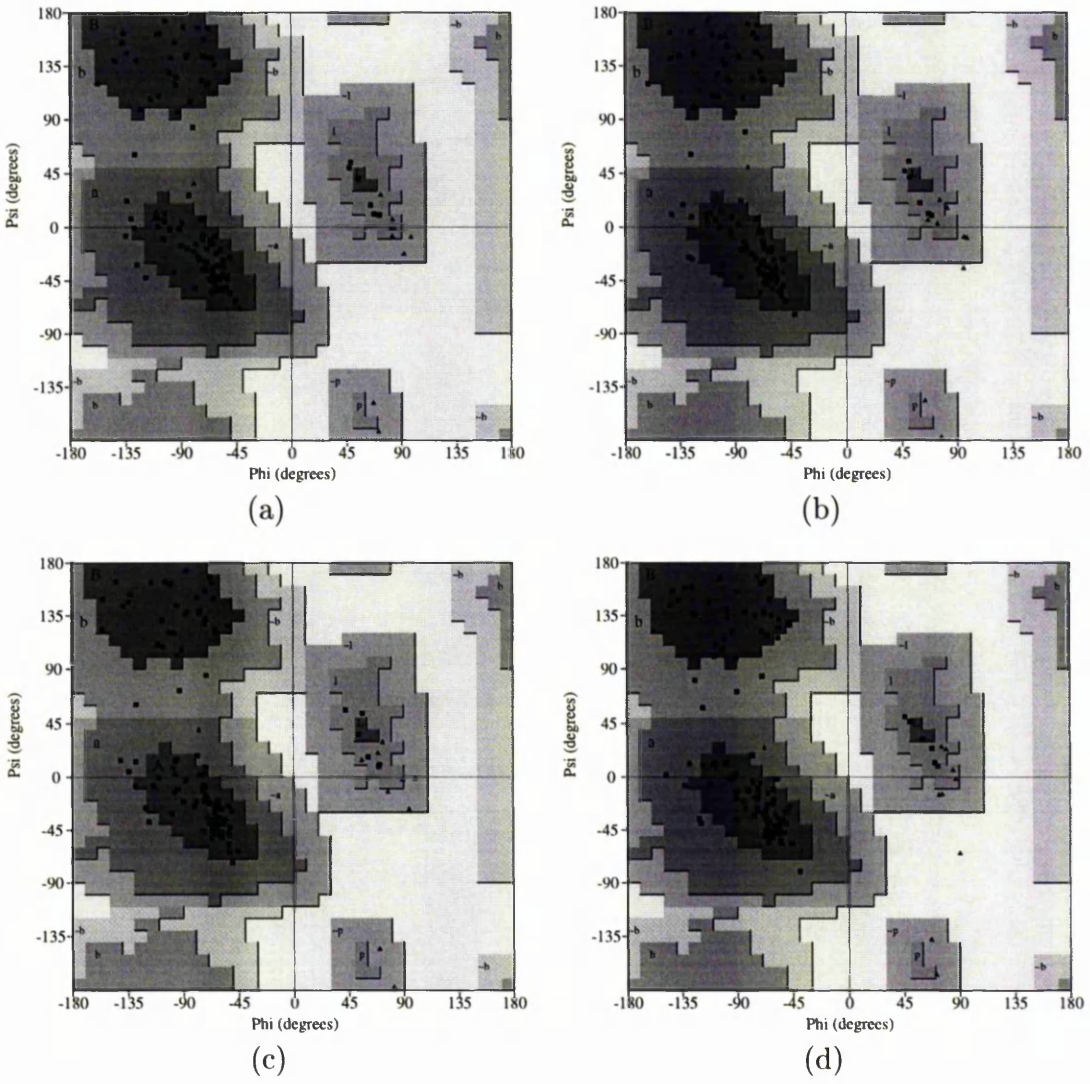

Figure 4.17: Ramachandran plots for tetragonal lysozyme for data collected with (a) 2° angular steps, (b) 4° angular steps, (c) 10° angular steps, and (d) 30° angular steps. Total angular coverage of 60°.

4.9 Summary

The ease with which recently available automatic readout detectors can be utilised is important, as is the extra sensitivity of those devices over photographic film in realising routine measurement of many more Laue diffraction images per crystal. The ability to measure many more images in a short time, limited by exposure and image scanning time, allows the problem of a lack of low resolution data to be overcome. It is noticeable in the increase of the low resolution data via smaller angular interval data collection and multiples deconvolution how effective the techniques are. The 2° interval case shows electron density maps as good as any monochromatic electron density maps for that resolution (2.5 Å).

Chapter 5

ESRF CCD detector calibration with the Laue method

5.1 Introduction

Inherently the image plate (and obviously film) do not have an ideal capability for time-resolved recording of X-rays[5] because of a poor readout time (or developing time) involved. The Charge Coupled Device (CCD) offers a faster readout and low noise detector[2, 3, 4, 111] and has recently become routinely available for X-ray data collection.[70, 111, 234, 243] Spatial distortions and non-uniform response occur, to some extent, in all area detectors.[172, 223] Any distortion and non-uniformity response have to be corrected and a standard procedure has to be developed. At the ESRF there is a CCD (with image intensifier device) which has good sensitivity and fast readout. This chapter is concerned with assessing the need for calibration corrections to the recorded image data in particular.

5.2 "Image Mapping" Corrections and Calibrations

Spatial distortions are divided into two types, gross distortions produced by inherent properties of the detector components and local distortions formed by irregularities in the components. Correction of spatial distortion is achieved by use of a grid constructed from an X-ray opaque material with an array of holes. By comparing the recorded image of this grid with the true mask geometry a transform can be calculated and applied to data collected to remove any spatial distortion.

The non-uniformity of responce to intensity of the detector is derived from a uniform incident flood field of radiation. Since it is likely that this might be wavelength dependent too, a series of flood field images with radiation of different wavelengths are ideally required. At the time of our first experiment at ESRF beamline 3 with the ESRF CCD detector such a sequence of non-uniformity calibrations were not available. Hence a set of Laue data were collected to try to ascertain the need for such a correction.

5.3 Equipment

The ESRF image intensifying CCD detector,[170] figure 5.1, was used on beamline 3, the Laue beamline,[148] at the European Synchrotron Radiation Facility (ESRF). This detector[36, 170] consists of a scintillator which converts the incident X-rays to light which is then converted to electrons and amplified by a photo-cathode.

The electrons are focussed electrostatically onto the CCD. The aperture of the detector is 15 × 17 cm with an overall pixel size of about 250 μm . This resolution results from the combination of several optical elements and the CCD resolution itself, 24 μm . The CCD comprises 1024^2 pixels with a readout speed of 2×10^5 pixels s^{-1} (ie. each whole image can be readout in seconds). In operation the CCD is cooled by a Peltier element to -25° and has a dark current of ≈10 electrons with a dynamic range of 1:30000 per pixel.

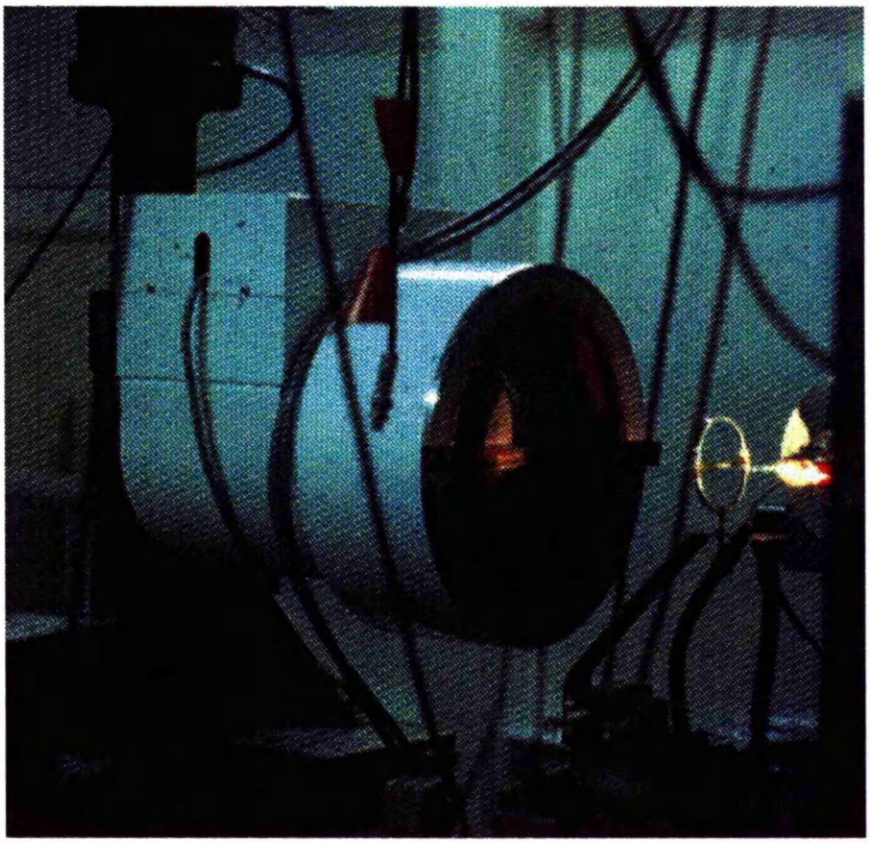

Figure 5.1: Image intensifying CCD detector installed on ESRF beamline 3 (seen without electrostatic shielding)

5.4 Experimental

Laue data were collected, in fact, from a lysozyme crystal grown on the IML-2 mission[130, 221] (see chapter 8). An initial exposure of 400 msec was made onto photographic film with a crystal to detector distance of 96 mm. Nine exposures of 20 msec were then taken using the CCD detector at 1° spindle intervals (0 to 8°) with crystal to detector distance of 210 mm. A further nine exposures were made in 8° intervals (16 to 80°) and a grid image recorded for spatial distortion correction. Figure 5.2 shows an example of a recorded image and the resulting spatially corrected image. Hence the 1° interval data would greatly assist determination of the uniformity of response of the CCD and the 8° interval data covering a full 64° range would allow a complete data set to be obtained (for comparison with chapter 4).

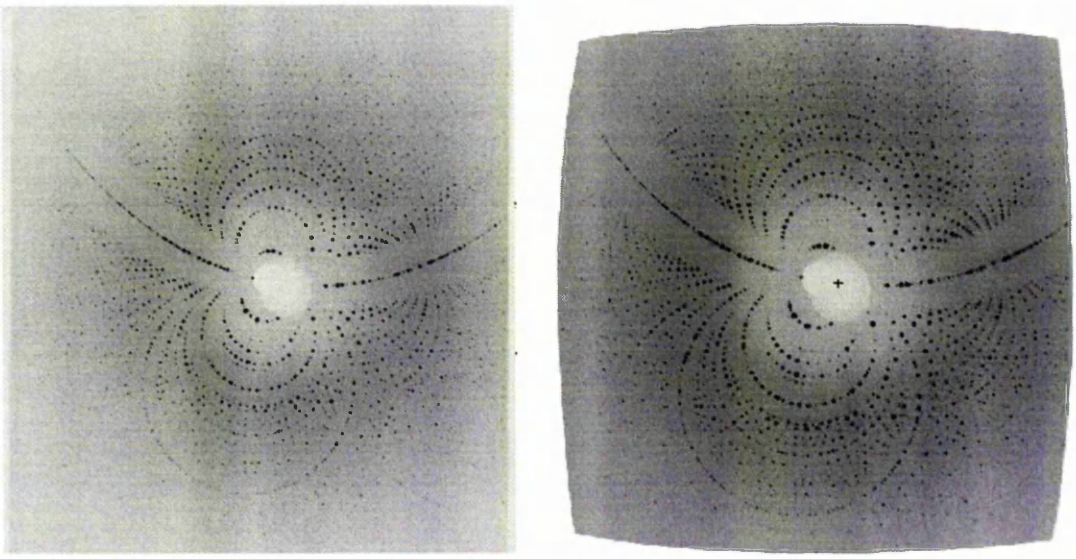

(a) (b)

Figure 5.2: ESRF CCD images recorded from lysozyme (a) uncorrected and (b) with distortion correction applied

5.5 Data Processing

The spatial distortion correction effect is seen with the initial rectangular image produced directly from the CCD (figure 5.2(a)) compared to the almost 'TV screen' like profile of the image used for processing (figure 5.2(b)). The spatial distortion correction procedure (section 5.2) was repeated for each image. These images are then properly spatially corrected. The CCD images were subsequently processed with LAUEGEN and INTLAUE to produce a set of integrated, indexed intensities (with positional information retained). The soft limits, λ_{min}, and d_{min} were derived using LAUEGEN (from a measure of the distribution of intensities with wavelength and resolution,[118] figure 5.3), at 0.35 Å and 2.00 Å respectively. The upper wavelength limit, λ_{max}, was evaluated at 1.00 Å by comparison with recorded images and predictions - a similar technique to finding λ_{min} and d_{min} could have been used but in practice very few spots were recorded for large λ because of the limited angular aperture of the detector.[118]

Positional refinement of the spot predicted positions gave a consistent average rms deviation from the recorded spot positions of 0.0287 mm (with a standard deviation of 0.0008 mm). The twist, tilt and bulge show quite a deviation from their mean values of, 0.504°, 0.098° and 0.005° respectively. There is, however, no evidence of major positional deviation in the spots despite the deviations in refined parameters found between successive images (plotted in figure 5.4 for the first nine images).

The data from the first nine images were initially wavelength normalised using LAUENORM. The resulting normalisation curve is shown in figure 5.5. In this case the peak occurs at 0.55 Å as compared the the image plate lysozyme data

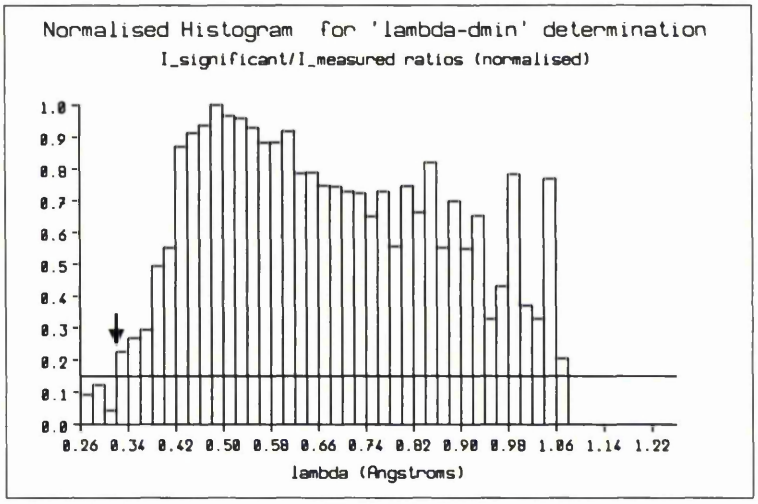

(a)

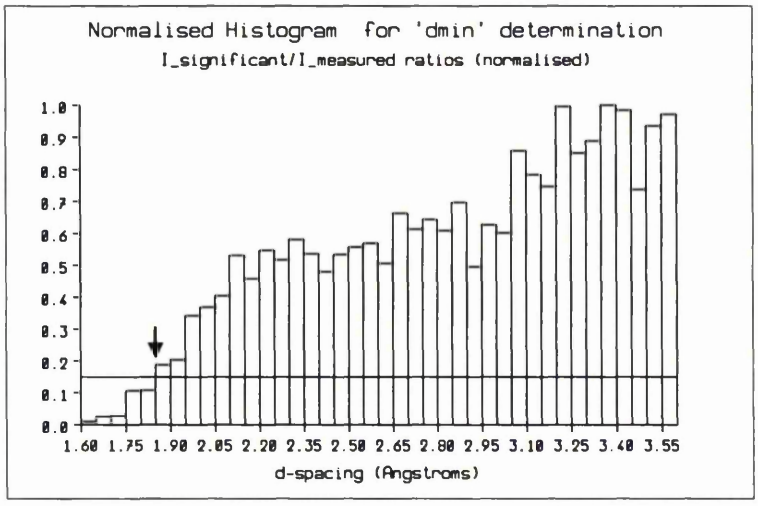

(b)

Figure 5.3: Histogram output from LAUEGEN[48, 118] of normalised intensities against (a) wavelength and (b) resolution for determination of λ_{min} and d_{min} soft limits respectively.

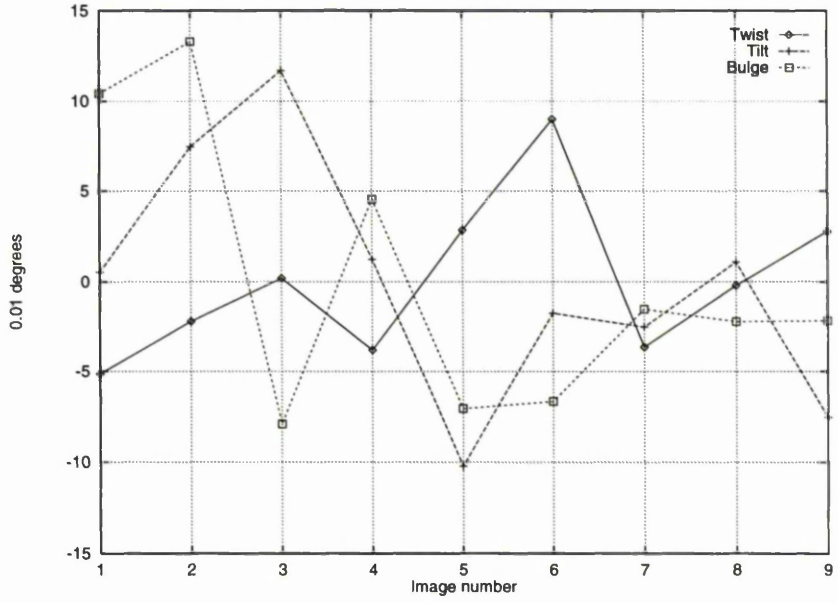

Figure 5.4: Deviation from the mean for the twist, tilt and bulge refinement parameters with ESRF CCD collected Laue data

collected on station 9.5 of the SRS, page 85, where the normalisation is unity at approximately 0.82 Å. This demonstrates the shift to useable shorter wavelengths with the higher brilliance ESRF compared to the SRS. The data was then reduced to a unique data set with the CCP4[65] programs ROTAVATA and AGROVATA. These results then serve as a baseline from which we can try and improve with the introduction of non-uniformity of response corrections. An attempt to get such a correction will now be described.

The images were separately treated with the program LAUESCALE to produce an intensity response surface. As discussed, in chapter 3, LAUESCALE can be used to calculate and apply an absorption correction surface. Hence, with the short wavelengths used absorption becomes negligibly small and can be ignored.[11, 12, 109, 126] The correction surface produced is therefore then a measure of the non-uniformity

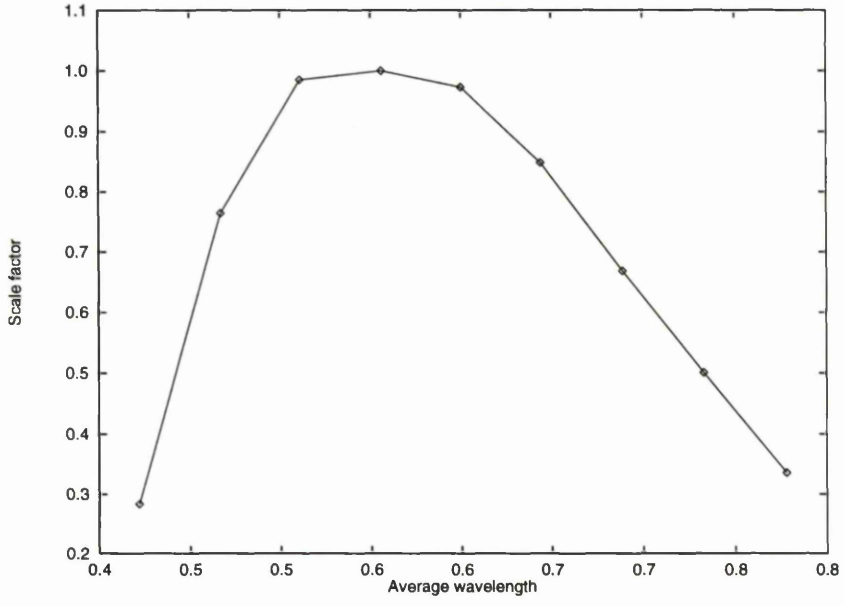

Figure 5.5: Wavelength normalisation curve produced from ESRF CCD collected lysozyme crystal data

of the detector response, *if we assume this is independent of wavelength.* LAUESCALE has to use a reference data set to scale the as-measured intensities against. The structure factors (converted to intensities) obtained from the PDB[22] deposited 6LYZ[31, 77] data set were used for this purpose. Hence, for each image a non-uniformity intensity response surface was calculated then a corrected (scaled) data set produced. The first nine data sets were then merged and used to produce a unique set of reflections again using ROTAVATA and AGROVATA for comparison with the case described in the previous paragraph (ie. without a correction).

As a cross-check in this procedure, in addition, for the first CCD image a photographic film exposure, figure 5.6(a), was recorded at the same spindle axis setting of the crystal (but a different crystal to detector distance). The CCD image was scaled to the film image. Photographic film has a uniform (non-varying) intensity

response across its surface for a given wavelength (variation less than 1%).[87, 241] The film data (produced from LAUEGEN and INTLAUE) were converted to a format suitable for input to LAUESCALE. Hence, a non-uniformity intensity response surface was again produced, in this case based on the film as a reference.

5.6 Results

The photographic image recorded is shown in figure 5.6(a) together with the corresponding non-uniformity response surface, (b). Figures 5.7 to 5.9 show the non-uniformity response for the 0° to 8° spindle positions intended for detector calibration. Figures 5.9 to 5.11 show the surface for the remaining images, spindle axis of 16° to 80°. In all cases contouring is shown with the 100% peak in the highest response position position of the surface decreasing in 5% steps from that.

As each image was recorded in time sequence it would be expected to see only slight variation in the overall response of the detector. The results shown here are therefore somewhat surprising as the response varies quite markedly. The deviation of the peak of the response from the centre of the detector is illustrated by figure 5.12. Image number 7, figure 5.8(c), has two peaks visible and the highest one, 100% response, is chosen.

In comparing the corrected data (non-uniform intensity response scaling applied) to the uncorrected data the $R_{factors}$ (more correctly termed R_{merge}, see page 54) are shown in figure 5.13 plotted against intensity and resolution, d_{min}. The data were processed to 2.0 Å (just above the LAUEGEN estimate although from

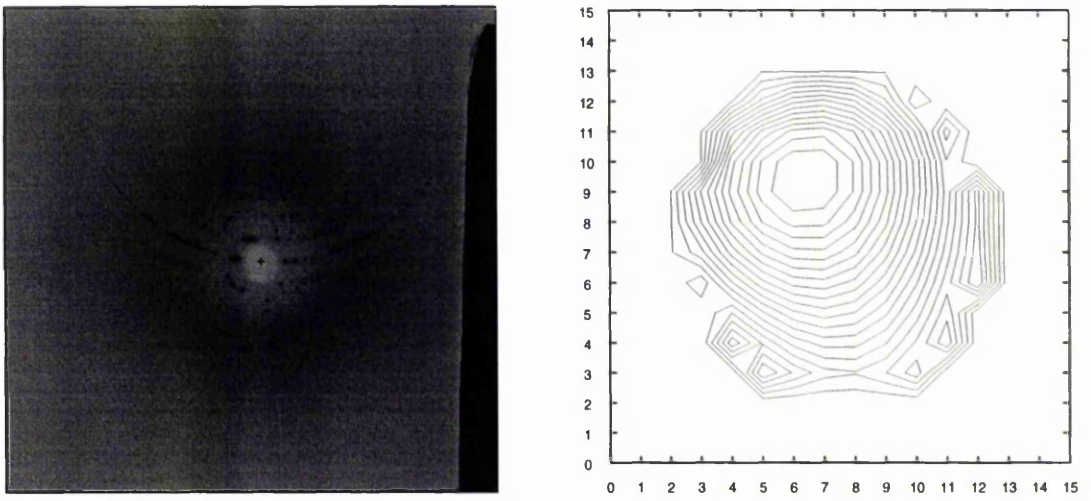

(a) (b)

Figure 5.6: ESRF (a) Laue data recorded photographically from tetragonal lysozyme. The large dark region visible at right is due to a developing problem at the time of data collection. (b) The corresponding CCD detector response function derived from film (a) and CCD image 5.2. The contours range from 100% response at the centre to zero response at the edges (ie. each contour is a 5% decrease in sensitivity).

figure 5.13, a more reasonable value would seem to be 2.3-2.5 Å). The low intensity data is poor below the intensity value of approximately 1250. For the R_{factor} versus intensity plot the final intensity data bin was not included in the graph because of the wide range of the bin and the few reflections included - corrected data, intensity 5000 to 16988 with 55 reflections (8 unique), uncorrected data, intensity 5000 to 28768 with 310 reflections (38 unique).

5.7 Discussion and Concluding Remarks

Producing a non-uniformity correction with Laue data for an image intensifying CCD detector has posed a challenge. Pixel to pixel uniformity is very likely

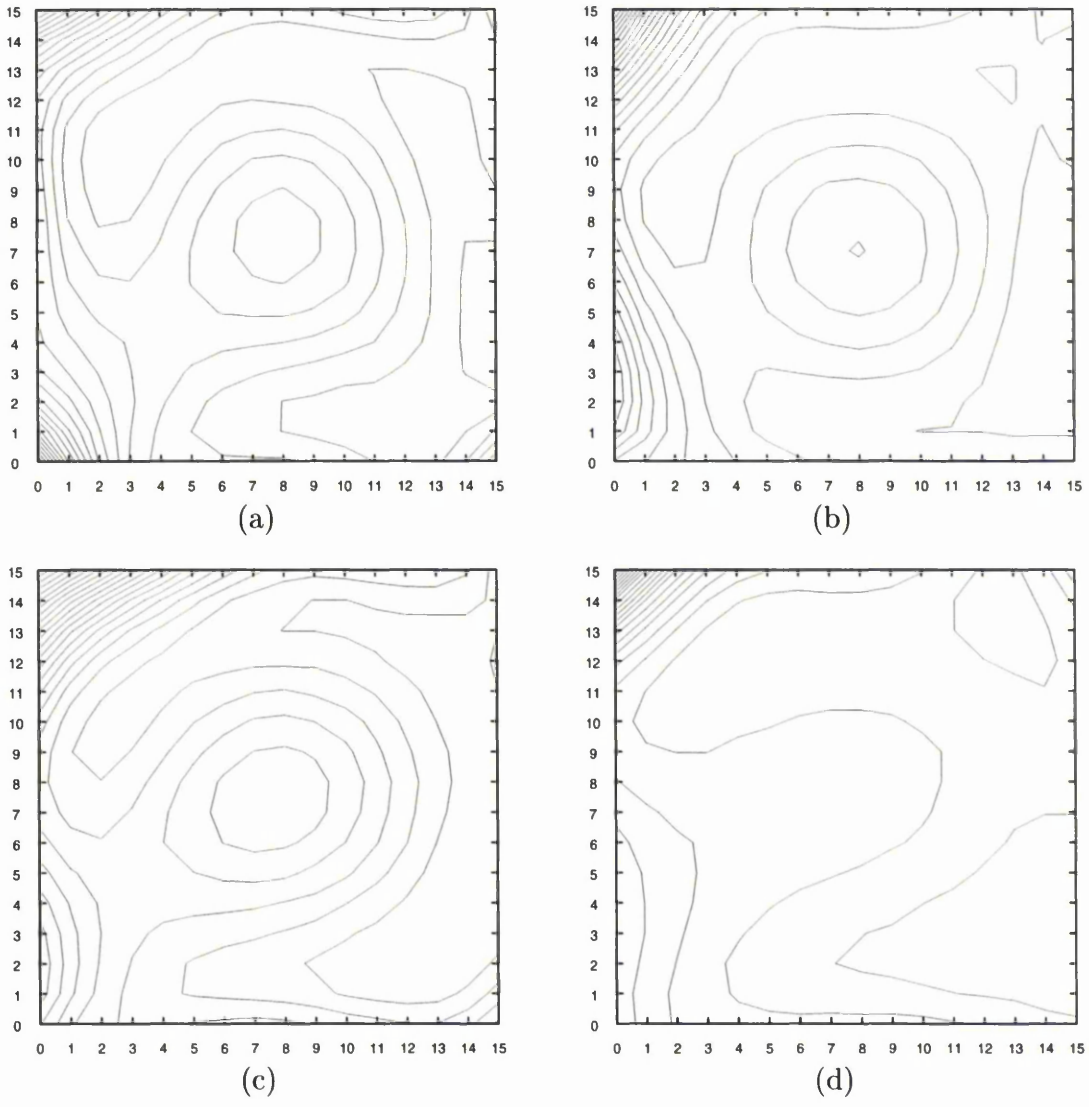

Figure 5.7: Intensity response surfaces for ESRF Beamline 3 CCD detector with tetragonal lysozyme for exposures at spindle axis settings of (a) 0°, (b) 1°, (c) 2° and (d) 3°. Contouring is from 100% response at the centre in 5% steps from that. Response surface (a), 0°, should be compared with figure 5.6(b).

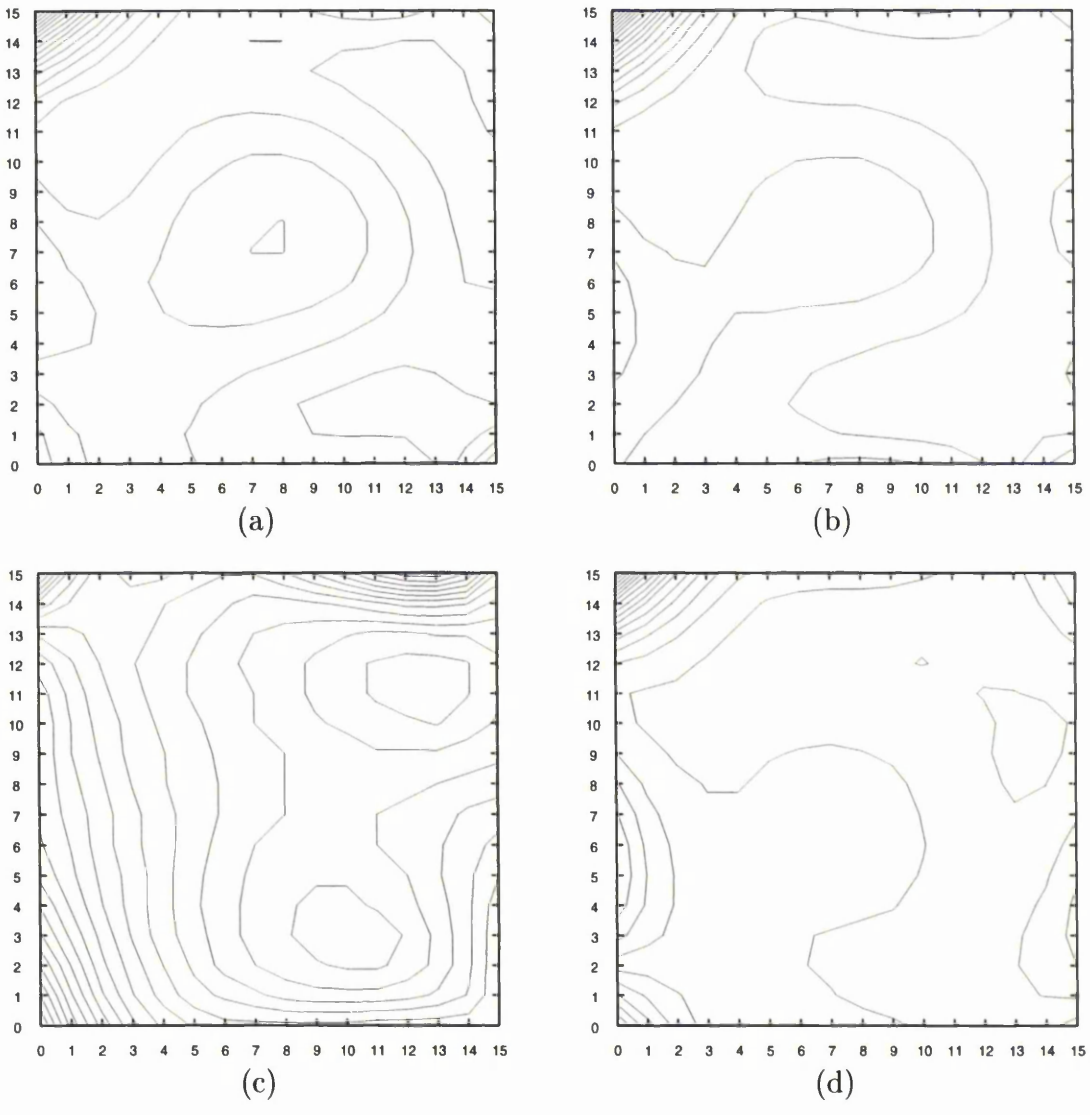

Figure 5.8: Intensity response surfaces for ESRF Beamline 3 CCD detector with tetragonal lysozyme for exposures at spindle axis settings of (a) 4°, (b) 5°, (c) 6° and (d) 7°. Contouring is from 100% response at the centre in 5% steps from that.

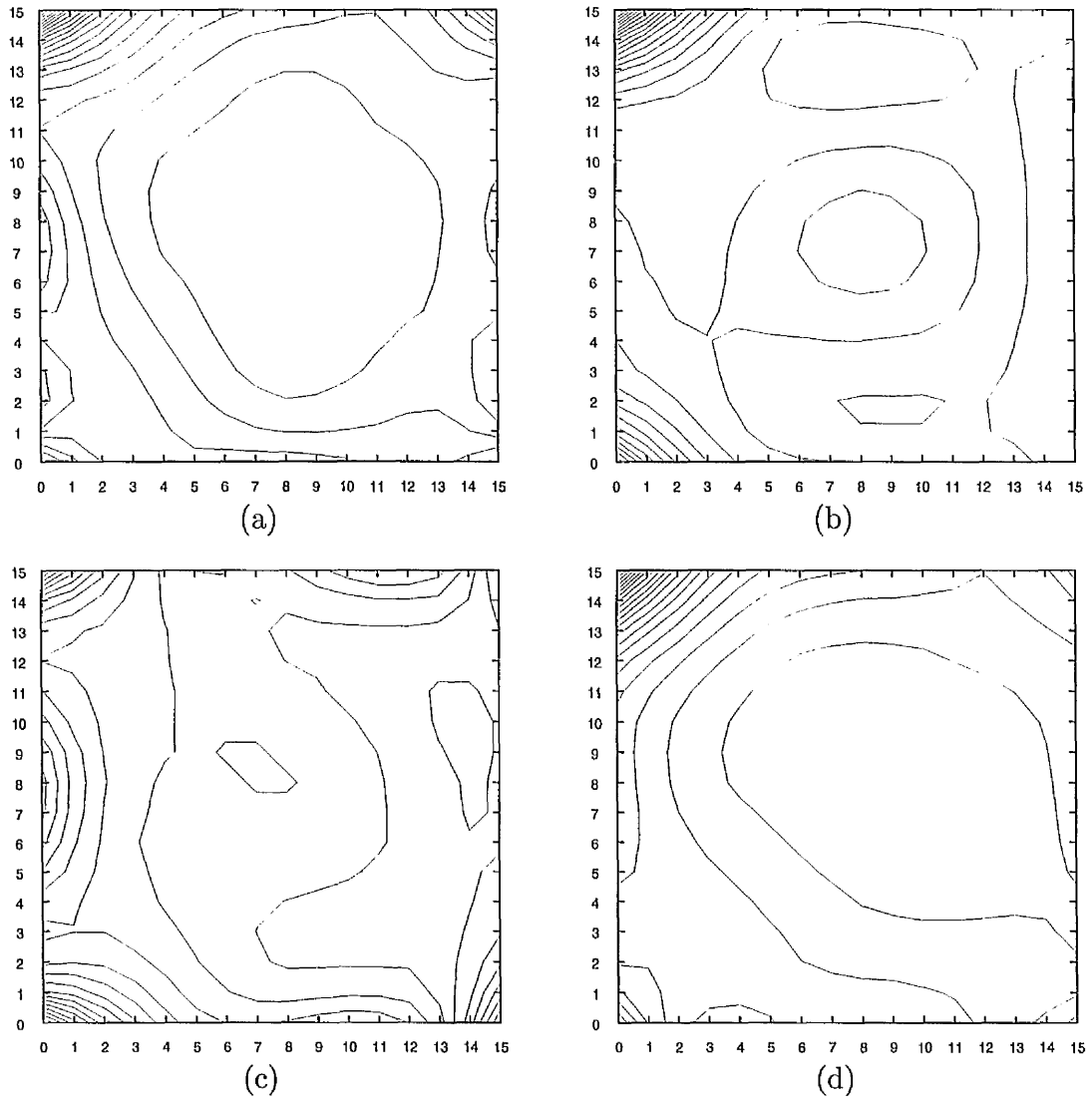

Figure 5.9: Intensity response surfaces for ESRF Beamline 3 CCD detector with tetragonal lysozyme for exposures at spindle axis settings of (a) 8°, (b) 16°, (c) 24° and (d) 32°. Contouring is from 100% response at the centre in 5% steps from that.

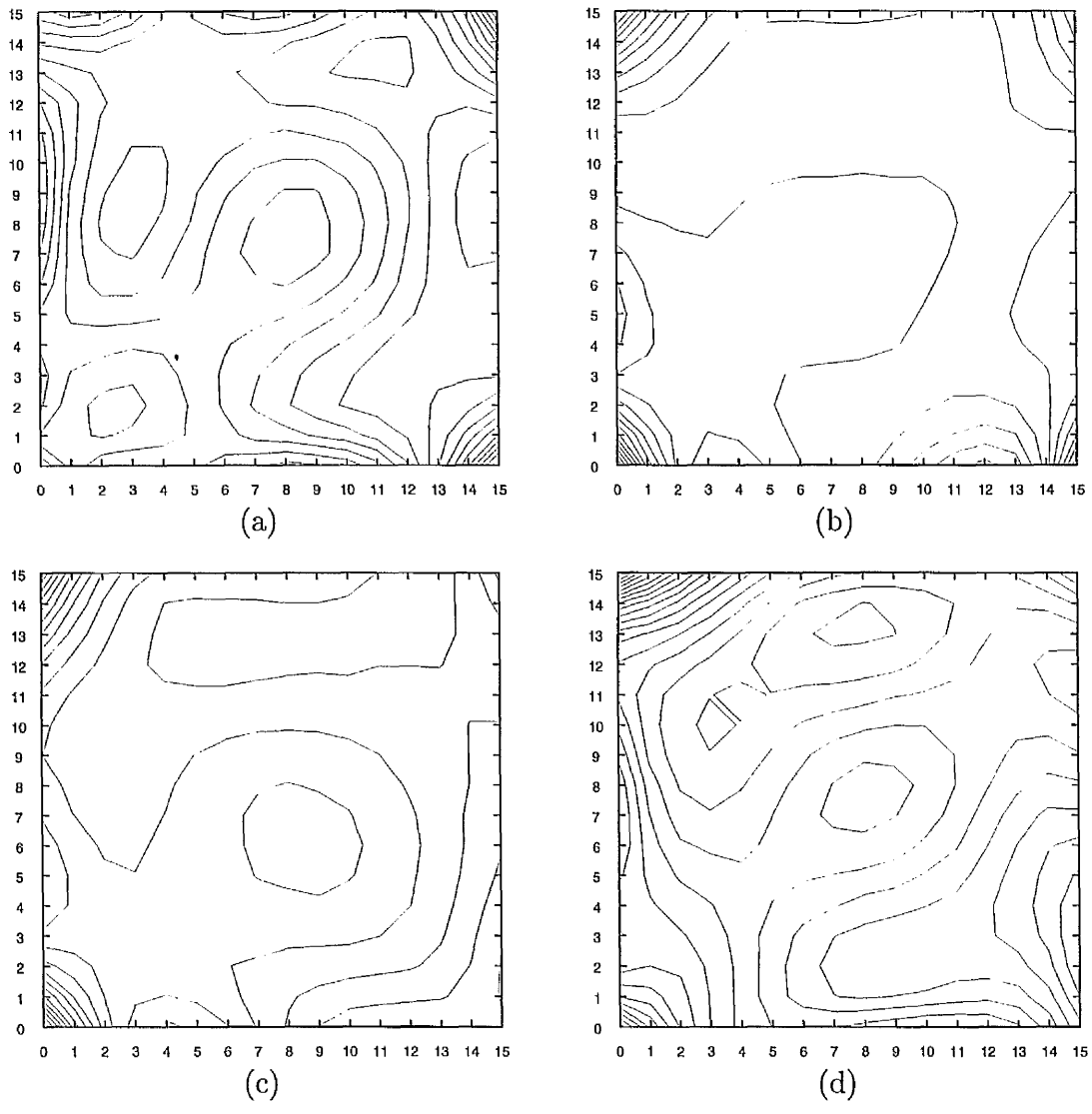

Figure 5.10: Intensity response surfaces for ESRF Beamline 3 CCD detector with tetragonal lysozyme for exposures at spindle axis settings of (a) 40°, (b) 48°, (c) 56° and (d) 64°. Contouring is from 100% response at the centre in 5% steps from that.

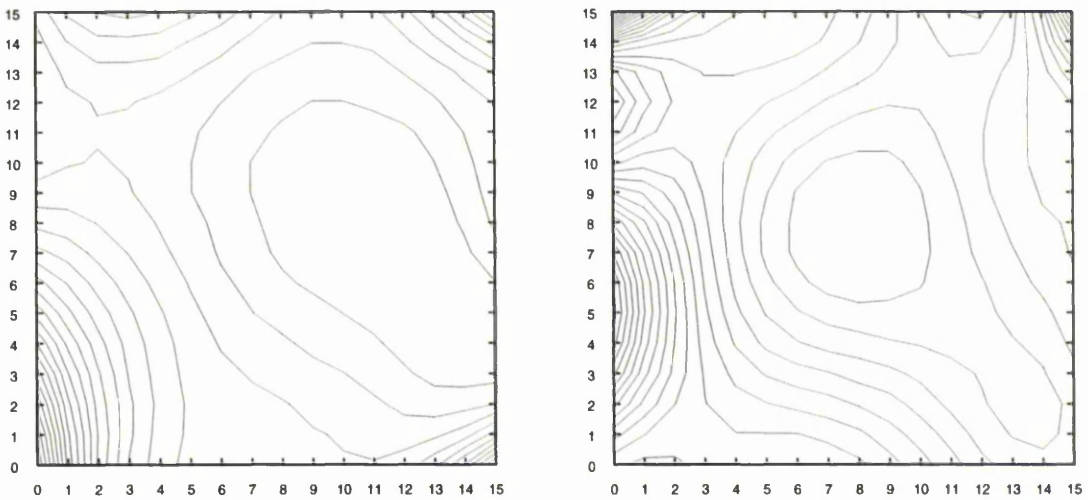

Figure 5.11: Intensity response surfaces for ESRF Beamline 3 CCD detector with tetragonal lysozyme for exposures at spindle axis settings of (a) 72° and (b) 80°. Contouring is from 100% response at the centre in 5% steps from that.

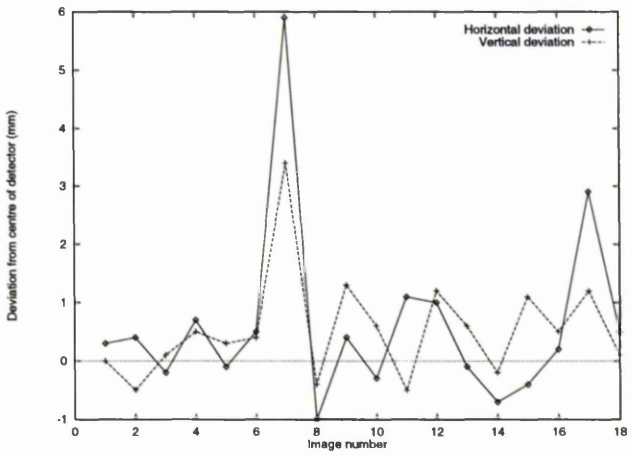

Figure 5.12: Deviation of peak intensity response across CCD detector in horizontal and vertical planes from the centre

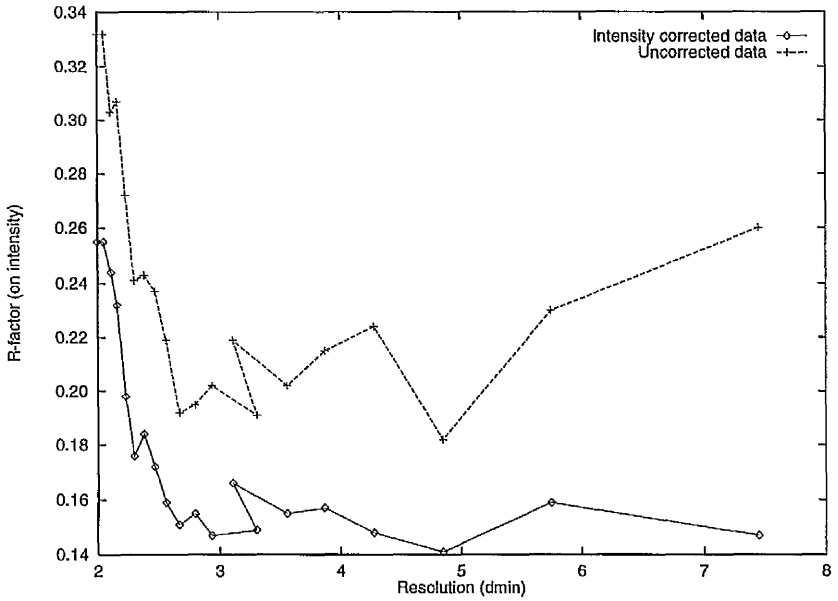

(a)

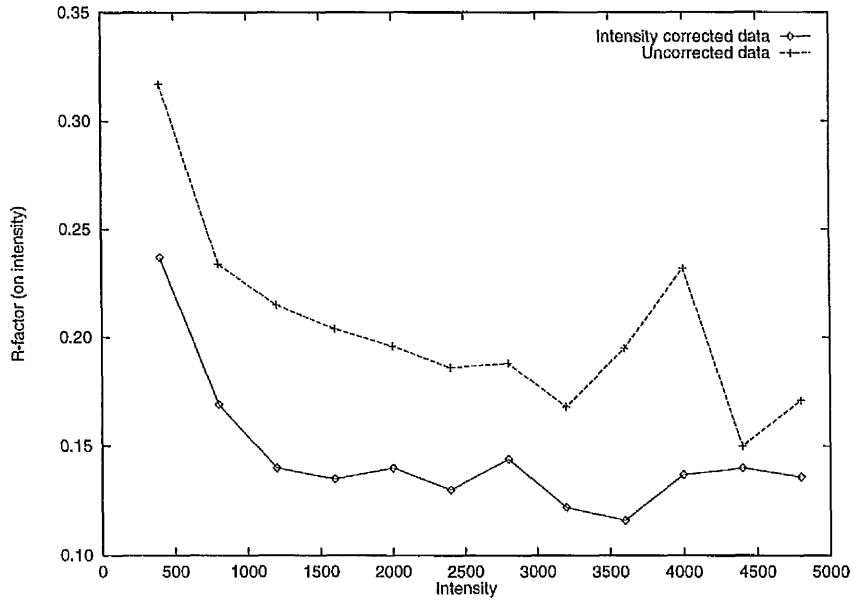

(b)

Figure 5.13: R_{factor} (on Intensity) plotted against (a) d_{min} and (b) intensity for both intensity corrected (via. LAUESCALE and monochromatic data) and uncorrected data

to depend on wavelength since the path through the scintillator changes with wavelength and different sensitivity/detector absorption problems may be apparent. Nevertheless, the present correction surfaces determined and applied have improved the overall data quality and give an indication of the detector performance. Further improvements are required however if the CCD data are to be of a quality to be considered for structure refinement.

For this data collection the detector was used without any electrostatic shielding. Recent improvements to the beamline have included improved shielding around the detector and a cone of shielding toward the crystal. The variations in uniformity response that we have observed (ie. figures 5.7 to 5.11) could well be due to variations in the magnetic field. However, figure 5.6(b) and figure 5.7(a), do not agree either for the same CCD image which suggests some systematic error is occurring in the calculation procedure. The principal weakness appears to be our assumption that each pixel non-uniformity correction is independent of wavelength. It is possible that there may be some variation in the spatial distortion and indeed there is quite a variation in the twist, tilt and bulge parameters of the refinement. An additional limitation for the response surface derived from film, figure 5.6(b) is that no account of the wavelength response of the film[61] was taken.

Very recently,[171] a proceedure for the ESRF CCD uniformity of response estimate has been developed involving a sequence of different monochromatic flood fields onto the detector. These need to be applied and the final results compared with figure 5.13.

Chapter 6

Future Development of the Synchrotron Laue Method

6.1 Discussion and Conclusions

Chapter 3 showed that the Laue method has proved effective for small molecule structural solution and refinement even with a small crystal. In chapter 4 the image plate has proved to be effective in collecting a large number of images in a short time and has been used to advantage in collecting small angular step data for a protein crystal in order to investigate the 'filling of the low resolution hole'. The speed and ease of data collection has been proved and essentially the 'low resolution hole' can indeed be filled. A fine angular step is more effective than multiple deconvolution for the medium bandpass used here (0.40 Å to 1.55 Å). The Large-angle Oscillation Technique (LOT)[249] for low resolution data collection appears to be an alternative option to fine angle Laue data sampling. By use of a station that can switch from monochromatic to Laue mode a complete data set could be collected in one run with the additional benefit that the crystal orientation matrix can be determined monochromatically prior to Laue exposures,

making prediction of the Laue patterns quite straightforward.[19] However, for the fastest exposures (< 1 msec) it is important to consider the limit to rotating crystal/monochromatic methods (nb. an ultracentrifuge rotor arm can reach 60000 rpm ie. 1 revolution per msec; Laue exposures, in contrast, can be as short as 50 psec !).

In chapter 5 calibration of a detector has proved challenging. The procedures used have improved data quality but not to the standard required. Electrostatic screening of the detector on the beamline, which was not employed at the time of our run, but has been introduced subsequently, will reduce any CCD calibration instabilities *with time*. So, although the use of the Laue method with a test crystal has proved to be a rapid diagnostic, it may need to be supplemented by monochromatic information on the pixel to pixel variations of response over a set of selected wavelengths.

6.2 Future Work: Overview

At present no protein structure has been solved *de novo* with Laue data alone (though various areas of progress are being made eg. in the evaluation of cell parameters from Laue photographs[52, 53] and computational power). This has to be an area for future work.

The Laue technique comes into its own when applied to time-resolved studies. Rapid data collection should allow fast time dependent changes to be monitored for suitable biochemical systems. Recent work has been carried out with site-directed mutagenesis to mutate the key rate determining catalytic residues of

isocitrate dehydrogenase and its substrate intermediates.[33] Laue date was then recorded and steps on the overall pathway then visualised via these time-resolved techniques. Time-resolved techniques show great promise. Perhaps most interesting and revealing of all will be to use the Laue technique to "time-resolve" the ordering of parts of a protein structure at key periods of a reaction. Such portions being invisible to static (standard) crystallography techniques (eg. see Scheidig (1995)[207]).

Part II

Microgravity Crystallization and Application

Chapter 7

Microgravity in Crystallization

7.1 Introduction

Unlike most conventional crystals, protein crystals are, in general not initiated from seeds but are nucleated *ab initio* at very high levels of supersaturation. It is the high degree of supersaturation required for nucleation that in large part distinguishes their formation and growth from that of smaller molecule crystals. A consequence of this excessive supersaturation is that once a stable nucleus has formed it has to grow under very unfavourable conditions of supersaturation.[45, 96, 202] Growing crystals accumulate molecules rapidly resulting in statistical disorder and a high frequency of defects.[175] Because dislocations tend to promote even more rapid growth a cascade results.[175]

The unfavourable conditions result with earth-grown crystals because the rate of change of density (of protein and precipitant) with temperature is negative, and, with concentration is usually positive under earth's gravity. Hence crystal growth is always accompanied by a rising buoyant convection current which is

often oscillating and/or unstable. These convective gradients[17] are clearly visible, using Schilieren optics, as plumes emanating from the upper face of the crystal.[60] This oscillating "turbulent" convection drastically modifies the convection gradient along the growth interface[60] between crystal and solution producing notched surface structures and liquid inclusions.[179] The supersaturation at the surface will vary significantly over a growing face depending on the flow velocity of the plume causing a depleted supersaturation region to appear at the root of the convection plume. The size of individual protein aggregates suggests that their alignment at the interface of the growing crystal with the solution may be disturbed even by low level convection irregularities with consequent damage to crystal perfection.[214] Terminal size (ie. the final size reached by a crystal) may be related to the extreme sensitivity of buoyant convection to changes in crystal size.[60] Solutal convection around the surface of the crystal may hinder attachment of growth units. This speculation is reasonable with the low bond strengths involved in protein crystallization and the large dimension of the growth units, in particular, thought to consist also of multimolecular clusters.[189] The influence of convection on growth has been reviewed by Wilcox.[250]

Another problem in gravity is that growing crystals will sediment which can interfere with single crystal formation[248, 130] (page 173). An additional problem with gravity is secondary nucleation, which either involves crystalline particles torn out of a parent crystal by solid impact, or fluid attrition (through turbulence), or locally induced supersaturation in the liquid layer next to a seed crystal.[198] Eliminating convection and turbulence by use of microgravity would reduce these secondary nucleation effects.

The relative weakness of protein-protein interactions[102] suggest that temperature and gravity may set lower and upper limits on observable crystal size respectively.[177] For very small aggregates of individual protein molecules thermal noise provides a lower cutoff below which Brownian motion can disrupt ordering. Conversely for larger aggregates gravity begins to distort regular ordering and provides an upper cut-off above which acculumulation of misalignments would build in gravity induced strain.[177] The result of these two cut-offs is a window of sizes in which stable crystals could survive intact in thermal and gravitational fields. By use of microgravity (and stable temperature environments) the crystal size may be maximised by reduction of the gravity induced strain and thermal motions.

7.2 Eliminating Convection

To investigate microgravity as a growth medium to alleviate convection, turbulance and sedimentation experiments, were undertaken using sounding rockets (European TEXUS program).[156] The protein β-galactosidase was used as a test protein with the diffusion process being studied by Schlieren optics. Ground controls showed turbulent convection in the diffusion process. The microgravity-grown samples (with 6 minutes of microgravity) showed a strictly laminar diffusion process with turbulent convection only being observed on re-entry of the payload to the gravitational sphere of the earth. Surprisingly, after such a short time for crystal growth, several single crystals were obtained from the microgravity experiment. As a macromolecular crystal begins to form in microgravity a depletion zone is thought to be established around the nucleus and expand as

the crystal grows.[160] This zone is a volume of space around the growing crystal which contains less protein than the overall protein solution due to the protein being incorporated into the crystal. Because protein diffusion is slow the depletion zone is quasi stable, and hence protein forming the crystal (and depleting the zone) is slowly replaced with more protein from the surrounding solution. The overall effect is then that the surfaces of the growing crystal interface with a local solution phase containing a significantly lower concentration of protein nutrient than exists in the bulk solvent ie. there is a reduction in the degree of supersaturation of the local solution and creates for itself an environment equivalent to a region where optimal growth might be expected to occur (nucleation point and low supersaturation).

Methods of eliminating convection, other than microgravity, have been studied[175] including low gravity simulation systems ($d\rho/dc \rightarrow 0$, ie. rate of change of density, ρ, with concentration, c, tending to zero), microscopic growth systems (reducing convection by scaling down the system), configurational stabilisation (configuring the experiment so that density gradients inhibit rather than promote convection) and growth of crystals in gels. Low gravity simulation systems have been found (eg. tetramethyl ammonium chloride/heavy water and thymol diethyl carbonate) but are rare and too unusual in general to be extrapolated to systems in protein crystallography. Microscopic crystal growth does reduce convection for crystals of small dimension (ie. less than 1 μm) but cannot produce usable crystals for X-ray diffraction (due to their small size). Configurational stabilisation techniques are more promising for microgravity simulation but are complex and studies have only been performed on small molecules.[175] Crystal growth in gels has been successful and offers some of the advantages of microgravity.[198]

A gel forms a microscopic mesh through which the solutions permeate. As a crystal grows it either incorporates some of the gel in the crystal or pushes the gel aside thereby causing rupture and or dislocation of the gel framework. It has been noted[155, 156] that fragile crystals, especially those growing as needles, break and are destroyed when they touch the network of the gel. Depletion of the solute is uniform around the crystal-gel interface and convection is reduced as the liquid is trapped in the gel texture. Crystals do not sediment on the bottom of the growth cell but rise being sustained by the gel matrix. Gels reduce the nucleation density resulting in fewer, larger crystals. However, only limited improvements in the X-ray diffraction data quality have been seen[162] and in any case with the $I/\sigma(I)$ ratios of microgravity-grown crystals being better than the gel-grown ones. However, the gel-grown ones showed an improvement over crystals grown via regular techniques of ground crystallization.

7.3 X-ray Characterisation of Crystals

Basics and Definitions

In a diffracting crystal there are three types of disorder.

- Firstly, all (or virtually all) of the molecules in the crystal are very close to the mean orientation and lattice point position having a scatter about the lattice point roughly that of the average statistical disorder of all the molecules in the crystal. In essence, all of the molecules are reasonably ordered and the resolution limit of the X-ray diffraction data gives a measure

of that average residual statistical disorder.

- Secondly, there are specific defects and dislocations (as observed by Durbin and Feher[85] using electron microscopy). These defects will contribute virtually no constructive component to the crystal diffraction intensities but only to the X-ray background scatter. Defects and dislocations therefore will reduce the number of usefully scattering unit cells to which the intensity is proportional while at the same time increasing diffuse scatter or background. The estimated error in intensity, $I/\sigma(I)$ includes a measure of this scatter.

- Thirdly, the crystal may have a mosaic structure where there are several (or many) three dimensional regions of a crystal slightly misaligned to each other. In the limit of very many small 'mosaic' blocks a crystal will have a 'crumbly' nature.

The maximum extent of the diffraction pattern or resolution limit for any protein crystal is a function of the inherent statistical disorder of the molecules rather than thermal effects which predominate in most crystals.[160] The maximum resolution is the inverse value of the largest value of the scattering vector modulus, S ($S = 2\sin\frac{\theta}{\lambda}$), for which measurable Bragg intensities can be extracted from a diffraction pattern recorded in given experimental conditions. In practice, definitions of resolution are based either on the ratio $I/\sigma(I)$ in resolution shells or on values of R_{sym} (the relative disagreement between intensities of symmetry equivalent reflections) as a function of S as well as on completeness of observed data. For example $I/\sigma(I)$ should be > 3, R_{sym} should be $< 20\%$ and completeness $> 50\%$ in the highest resolution shell.

Another way of assessing the crystalline order is the Wilson plot which can be used to evaluate the overall B value for a crystal. The B value is a parameter that reflects the internal order within a crystal whereby $B = 8\pi^2 u^2$ and u is the mean square amplitude of atomic displacement. Relative Wilson plots, also known as difference Wilson plots, are useful for comparatively assessing the internal order of similar protein crystals grown under different growth conditions. The slopes of these plots of $\ln(\sum \frac{Fa^2}{Fb^2})$, where F is the crystallographic structure factor amplitude of crystals respectively of type a and b, versus $4\frac{\sin^2\theta}{\lambda^2}$ (resolution) are directly related to the difference in overall B values within the two crystals.

The method utilised in this thesis for the evaluation of crystal perfection is measurement of the mosaic spread. This requires a very high resolution diffractometer and synchrotron source. Mosaic spread measurement is independent of processing software and gives a direct indication of the protein crystal *geometric* perfection. The mosaic spread, η, is a parameter associated with the mosaic crystal model[68] which is commonly used to define ideally imperfect crystals. Protein crystals are thought to belong to such a categorisation. A mosaic sample, as described in section 2.8, is an assembly of a number of perfect domains slightly misoriented with respect to each other and η is the extent of the angular misalignment of each domain with respect to every other domain. The overall mosaicity is a convolution of η with the intrinsic rocking width, ω_h, of each domain. The intrinsic or diffraction grating angular spread of a reflection can be derived from the dynamical theory of X-ray diffraction, in SI units;

$$\omega_h = \frac{1}{\pi^2 \varepsilon_o} d_h^2 \frac{e^2}{mc^2} \frac{\tan\theta_B}{V_o} |F_h| \tag{7.1}$$

where d_h^2 is the interplanar spacing for the Bragg plane $h(=h,k,l)$, θ_B the Bragg angle, V_o the volume of crystal unit cell and $|F_h|$ the structure factor amplitude. The mosaic spread, η, is usually thought to be greater than the intrinsic rocking width ω. This, as we shall show, is actually a misconception. Experimental rocking widths for good macromolecular crystals are dominated by instrument smearing effects which consequently must be made as small as possible by choice of perfect monochromator crystals and tight slitting down to reduce beam divergence if the true values of η and ω are to be measured.

Assuming a perfect single domain crystal with typical unit cell dimensions, ω values calculated on the basis of dynamical theory are small,[124] less than 0.0003°. From equation 7.1 widths much larger than average are expected from strong and asymmetric ($|\gamma_h| > 1$) reflections at low resolution. Widths are also dependent on the inverse unit cell volume.

The experimental rocking width, $\phi_{R(\underline{h})}$ of a particular reflection is a convolution of the overall sample reflecting range with the X-ray beam geometric and spectral parameters.[108, 124]

$$\begin{aligned}\phi_{R(\underline{h})} &= \left\{ L^2 \left(\left[\frac{\delta\lambda}{\lambda} \right]_{corr} d^{*2} + \zeta_{\gamma H} \right)^2 + \gamma_v^2 \right\}^{\frac{1}{2}} \\ &+ 2 \left(\frac{d^* \cos\theta_B}{2} \left\{ \eta + \left[\frac{\delta\lambda}{\lambda} \right]_{conv} \tan\theta_B \right\} \right) L \end{aligned} \tag{7.2}$$

where L is the Lorentz factor, γ_H and γ_v are the beam cross fire angle in the horizontal and vertical, d^* is the reciprocal of d_h, $\zeta_{\gamma H}$ is the cylindrical coordinate in reciprocal space parallel to the rotation axis of the reflection, $\underline{h}$, in question, $[\frac{\delta\lambda}{\lambda}]_{corr}$ is the spectral dispersion correlated with direction and $[\frac{\delta\lambda}{\lambda}]_{conv}$ the spread

along each direction. Accurate estimates of the synchrotron radiation beam parameters can be made and deconvoluted from $\phi_{R(\underline{h})}$ to give η, provided these other factors are not dominating the value of $\phi_{R(\underline{h})}$. A particular problem is the nature of the mathematical model for combination of different factors to give the overall rocking width. If each contribution is a Gaussian intensity distribution they add "in quadrature" rather than by simple addition. In the former model then a single large term (eg. beam divergence) can quickly mask all other terms. For example, if $\gamma_H = 0.06\ ^\circ$ (1 mrad) and $\omega = 0.0005\ ^\circ$ were added as $\sqrt{\gamma_H^2 + \omega^2}$ then γ_H needs to be $\leq \omega$ for ω to be probed.

Methods Used to Probe η and, Finally, to Reach ω_h

Two methods can provide estimates for rocking widths, either a monochromatic beam and rotating sample or the Laue method. In the Laue method (polychromatic beam, stationary sample) rocking widths of individual reflections are derived from the radial extension of diffraction spots on the detector after making corrections including beam divergence, crystal to detector distance and detector point spread function. The Laue method allows a fast survey of a large number of reflections and is most suitable for comparing various samples. The monochromatic method is used for more detailed analysis giving accurate reflection profiles of a limited number of reflections in a longer time period at selected regions of reciprocal space (eg. high resolution). Moreover, identical reflections can be compared for different individual crystals (eg. microgravity-grown and earth-grown crystals).

For the Laue method the mosaicity of the sample is derived from the size and

shape of the Laue diffraction spots. Their radial extension[9] is given by equation 7.3 in the limit of an incident X-ray beam of zero size and zero divergence;

$$\Delta_{radial} = 2\eta \frac{D}{\cos^2 2\theta} \tag{7.3}$$

where D is the crystal to detector distance and θ the Bragg angle. For η to be measurable by the Laue method as low a divergence as practically possible (eg. $\approx$ 10 μrad) is established by slitting down the beam and using a small collimator (eg. 0.2 mm) to keep the beam cross section small. In addition as long a crystal to detector distance as possible is used (2.4 m on station 9.5 of the SRS) and a detector such as X-ray sensitive film with a fine pixel size is employed. The size of the direct, non diffracted beam, measured at the film position, allows for proper account of the practical size and divergence of the beam to be made. This is then subtracted from the measured diffraction spot size to finally yield Δ_{radial} from which η is extracted assumed to be at full width (ie. 6σ) then converted to a full width at half maximum (FWHM) (ie. 2.3σ).

The monochromatic method, in contrast, makes use of a diffractometer with a small angular step size, controlling the crystal orientation, combined with a monochromatic synchrotron beam of very low divergence and small $\delta\lambda/\lambda$. Reflection rocking curves are measured and the FWHM determined. The crystal sample mosaicity, η, can be determined by deconvoluting the instrument resolution function, IRF', out of the overall measured reflection width, ϕ_R using[64];

$$\eta = \sqrt{\phi_R^2 - IRF'^2} \tag{7.4}$$

The IRF' is based upon

$$IRF^2 = (2.3\sigma_y/P)^2 + (\Delta\lambda/\lambda)^2 \tan^2\theta \tag{7.5}$$

where σ_y is the vertical beam size, P the source to sample distance, $\Delta\lambda/\lambda$ the relative wavelength range and θ the Bragg angle of the monochromator. The dimension of the sample, C_v and vertical beam divergence, w_d, are taken into account then with;

$$IRF'^2 = IRF^2 + minimum\left[w_d^2, \left(\frac{C_v}{P}\right)^2\right] \tag{7.6}$$

(usually $\frac{C_v}{P}$ is indeed $< w_d$).

The formulae, 7.4 to 7.6, assume that a horizontal rotation axis for the crystal is used with the scintillation counter moving in the vertical plane (ie. the so-called normal beam equatorial method with the diffractometer mounted on its side as at the synchrotron for a horizontally polarised X-ray beam).

Both methods described complement each other. The Laue method because of its high speed allows a large number of samples to be examined. The diffractometer method allows a few crystals to be studied in high detail and the resolution limit to be readily explored.

7.4 Previous Microgravity-Grown Crystal Analysis

The first protein crystallization experiments ~~were~~ carried out in microgravity were conducted aboard the Spacelab-1 in 1983 and involved the liquid-liquid method.[155, 156] This produced apparently astonishing claims of lysozyme crystals with 1000 times larger volume than crystals grown on earth. Unfortunately the microgravity crystals grown were no larger than the lysozyme crystals grown by standard laboratory techniques on earth. The device used on earth had simply produced very small crystals. Hence, in future, in order to get an unbiased view, crystals grown in microgravity, crystals grown on earth in the microgravity hardware, and the best earth grown crystals from typical laboratory devices must be compared. However, the results had shown that microgravity environment with identical materials and approach had produced differing results. Hence microgravity was indeed a real parameter, or variable, for crystal growth as had been suspected from considerations of convection described in section 7.1.

The first protein crystallization experiments in an unmanned space capsule were carried then out on the Photon satellite mission (April, 1988).[236] The advantages of such a capsule being much lower levels of microgravity than a manned facility (ie. no astronaut disturbances) Catalase crystals were produced that were larger than the earth controls and forming separate crystals rather than clusters or rosettes as on earth. Also, ribosomal subunits crystallized in microgravity, but not on earth, adding weight to the observation that microgravity facilitated nucleation.[156]

The COSIMA-1[89, 134] mission (August, 1988), also unmanned, was flown using a Chinese Long March rocket with re-entry capsule from the Juquan Space Centre (Inner Mongolia). During re-entry the decel eration level increased to 13 g and ended with opening of a parachute causing a 60 g shock for 5-10 milliseconds. There were also reported to be problems in recovering the crystals in the Gobi desert with appropiate thermally insulated storage hardware. In no case was there an improvement of crystallization over ground based techniques. A second mission, COSIMA-2[134, 14] using Russian launch facilities, involved crystallisation of bovine pancreatic ribonuclease S. The microgravity crystals yielded a considerably larger fraction of significant diffraction spots than similar ground crystals and slightly lower overall B factors were seen. However growth of thermolysin and a 23 kD lysozyme from Streptomyces coelicolar produced crystals with signal to noise statistics somewhat poorer than earth-grown samples. This would imply that the particular method chosen for microgravity growth might be limiting in itself, somewhat like the first Spacelab-1 mission.[155, 156]

Further experiments on protein crystal growth under microgravity were performed on NASA parabolic flights and four Shuttle missions (STS-51D, 51F, 61B and 61C) between April 1985 and January 1986 for development of vapour diffusion crystallization equipment.[76] Designs emphasised simplicity, no external power, minimal space, self contained, ease of use and observable via photography. These experiments produced no quantitative results but did show improvements in crystal morphology with the absence of gravitational sedimentation in microgravity. The resulting equipment that was subsequently developed was flown on STS-26 (September, 1988) with 11 protein systems[74] using a vapour diffusion crystallization technique. Crystals resulted for γ interferon D, porcine

elastase, isocitrate lysase and concanavalin. The first three proteins displayed more uniform morphologies and yielded diffraction data to significantly higher resolution than the best earth grown crystals. Relative Wilson plots indicated that the microgravity grown crystals were more highly ordered at the molecular level than crystals grown by the same method on earth. (Concanavalin displayed higher resolution diffraction but analysis was incomplete due to X-ray data collection difficulties).

The Russian space station, Mir, was used for long duration crystal growth experiments[229] of chicken egg white lysozyme and D-amino transferase from December 1989 to February 1990. The resulting crystals of D-amino transferase were larger than the earth grown controls and diffracted to slightly higher resolution. Lysozyme crystals grown using vapour diffusion differed little from those grown on earth under identical conditions and were slightly inferior to crystals grown on earth by other standard techniques in terms of average number of crystals and crystal size. Of interest to this study was the formation of crystals in different morphologies to those found on earth under similar conditions.

Short experiments were also carried out using sounding rockets with ribonuclease A and pancreatic trypsin.[217] Preliminary experiments indicated that crystals could be grown from supersaturated solutions *utilising seed injection* in a very short time, the microgravity time available (at 10^{-4} g) being seven minutes. In general more and larger crystals were grown in microgravity over ground controls. Ribonuclease A crystals had poorly defined habits but diffracted to higher resolution (1.06 Å) than previous laboratory grown samples (1.26 Å). The crystallization process could not be stopped at reentry and total crystallization time was around 90 minutes.

Further experiments on Shuttle flights, STS-29, 32 and 31 yielded protein crystals of more uniform morphologies and diffraction data of better quality than for *some* of their earth grown counterparts.[71, 75] For each of these Shuttle missions approximately 20% of the proteins flown were found to grow crystals which exhibited better morphologies or yielded better diffraction quality data than their earth-grown counterparts. However, approximately 40% did not yield any crystals and the remaining 40% yielded crystals too small for X-ray analysis or produced data of poorer quality than the best earth- grown.

The USML-1 (United States Microgravity Laboratory) mission, June 1992, was launched specifically to conduct a variety of materials processing and fluid dynamics experiments in microgravity. Hardware developed for this mission provided several additional capabilities than previously available. These included the ability of human intervention to set up and run experiments with a real time down link to the ground based investigators. This allowed observation and suggestions to be made to improve experiments as they took place. Thirty three proteins were used for crystallization[73] resulting in larger crystals with more uniform morphologies yielding diffraction data to significantly higher resolution then the best earth grown.[72]

Chicken egg white lysozyme and an acidic phospholipase A_2 were crystallized under 13 days of microgravity on a Chinese unmanned mission, August 1992.[25] The microgravity samples produced larger crystals with many microgravity-grown lysozyme crystals displaying dimensions ranging from 1.1 to 1.4 mm whilst few earth-grown controls exceeded 1.1 mm. The microgravity-grown crystals of acidic phospholipase A_2 were typically 5 to 7 times larger than their earth-grown counterparts. In both microgravity samples fewer crystals were produced than on

earth. The earth-grown phospholipase crystals are usually long hexagonal prism type crystals, the microgravity-grown crystals produced were shorter and bulkier. The microgravity-grown crystals diffracted to higher resolution than the ground controls, the lysozyme producing more significant diffraction data especially at the higher resolution ranges (up to 1.6 Å).

Of course the microgravity crystallization results represent a small data population relative to the the best crystals produced by any method on earth often over many years or decades. Optimisation of conditions for microgravity crystallization takes time and opportunities are still limited. Our flight opportunities have been with the European Space Agencies (ESA) Advanced Protein Crystallization Facility[34, 222] (APCF). At the time of writing this has been flown three times on the Spacehab-1 mission, the International Microgravity Laboratory-2 (IML-2) mission and the United States Microgravity Laboratory-2 (USML-2) mission. The APCF is a new facility and few results have yet been published, the work in this part of the thesis describes our results with it.

Chapter 8

Crystallization of Lysozyme in Microgravity

8.1 Introduction

Chicken egg white lysozyme is the standard test material used to investigate protein crystal growth and nucleation.[15, 84, 136, 188] Lysozyme is well suited to an investigation of microgravity crystallization because it is cheap, readily crystallizable and there is an extensive literature of studies and results.

Calculations based on the (110) lysozyme crystal face growth rate[187] predict that convective flow exists at crystal sizes as small as 10 to 100 μm under earth gravity. Beginning within this size range the transport of solute ceases to be purely diffusive becoming increasingly dominated by convective flows which transport new solute to the growth interface. A higher growth rate results in a larger growing surface which depletes the boundary layer fluid more rapidly resulting in even steeper density gradients and thus stronger flows.[188] These solutial density gradient driven effects are the primary factors in cessation of crystal growth. Hence,

these studies make lysozyme an ideal case to study what happens when this flow is not present ie. as generally is the case in a microgravity environment.

8.2 Apparatus for Crystallization in Microgravity

The Advanced Protein Crystallization Facility[34, 222] (APCF) has been constructed by Dornier GmbH under contract to a European Space Agency specification. Three types of crystallization method are available in the APCF, namely, dialysis, liquid-liquid diffusion (free interface) and vapour diffusion (hanging drop).

Liquid-liquid diffusion requires the placing of a physical barrier between the protein and precipitating solution during ascent of the Shuttle. Once the barrier is removed and growth starts crystals can appear throughout the reactor. The incidence of crystals throughout the whole reactor causes problems with diagnostic monitoring of the crystallization as a large volume has to be monitored by any diagnostic technique. Vapour diffusion methods need to protect the crystal containing droplets from being jostled in the vapour chamber when being exposed to reentry and earth gravity. This is accomplished by pulling the droplet back into a syringe. This physical manipulation of a droplet containing fragile protein crystals increases the risk of damage to the crystal before it reaches earth. Vapour diffusion (hanging/sitting drop) may also suffer Marangoni convection.[174] Marangoni convection results from surface tension gradients (due to the surface area of the drop) induced by temperature gradient or concentration gradients that generate surface flows which may spread to the whole volume. Marangoni effects are independent of gravity and are the main source of convection in microgravity

experiments[174] where there is a liquid vapour interface.

Dialysis crystallization offers several advantages over other methods[216] of crystallization. The bubble free liquid acts as a protection for the fragile crystals (the crystals need not be manipulated until X-ray diffraction experiments are about to be carried out). Visual monitoring is easy to implement with crystals growing only on the protein solution side of the dialysis membrane. Ions and soluble small molecules as well as water can easily be exchanged. Ground control experiments are easy to carry out as control of the crystallizing conditions is dependent only on the dialysis membrane. To preclude the effects of Marongoni convection, and for the above reasons, we have made use of the dialysis reactor for our experiments rather than the liquid-liquid or vapour diffusion reactors available.

The dialysis reactor, shown schematically in figure 8.1 and pictured in figure 8.2, consists of two quartz glass blocks with one cuboid volume for the protein solution and one cuboid volume for the salt solution and a small volume for buffer solution. The buffer and salt solution volumes are separated by a rotatable plug with a 'T' shaped channel containing salt solution. This channel ensures that the salt solution in the plug and that in the salt volume are kept in contact. The protein and salt solution volumes are sealed with silicon O rings and vacuum grease. In each volume there is a small air gap between the solutions and the chamber covers created by a special silicon seal and dialysis membrane to provide compensation for small volume changes that might arrise due to slight temperature deviations. The protein chamber has plane surfaces permitting distortion free optical observation. Metal inserts allow fixation of the cover plates and rotation of the plug.

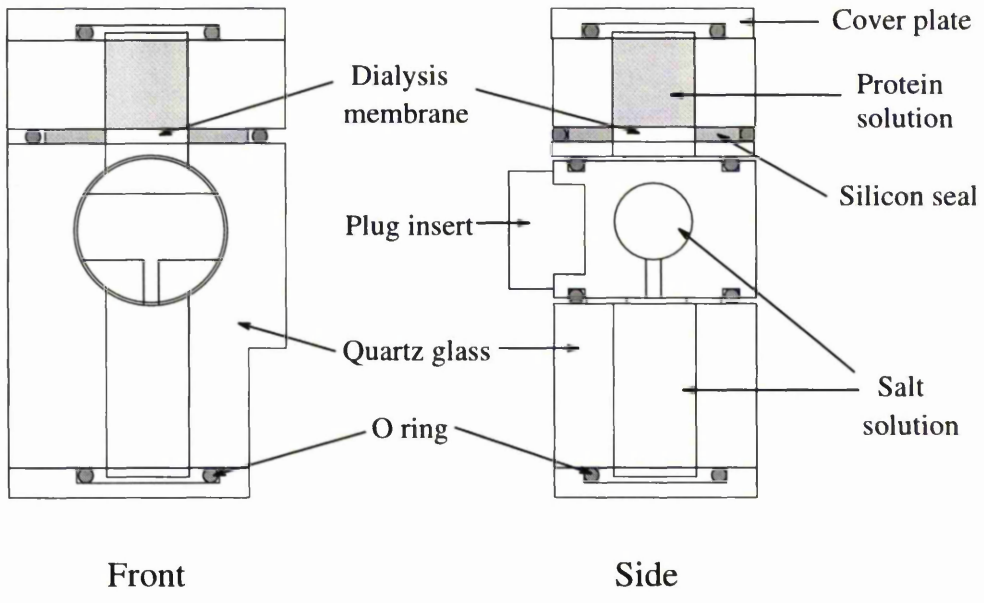

Figure 8.1: Schematic diagram of ESA's APCF dialysis reactor

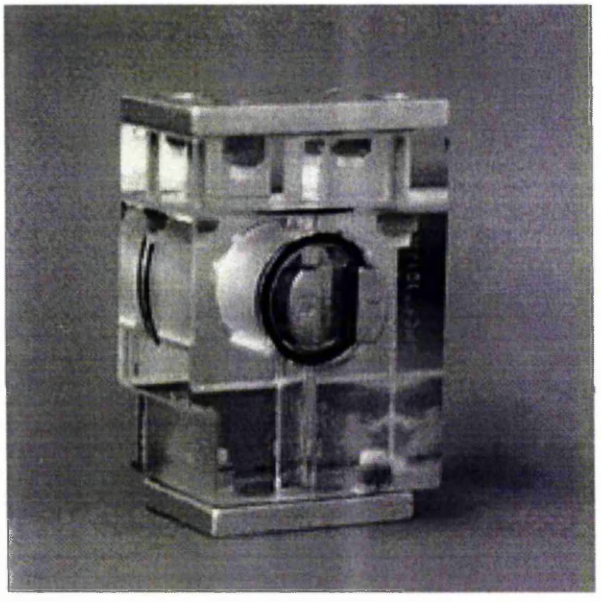

Figure 8.2: Photograph of the dialysis reactor

A dialysis reactor system has many components thus increasing the possibility of bacterial contamination. The system also has to be leak-proof and bubble free. All the liquids filling the reactor must be degassed. With these concerns in mind the reactor design readily allows for cleaning, sterilization, and leak tightness. A further design feature is easy optical observation.

During the preprocess phase the salt and protein solution are kept separated. To start and stop the process the plug is rotated by 90° so that all volumes come into contact. This is achieved, in fact, by the simple press of a button on the outside of the APCF. Several sizes of protein, buffer and salt volumes are available. The reactors are filled according to a detailed procedure. Because of the remote possibility of the apparatus being exposed to vacuum all the solutions are degassed by prior boiling under vacuum conditions before being used to fill the reactors.

With the APCF 48 reactors in total are accommodated in an insulated chamber, figure 8.3, kept at constant temperature ($20° \pm 0.1°$) with Peltier elements. The reactors are mounted on four mechanical drives, two groups of six reactors, each drive allowing simultaneous activation and deactivation of reactors. A movable CCD camera (582 lines with 500 pixels per line) is installed such that twelve reactors can be monitored, 6 reactors can be observed with a narrow field of view (4.9 mm × 3.7 mm) and 6 reactors with a wide field of view (8.5 mm × 6.4 mm) system of optics.

Illumination is provided by an 850 nm polarized LED with an analyser that can be rotated during the mission. The video images are digitised and recorded on 'Exabyte' tape together with facility data eg. internal temperatures from several

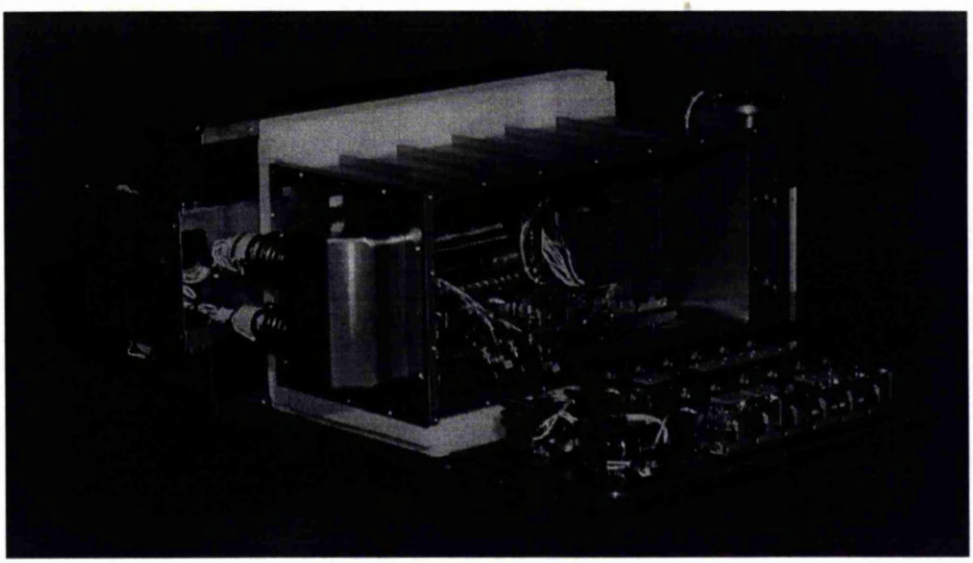

Figure 8.3: Photograph of APCF with the process chamber open. Visible are 18 reactors and internally the camera drive with 6 reactors. In total there are 48 reactors, two sets of 18 and two sets of 6.

probes, power consumption etc.

8.3 Previous Work on Lysozyme Crystal Perfection: The Spacehab-1 Mission

The initial experience of the Manchester group was gained from the Spacehab-1 mission.[246, 248] In this case dialysis reactors were used with 21 mg of lysozyme (3 x crystallized, dialysed and lyophilized powder of chicken egg white lysozyme) dissolved in 250 μl 0.04 M acetate buffer (pH 4.7) to fill the protein volume. The salt volume was filled with 1.35 M NaCl and the buffer volume with 0.04 M acetate buffer (pH 4.7). Solubility under these conditions is given as[136] $\approx$ 2

mg/ml therefore the solution is at a supersaturation level of 42 times or greater. Sodium azide was also added as an anti-fungal agent (1.92×10^{-3} mg per 188 μl). The effects of sodium azide on crystal growth have been investigated[1] showing that the rate of crystal growth seems to be increased. Addition of anti-fungal agents prevents ageing effects in the solution[59] reducing nucleation which would otherwise produce many more smaller crystals (a result we have been trying to avoid). Identical solutions were utilised for the microgravity mission and for the ground-control experiments in all the Manchester work described in this thesis.

Laboratory trials prior to the Spacehab-1 mission had yielded crystals growing on the walls of the protein volume which led to difficulties in harvesting usable crystals. To overcome this problem the protein volume was siliconised: 10 minutes siliconisation treatment for the Spacehab-1 flight reactors and 5 minutes for the ground control reactors - 10 minutes siliconisation on the ground control reactors had led to sedimentation but this would not be a problem for the microgravity reactors. Treatment for 5 minutes was a reasonable compromise as any crystals grown on the wall could be harvested with only a small risk of crystal damage.

The microgravity crystallization time available was 7 days and 10 hours on the Spacehab-1 mission. Due to a launch delay with the STS-57 shuttle carrying the Spacehab-1 mission the reactors stayed in a preprocess state (protein and salt solution separated) for 28 days. During this time precipitate was observed in some of the reactors. As this was more noticeable in the flight reactors than in the ground controls it was decided that the reactors for the mission should be swapped. The mission launched on June 21st, 1993, carrying one APCF unit with another used as the ground control unit. Manchester had 4 out of 48 reactors allocated in each facility. CCD video monitoring was to be available on one of

our reactors but there was a failure of this in the microgravity reactor during the flight so only ground-control images were available.

The resulting crystals for both the mission and the ground-control experiments were of an average size 0.8 mm along the longest dimension. The reactors subjected to microgravity showed 80% of the crystals growing on the walls with the rest on the top and bottom membranes. The reactors used as the ground control suffered from sedimentation and only 10-20 usable crystals could be obtained from the four reactors.

Evaluation of the crystal perfection was done via Laue diffraction spot size measurement with a tightly slitted down beam and a very long crystal to film distance (2.37m) on station 9.5 of the Daresbury SRS. Three microgravity grown and two earth grown crystals were analysed. Microgravity crystals were found to have rocking widths three times smaller than the earth grown controls, ie. 0.0012(3)° at minimum compared to 0.0032(1)° respectively.

Some 5 months later further tests of crystals from Spacehab-1 and the ground controls were done at the Laboratorie Utilisation Rayonnement Electromagnetique (LURE) with monochromatic rocking width measurement techniques. The values obtained there, from 11 microgravity crystals and 9 earth grown crystals, were 0.0091°(±0.0025°) and 0.0130°(±0.0050°) respectively. It is possible that the mounting of crystals in Manchester prior to travel to LURE was not ideal. All subsequent work has involved opening reactors and mounting of the crystals at the synchrotron to remove this factor from consideration. More detail of the Spacehab-1 work can be found in Helliwell *et al.* (1995)[130] and Weisgerber (1993).[246]

8.4 The IML-2 mission

The IML-2 mission was scheduled to have a longer duration than the previous Spacehab-1 mission, ie. 12 days and 11 hours as opposed to 7 days and 10 hours respectively. In order to take advantage of this the salt solution concentration was reduced from 1.35 M of the initial mission to 1.26 M so as to prolong the crystallization time. The lysozyme protein used was commercially available (Sigma 3 $\times$ crystallized, dialyzed and lyophilized), lot number 111H7010, without further purification.

Prior to setting up the crystallization solutions in the reactors, the metal and quartz glass parts of the reactors were cleaned by washing with a detergent solution and cleansing with distilled water. Sterilisation was then achieved by washing using a 20% ethanol solution followed by 6 hours in a sonic bath at 20°C filled with water then 12 hours in a thermostat controlled oven at 60° C. Autoclaving was not used as, during the first mission, it was found to cause cracks in the reactors. Silicon seals, O rings and the dialysis membrane were used from fresh supplies and cleaned using distilled water.

The reactors were filled 8 days before the mission at Giessen in Germany. Solutions were made up in the home laboratory with degassed, deionised water. The lysozyme was added to the buffer just before filling and centrifuged at 1000 rpm for one minute to separate any solid particles. Aseptic techniques were used throughout both for filling and the later opening and mounting of crystals. The silicon seals around the piston were degassed in distilled, deionised water and kept in the degassed, deionised water under airtight conditions until they were mounted into the reactor. At the time of reactor filling a heat wave was affecting

the Giessen area with temperatures climbing to 30°C in the laboratory. Identical reactors were prepared and used as control references in the home laboratory one day later using the same solutions and lysozyme batch (but at more ambient temperatures, ≈23°C).

The filling process followed a carefully defined procedure, piston and seal were assembled in the reactor and the salt volume was filled and sealed. Buffer solution was used to wash out the buffer volume and which was then filled with more buffer solution. The dialysis membrane was inserted and the protein volume placed onto the bottom part of the reactor. Finally the protein chamber was filled and sealed. All filling was carefully monitored. The joints between the two parts of the reactor and cover-plates were tightened to an exact torque.

The reactors were subsequently transported to Kennedy Space Center in temperature controlled boxes at 20°C. The earth-control reactors were kept in insulated chambers within the home laboratory with no active temperature control (both APCF's were flying on the mission and no additional facility was available as a ground control). Before the reactors were inserted into the APCF facility, and handed over to NASA, photographs were taken of the protein reactor chambers. There was no sign of any crystal formation before the mission. The mission launched on 8th July, 1994, and performed as expected setting a then record for the longest Space Shuttle mission to date, nearly 15 days. CCD monitoring of the growing crystals took place (figures 8.4 and 8.5). The video showed the first crystals appearing at approximately at 37 hours after activation of the reactor. The CCD camera scans 12 reactors in turn so there is a time lapse of 8 hours and 40 minutes between exposures. The final image was recorded at 296.32 hours, after which the reactor was deactivated. Two initial images were made with laser

illumination to look for nucleation scattering but none was present at the observation time. The software operates in such a way that once LED illumination is activated for CCD observation the laser cannot be reactivated. The CCD images record not only the protein chamber but also the chamber temperature, time and number of the exposure making it possible to obtain a measure of the growth rates by simply measuring the crystal size directly from the image.

A polarizer is fitted between the LED and CCD which can be rotated to enhance the contrast, improve the quality of the images and make observation of the birefringence possible. The rotation of the polarizer is programmed into the software before the mission and its effects cannot be monitored until the APCF data tapes are examined after the mission.

8.5 Results

Exceptionally nice tetragonal crystals were produced, figure 8.6, in terms of morphology and size, average size 1.8 mm along the longest dimension with a maximum size of 2.5 mm. The ground control crystals, with identical materials were smaller, 0.6 mm on average, 0.8 mm at maximum. Sedimentation and clumping were not in evidence for the microgravity-grown tetragonal lysozyme crystals but had occurred in the earth-grown case. Interestingly, in the microgravity reactors exceptionally beautiful orthorhombic crystals grew eg. even out of the face of a tetragonal crystal (figure 8.12).

The CCD camera images showed a good example of the microgravity growth of the (110) face of a tetragonal lysozyme crystal. This growth is plotted over time

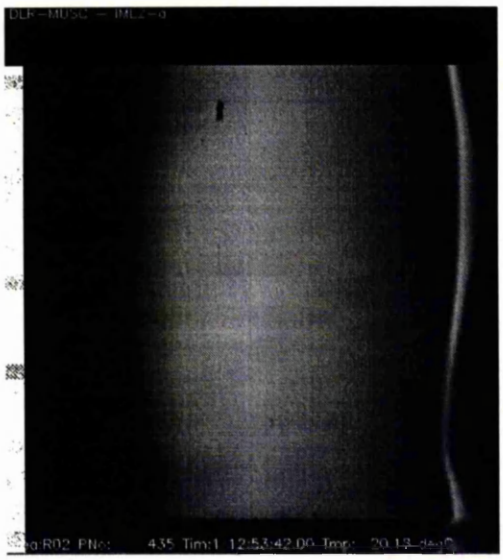

(a) 36:54 hours

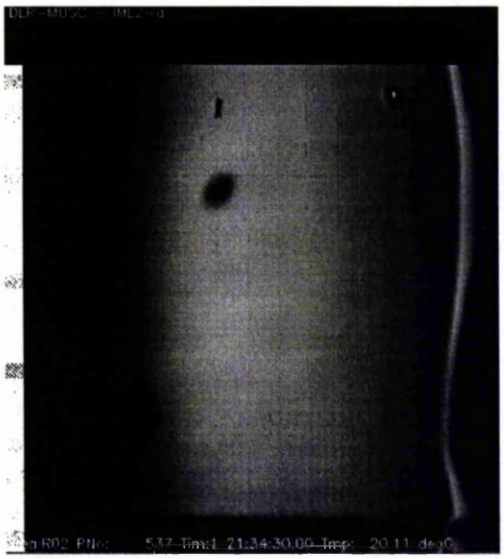

(b) 45:34 hours

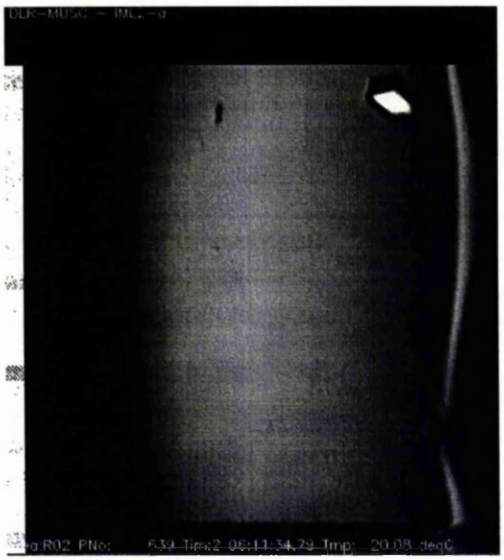

(c) 54:11 hours

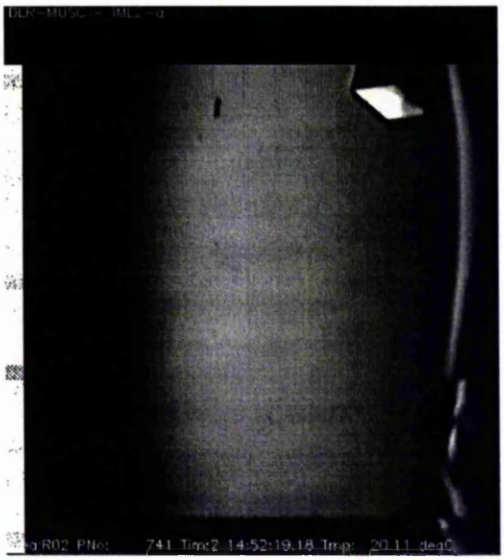

(d) 62:52 hours

Figure 8.4: Video images of tetragonal lysozyme, clearly showing the 110 face, of a growing tetragonal lysozyme crystal (top right) in a microgravity reactor at times of (a) 36:54 hours, (b) 45:34 hours, (c) 54:11 hours and (d) 62:52 hours during the IML-2 mission

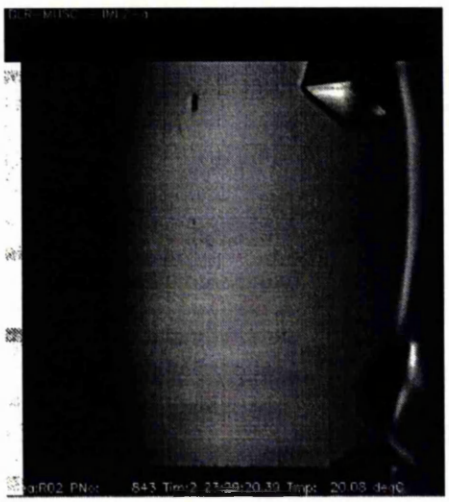

(a) 71:29 hours

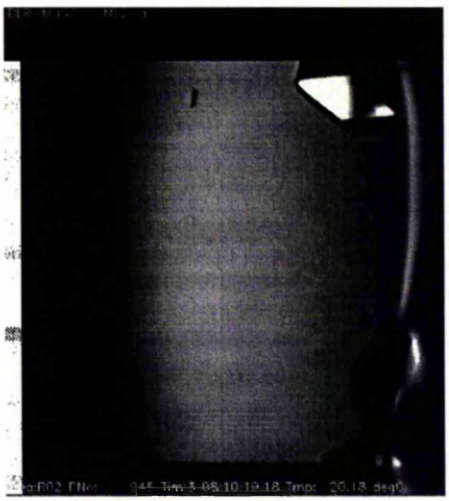

(b) 80:10 hours

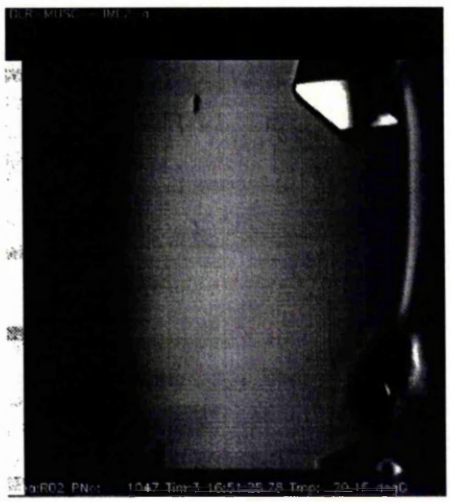

(c) 88:51 hours

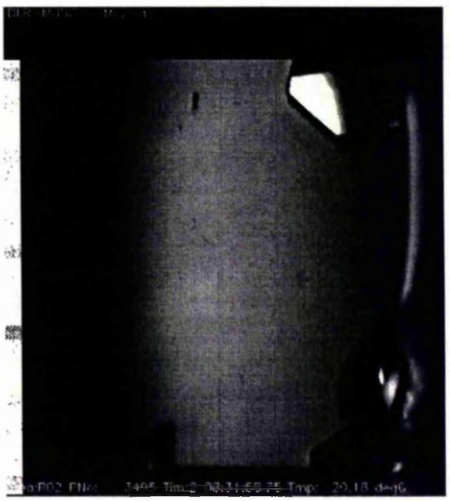

(d) 296:32 hours

Figure 8.5: CCD video images of tetragonal lysozyme, clearly showing the 110 face, of a tetragonal lysozyme crystal (top right) in a microgravity reactor at times of (a) 71:29 hours, (b) 80:10 hours, (c) 88:51 hours and (d) 296:32 hour (near the end of the mission prior to descent).

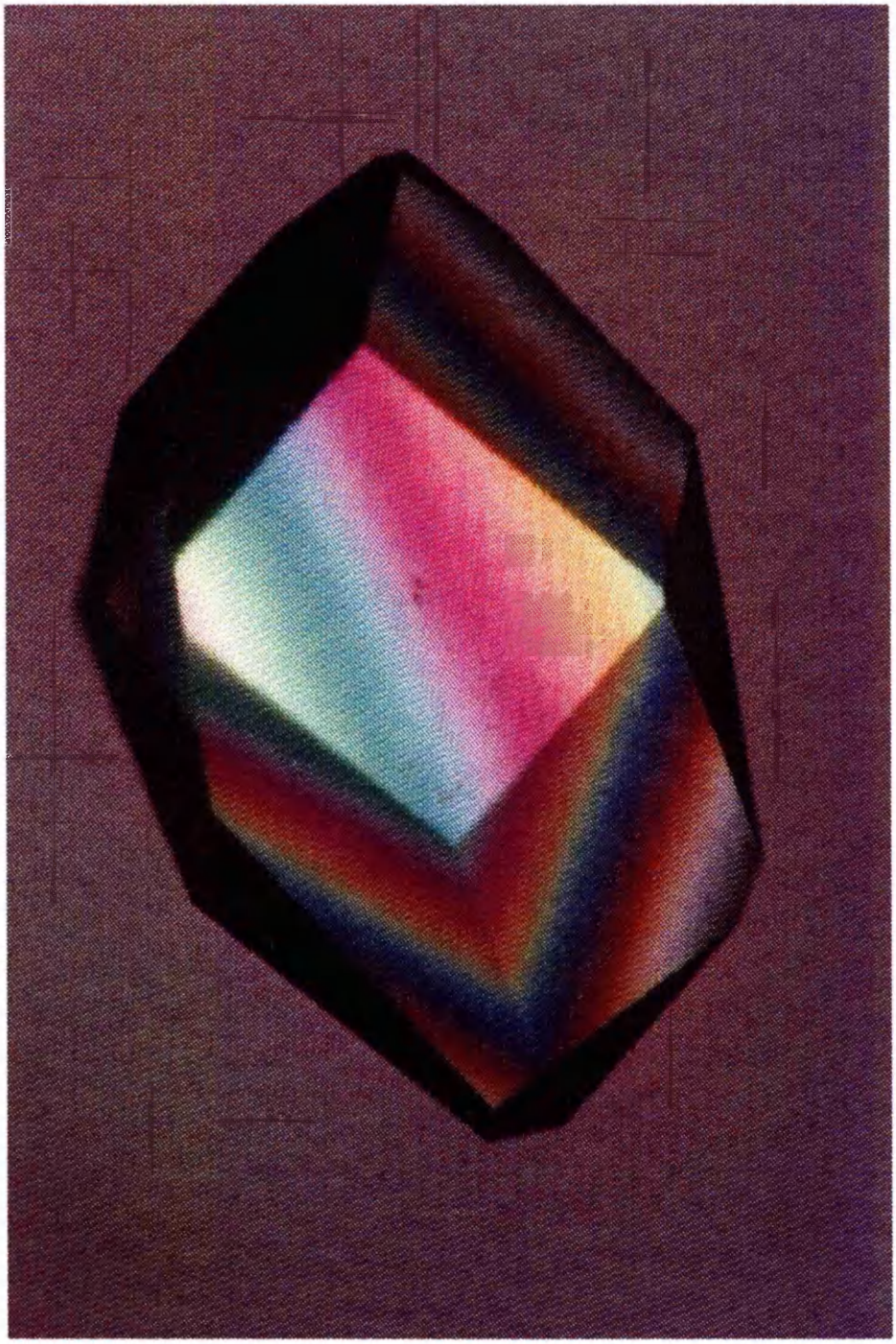

Figure 8.6: Photograph of typical tetragonal crystal produced on the IML-2 mission. Crystal length, along the longest dimension, 2.5 mm

in terms of length and width of the face, figure 8.7. Initially the face propagates in a rhomboid shape with the edge of the other perpendicular (110) face becoming visible at the 80.10 hours point. The crystal has grown so as to preserve the habit and edge ratio evident at the earliest stage of visibility. Ultimate shape appears to be determined at, or shortly after, nucleation.

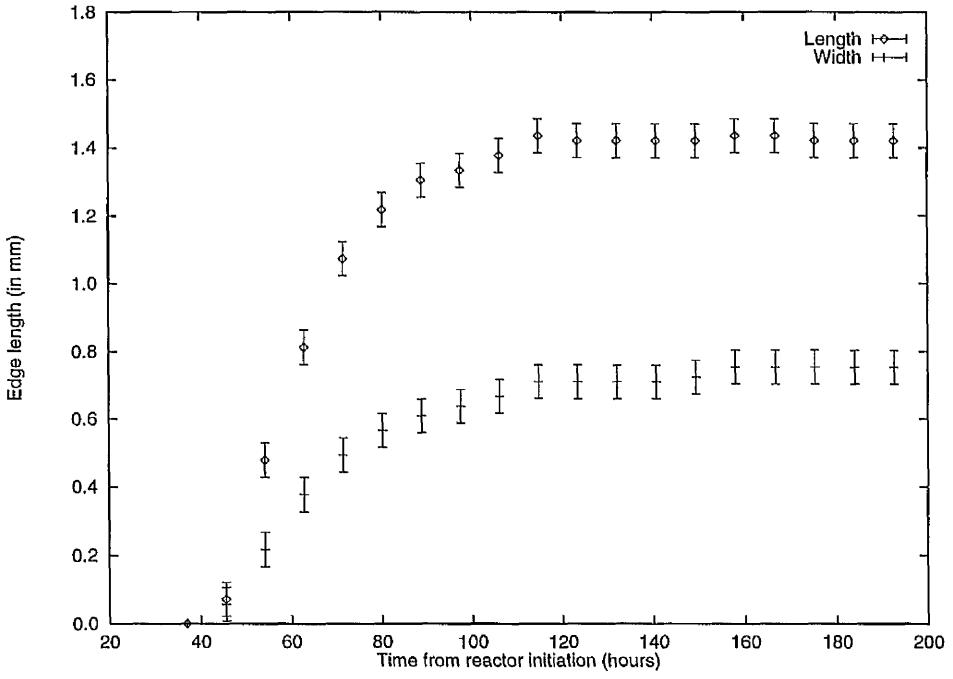

Figure 8.7: Plot of the growth of the (110) face over time (length and width) under microgravity conditions

The CCD system is not ideally suited for measuring growth rates as the images are only recorded approximately every 8 hours and 40 minutes from each reactor in the APCF. With the narrow field of view optics used in this case only one crystal could be observed in detail. Because of the small depth of field, several exposures were taken at different focus positions within the protein chamber to ensure that any crystals visible would be in focus. Wide-field-of-view optics would

provide more visible samples but an overall loss in detail. Additionally, due to the larger depth of field a reduced number of exposures at different focus points would be required decreasing the sampling time between reactor observation.

The growth rate for tetragonal lysozyme is defined[84] by;

$$G = \frac{1}{2}\frac{dL_A}{dt} \tag{8.1}$$

where dL_A/dt is the rate of change of the width of the (110) face in time. Figure 8.8 illustrates the (110) and (101) faces seen on tetragonal lysozyme. Plotting the rate of change of growth, figure 8.9, shows an initial peak of growth rate followed by a decline then several further peaks.

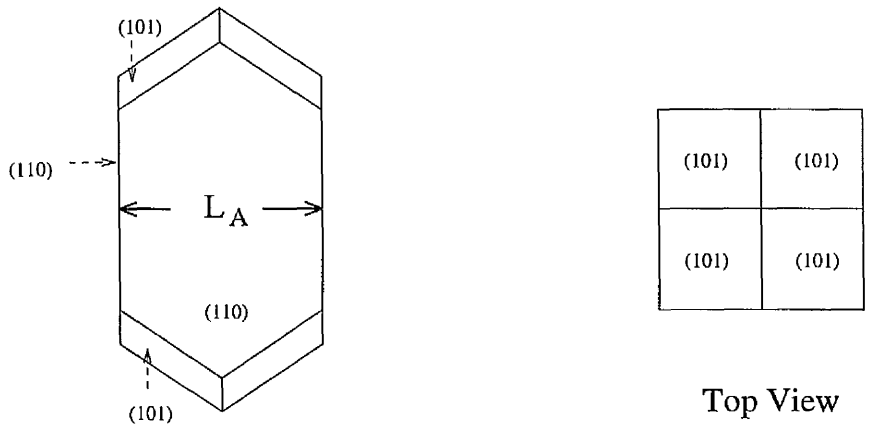

Figure 8.8: Illustration of the (110) and (101) faces of tetragonal lysozyme

The growth rate has been calculated by using the difference in half width over the difference in time (equation 8.1). Unfortunately the low CCD picture rate means there are few sampled points; nevertheless, it is interesting that the growth

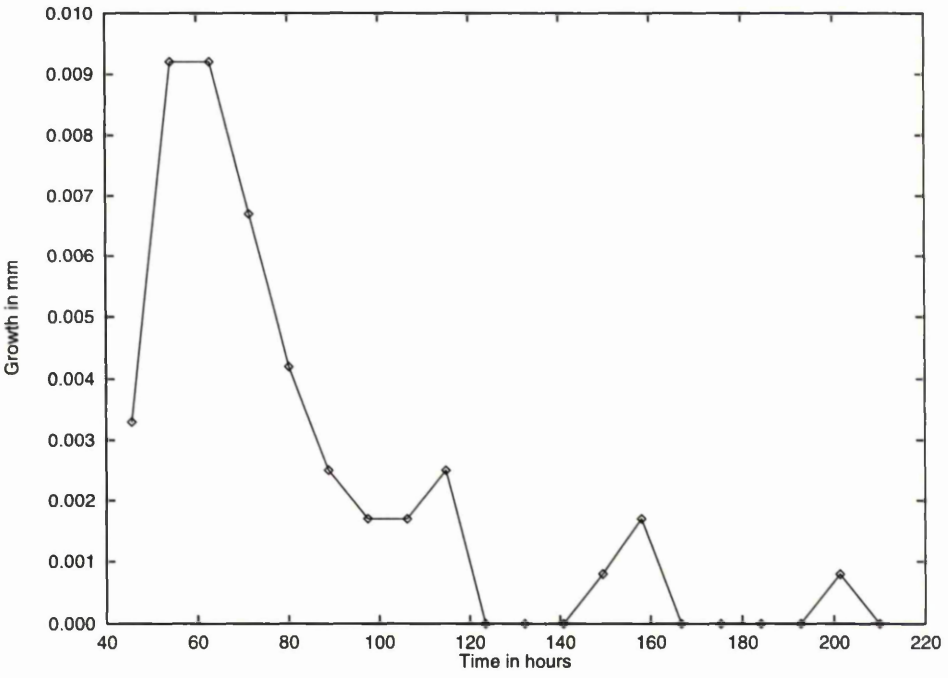

Figure 8.9: Plot of the growth rate over time under microgravity conditions

process seems to start and stop at intervals (figure 8.9). Crystal growth has been previously observed to occur in spurts and steps[147] in ground based experiments but not with ground controls in this case. Large crystals tend not to be obstructed by smaller crystals but simply continue growing and push them out of the way.[147]

Of particular note with the flight reactors was also the presence of orthorhombic crystals, albeit in a minority, with the expected tetragonal group, figure 8.10. Two distinct types were in evidence, clumps of orthorhombic crystals (maximum length approximately 1.0 mm), figure 8.11 and single 'needle' shaped crystals (up to a length of 2.1 mm) extruding from the surfaces of a minority of the tetragonal crystals, figure 8.12. No orthorhombic crystals were present in the ground control reactors. Ground studies have shown[147] "very few if any" cases of

crystals initiating and growing from the surface of another. In ground studies all aggregates observed tended to originate from nuclei that came together due to gravity or from solution currents present in the samples. Here the clumping occurs under microgravity conditions and remains to be explained.

8.6 Discussion

The Value of CCD observation

The value of CCD observation as a diagnostic for protein crystal growth is well illustrated, even in this non-ideal case, where a limited amount of data has still produced some useful quantitive results. It is of no surprise then that CCD monitoring systems are being fitted to other crystallization facilities.[203]

Crystal Growth Rate Observation

If we are to understand the crystal growth rate in microgravity it is useful to describe calculations aimed at relating the growth rate (based on concentration of available protein[32, 84, 97]) to the rate limiting step involved.[32, 95] On earth and in microgravity this rate limiting step may well be different. Screw dislocation control[97] is unlikely to be important in crystal growth as calculated values exceed the diffusion limited rate even at very low supersaturation. Theory[97] has produced two equations for the growth rate limiting steps of diffusion control and surface nucleation control. According to the diffusion control equation,

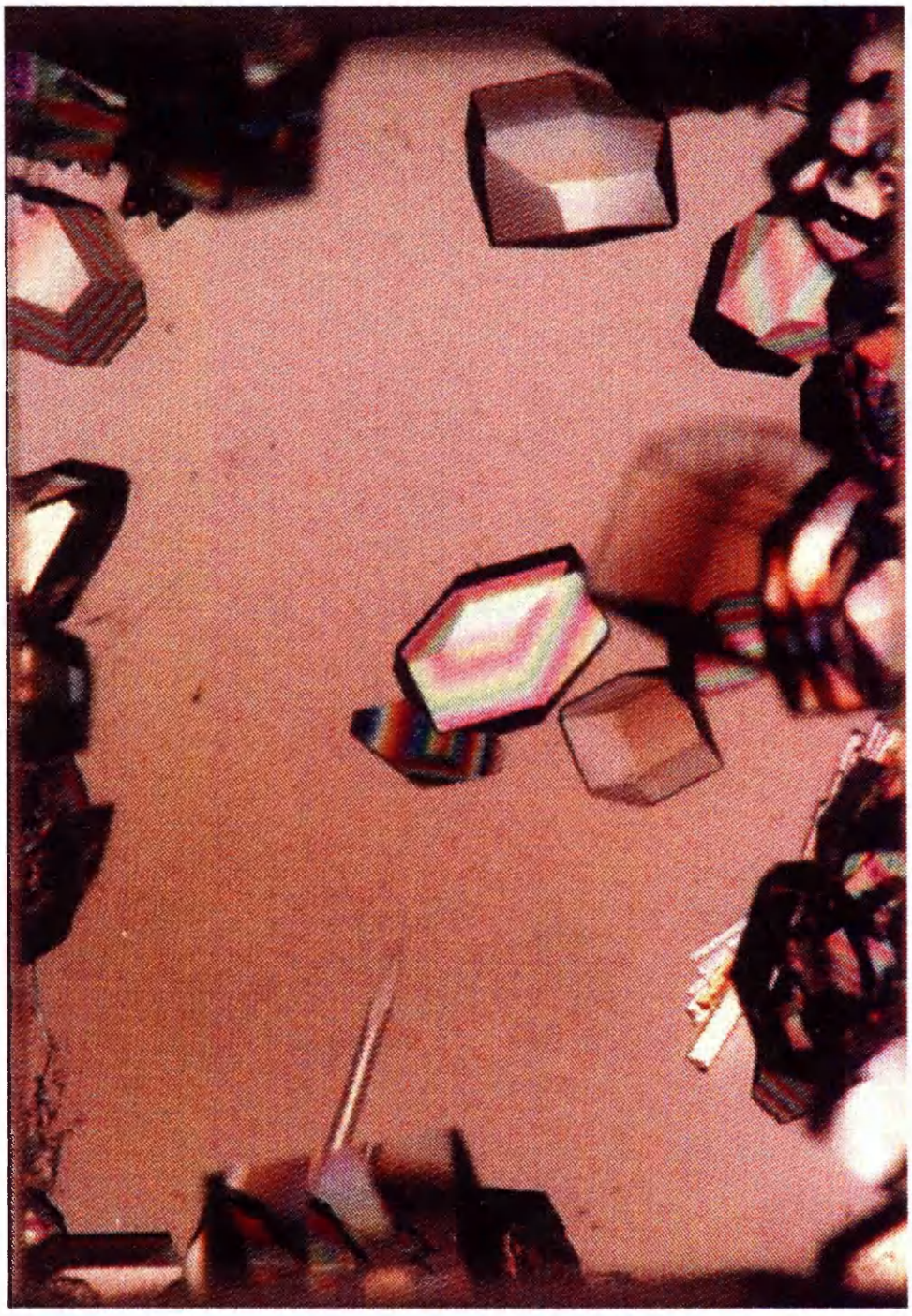

Figure 8.10: A photograph of the reactor at the end of the IML-2 mission. Width of the reactor is 5 mm

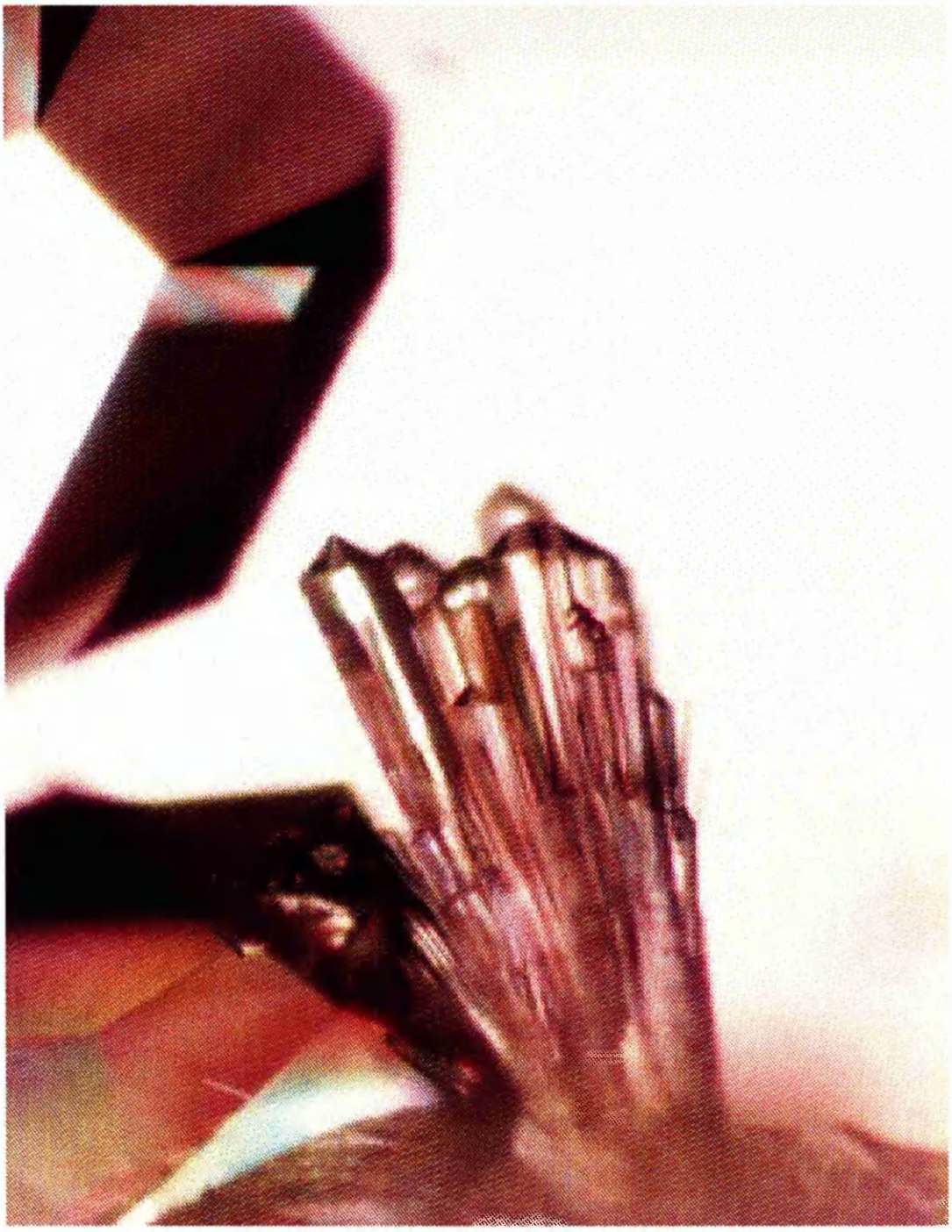

Figure 8.11: Clumps of microgravity grown orthorhombic crystals. Maximum length of the crystals making up the clump is approximately 1 mm

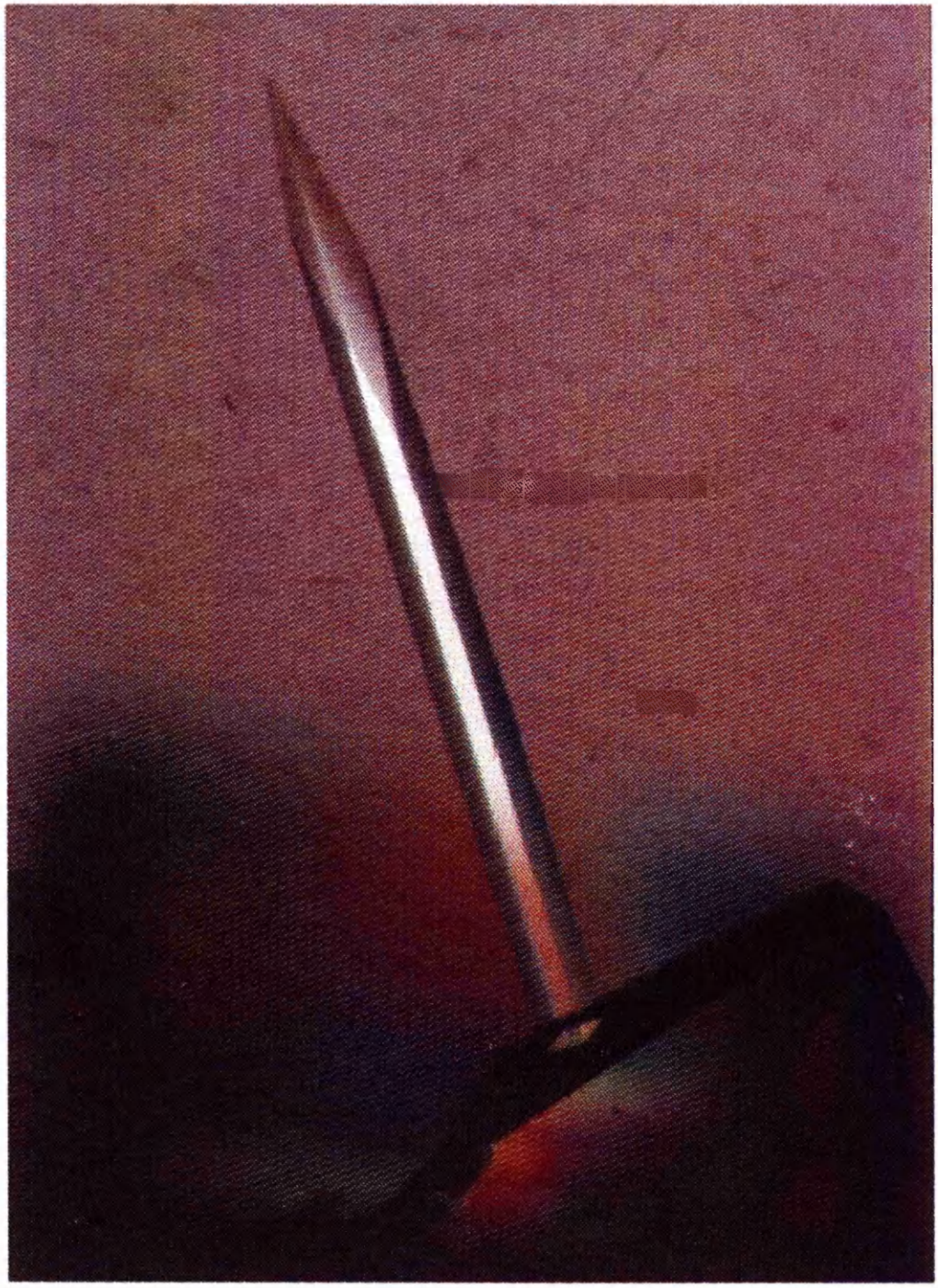

Figure 8.12: Needle shaped microgravity-grown orthorhombic crystal extruding from tetragonal crystal. Length of needle shown is 2.1 mm

$$G = Dv\frac{(c-s)}{t} \tag{8.2}$$

where t is the depletion layer surrounding the crystal, D the diffusion coefficient, c concentration of solution in molecules cm^{-3}, s the saturated concentration, and v the molecular volume, the growth rate is proportional to the concentration of protein (assuming it is much greater than supersaturation) and the diffusion coefficient. The surface nucleation control equation has a similar dependence on protein concentration and diffusion but is dominated by the final exponential term;

$$G = 1.7\ Dd(c-s)^{\frac{2}{3}} \exp\left(\frac{-\pi\gamma^2}{3k^2T^2\ln(c/s)}\right) \tag{8.3}$$

Where d is the molecular diameter, γ the molecular surface energy of the crystal solution interface, k the Boltzmann constant and T the temperature. With further experiments utilising different concentrations and/or fundamental measurements of the properties of lysozyme it is possible to describe the growth process in terms of the rate limiting step in microgravity by fitting these equations to the available data. A dependence of growth rates, of tetragonal lysozyme, on supersaturation has been seen.[84] This suggests that growth occurs predominately by a lattice defect mechanism at low supersaturation and by two dimensional nucleation at moderate to high supersaturation. In two dimensional nucleation layers are added to the crystal by nucleation, spreading and eventual merging of the two dimensional clusters of molecules on the surface. Additionally, at supersaturations above 1.6, growth of a lysozyme crystal has been observed by laser Michelson interferometry to occur by surface nucleation.[238] These growth

limiting step equations do not explain the spurts of growth, as we have observed (figure 8.9).

The observation of several spurts and lulls in the growth rate is interesting and is not seen to occur in similar earth based experiments by ourselves and others.[173] Here it must represent "regularly occurring" interruptions to growth. These interruptions may be related to periods of short gravitation jitters or maybe the formation of successive mosaic blocks (see chapter 10) in the crystal (energy to create a grain boundary) or different rate limiting steps being applied. Further investigation needs to be carried out into this. It has been shown with lysozyme[95] that the faster crystals grow the larger number of them and the smaller their terminal size. Crystals that have reached terminal size, when cut into spatially separated pieces grow to approximately the same terminal size with re-growth occurring on the freshly exposed surfaces. A possible cause of growth not occurring on the "old" surface may be the poisoning of favourable growth sites on the surface by impurity.[99] Laser scattering tomography of the orthorhombic form shows that the number of micro defects greatly increases from the centre toward the surface.[205] In this case surface impurities may be the cause of growth cessation but if so it would seem that these impurities occur more quickly in the earth grown crystals due to their smaller size. It has been shown with lysozyme that protein impurities present in ground control studies are reduced or eliminated entirely in the microgravity case.[153] This may be a process that is being seen here.

The growth rate plotted here, figure 8.9, is very similar to an oscillation function with exponential damping, growth rate very quickly reaching zero. Figure 8.9 suggests then, that if, by some form of more sensitive monitoring, growth had

been terminated at 100 hours, a more perfect (albeit smaller) crystal would have resulted.

Towards an explanation of orthorhombic lysozyme crystal formation

Chicken egg white lysozyme undergoes a phase transition at ≈25°C with the crystallographic result that orthorhombic rather than tetragonal crystals are produced.[93] The specific temperature of this transition is a function of salt concentration and pH. Crystal growth studies indicated a time dependence in the phase change.[23] Protein solution stored at high temperatures still gave orthorhombic crystals upon cooling then crystallizing. Thus a majority impurity may be lysozyme itself but in the high temperature or physiological form. It would seem possible that the high temperatures encountered during filling in Giessen (30 °C) caused this critical temperature to be reached in the solutions as the only cooling available was the fridge in which the lysozyme was stored. The solutions had cooled for filling the next day in Manchester. If this were true it implies that heating for a brief period of time (the reactors were kept at 20° once filled) *sets* a proportion of lysozyme in the solution to crystallize in the orthorhombic form.

Lysozyme growth units are larger than monomers[178] and hence there is a preclustering in solution (above supersaturations of 22 mg/ml aggregates larger than dimers are present in solution[251]), indeed tetragonal lysozyme growth has been shown to occur by addition of aggregates preformed in solution.[189] The unit cell of tetragonal lysozyme crystals is an octomer[28] and there is evidence that octomers are present in supersaturated lysozyme solutions.[35] Electron microscope

measurements have revealed that the single step height on a growing tetragonal lysozyme crystal face corresponds to that of an octamer unit cell.[85] In the lysozyme solution there exsists monomers, dimers, tetramers, octamers and higher order aggregates distributed in quantity as a function of temperature and concentration.[173] At supersaturations and/or low temperatures the higher order aggregates predominate.[35, 173, 176] At saturation and/or higher temperatures the lower order aggregates predominate in the lysozyme solution.[35, 189, 251, 252] The unit cell of the orthorhombic lysozyme crystal is a tetramer.[13, 24] It is therefore not surprising at higher temperatures (where the higher order aggregates (eg. octamers) are reduced) that orthorhombic crystals are formed. If the tetragonal form obtained at 20 °C is sealed and held at 40 °C the crystals dissolve and without change in pH, ionic strength or protein concentration a transformation into the orthorhombic form is observed.[23] The orthorhombic crystals remain stable in mother liquor from -4 to 60 °C whereas the tetragonal ones disappear as soon as room temperature exceeds 25 °C. This gives rise to the question of whether tetragonal lysozyme is a meta-stable form with orthorhombic being the stable form. In *vivo* all chemical reactions in birds take place at about 40 °C.

Dramatic shifts can be observed[23] in the catalytic properties of lysozyme over temperature changes of a few °C and it is therefore not surprising that there would be an accompanying change in the crystal form even though the net structural changes are small[24] (the root mean square differences in the coordinates of the corresponding backbones are only 0.46 Å). There are some appreciable local differences involving the main and side chains on the surface but in general these arise from different modes of packing in the two crystal forms. Orthorhombic lysozyme is particularly stable at tetragonal temperatures whilst the reverse is

apparently not true.[24]

It is not possible to say whether the orthorhombic form has crystallized at the same time as the tetragonal crystal or even if they grew in microgravity because CCD video observation was limited to one portion of one reactor with the narrow-field-of-view optics. The initial supersaturated solution favours nucleation and, at the point where the tetragonal crystals have finished their growth, the supersaturation level is going to be much lower, favouring growth under earth gravity conditions. In a dilute mixture of two crystal forms the transfer of solute molecules from the higher to the lower solubility form (less stable to more stable) will be a function of the surface areas, diffusive paths and detachment and attachment kinetics. For lysozyme crystals at low solute concentrations these would all be rather slow processes.[46] It seems unlikely, because of the orthorhombic crystals size, that they grew between the Shuttle de-orbiting and photographing of the crystals a few hours after they had landed.

A potentially key point is that there were differences in the ground control and microgravity conditions. At present there exists only two APCF facilities and one engineering model used for equipment and software development. Both APCF facilities flew on the IML-2 mission so no ground control APCF facility was available (unlike the case for Spacehab-1). Hence for IML-2 the laboratory controls were grown in an insulated chamber which minimised temperature changes to approximately $\pm 2°C$ but did not have the temperature stability of the APCF ($\pm 0.1°C$).

8.7 Summary and Main Findings

The IML-2 mission produced exceptionally beautiful microgravity-grown crystals of lysozyme with average size 1.8 mm along the longest dimension compared to 0.6 mm for the earth-grown controls. Of note in the microgravity-grown crystal reactors was the formation of two types of orthorhombic crystals, single needle type and clumped groups.

The CCD observation system employed has proved effective for monitoring the growth process, albeit with limited exposures. The growth itself has displayed interesting characteristics with the spurts and lulls in the process not present in similar earth based experiments.

We have highlighted the high ambient temperatures at the time of filling the microgravity reactors as a possible source of the orthorhombic microgravity-grown crystals. The effect of microgravity on the aggregation of protein molecules in solution is another possible source of the tetramer formed orthorhombic crystals and looks to be an exciting area for future investigation.

Chapter 9

Diffraction Characterisation of (IML-2) Microgravity Grown Crystals

9.1 Introduction

Initial experience with the evaluation of microgravity grown crystals from the Spacehab-1 mission provided evidence of very much reduced mosaic values.[248, 246] Further experiments at LURE some 5 months after the return to earth apparently showed a degradation in the crystal quality[247] although the microgravity crystals, on average, still appeared to be better. This seemed to be due to ageing effects, which might be expected with some proteins even if simply by denaturation of the molecule. Later the LURE results were attributed (based in fact on the work done and reported in this chapter) to the mounting of crystals in the home laboratory a few days before use and subsequent travel to the synchrotron. This initial work allowed planning of the IML-2 crystal evaluation to be carried out. The likely mosaic values to be obtained having been previously calculated on theoretical grounds.[124]

The diffraction characterisation of the IML-2 crystals was carried out at the European Synchrotron Radiation Facility (ESRF). Initial studies were carried out on the Laue beamline[148] (BL-3) three months after the return to earth of the crystals. Monochromatic studies were then made on the Swiss-Norwegian beamline of the ESRF a further three months after the ESRF Laue studies. These two diffraction methods are complementary. The Laue method allows a rapid sampling of the reciprocal space and monochromatic methods allow a detailed study of individual reflection profiles. The IML-2 results, especially the ones some six months after return to earth, show that tetragonal lysozyme crystals grown in microgravity have 3-4 times lower mosaicity than earth-grown controls. These results agree then with the results from Spacehab-1.

9.2 Evaluation of Crystal Perfection with the Laue Method on ESRF BL-3

Beamline 3 of the ESRF is a station optimised for Laue diffraction work.[148] For the experiment, initially one reactor was opened for crystal harvesting whilst the beam was being aligned. There were problems mounting these crystals. The large size of the crystals necessitated capillary diameters of 2.5-3.5 mm. These have a smaller wall thickness to diameter ratio than the more typically used capillary sizes (eg. 1 mm or less). These large, standard glass capillaries, proved very fragile and suffered a high failure (breaking) rate during mounting (approximately 20% were usable). Furthermore *micro-cracks in the capillaries that initially appeared undamaged*, unfortunately caused the crystals that could be mounted to dry out over a period of time. Another "unwanted" effect of using such large capillaries

was that they used up a lot of mother liquor during mounting. No artificial mother liquor was used for the IML-2 mission in case this affected the quality of the crystals (this had been used in the case of the Spacehab-1 mission for crystals that were measured at LURE). Consequently only three to four crystals were available at most from each reactor for experimentation.

Laue exposures were made onto X-ray sensitive film situated 2120 mm from the crystal. The beam was trimmed down to obtain a very low divergence (0.01 mrad horizontally and 0.01 mrad vertically). The crystal initially mounted proved unusable because of drying out and a second reactor was opened but these crystals also suffered drying out within the large glass capillaries. Also, station alignment took longer than expected and the crystals had to be left for some time before use.

An orthorhombic crystal from one reactor was also mounted and several Laue exposures made onto CCD. Data processing of these confirmed the crystal was orthorhombic and that the needle shape was not a result of differential growth rates between the 110 and 101 faces.[84] This needle shaped crystal was, fortunately, able to be mounted in a 0.5 mm diameter capillary. Consequently, in this case, no crystal drying out was experienced.

9.3 Evaluation of Crystal Perfection by Monochromatic Methods

Equipment

The ESRF Swiss-Norwegian beamline has a Huber ψ circle diffractometer from the University of Karlsruhe on station A, figure 9.1. The primary role of this diffractometer has been for the direct determination of triplet phases.[138, 245] The instrument contains two circles (θ, ν) for the detector with axes perpendicular to each other and four circles for the crystal motion. The first crystal axis is parallel to the first detector axis ($\omega - 2\theta$ relation). Perpendicular to the ω axis a second axis for the ψ rotation is installed. This ψ axis bears an Eulerian cradle with motions χ and ϕ. Thus an arbitrary scattering vector $\underline{h}$ can be aligned with the ψ axis and a ψ scan (ie. rotation around a reciprocal lattice vector for any hkl) performed by moving only one circle (with a consequent improvement in accuracy). All circles are driven by computer controlled stepper motors.

The instrument resolution function (IRF') is calculated at 0.00195° from equations 7.4 to 7.6, page 160, with source to instrument, $P = 45$ m, Bragg angle of monochromator, $\theta_B = 9.18°$, vertical beam source size, $2.3\sigma = 200$ μm, relative wavelength range, $\delta\lambda/\lambda = 2 \times 10^{-4}$ and sample dimension (from collimation) of $C_v = 0.6 \times 10^{-3}$ m. The station utilises a double crystal Si(111) monochromator. This diffractometer has a very fine step size of 0.0001° enabling very high angular resolution scanning of rocking widths. The beamline is on a bending magnet of the ESRF 6 GeV synchrotron and so is an intense, collimated, source of X-rays especially at short wavelength like 1 Å.

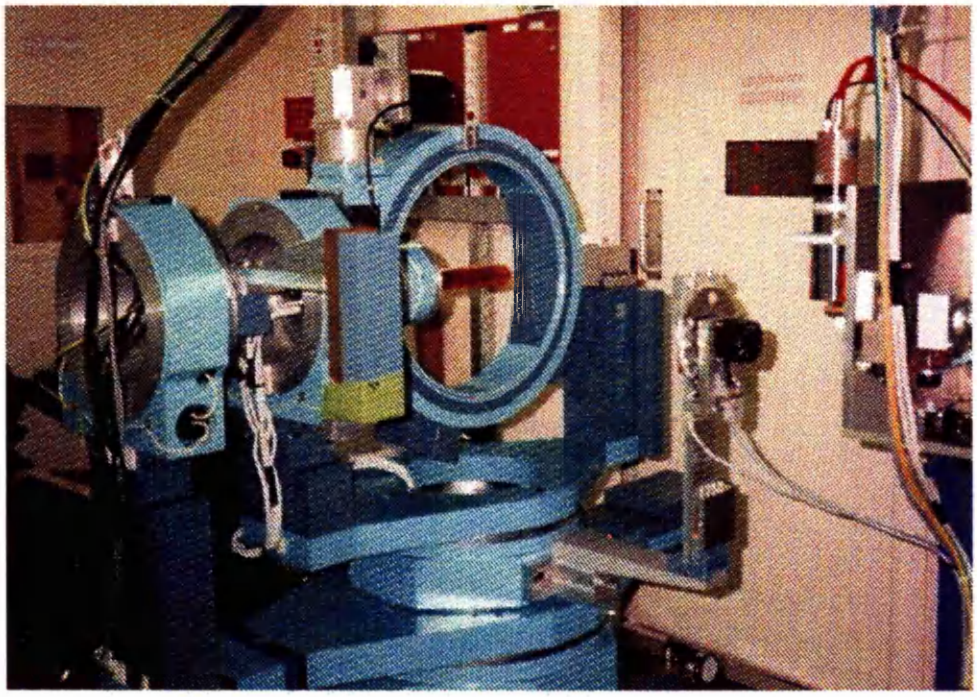

Figure 9.1: ψ circle diffractometer used for data collection showing capstan shield in place. Photograph kindly supplied by Dr. P. Pattison of the Swiss-Norwegian beamline, ESRF

Experimental

Measurements were made on one earth-grown control crystal and on three microgravity-grown crystals. The ground control crystal ($0.7 \times 0.6 \times 0.5$ mm^3) was mounted in a 1.0 mm diameter glass capillary. Because of the accuracy of the diffractometer the sample was mounted with somewhat less mother liquor than normally used for mounting to prevent any slight motions when a capillary is rotated. Thermal vibrations in the hutch also cause motion of a capillary which had been seen previously in direct phase determination experiments. A capstan shield was used to shield the capillary from thermal vibrations, figure 9.1 (It is interesting to wonder if shielding like this in general may improve the overall

quality of data as this slight motion must be reflected in the diffracted intensities to some small extent in standard apparatus).

A microgravity-grown crystal was mounted in a glass capillary of 1.5 mm diameter but dried out quickly during data collection. Micro-cracks were not evident but as previously mentioned, a less than usual quantity of mother liquor was used in the mounting and too little may have been used in this case. A second such crystal in a similar capillary but with slightly more mother liquor, was used but this showed signs of the crystal drying out towards the end of data collection, this time presumably due to mounting in a glass capillary. Finally a microgravity crystal ($1.5 \times 0.6 \times 0.6$ mm^3) was successfully mounted in a 2.0 mm **quartz** capillary for which there were no signs of micro-cracks. Data collection (described below) from this proceeded successfully.

The strategy employed for data collection involved initial measurements of a small batch of reflections (10 or so) to determine the orientation matrix of the crystal, necessary to index the reflections (not carried out in the Spacehab-1 Laue evaluation). This was followed by a sequence of measurements of reflections suitable for triplet phasing in conjunction with repeated measurements of a set of standard reflections. A high resolution search was readily made with the quartz capillary mounted microgravity crystal whereby a scan of the (32 57 0) reflection, of 1.2 Å resolution was made. No evidence of diffraction to this resolution was seen with the earth-grown control crystal and is better than reported ever before for tetragonal lysozyme to our knowledge (see page 204).

Results

The ground control crystal exhibited rocking widths ranging from 0.0067° to 0.0169°, calculated at Full Width at Half Maximum (FWHM), table 9.1. In the case of some reflections a composite structure of the peak was resolved ie. the reflection was seen to be made up of two or more separate peaks. The rocking widths of these component peaks were also evaluated at FWHM. Reflections measured are also listed in table 9.1, those reflections where composite peaks were observed and measured are indicated with an asterix. Table 9.2 lists the rocking widths at FWHM from the composite component.

No.	hkl value	ψ angle	rocking width	No.	hkl value	ψ angle	rocking width
1	4 7 0	65	0.0069	16	7 7 6	65	0.0130
2	4 7 0	65	0.0075	17*	7 7 6	-162	0.0118
3	-4 7 0	65	0.0075	18*	0 0 8	0	0.0100
4*	-2 3 -2	-162	0.0112	19*	0 0 8	-45	0.0100
5*	2 -3 2	162	0.0118	20	0 0 8	45	0.0124
6	16 16 0	0	0.0167	21	16 16 0	0	0.0159
7	16 16 0	45	0.0126	22	16 16 0	-45	0.0118
8	16 16 0	-45	0.0143	23	16 16 0	45	0.0139
9*	-16 16 0	0	0.0124	24	-16 16 0	0	0.0108
10*	-16 16 0	45	0.0106	25	-16 16 0	-45	0.0149
11*	-16 16 0	-45	0.0124	26*	-16 16 0	45	0.0067
12*	0 0 8	0	0.0124	27*	0 0 8	0	0.0118
13	0 0 8	45	0.0149	28*	0 0 8	-45	0.0118
14*	0 0 8	-45	0.0118	29	0 0 8	45	0.0169
15	7 7 6	0	0.0137				

Table 9.1: List of earth-grown crystal reflections comprising rocking width data (secondary composite value excluded). The sequence number is that used throughout the experiment run and forms the numbers on the abscissa of figures 9.2 and 9.3. The * denotes that it was possible to derive a secondary FWHM value from the angularly-resolved component structure of the reflection

No.	hkl value	ψ angle	rocking width	No.	hkl value	ψ angle	rocking width
4	-2 3 -2	-162	0.0112	5	2 -3 2	162	0.0138
9	-16 16 0	0	0.0101	10	-16 16 0	45	0.0081
11	-16 16 0	-45	0.0091	12	0 0 8	0	0.0131
14	0 0 8	-45	0.0098	17	7 7 6	-45	0.0116
18	0 0 8	0	0.0122	19	0 0 8	45	0.0072
26	-16 16 0	-45	0.0114	27	0 0 8	0	0.0122
28	0 0 8	45	0.0095				

Table 9.2: List of earth-grown control crystal (composite reflection) rocking width data

The first microgravity-grown crystal mounted in a glass capillary did not give useful results. The second crystal, again in a glass capillary, exhibited rocking widths ranging from 0.0056° to 0.0213°, with the rocking width increasing toward the end of data collection evidencing crystal drying out, as indicated in figure 9.2. Table 9.3 shows the reflections measured and the corresponding rocking width values.

The third microgravity-grown crystal, mounted in a quartz capillary (which does not seem to exhibit the property of micro-cracks), gave rocking widths in the range 0.0019° to 0.0106°. A plot of these rocking widths (table 9.4) is shown against the earth control data (table 9.1) in figure 9.3. These were clearly improved over the earth control values. By plotting the distribution of the rocking width values, figure 9.4, it is seen that the average rocking widths for the microgravity-grown crystal is approximately three times less than those of the earth-grown. In this figure the separated rocking widths of the composite peaks,

No.	hkl value	ψ angle	rocking width	No.	hkl value	ψ angle	rocking width
1	-4 7 0	-170	0.0059	2	4 -7 0	-170	0.0069
3	-6 -9 6	-174	0.0077	4	-6 -9 -6	0	0.0081
5	6 9 -6	-174	0.0118	6	-1 -6 2	179	0.0056
7	1 6 -2	179	0.0130	8	-5 7 1	170	0.0042
9	2 7 -1	-141	0.0073	10	2 7 -1	-141	0.0086
11	-2 -7 1	-141	0.004 8	12	-5 7 1	170	0.0044
13	-5 7 1	170	0.0057	14	-3 3 2	179	0.0045
15	3 -3 2	179	0.0073	16	-3 2 1	176	0.0061
17	3 -2 -1	176	0.0061	18	22 8 1	140	0.0142
19	-2 3 1	180	0.0056	20	2 -3 -1	180	0.0052
21	6 0 -4	167	0.0073	22	-6 0 4	167	0.0102
23	-5 1 5	180	0.0110	24	5 -1 -5	180	0.0090
25	-3 2 -2	171	0.0175	26	3 -2 2	171	0.0151
27	-2 -3 4	176	0.0187	28	2 3 -4	176	0.0163
29	1 7 4	4	0.0166	30	-1 -7 -4	4	0.0199
31	-4 7 0	-170	0.0078	32	-4 7 0	-170	0.0069
33	4 -7 0	-170	0.0082	34	6 7 -4	-161	0.0151

Table 9.3: List of microgravity-grown crystal reflections comprising rocking width data using a *glass* capillary for mounting

as listed in table 9.2 are also shown. Even the resolved components of the earth-grown crystal reflections do not match the bulk of the values for the microgravity-grown crystal reflections.

A special strength of this work is the chance to explicitly compare the identical *hkl*'s from each crystal type. Such a comparison is illustrated in the 0 0 8 and 7 7 6 reflections, shown in figures 9.5 and 9.6. Three scans are shown in each case at ψ angles of 45°, 0° and -45° respectively. The half maximum of each component of the reflection has been evaluated in each case where there is either no appreciable composite structure or the composite structure can be resolved separately from the main peak. These are indicated in the figures by a short horizontal line with

No.	hkl value	ψ angle	rocking width	No.	hkl value	ψ angle	rocking width
1	16 16 0	0	0.0017	2	16 16 0	45	0.0022
3	16 16 0	-45	0.0039	4	16 -16 0	0	0.0096
5	16 -16 0	45	0.0068	6	16 -16 0	-45	0.0069
7	0 0 8	0	0.0059	8	0 0 8	45	0.0020
9	0 0 8	-45	0.0086	10	7 7 6	0	0.0059
11	7 7 6	45	0.0023	12	7 7 6	-45	0.0044
13	7 4 0	60	0.0055	14	-7 -4 0	60	0.0025
15	-7 -4 0	179	0.0061	16	3 -9 1	179	0.0106
17	7 -2 1	175	0.0038	18	-7 2 -1	175	0.0075
19	19 -3 -5	-180	0.0063	20	-19 3 5	-180	0.0037
21	11 10 5	-51	0.0050	22	-11 -10 -5	-51	0.0037
23	13 9 8	20	0.0063	24	-13 -9 -8	20	0.0037
25	-14 -7 -3	158	0.0052	26	14 7 3	158	0.0030
27	3 -5 -2	169	0.0041	28	-3 5 2	169	0.0064
29	1 -3 -7	156	0.0069	30	-1 3 7	156	0.0044
31	-3 13 5	170	0.0046	32	3 -13 -5	170	0.0088
33	3 13 5	171	0.0061	34	-3 -13 -5	171	0.0086
35	-5 7 7	161	0.0057	36	5 -7 -7	161	0.0050
37	4 6 7	160	0.0042	38	-4 -6 -7	160	0.0039
39	-14 -7 -3	158	0.0050	40	14 7 3	158	0.0017
41	16 -7 -3	-171	0.0050	42	-16 7 3	-171	0.0052
43	-10 -15 -3	-180	0.0037	44	10 15 3	-180	0.0075
45	14 13 6	-165	0.0061	46	-14 -13 -6	-165	0.0032
47	-14 -13 -6	-9	0.0059	48	14 13 6	-9	0.0033
49	16 16 0	0	0.0025	50	16 16 0	45	0.0017
51	16 16 0	-45	0.0033	52	16 -16 0	0	0.0059
53	16 -16 0	-45	0.0017	54	0 0 8	0	0.0037
55	0 0 8	45	0.0020	56	0 0 8	-45	0.0039
57	7 7 6	0	0.0040	58	7 7 6	45	0.0010
59	7 7 6	-45	0.0037	60	7 4 0	59	0.0025
61	-7 -4 0	59	0.0025				

Table 9.4: List of microgravity-grown crystal reflections comprising rocking width data (crystal mounted in *quartz* capillary).

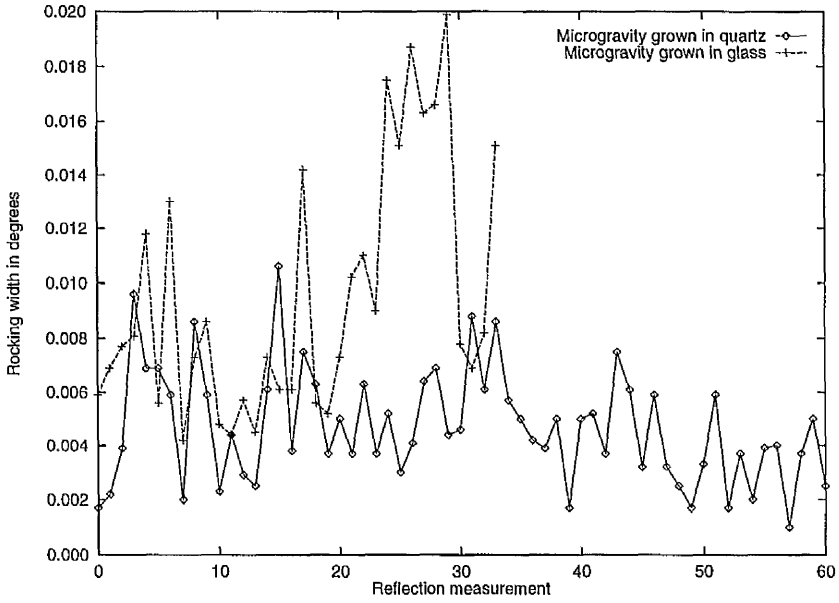

Figure 9.2: Rocking widths of microgravity-grown lysozyme crystals mounted in *quartz* and *glass* capillaries. Notice how, for the glass capillary case, the rocking width is steadily increasing with time.

the corresponding deconvoluted (ie. IRF' deconvoluted out) rocking width. In each separate case the integrated intensity of the scans are similar as would be expected when due allowance for the differences in crystal volume is made (the microgravity-grown crystal being twice the volume of the earth-grown crystal).

It was noticed that the space crystals exhibited far higher peak intensities for reflections than the corresponding earth grown crystal reflections. Typical reflections (16 16 0, and 7 7 6) are shown in figure 9.7 plotted on the same axes. The integrated intensity of the space grown crystal reflection is approximately double that of the earth grown (corresponding to their relative volumes) but the peak intensity of the reflections from the microgravity grown are almost an order of magnitude greater than the earth grown. This is the effect of a narrow rocking

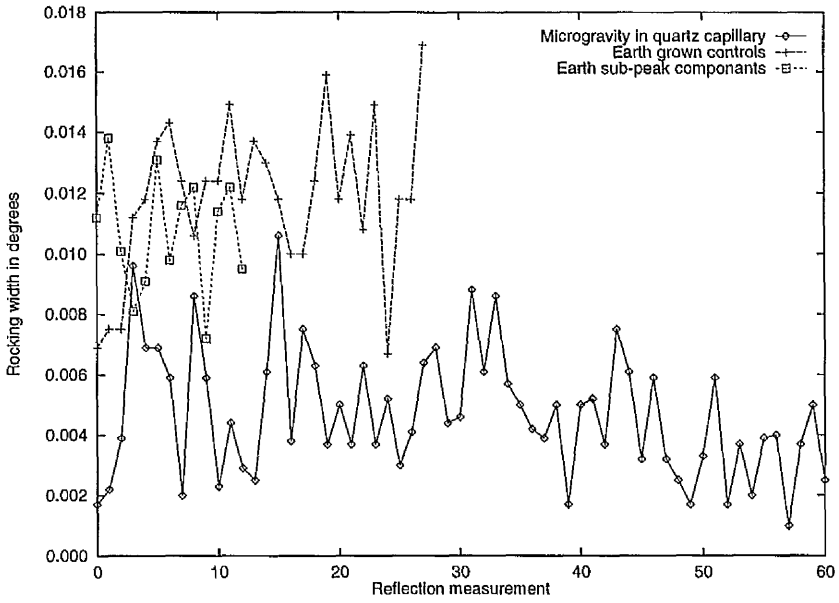

Figure 9.3: Rocking widths of microgravity-grown and earth-grown lysozyme crystals. Microgravity crystal (size $1.5 \times 0.6 \times 0.6$ mm^3) mounted in a quartz capillary; earth-grown control (size $0.7 \times 0.6 \times 0.5$ mm^3) mounted in a glass capillary

width (contributing a factor of 4) and increased crystal size (contributing a factor of 2).

The scan performed on the (32 57 0) reflection (at 1.2 Å resolution) produced a well defined peak, figure 9.8. Diffraction to further resolution was not looked for due to beam time and computational limitations. Quite a high background is shown for the 1.2 Å reflection but this could be reduced by a factor of five with optimisation for high resolution studies.[221] No diffraction to 1.2 Å resolution resolution was present in the earth-grown control crystal although a single crystal sample out of a large quantity ($\approx$ 40) of vapour diffusion earth-grown lysozyme crystals (used for triplet phasing experiments during this beamtime) did show similar diffraction at these resolutions (albeit at much reduced intensities).

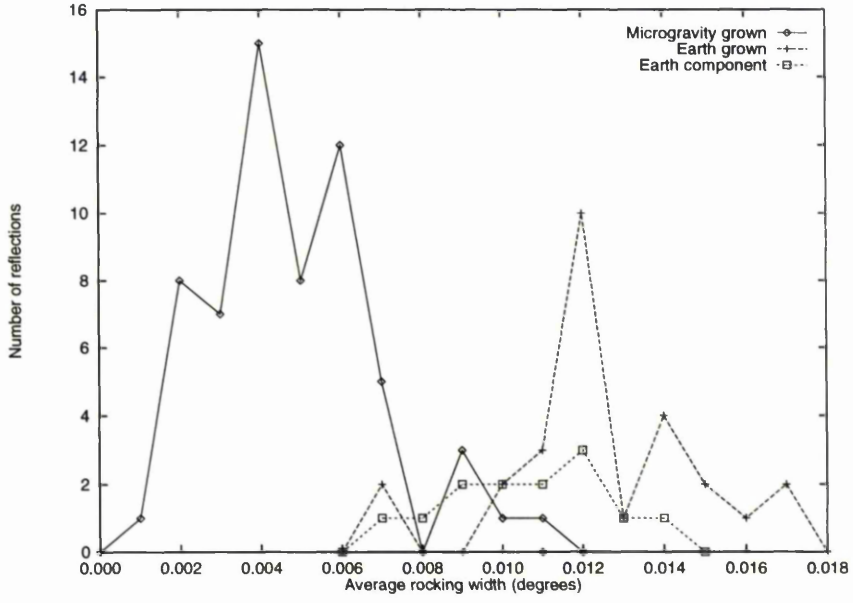

Figure 9.4: Distribution of microgravity-grown and earth-grown lysozyme crystal rocking widths

9.4 Discussion

The increased peak intensity, far greater than that expected from crystal volume considerations, yields a much greater signal to noise ratio during data collection thus allowing weaker reflections to be recorded better with microgravity-grown crystals than the earth-grown control crystal.

There are a number of reports of enhanced I/σ for microgravity grown over earth grown crystals.[160, 75] Our results point to the physical basis of why $I/\sigma(I)$ might be better. Namely this can be attributed to fewer, more perfectly arranged mosaic blocks. In turn, this leads to narrower rocking widths. Hence, the peak intensities of reflections have been enhanced, here by a factor of 4 due to rocking width alone and a further factor of 2 due to the crystal volume increase. Evidence of a

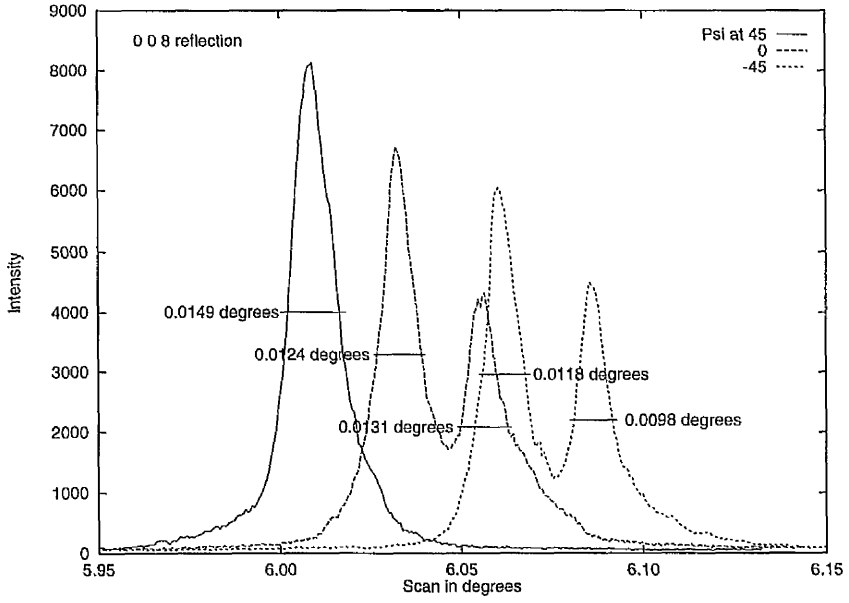

(a)

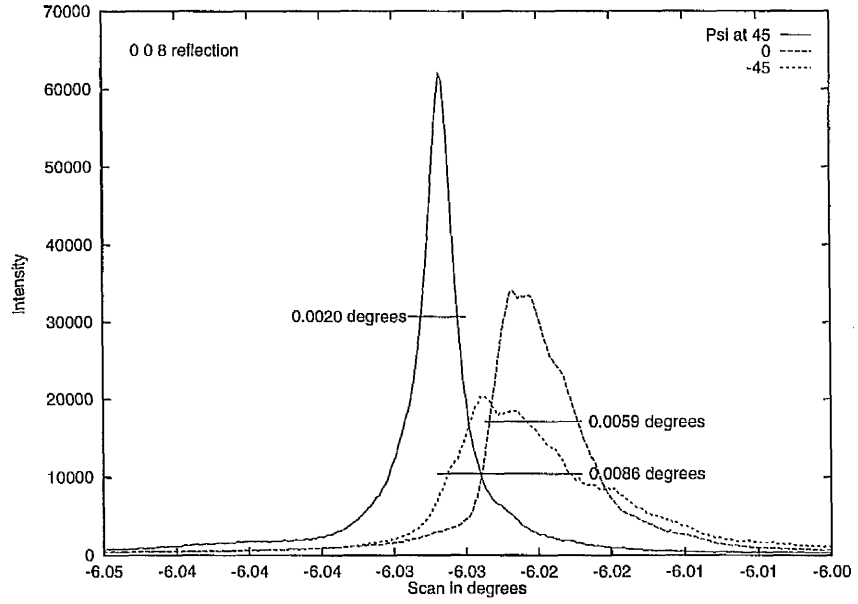

(b)

Figure 9.5: 0 0 8 crystal reflection, (a) earth grown, (b) space grown.

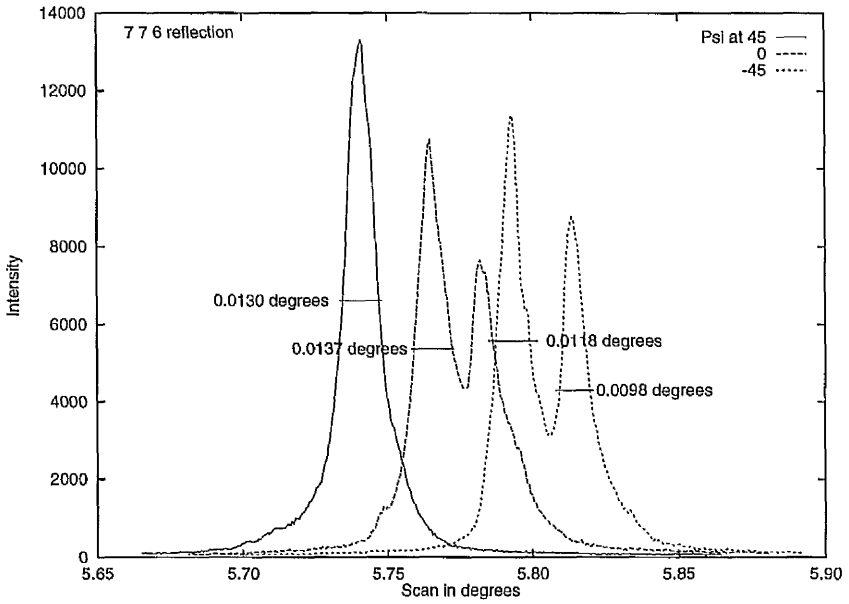

(a)

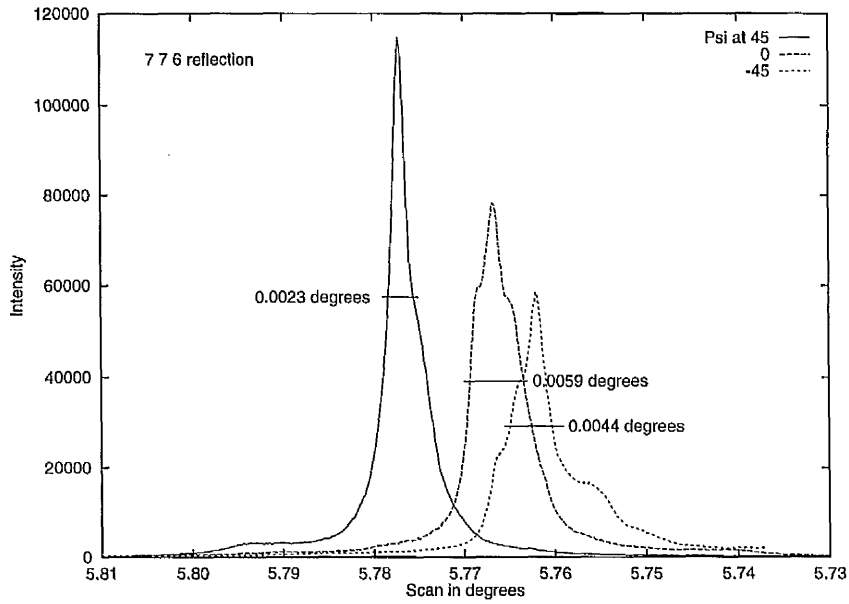

(b)

Figure 9.6: 7 7 6 crystal reflection, (a) earth grown, (b) space grown.

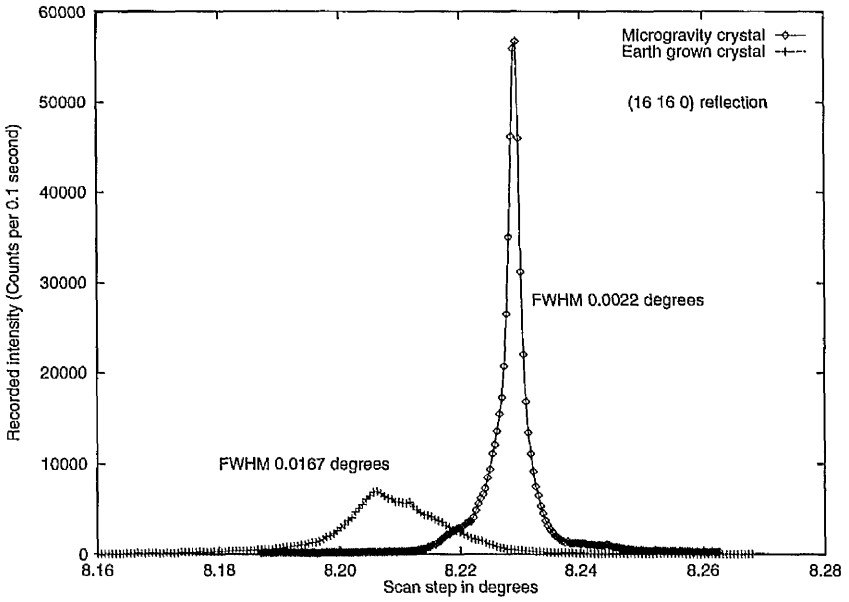

(a)

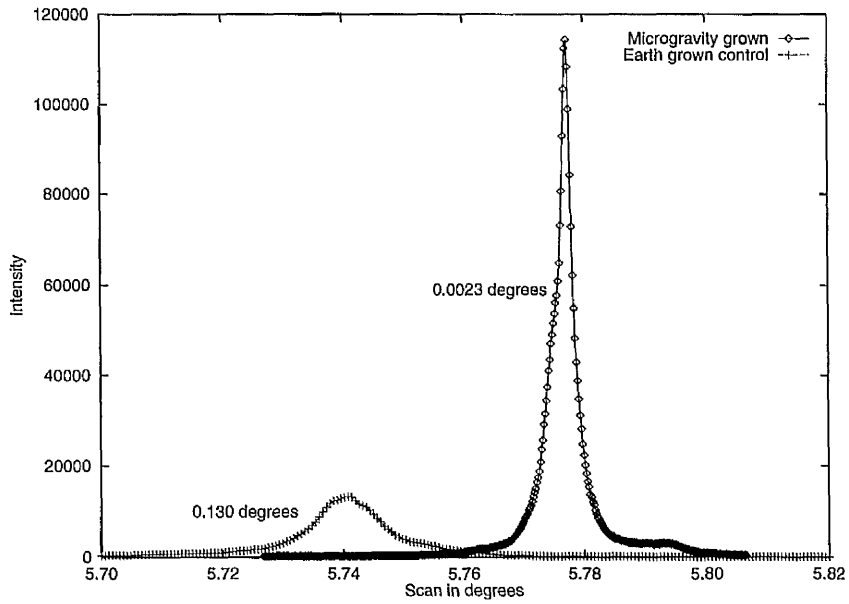

(b)

Figure 9.7: Typical intensities of microgravity and earth-grown reflections, (a) 16 16 0 and (b) 7 7 6

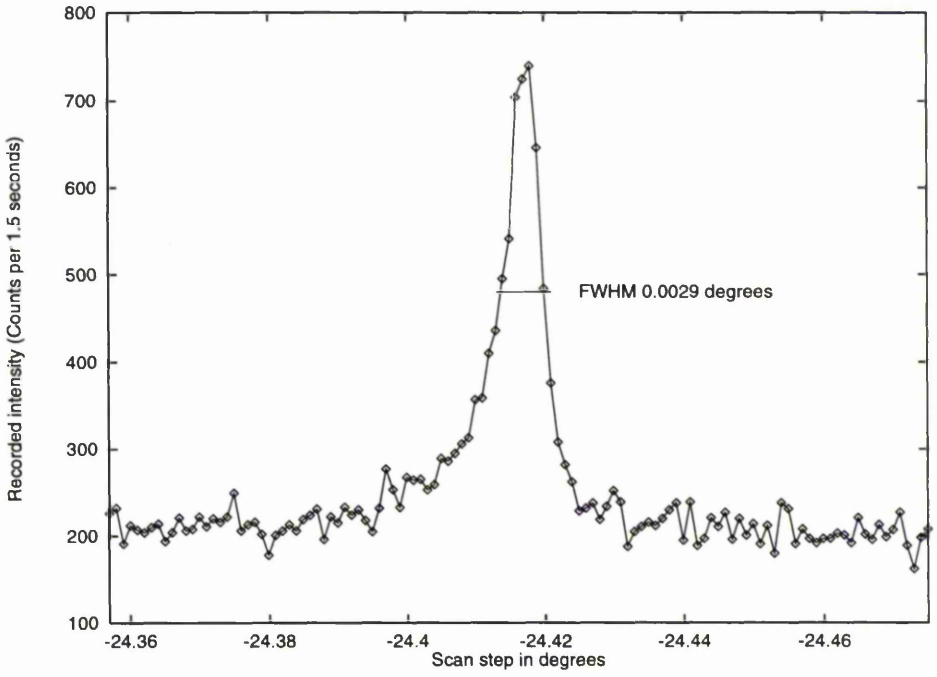

Figure 9.8: Reflection (32 57 0) recorded at 1.2Å resolution for a microgravity-grown crystal. The labelled full width at half maximum value has the instrument resolution function deconvoluted out

resolution enhancement (ie. to 1.2 Å and beyond) is promising and would be expected with consideration of the increased $I/\sigma(I)$ ratio obtained. This ultimately points to more detailed structural data being obtained from microgravity-grown crystals (than earth-grown crystals).

The precise measurement of perfection in this way is relatively new.[124, 64, 100] In our large IML-2 crystals there is indeed some evidence of more than one mosaic block comprising a "sample" in that the measured rocking widths are a good deal larger than for the smaller Spacehab-1 crystals (see also chapter 10). In the absence of diagnostic feedback control of the crystal growth process, the termination of the growth at a crystal size equal to one mosaic block cannot be

judged at all. Even with more feedback diagnostics it may be well-nigh impossible to terminate crystal growth as a process (once started) ie. without mounting the crystal in space ! Nevertheless feedback control, eg. by laser light scattering to monitor the nucleation stage and interferometry (eg. Snell *et al.*[220]) for the ensuing stages, should clearly allow more insight into the microgravity and earth-grown crystal growth process. It is not inconceivable that, on earth, procedures might be routinely developed where more perfect crystals could be grown so as to match the standard set by the microgravity grown crystals. It must also be the case that essentially perfect crystals do grow for some or even a large part of the time on earth. Indeed the evidence of regular vapour diffusion earth-grown lysozyme crystals, referred to on page 204, would seem to substantiate this with approximately 1 in 40 crystals displaying much improved diffraction over the rest.[244]

9.5 Summary of Main Findings

Rocking width measurements on the microgravity-grown crystals demonstrated an improvement over the earth-grown control case, 0.0019° and 0.0067° at minimum respectively. The reduced rocking width led to an increase in the peak height of reflections improving the signal to noise ratio for microgravity-grown crystals. This led to a weak high resolution reflection (1.2 Å) being observable in the microgravity-grown case but not in the ground-control case.

Chapter 10

Mosaic Block Structure of Microgravity-Grown Crystals and X-ray Topography Studies

10.1 Introduction

X-ray topography involves illumination of a crystal with either a monochromatic or polychromatic source with detection of the diffraction pattern on a high resolution detector. For the work described in this chapter the Lang transmission technique[149, 150] (stationary crystal, stationary film and monochromatic incident wavelength) is used. A review of this technique and other topographic techniques, including the use of the Laue method,[112] is given by Tanner, 1976.[233] The Lang technique produces so-called section topographs which are suited to resolving individual dislocations in less than perfect crystals.[79] The resulting reflection topographs produced are direct images of the whole crystal and show varying contrast throughout a crystal in each spot. Two types of contrast occur, namely

orientation and extinction contrast. Orientation contrast results from the misalignment between different perfectly diffracting regions (blocks) of the crystal - one region (block) perfectly aligned will produce a higher intensity diffraction than the other, misorientated region at any one angular setting of a crystal. Extinction contrast arises from distortions of the crystal lattice around a defect giving rise to different diffraction conditions from those in the surrounding lattice of the crystal. Topographs are also very sensitive to crystal surface damage, stresses and other internal defects.

10.2 Experimental

Lysozyme crystals from the IML-2 mission, described in chapter 8, were mounted in quartz capillaries for topographic examination. The crystals again presented problems during mounting due to their large size in that capillary action and suction were ineffective and a small mechanical force had to be applied to the edge of the crystal. Experiments with two microgravity-grown crystals and one earth-grown ground control are described in this chapter. Crystal size was 1.1 × 0.9 × 0.9 mm^3 for the first microgravity-grown and 1.5 × 1.1 × 1.1 mm^3 for the second microgravity-grown crystal. They were each mounted in quartz capillaries of diameter 2.0 mm. A ground control crystal, size 1.1 × 0.9 × 0.9 mm^3, was mounted in a capillary of diameter 2.0 mm.

The recording of the topographs took place at the Brookhaven National Synchrotron Light Source (NSLS) on beamline X-26C in conjunction with Dr. Vivian Stojanoff there (as resident topographic specialist). A monochromatic 1 Å wavelength beam and Si (111) monochromator (at an angle of 9.17°) were used with a

source to instrument distance of 19.5 m. For each crystal a preliminary exposure was taken on an X-ray sensitive Polaroid (exposure time 600 seconds, crystal to film distance of 7.5 cm) to determine that a number of diffraction spots would be visible on the main topograph exposure, and to verify the crystal diffraction power. The topograph exposure was then made onto high resolution X-ray sensitive film (Kodak - Industrex film SR5) (exposure time 2000 seconds, crystal to film distance of 10.0 cm). The process was repeated with the crystal rotated around the spindle axis by 90°.

Dense packing of the grains in the film means that as uniform as possible development must be carried out (6 minutes in 1:1 Kodak D19 developer) with precise temperatures, deionized water and fresh solutions. The topograph, each consisting of a single diffraction spot, is recorded at a magnification of unity and later enlarged optically for viewing and photographic recording; this is then the topograph for each *hkl* reflection.

10.3 Results

Only initial qualitative assessment of the crystals have been made so far, owing to the experiments having taken place very recently but the results even at this stage are very interesting and worth recording here.

Figure 10.1 shows topographs from the first migrogravity-grown crystal for two different reflections recorded on the same exposure.

Contrast is visible in approximately one half of the crystal whereas for the other

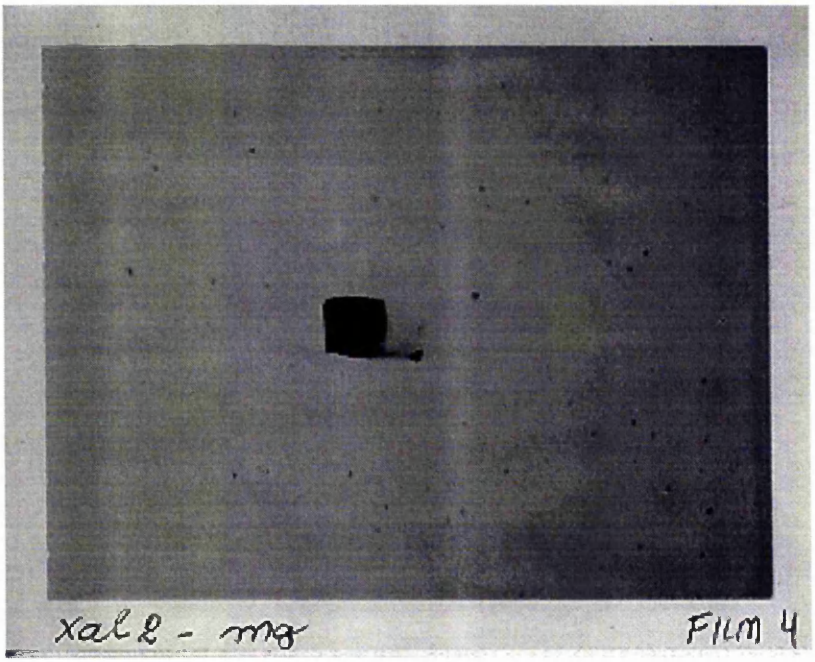

(a)

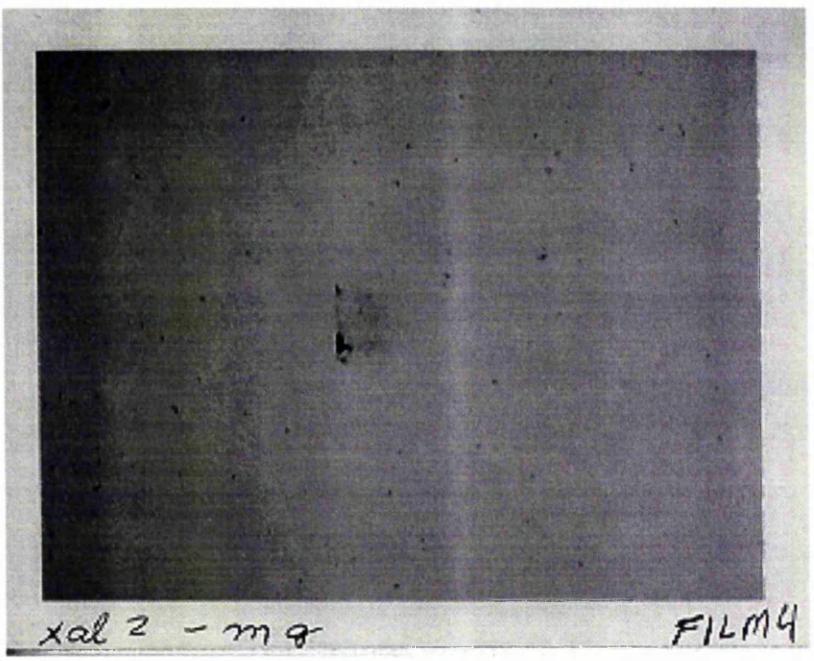

(b)

Figure 10.1: X-ray topograph recorded from a microgravity-grown lysozyme crystal for two different reflections. Crystal dimensions 1.1×0.9 mm^2 (in projection)

reflection, figure 10.1(b) this contrast is not visible. The contrast seen in figure 10.1(a) occurs in a plane and is likely to be caused by a mosaic block boundary. Noticeable in the corner of the topograph is contrast which is probably due to damage caused by the use of some mechanical force for mounting the crystal. The crystal was mounted in a circular capillary but there does not appear to be any "continuous" stress caused within the crystal due to interaction of flat faces with the capillary.

In a topograph from the second microgravity-grown crystal, figure 10.2, several mosaic blocks can be visualised along with what looks like extensive damage to one edge of the crystal.

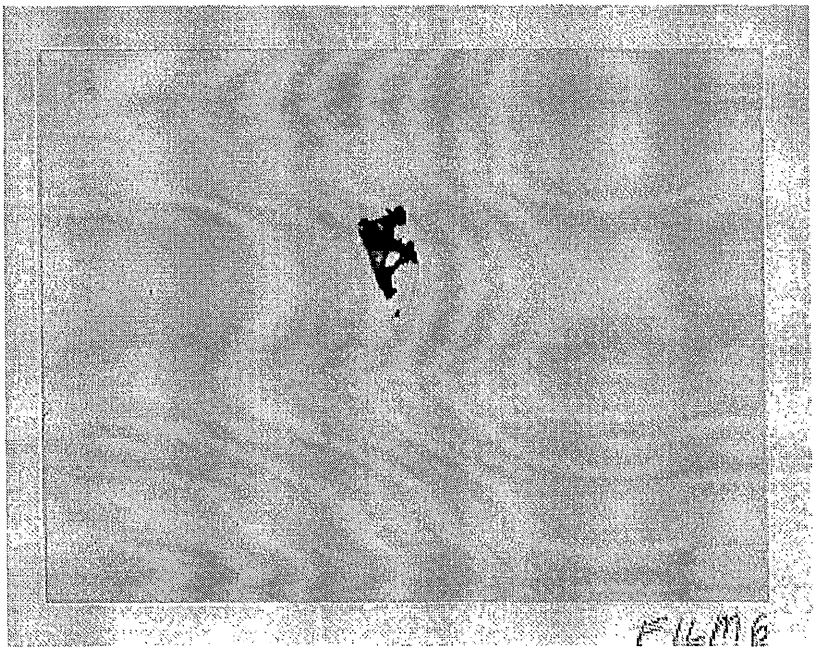

Figure 10.2: X-ray topograph recorded from a microgravity grown lysozyme crystal. Crystal size 1.5×1.1 mm^2. Five mosaic blocks are visible of size, then, of $\approx$ 0.5×0.3 mm^2 cross sectional area

The topograph, figure 10.2 , shows five "perfect" regions (mosaic blocks), approximate area 0.5 × 0.3 m^2, with grain boundaries making up the one individual crystal.

The topographs from the ground control crystal, figure 10.3, show a high density of defects along the whole crystal rather than individual blocks. It appears to be 'crumbly' in nature rather than showing the definite block structure seen, especially in figure 10.2.

10.4 Extinction Effects

The intensities measured in X-ray diffraction are related to their respective structure factors by a kinematical approximation. This makes the assumption that the incident wave is not affected apart from the results of simple diffraction by its passage through the crystal. Effects that are not considered are energy transfer within the crystal and destructive interference caused from diffracted waves. Both these effects are termed extinction. X-ray diffraction is properly described by dynamical theory. The dynamical theory leads to the kinematical approximation in the limit of thin or non-absorbing crystals. This can be expressed in terms of the extinction length[20] Λ, given by

$$\Lambda = \frac{V}{(aC)} \frac{1}{|F_H|\lambda} \tag{10.1}$$

where V is the volume of the unit cell, a is the classical radius of the electron, F_H the structure factor and C a polarisation factor. For a crystal with thickness

(a)

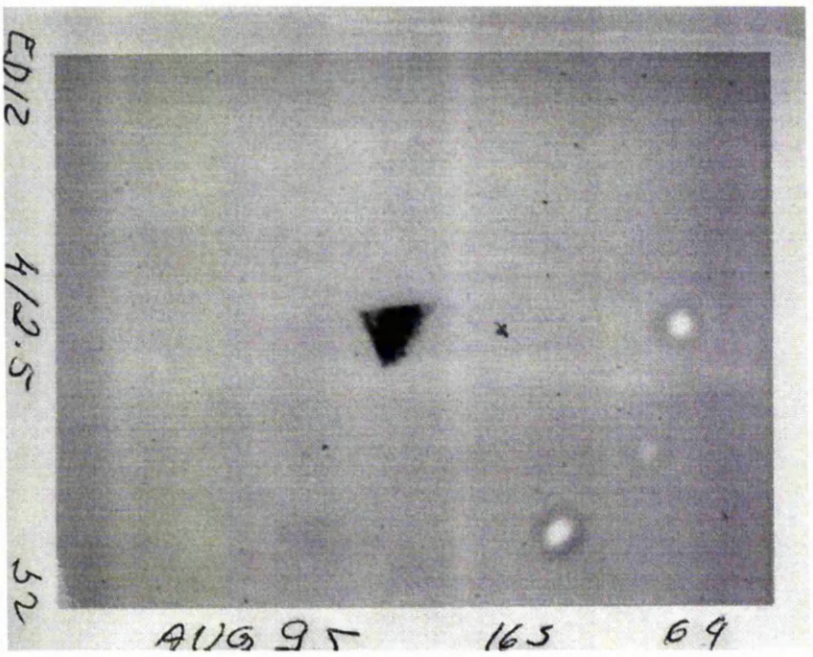

(b)

Figure 10.3: X-ray topograph recorded from an earth-grown lysozyme crystal at two different reflections. Crystal dimensions 1.1×0.9 mm^2 (in projection)

t for the perfect part;

- if $t << \Lambda$ the kinematical approximation is valid (even for a perfect crystal)
- if $t >> \Lambda$ the dynamical effects need to be considered
- if $t \approx \Lambda$ then both kinematical and dynamic effects are seen

Fourme *et al.*[100] have calculated, from equation 10.1 with C=1 and $\lambda = 0.9$ Å, the minimum extinction distance for lysozyme as 500 μm. In the case of the microgravity-grown crystals seen here then $t \approx \Lambda$ and dynamical effects need to be considered.

Primary and Secondary Extinction

The extinction due to dynamical effects, as previously stated, occurs in two ways termed primary and secondary extinction. Primary extinction occurs due to destructive interference with the incident and reflected beam. At the Bragg angle every incident wave can suffer multiple reflections from different lattice planes. After an odd number of reflections the direction will be the same as the diffracted beam, after an even number the same as the incident beam. Each scattering causes a phase lag of $\pi/2$ thus the un-scattered radiation is joined by doubly scattered radiation (with much reduced intensity) with a phase lag of π. Consequently destructive interference occurs. The same result occurs along the direction of the incident beam. The net result is that both incident and diffracted beams are weakened because of dynamical effects.

Energy transfer within the crystals is treated with secondary extinction. The

lattice planes first encountered by the incident beam will diffract a significant fraction of the primary intensity so that deeper planes receive less incident beam. This causes a weakening of the diffracted intensity mainly observable for high intensity low resolution reflections. Secondary extinction is equivalent to an increase in the linear absorption coefficient (negligible for small crystals) and can be corrected for in data processing.

Perfect and Imperfect Crystals

Crystals used for X-ray diffraction can be described as lying between two extremes, ideally perfect and ideally imperfect.

An ideally imperfect or "mosaic" crystal is built up of a large number of (small) blocks which are slightly misorientated with respect to each other. Each block is in itself perfect but so small that its integrated intensity is proportional to its volume (ie. extinction effects too small to be noticed). An incident X-ray beam onto such a mosaic crystal will penetrate deeply before it reaches an identical orientation mosaic block. In this case the interference effects of primary extinction become so negligible they are not observed. In an ideally imperfect crystal the blocks are so small and their disorientation so large that the amount of energy lost by reflection is negligible compared with that lost by absorption, secondary extinction is not seen.

In a perfect crystal the dynamical equations show that energy is, in fact, diverted into the reflected beam but at the same time the angular range of the reflection becomes exceedingly small. If extinction is large (ie. $t >> \Lambda$ there is a resultant decrease in the integrated intensity observed by routine data collection methods.[58]

However, if $t \leq \Lambda$ then extinction will not be a problem *and* the unit cells all line up perfectly to give the strongest possible peak height above background (*cf.* undulator magnet shimming !).

Monitoring Extinction Effects

Extinction effects can be monitored by various methods which will be described. Extinction increases with increasing wavelength[58];

$$I_{obs} = I_{corr}\left[1 - \left(P^2 + \frac{S^2}{\mu}\right) C\lambda^2\right] \tag{10.2}$$

where I_{obs} is the observed intensity, I_{corr} the corrected intensity, C the polarisation factor, λ the wavelength and P and S constants for primary and secondary extinction respectively. The linear absorption coefficient μ varies with λ^3 between absorption edges. With decreasing wavelength, absorption decreases and scattering efficiency decreases - *both* push toward the weak scattering limit, ie. kinematical approximation. Data collection at two or more wavelengths will show up the extinction effects. Initial refinement of the data excluding the strong low resolution F_{obs} then later comparison with those F_{obs} and matching F_{calc} will reveal any systematic extinction tendency.

10.5 Discussion

X-ray topography is a non-destructive method for revealing strains and internal (defect) structure in nearly perfect crystals. It has been used extensively in the

analysis of inorganic crystals[16, 88, 105, 139, 145] and has a good sensitivity to small distortions and variations of the lattice. This (as far as we are aware) is the first time mosaic blocks have been visualised within a protein crystal.

The size of the mosaic blocks is such that extinction effects become apparent and should be monitored. In this case the thickness of the perfect region, t, appears to be approximately that of the extinction length, Λ (from equation 10.1). This results in reflections at low resolution (strong intensity) which display extinction effects and higher resolution (weaker reflections) for which the kinematical approximation is valid. The higher resolution reflections can be used without any further corrections.

X-ray topography has shown the defects due to handling and thereby reveals flaws in the crystal mounting techniques. Probably the best way to solve this handling problem for X-ray topographic analysis is to grow the crystals in individual chambers that could be taken to an X-ray station for inspection with out crystal mounting being required. One can argue that the absorption caused by the mother liquor would be detrimental to an X-ray inspection but the effect on X-ray topographic images essentially translates to a simple need for a longer exposure.[227]

Atomic force microscope studies of lysozyme crystals[82, 83] have not produced evidence of the mosaic block structure but this is not surprising since the scanned area seems to be limited to 30 μm^2 or so.[161] Electron microscope studies of lysozyme[85] have also shown no evidence of the mosaic block structure, again though the area scanned is small, 2 μm^2 or so. In the electron microscope study micrographs of the interior of the lysozyme crystal were obtained by fracturing

the crystal through freezing at -110 °C. It is interesting to wonder if evidence of the increase in mosaic block misorientation or decrease in mosaic block size (through splitting etc.) on freezing could be investigated through X-ray topography or more simply can we use topography to see defects/block structure (if any is left) on freezing a protein crystal ?

10.6 Summary

The microgravity-grown crystals demonstrate large visible mosaic blocks. Dynamical effects (extinction) should become appreciable when the perfect mosaic block size approaches this value.[100] The microgravity-grown crystals should clearly start to demonstrate extinction effects by consideration of the mosaic block size seen and this will have to be taken into account in the use of intensity data (eg. in protein model refinement). The earth-grown control crystal, in contrast, appears to consist not of large individual blocks but many defect lines giving the crystal a rather 'crumbly' appearance.

X-ray topography of protein crystals is clearly a useful technique expanding the array of diagnostic methods for the study of protein crystals grown by all methods which can therefore be harnessed to produce better protein crystals for crystal structure analysis.

Chapter 11

Interferometer Concentration Measurements

11.1 Introduction

Mapping of solution properties during the growth of crystals can include mapping of convection and/or solution temperature, diffusion and concentration.[214] In microgravity dialysis growth techniques (as described in chapter 8) there is no convection (excepting Marangoni convection in the vapour diffusion case) so diffusion and concentration become the prime measurements of interest. Optical techniques do not perceptibly affect the solution being studied and can map its properties with a spatial resolution of less than a micrometre and temporal resolution of less than a millisecond. The parameter actually measured may be either, refractive index or relative phase changes, displacements, velocity components and variations in the solution by optical absorption. Measurements of these properties where possible with non-optical probes eg. thermistors, pH/ion electrodes etc. impinge on the crystallization process and give inadequate data points.

Refractive index methods are all based on the fact that the spatial distribution of the refractive index of the solution affects both the curvature and optical path lengths of each ray of light. Refractive index variation can be mapped with Schlieren optics, interferometry or holographic techniques. Displacement measurement involves time lapse observation by conventional (video, photographic) imaging techniques or by laser techniques with visible marks in the solution. Growth of crystals can be easily mapped but convection measurements cannot readily be made. Velocity components in the solution can be measured directly with laser Doppler anemometry where the velocity of the particle is determined by measuring the beat frequency of light scattered from the particle with light from a reference beam. Although it has been sufficiently refined as to be capable of detecting flow velocities as low as a few microns per second it does however require elaborate and expensive apparatus and the necessity of adding light scattering particles to the solution. Concentration mapping by absorption is inherently less sensitive than other optical techniques.

The most promising techniques for imaging and measuring diffusion and concentration around a growing protein crystal appear to be Schlieren optics and interferometry. A Mach-Zehnder interferometer has been constructed by Dornier and implemented into the engineering model of the APCF. A review of interferometry can be found in Francon, 1966[101] and Steel, 1983.[224] The Mach-Zehnder interferometer as a diagnostic tool was primarily chosen because it is compact and could be easily and simply implemented into the existing APCF (and with minor modification phase shifting can be incorporated to improve its sensitivity at a later date - to be discussed below).

As a result of the successful IML-2 mission, ground trials were performed with

the APCF engineering model and Mach-Zehnder interferometer, using identical solutions to the IML-2 mission, to asses its use as a diagnostic tool. It is ultimately planned to fit this facility to the microgravity flight models of the APCF.

11.2 Equipment

The Mach-Zehnder interferometer, shown in figure 11.1 with schematic in figure 11.2, consists of two beam splitters and two totally reflecting mirrors. A 780 nm (near infrared) laser diode (chosen for its stability) is used as the light source with CCD video camera as detector.

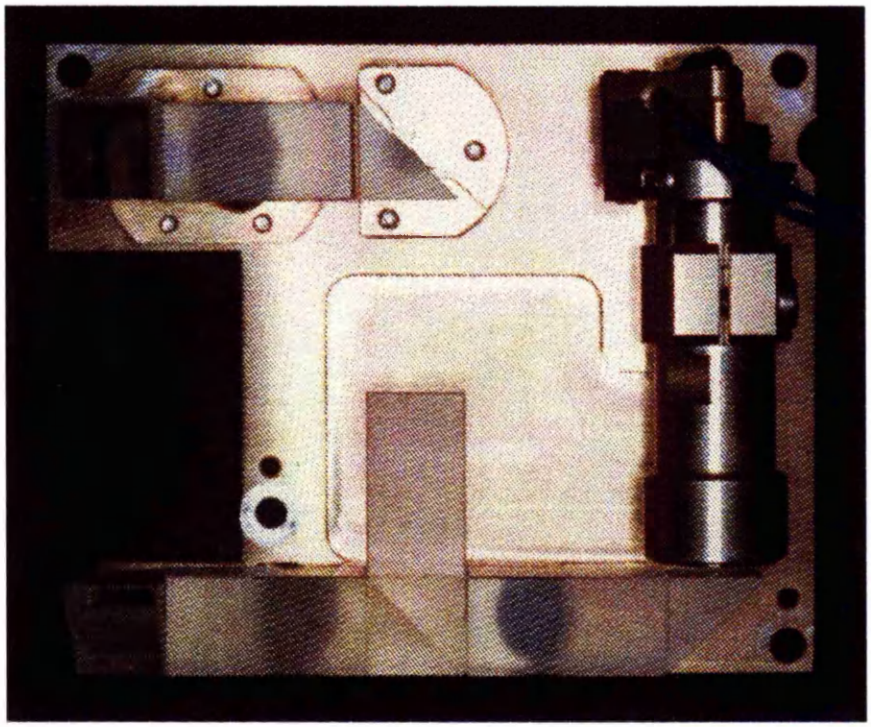

Figure 11.1: Photograph of the Mach-Zehnder interferometer (that has been installed in the engineering model of the APCF) showing clearly the laser, light path, beam splitters and mirrors

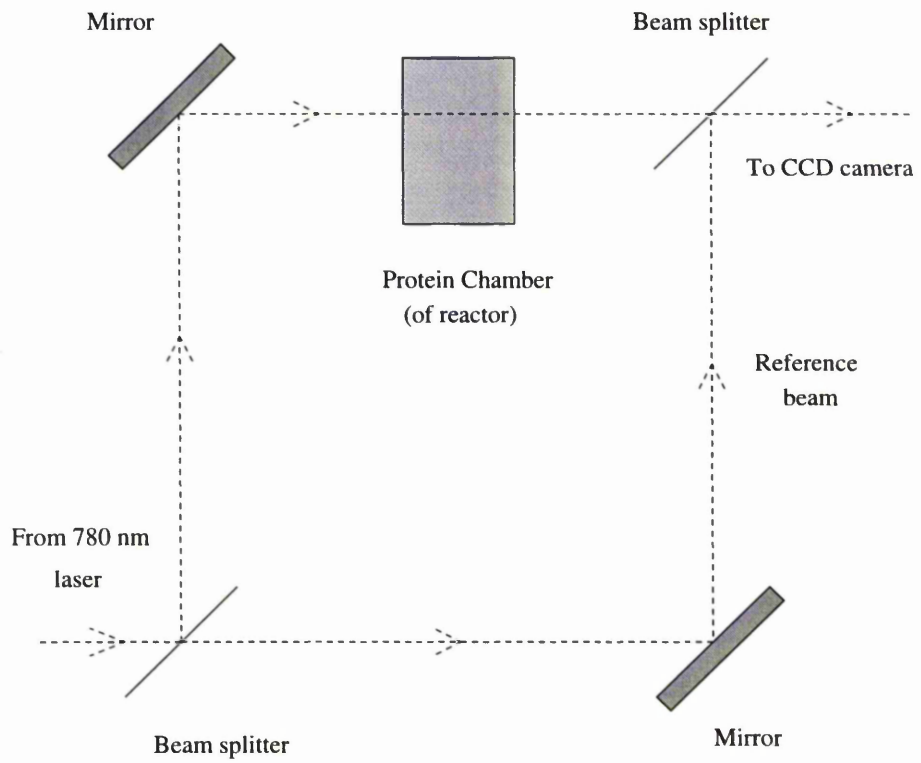

Figure 11.2: Schematic diagram of the Mach-Zehnder interferometer

The two beams travel within the apparatus along separate paths. The reactor is inserted in one path and the resulting interference with the reference path produces fringes. As the diffusion process (of salt into the reactor) carries on there is a change in the concentration of the solution in the reactor and a corresponding change in refractive index. As the protein crystals form the overall protein concentration in solution is reduced. Again there is a change in refractive index. Consequently there is a motion of fringes as diffusion and crystallisation takes place. The optical paths of the interferometer are constructed from quartz glass, the same material that makes up the crystallization reactor. This also induces a certain ruggedness into the system as concerns have been raised that optics, especially interferometry, will not be robust enough against the mechanical shock

and vibration associated with space launches.[237] A small air gap occurs in the measuring beam as the interferometer is mounted so it can move from reactor to reactor with the CCD camera. There is a corresponding air gap in the reference path to take account of this.

11.3 Theory

The two light paths are of identical length with one light path travelling through the protein chamber of the reactor. The phase difference between the two light paths δ is given by;

$$\delta = \frac{2\pi}{\lambda} nd \tag{11.1}$$

where n is the refractive index of the solution in the protein chamber, λ the incident wavelength and d the path length of light through the chamber. For the destructive interference (an increase in the grey to black level on the CCD image, termed a dark fringe) the phase difference between two peaks has to be equal to π, therefore, from equation 11.1 , a dark fringe is formed when;

$$(m)\frac{\lambda}{d} = n_m \tag{11.2}$$

where m is any integer number. As the refractive index of the solution changes more fringes will be produced, in the case of $m + 1$;

$$(m+1)\frac{\lambda}{d} = n_{m+1} \tag{11.3}$$

where n_m and n_{m+1} are the refractive indexes causing two adjacent dark fringes. The change in refractive index between each dark fringe, $\Delta n = (n_{m+1} - n_m)$, or peak to peak sensitivity of the instrument is given from equations 11.2 and 11.3;

$$\Delta n = \frac{\lambda}{d} \tag{11.4}$$

To relate the Δn value to concentration it is necessary to calibrate the interferometer by measurement of the refractive indexes of the separate solutions involved, in this case, water, buffer, salt solution and the initial protein solution.

11.4 Calibration

The refractive index of water is known at various wavelengths, temperatures and pressures. Using a Brice-Phoenix differential refractometer,[42] with water as the initial reference solution, the refractive indices of buffer, salt solution and protein solution were measured at 436 nm (blue) and 546 nm (green) wavelengths. The differential refractometer measures the precise refractive index difference between a dilute solution and its solvent.

Overall precise temperature control is not needed since the temperature coefficient of the difference in refractive index between a solution and its solvent is much smaller than that for the refractive index of solution or solvent alone. However the solution and solvent being measured must have the same temperature to

0.01 °C or better. In order to achieve the same temperature a sinter fused glass cell divided into two compartments, with a thin, 1.2 mm glass partition, is used to hold the solution and solvent. The dividing glass partition is thin enough to allow thermal equilibration. The standard cell is suited for refractive index measurements up to 1.62 and for determination of refractive index differences up to 0.01 units with a sensitivity of ± 0.000003 units.

The monochromatic light beam after passing through a semi transparent mirror and a vertical slit enters incident to the normal of the first surface of the differential refractometer cell. The light beam emerging from the cell is deviated through an angle proportional to the refractive index difference between the two liquid media. The deviation is measured through a microscope with attached micrometer eyepiece.

Before measurements can be made the instrument itself has to be calibrated using a solution that has a known refractive index difference between its solvent (in this case KCl solution and distilled water). Deviation readings are made with the cell, filled with solvent, incident to the light beam (d_1) and then rotated 180°, (d_2). A similar procedure is repeated for the solution in one chamber of the cell and solvent in the other, (d_1' and d_2'). The values are averaged and the total deviation calculated from;

$$\Delta d = (d_2 - d_1) - (d_2' - d_1') \tag{11.5}$$

The refractive index difference is then given by;

$$\Delta n = k\Delta d \tag{11.6}$$

Where Δn is the known refractive index difference between solution and solvent and k is the required calibration constant for the incident wavelength. Once the calibration constant is determined any angular deviation of the light beam (at the calibrated wavelength) may be directly converted to a refractive index difference.

The k value for a given wavelength is inversely proportional to the magnification at that wavelength of the optical system of the instrument. It can be calculated for different wavelengths with magnification constants given, by the manufacturer, for that particular instrument. For all measurements the light source must be warmed up and allowed to stabilise for reproducibility in measurement.

The refractive index differences between water and buffer, buffer and salt and salt and protein were found for wavelengths of 546 nm and 436 nm as shown in table 11.1.

Solution	Δn_{546}	Δn_{436}
buffer - water	0.00066	0.00091
salt - buffer	0.00969	0.01218
protein - salt	0.00390	0.00420

Table 11.1: Refractive index differences of solutions

The refractive index of water at 20° C is known at 546 and 436 nm as 1.3343 and 1.3402 respectively. From this and the refractive index differences the refractive indices of buffer, initial salt and initial protein solutions can be calculated.

The Mach-Zehnder interferometer uses a wavelength of 780 nm and so consequently the refractive indices have to be converted to this wavelength by use of

the first two terms of the Cauchy formula;

$$n = A + \frac{B}{\lambda^2} + \ldots \tag{11.7}$$

A and B are constants for a particular solution, the refractive index at 780nm (infra-red) is calculated and shown in table 11.2.

Solution	n_{546}	n_{436}	A	B	n_{780}
Water	1.3343	1.3402	1.32386	3113.54	1.3290
Buffer	1.3350	1.3411	1.32424	3204.22	1.3295
Salt	1.3447	1.3533	1.32959	4507.04	1.3370
Protein	1.3486	1.3575	1.33294	4669.76	1.3406

Table 11.2: Refractive indices of solutions

Knowing these values enables the refractive index increments measured by use of the interferometer during the experiment to be related to the actual concentrations of the various solutions. The effect on refractive indices of different wavelengths is well illustrated by a plot of the Cauchy formula for the differing solutions over a wavelength range of interest, figure 11.3.

11.5 Experimental

The lysozyme used for this trial utilised the recipe from the previous STS-65 mission. In line with the microgravity experiment the protein chamber had also been treated with a siliconisation solution (Sigmacote) for a period of ten minutes. The reactor (APCF dialysis 188 μl) once filled was kept at a constant temperature

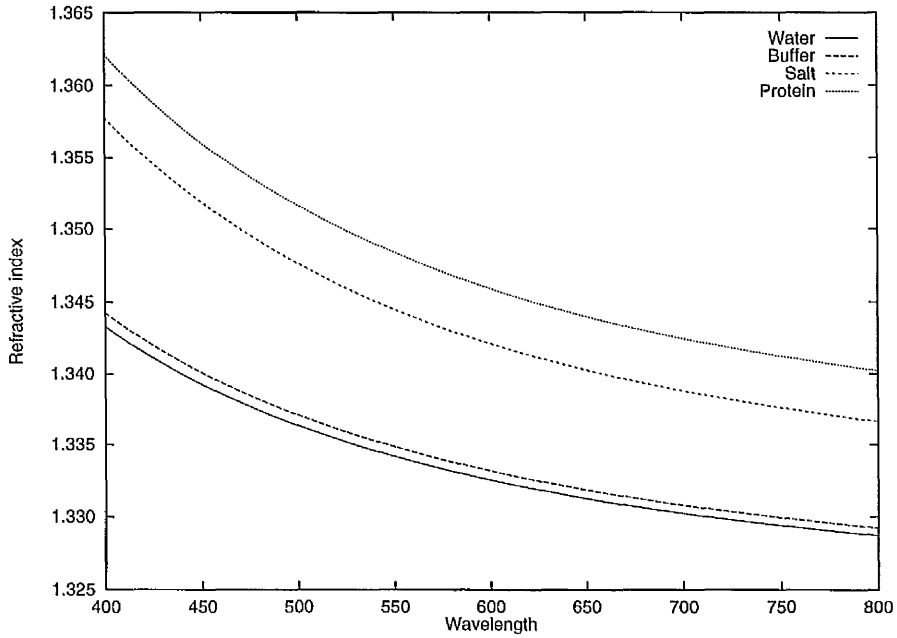

Figure 11.3: Plot of the Cauchy function for water, buffer, salt and protein solutions over a wavelength range, 400 nm to 800 nm

of 20° ±0.1°C for preprocess and during crystallization.

By making use of the CCD video camera already installed in the APCF, a Mach-Zehnder interferometer has been accommodated in the engineering model of the APCF such that 5 of the normal 2 × 6 observed reactors can make use of it. The reactor was inserted into the engineering model and the system initiated to perform an experiment according to flight conditions. The facility was orientated such that the reactor was in the vertical position with the protein reservoir on top so that diffusion works against gravity - previous experiments by the Dornier staff have shown that the diffusion process is lease turbulent in this orientation. A total of 1292 digitised fringe images were recorded on tape. An example of an image illustrating the measuring window used and the location of the dialysis

membrane is shown in figure 11.4.

The image, figure 11.4, depicts the reactor in the vertical orientation (as seen in figure 8.1 on page 169) with the protein chamber visible showing fringes in the upper part of the image. The dialysis membrane is directly below the fringes. The dialysis membrane is flat, the two peaks that impinge into the protein chamber above it are caused by the corners of the cuboid protein chamber pressing against a circular silicon seal. Just visible at the bottom of the image are fringes caused by diffusion of salt into the protein chamber. These fringes (caused by salt diffusion only and having no component to do with the protein solution) can provide a way to separate the refractive index change due to protein leaving the solution and salt diffusing in. The horizontal fringes move in a vertical direction. When the reactor is orientated differently the fringe motion is very turbulent. Without the diffusion membrane, ie. free interface diffusion, the process, even in the ideal (vertical) orientation the process is still very turbulent (previous experiment by Dornier staff).

As an extension to the flight configuration the CCD images were also recorded by time lapse video and analysed in real time via an attached PC. The OPTIMAS image processing software was configured to define a window on the image, and measure the average grey level within that window. It is possible to measure several windows at once. The window size and position can be varied but in this case a size of approximately 1.10 $\times$ 0.28 cm was used with the long axis of the measuring window being parallel to the diffusion membrane positioned as shown in figure 11.4.

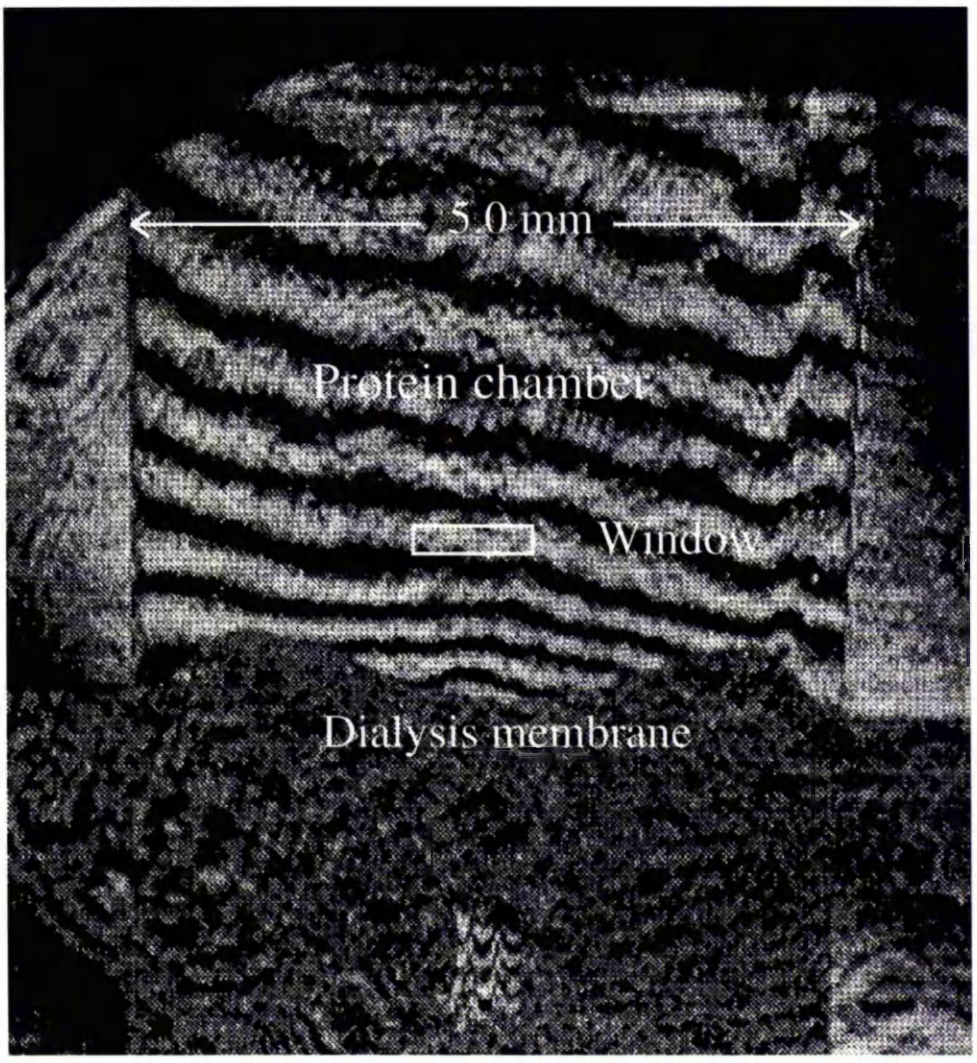

Figure 11.4: Example of fringes (dark bands seen within the protein chamber and barely visible below the dialysis membrane) recorded by the video camera with wide field of view optics. The measuring window used for the experiment is shown as a white box. The fringe motion is from the dialysis membrane in a vertical orientation toward the top of the reactor reversing after the 40 hour point. The width of the protein chamber is 5.0 mm, visible height is 2.8 mm.

11.6 Results

Figures 11.5 and 11.6 show the interferometer images recorded by the CCD camera between the times of 00:06 hours and 42:12 hours. The initial image, figure 11.5(a), shows the protein chamber before the diffusion process has started (the protein and salt solutions have only just been brought into contact). The Mach-Zehnder interferometer has been adjusted such that a minimum number of fringes are seen at the start of the experiment. Figure 11.5(b) at 00:42 hours shows the salt solution diffusing into the protein chamber with closely spaced fringes appearing above the dialysis membrane moving in a vertical direction, upwards. By 01:30 hours there are many closely spaced fringes visible within the protein chamber giving a maximum number of fringes visible at 02:29 hours (figures 11.6(c) and (d) respectively).

After time the diffusion process gradually starts to slow, figures 11.6(a) to (d) illustrate this. At 08:59 hours, figure 11.6(a), the number of fringes visible in the protein chamber has decreased and the fringe spatial separation increased. This trend is observed also at 14:00 hours and 23:59 hours, figures 11.6(b) and (c) respectively. The final image illustrated here at 42:11 hours, figure 11.6, shows the point where the salt diffusion appears to have stopped and the fringe pattern seen approaches that of the initial image, figure 11.5.

Of note, especially in figure 11.5(c) and (d), and figure 11.6(a) and (b), is turbulence visible in the right hand side of the protein chamber. This is possibly due to an irregularity in the silicon seal but has not yet been investigated.

By studying the time lapse video of the fringe motion it was noted that the initial

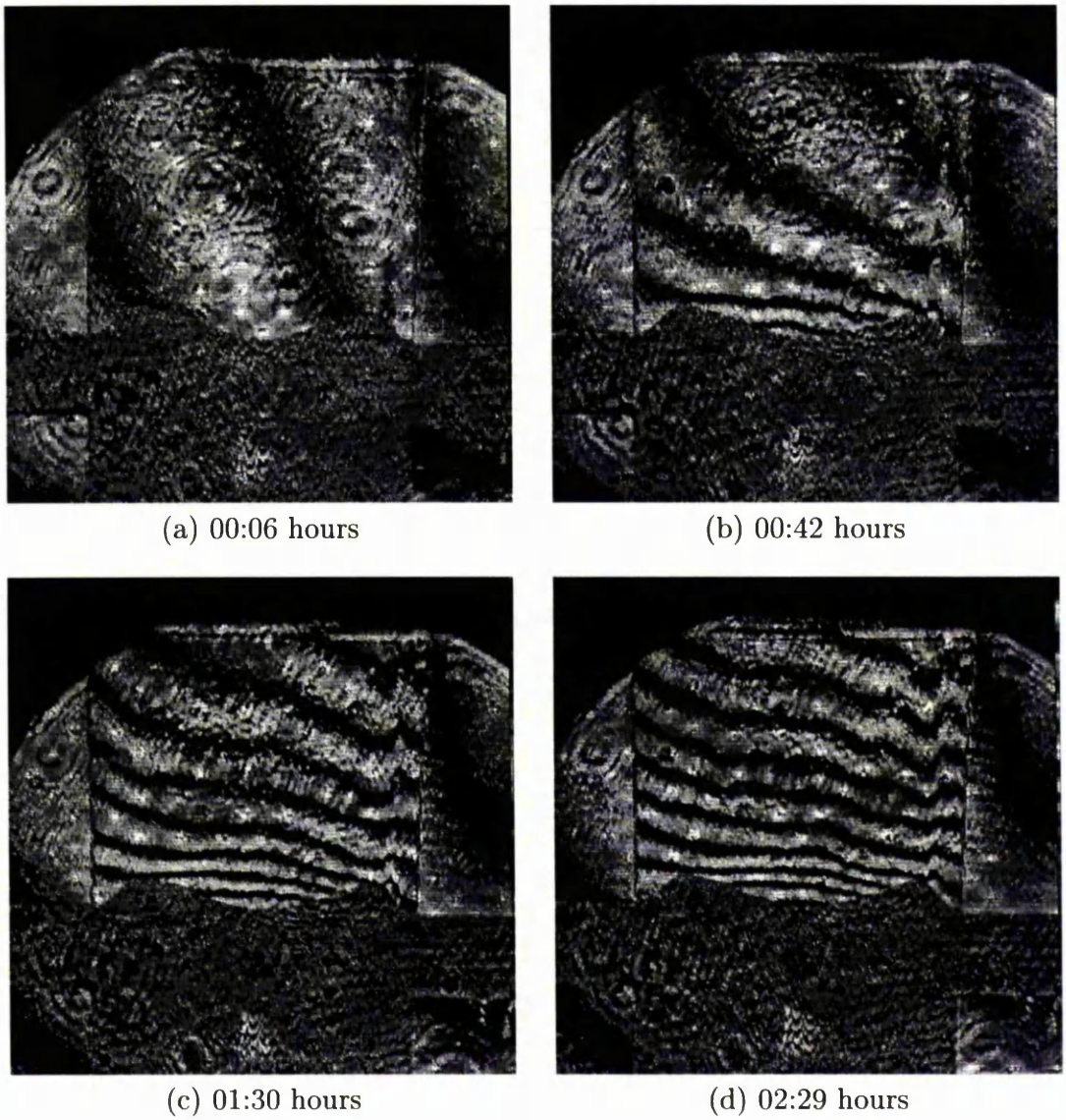

(a) 00:06 hours

(b) 00:42 hours

(c) 01:30 hours

(d) 02:29 hours

Figure 11.5: Images recorded from interferometer times equal to (a) 00:06 (b) 00:42 (c) 01:30 and (d) 02:29 hours

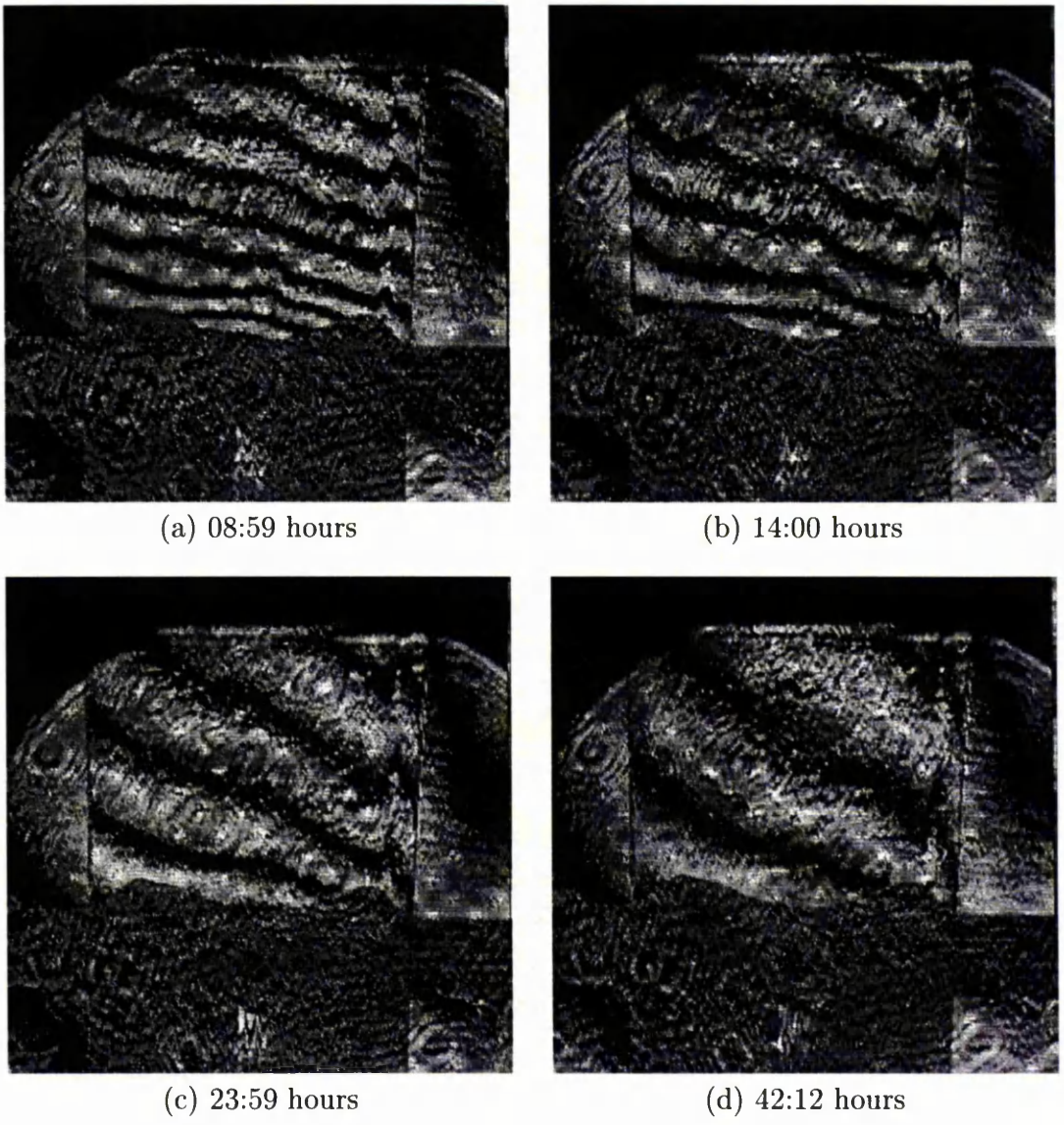

(a) 08:59 hours (b) 14:00 hours

(c) 23:59 hours (d) 42:12 hours

Figure 11.6: Images recorded from interferometer times equal to (a) 08:59 (b) 14:00 (c) 23:59 and (d) 42:12 hours

vertical upward motion of the fringes reverses at the 40 hour mark. The fringes start to move downwards. As each fringe crosses the sampling window a peak is observed in the grey level, figure 11.7. The ~~cumulative~~ number of peaks are plotted and totalled against time, figure 11.8 and shows the turning point in the gradient at the 40 hour mark.

The whole experiment was stopped after 162 hours. At this point an image of the protein volume was recorded with LED illumination, figure 11.9. Many crystals up to a length of 1.5 mm have grown, all located on the ~~the~~ membrane and silicon ring sealing the protein reservoir block to the rest of the reactor. This is due to the siliconisation process and the effects of gravity. In this case λ, the incident wavelength, is 780 nm and d, the light path through the protein chamber is 5 mm. Therefore, from equation 11.4, the change in refractive index between two adjacent fringes is given by 1.56×10^{-4}.

During the first forty hours of the experiment 35 peaks in the grey level were monitored corresponding to 35 fringes passing the sample window. From equation 11.4 this corresponds to a refractive index change in the protein chamber of 5.46×10^{-3}. A total of 52 peaks were monitored for the remainder of the experiment corresponding to a *decrease* in the refractive index of 8.11×10^{-3} after taking into account the reversal in direction of fringe motion.

At 780 nm the refractive index for 1.256 M NaCl solution (7.34 g per 100 ml) is $n_{salt} = 1.3370$. For every 1g per 100 ml the increment in refractive index is calculated as 1.09×10^{-3} $((n_{salt} - n_{water})/7.34)$. Therefore for the increment observed the salt concentration in the protein chamber reaches 5.01 g per 100 ml or 5.01% $(5.46 \times 10^{-3}/1.09 \times 10^{-3})$. Within the accuracy of the peak to peak

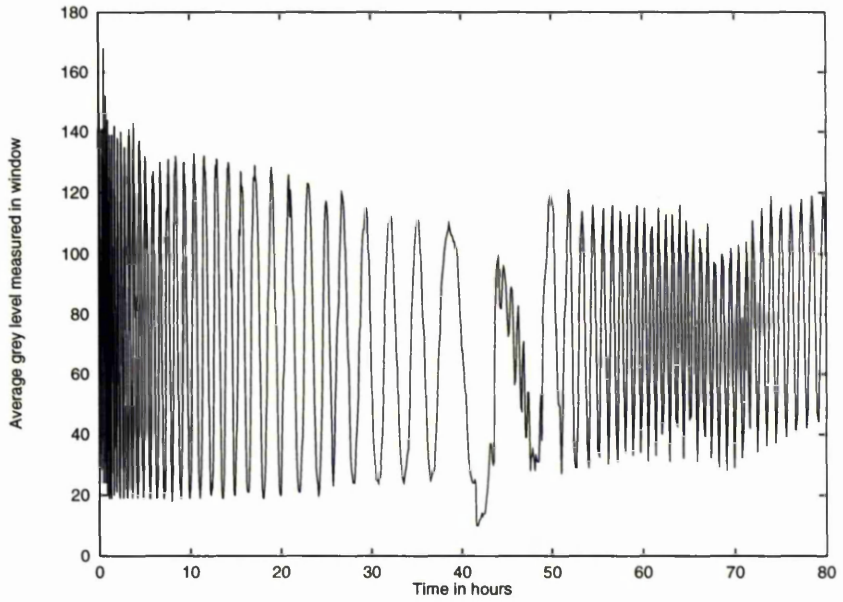

(a)

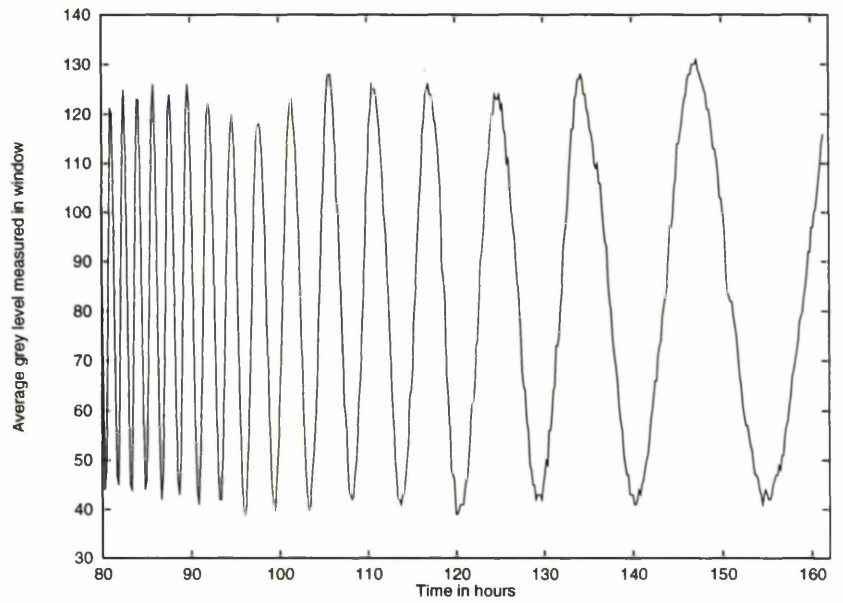

(b)

Figure 11.7: Plot of averaged grey level during experiment from (a) start till 80 hours and, (b) 80 hours till completion at 162 hours.

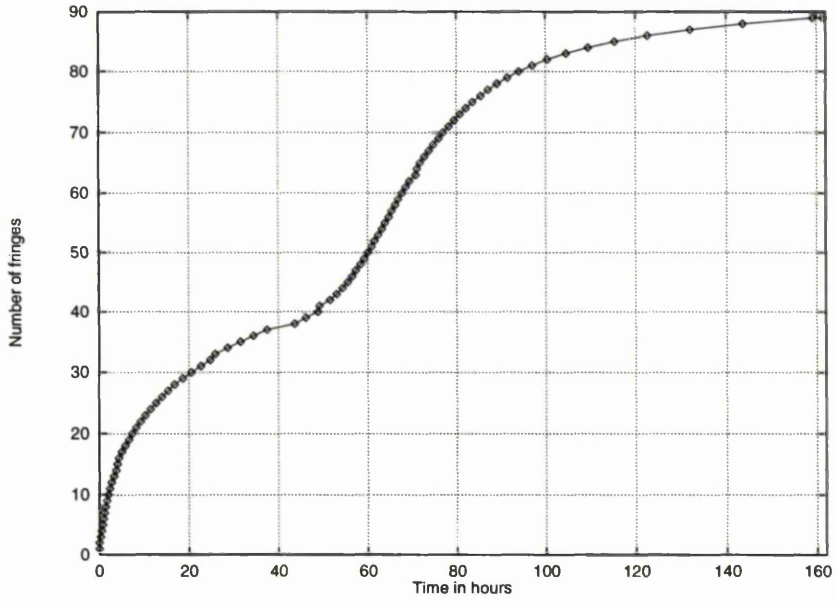

Figure 11.8: Cumulative total number of fringe peaks plotted against time. Note that at 40 hours there is a turning point in the curve which corresponds to a reversal of fringe motion.

measurement of the instrument (±0.14% for the NaCl solution) the NaCl solution has reached equilibrium throughout the reactor.

The refractive index of the initial protein solution of 21 mg lysozyme per 250 μl buffer is $n_{prot} = 1.3406$ and for buffer alone is $n_{buff} = 1.3295$. For every 1 mg per 1 ml the refractive index increment is calculated at 1.32×10^{-4} $((n_{prot} - n_{buff})/84)$ therefore for the increment observed 11.55 mg of protein in the reactor has formed into crystals leaving 4.24 mg of protein in solution within the peak to peak measurement (±0.22 mg for protein).

This concentration, c, was checked with spectrophotometric absorption measurements making use of the combined Beer-Lambert relationship;

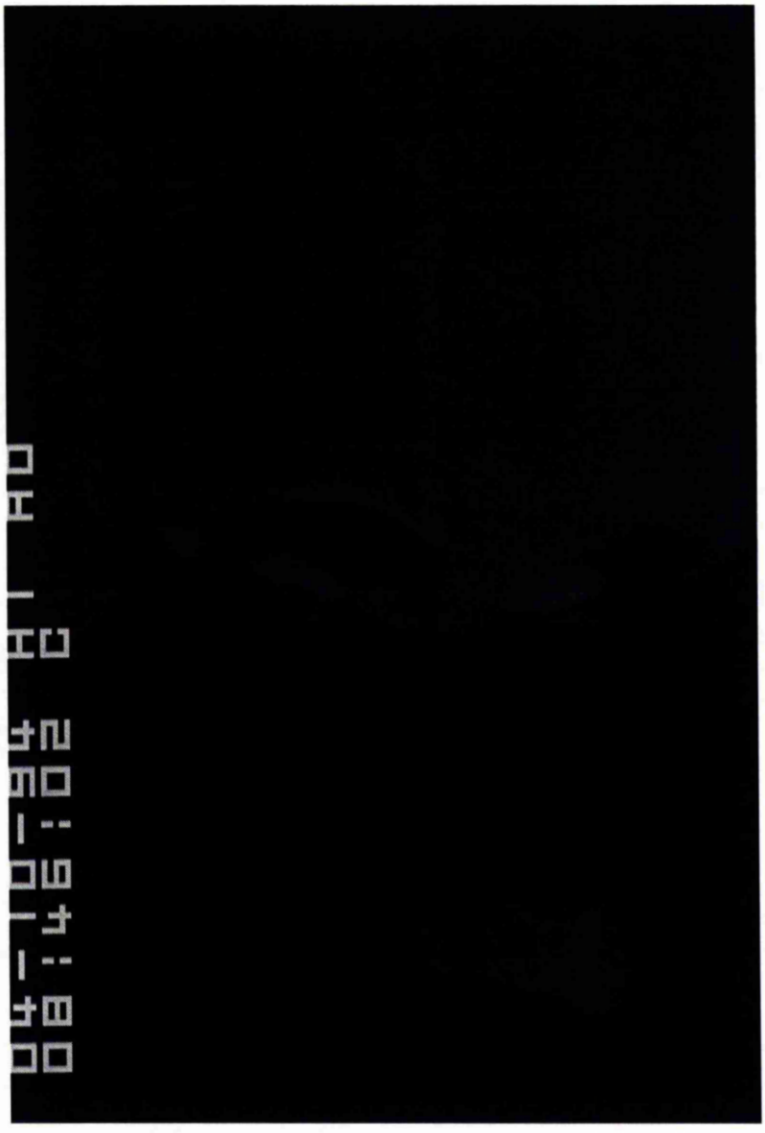

Figure 11.9: Protein chamber image at end of experiment.

$$c = \frac{A}{\epsilon d} \tag{11.8}$$

where A is the measured absorption, ϵ is the molar absorptivity and d is the path length of light through the sample. For lysozyme, ϵ is given[218] as 2.63 $A_{280\ nm}$ mg^{-1} ml^{-1} cm^{-1}, d is 1 cm and A is measured at 280 nm for dilutions of 1, 2 and 10 μl final solution in 1 ml equilibrated buffer and salt solution. The resulting concentration values showed 6 mg/ml or 1.128 mg of protein left in solution. This is less than the interferometer measurement allowing for error but can be explained in that the reactor used for concentration measurements was not that used in the interferometer trial. It was from one of the earth-grown ground controls. This reactor was activated under ambient laboratory conditions and one would not expect as much crystal growth due to temperature and resulting supersaturation fluctuations. Small errors also result in the dilution and preparation of the solution used for dilution. In essence the concentration measured by the interferometer agrees with that found spectrophotometrically for the protein left in solution at the end of the crystallization.

It is possible to position the measuring window at any point within the recorded image for analysis for grey level measurement. This has been carried out with the window at various heights along the vertical axis of the protein chamber. The cumulative total of fringes passing through the window at various heights was measured over times 1,2,3,5 and 9 hours respectively. This provided information on the spatial distribution of the refractive index change and therefore concentration throughout the protein chamber, illustrated in figure 11.10.

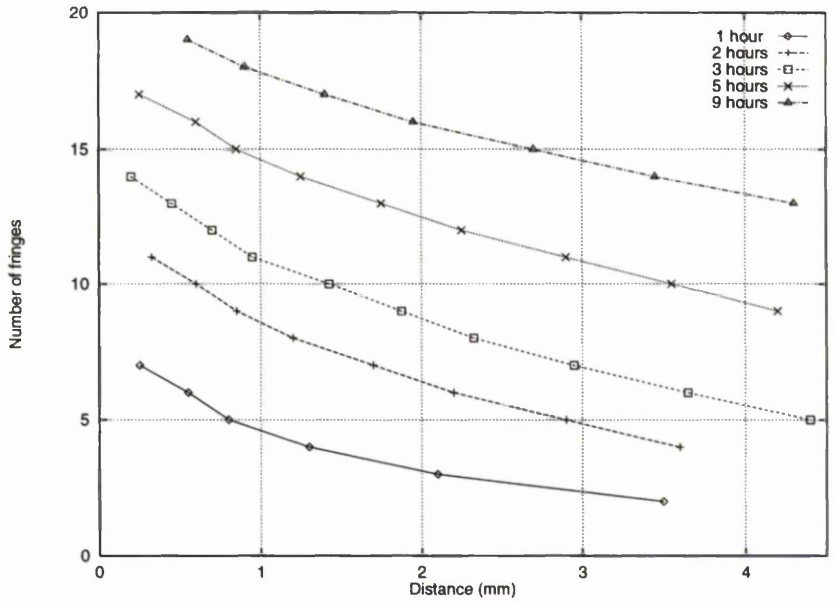

Figure 11.10: Spatial concentration measurements through the protein chamber.

11.7 Limitations and Overcoming Them

In similar, 'by eye' monitored, experiments with the dialysis reactor crystals first started to become visible after approximately the 40 hour point. From this fact and from figure 11.8 it would seem that the diffusion process of salt has finished (at approximately the 40 hour point) before crystallization has started. If this were not the case full calibration and theoretical studies of diffusion within the reactor, for example Wagner *et al.*,[242] would be required to separate the components. The change of refractive index with concentration of salt and protein can also be modelled mathematically using the differential of the Lorentz-Lorentz equation[240] with the assumption that concentration changes are proportional to density changes in crystal growth. This gives[240]

$$\frac{dn}{dc} = k\frac{(n^2-1)(n^2+2)}{n} \tag{11.9}$$

where n is the refractive index, c, the concentration and k, a constant of proportionality. Thus if $\frac{dn}{dc}$ at one n (or λ) is known it can easily be determined for other wavelengths by application of the Cauchy equation, 11.7 and the differential Lorentz-Lorentz equation, 11.9. It should be noted that refractive index varies with temperature so constant temperatures should be used throughout.

A method to experimentally resolve the diffusion and crystallization process separately would be to add another measuring window below the other side of the diffusion membrane so that the salt flow into the protein chamber could be separated from the protein being salted out of solution. For the depletion area likely to be found round the growing crystal other methods of resolving the processes separately would be needed. A possibility would be Ultra Violet (UV) observation of the system or the use of a coloured protein to produce values on the rate of protein leaving solution.

All the fringe measurements in this experiment have made use of counting the progress of dark fringes through a positionally defined window over time. The CCD camera (with interferometer mounted) in the APCF is mobile and samples several reactors. It is therefore important that fringe motion is not missed otherwise the wrong refractive index could easily be assigned. The use of a wedge shaped volume within the protein chamber could allow a quantitative measurement of fringes and calculation of refractive index over a limited range of values.

11.8 Discussion

Mach-Zehnder interferometry has been used previously by others to examine small molecule crystallization and protein crystallization in ground based studies.[182, 180, 181] Interference fringes were observed bending at the growing interface around a crystal of a small molecule, $Ba(NO_3)_2$.[181] The bends represented the change of refractive index due to the decrease of concentration around the growing crystal. The concentration gradient is sharp near the crystal surface and much gentler in the bulk so a diffusion boundary layer was seen. Further development has been carried out with phase shifting. Instead of monitoring the interferogram with one CCD as in the earlier experiments[182] three CCD cameras were used[180] with a beam splitter and polarisers at 0°, 45° and 90° resulting in three interferograms with phase shifts $\lambda/4$ with respect to each other. That method provided a 25 times higher sensitivity than conventional interferometry. Studies on a $Ba(NO_3)_2$ crystal with phase shifting and a Michelson interferometer showed an order of magnitude improvement in sensitivity[179] compared to conventional (non-phase shifting) two beam interferometry methods. Interferometer studies of small molecule crystal growth have shown the width of the diffusion boundary layer around a crystal increasing as the supersaturation increases up to 2-3% but stabilizing to an almost constant value independent of supersaturation under stable buoyancy driven convection.[180] No studies with improved 'phase shifting' sensitivity, to our knowledge, have yet been performed on protein crystal samples.

11.9 Main Findings and Future Work

Changes in the concentration of the salt and protein in solution have been monitored as a function of time. The spatial concentration distribution in the protein chamber has been determined as a function of refractive index at 1, 2, 3, 5 and 9 hours from the start of diffusion allowing a 2 dimensional profile of concentration throughout the chamber, at these times, to be monitored.

In essence then interferometry is useful to give insight into the diffusion kinetics during crystal growth. It offers the chance, in the future, to monitor the alterations in the fringe behaviour in microgravity compared with earth, and thereby give further insight into the protein crystal growth process.

Chapter 12

Discussion, Conclusions and Future Work for Microgravity and Protein Crystal Growth

12.1 Discussion

Microgravity crystallization studies should produce benefits for earth based experiments. International cooperations are being formed and the basic principles of crystallization are being investigated. Indeed it is noticeable that fluid physics theories are now being applied to protein crystallization. The more expanded community is bringing in expertise from many diverse scientific areas and disciplines. Although the cost of a few microgravity crystallization experiments is very great the possible knowledge to be gained (and improved crystals) should benefit earth based crystallization.

Diagnostic techniques to monitor the nucleation and resulting growth are important again both on earth and in microgravity. The mapping of temperature

and concentration around a growing crystal is useful in investigating phenomena such as terminal size. The terminal size may be related to the extremely slow diffusivities of protein molecules and consequent gradients and/or depletion zones. Video images are a very useful diagnostic technique and automated image analysis techniques have been developed[258] which could be applied in the future. Cool lighting is necessary in all video observations as non cooled lighting has been shown to give rise to additional convective movements which may generate secondary nucleation.[186]

In all microgravity methods there is a possibility of heterogeneous nucleation on the container walls which might affect the crystals. In a contained environment samples experience residual accelerations caused by astronauts, extra vehicular activities, int~~r~~ vehicular activities, vehicle motion (and even coughs or sneezes !). The resultant accelerations can be either periodic or impulsively driven and some of them can be as strong as 1000 μg.[196] In microgravity situations electrostatic liquid drop nucleation has been proposed as a method for allowing containerless growth, early experiments have demonstrated it's validity under earth gravity.[196]

As discussed for the topographic investigation of microgravity-grown crystals (chapter 10) extinction effects should become important for consideration in data collection from high perfection protein crystals. Examining extinction in microgravity and earth-grown crystals will be a useful area of work to determine an ideal size for a perfect, microgravity-grown crystal. Extinction effects certainly need more study now that microgravity is producing samples with small mosaic values.

A most interesting aspect of the microgravity crystals is the improved signal to noise ratio seen (chapter 9). This is beneficial in recording the high resolution, weaker, data which give the greatest detail in a resulting protein structure. This benefit can lead to greater understanding of biological processes if similar improvements are seen for other crystal systems besides the results produced so far on lysozyme as our test case.

12.2 Conclusions

The X-ray crystallography process starts with producing *suitable* crystals. This is the major bottle neck at present. Microgravity has been investigated as an environment for crystallization as reported in this thesis and shown to produce nearly perfect crystals. Insights into the crystallization process and why signal to noise ratios can be enhanced has been seen. This work sets targets ~~of trying~~ to produce usable crystals of only a single mosaic block through termination of growth at an appropriate time eg. with inert liquid injection.[193] Indeed the terminal size of a crystal may be related to the mosaic block size and number of mosaic blocks making up the crystal. The size of the mosaic block may be dependent on the strength of the bonds between molecules making up a unit cell and the natural thermal motion of the molecules. This remains to be investigated.

The X-ray topographic examination of the microgravity-grown crystals has provided evidence for the mosaic block theory of crystal formation. This result will be useful in explaining the properties of microgravity versus earth grown crystals. Following this work, involving the measurement of perfection of crystals, future work is needed now both in exploiting the resulting perfection and understanding

how it is produced.

There exists two fields of thought within the microgravity crystallization community. One approach is to fly many samples with different crystallization conditions to empirically define the best conditions for microgravity and the other is to use well known systems to perform specific experiments on the *how* of crystal growth. In the longer term information on the process of microgravity crystallization gained from diagnostic methods will improve the whole area of protein crystal growth. Information about the best crystallization conditions for *one system* will not be as valuable to the whole protein crystallization field. Diagnostic systems should prove very valuable to establish how microgravity-crystal growth differs from earth-crystal growth and in the ideal case there should be instruments designed for the specific purpose of investigating crystallization as a routine diagnostic. In determining crystallization conditions more use should be made of optimisation techniques such as using incomplete factorial experiments.[55, 56, 54] This would yield information on where the optimal conditions may lie on a crystal response surface,[56] with minimal amounts of material, and allowing optimisation for further missions.

12.3 Future Work

Data collection at higher resolution, intrinsically weak reflections, requires fine collimation optics, high brilliance sources and rapid readout CCD detectors. At the synchrotron, high resolution diffractometers, high energy (short wavelength) X-ray beams, and large area detectors will be required to exploit the most benefit

from improved protein crystal perfection. Low X-ray background will also improve the signal to noise ratio of the data collected, which can be achieved through long crystal to detector distances (the background per unit area decreases due to the inverse square law provided the Bragg spots remain sharp).

In conventional "earth based" crystallography, freezing techniques are used to prolong the lifetime of the crystals in the beam and reduce thermal motion.[135] The freezing of crystals, however, results in an increase of crystal mosaic spread, though minimised with good choice of cryoprotectents[163] to about 0.25°. The advantages of a perfect crystal are then lost. The larger mosaicity is tolerated by virtue of the crystal to detector distance being kept small (eg. < 10-20 cm). To date there have been no freezing experiments on microgravity-grown crystals which remains a future area of research. Clearly we can expect to have to alter current freezing protocols eg. one option is to increase the number of freezing gas streams so as to direct them at the crystal from all sides thus reducing the *freezing time* of a crystal. If the perfection can be preserved, larger crystal to detector distances can be harnessed (eg. $\geq$ 1 m), the benefits of crystal lifetime on freezing can be combined with low X-ray background.

Diagnostic techniques are being implemented for observing the crystal growth process in microgravity. Diagnostic techniques are also needed to monitor the nucleation stage. The ability to monitor the nucleation stage is a prerequisite for the development of an automated, dynamically controlled protein crystal growth apparatus for microgravity or ground based experiments. The effect of supersaturation on crystal growth should be investigated. At present there is no evidence that microgravity in itself produces crystals where none can be formed on earth. There is however, evidence that once nucleation is achieved then depletion layer

formation promotes the most favourable growth conditions.[45, 96] Systems that produce even the smallest nucleation sites (maybe not even visible to the naked eye) with supersaturation may show vast improvements in growth in microgravity due to the depletion layer formation. The depletion layer formation and growth needs to be monitored, most suitably with interferometric methods.

X-ray topography measurements on crystals from the IML-2 mission were detailed in chapter 10. Additional measurements on earth-controls, more IML-2 lysozyme and NASA supplied crystals (grown via vapour diffusion on another Shuttle mission) using beamline X-26C[104] of the National Synchrotron Light Source (NSLS) have been made. This work showed the direct imaging of mosaic blocks, strains, defects and even the effects of handling damage. X-ray topography techniques, having visualised the mosaic block structure, should be applied to examining the differences between an unfrozen and frozen crystal. Further X-ray topographic measurements with crystals of proteins with varying water contents will allow a detailed understanding of what levels of microgravity will be required for perfect crystal growth. It would also be useful to look at the edges of mosaic blocks in detail with the use of atomic force microscopy[27, 116] (present studies with the atomic force microscope having studied small regions repeatedly measuring crystal growth[82, 83, 86] rather than a macro survey of the whole crystal).

The APCF CCD video images have allowed growth rates to be measured. Comparison of the growth rates with positions of strains/defects in the crystal and microgravity levels recorded over mission may show the effect of microgravity or lack of it on crystal growth.

Overall, an eventual aim should be to have a permanent manned diagnostic protein crystallization facility and a production crystallization facility in microgravity. Knowing the levels of microgravity needed would allow experiments to be stopped (if needed) during residual gravity moments such as due to extra-vehicular movements or allow the crystallization to be performed in a free flying tethered unmanned module. In a facility of this kind it would be important that data be passed down in real time to experimenters on the ground for control and suggestions to provide the best results from their experiments.

In all investigations of microgravity crystallization methods ground controls under as identical as possible conditions are needed. Without such, little idea as to why microgravity growth gives improvements over earth growth can be found. The microgravity-crystal growth conditions may be such that methods of simulating them on earth can be found to routinely produce high quality 'perfect' crystals.

References

[1] S. Aibara and Y. Morita. Crystal growth of hen egg-white lysozyme using a crystallization vessel produced for a Spacelab experiment. *J. Crystal Growth*, (116):289–293, 1992.

[2] N. M. Allinson. Development of non-intensified charge-coupled device area X-ray detectors. *J. Synchrotron Rad.*, 1:54–62, 1994.

[3] N. M. Allinson, R. Brammer, J. R. Helliwell, S. Harrop, B. G. Magorrian, and T. Wan. Charge coupled device (CCD) area detector for on-line (40-80 ms) acqusition of Laue diffraction data from protein crystals. *J. X-ray Sci. Technol.*, 1(143), 1989.

[4] N. M. Allinson, M. Colapietro, J. R. Helliwell, K. J. Moon, A. W. Thompson, and S. Weisgerber. Charge-coupled imagers for time-resolved macromolecular crystallography. *Rev. Sci. Instrum.*, 63(1):664–666, 1992.

[5] Y. Amemiya. Image plates for use with synchrotron radiation. *J. Synchrotron Rad.*, (2):13–21, 1995.

[6] Y. Amemiya, S. Kishimoto, T. Matsushita, Y. Satow, and M. Ando. Imaging plate for time-resolved X-ray measurements. *Rev. Sci. Instrum.*, 60:1552–1556, 1989.

[7] Y. Amemiya and J. Miyahara. Imaging plate illuminates many fields. *Nature*, 336:89–90, 1988.

[8] J. L. Amorós, M. J. Buerger, and M. C. Amorós. *The Laue Method.* Academic Press, New York, 1975.

[9] S. J. Andrews, J. E. Hails, M. M. Harding, and D. W. J. Cruickshank. The mosaic spread of very small crystals deduced from Laue diffraction patterns. *Acta Cryst.*, A43:70–73, 1987.

[10] S. J. Andrews, M. Z. Papiz, R. McMeeking, A. J. Blake, B. M. Lowe, K. R. Franklin, J. R. Helliwell, and M. M. Harding. Piperazine silicate (EU 19): the structure of a very small crystal determined with synchrotron radiation. *Acta Cryst.*, B44:73–77, 1988.

[11] U. W. Arndt. Area detectors for protein crystallography at storage rings. *Nuclear Instruments and Methods*, A(222):252–255, 1984.

[12] U. W. Arndt. Optimum X-ray wavelength for protein crystallography. *J. Appl. Cryst.*, (17):118–119, 1984.

[13] P. J. Artymiuk, C. C. F. Blake, D. W. Rice, and K. S. Wilson. The structures of the monoclinic and orthorhombic forms of hen egg-white lysozyme at 6Å resolution. *Acta Cryst.*, B(38):778–783, 1982.

[14] K. Asano, S. Fujita, T. Senda, and Y. Mitsui. Crystal growth of ribonuclease S under microgravity. *J. Crystal Growth*, (122):323–329, 1992.

[15] M. Ataka and M. Asai. Systematic studies on the crystallization of lysozyme. *J. Crystal Growth*, (90):86–93, 1988.

[16] A. Authier. X-ray topography as a tool in crystal growth studies. *J. Crystal Growth*, (13/14):34–38, 1972.

[17] J. K. Baird, E. J. Meehan Jr, A. L. Xidis, and S. B. Howard. Convective diffusion in protein crystal growth. *J. Crystal Growth*, 76:694–700, 1986.

[18] H. D. Bartunik, H. H. Bartsch, and H. Qichen. Accuracy in Laue X-ray diffraction analysis of protein structures. *Acta Cryst.*, A(48):180–188, 1992.

[19] H. D. Bartunik and T. Borchert. Combined use of monochromatic and Laue diffraction techniques for macromolecular structure determination. *Acta Cryst.*, A(45):718–726, 1989.

[20] P. Becker. The theoretical models of extinction. Their domain of applicability. *Acta Cryst.*, A33:243–249, 1977.

[21] C. A. Beevers and C. M. Schwartz. The crystal structure of nickelsulphate heptahydrate $NiSO_4.7H_2O$. *Z. f. Krist.*, 91:201–169, 1935.

[22] F. C. Bernstein, T. F. Koetzle, G. J. B. Williams, E. F. Meyer Jr, M. D. Brice, J. R. Rodgers, O. Kennard, T. Shimanouchi, and M. Tasumi. The Protein Data Bank: A computer-based archival file for macromolecular structures. *J. Mol. Biol.*, 112:535–542, 1977.

[23] J. Berthou and P. Jollès. A phase transition in a protein crystal: The example of hen lysozyme. *Biochimica et Biophysica Acta*, 336:222–227, 1974.

[24] J. Berthou, A. Lifchitz, P. Artymiuk, and P. Jollés. An X-ray study of the physiological temperature form of hen egg-white lysozyme at 2 Å resolution. *Proc. R. Soc. Lond. B*, 217:471–489, 1983.

[25] R. C. Bi, L. L. Gui, Q. Han, F. L. Shen, K. Shi, Y. P. Wang, S. Z. Chen, Y. L. Hu, X. T. Niu, J. Dong, Y. C. Zhou, and N. Q. Lin. Protein crystallization in space. *Microgravity sci. technol.*, VII/2:203–206, 1994.

[26] D. H. Bilderback, K. Moffat, and D. M. E. Szebenyi. Time-resolved Laue diffraction from protein crystals: Instrumental considerations. *Nucl. Instr. and Meth.*, 222:245–251, 1984.

[27] G. Binnig, C. F. Quate, and Ch. Gerber. Atomic force microscope. *Physical Review Letters*, 56(9):930–933, 1986.

[28] C. C. F. Blake, R. H. Fenn, A. C. T. North, D. C. Philips, and R. J. Poljak. Structure of lysozyme. *Nature*, 195:1173–1176, 1962.

[29] C. C. F. Blake, L. N. Johnson, G. A. Mair, A. C. T. North, D. C. Philips, and V. R. Sarma. Crystallographic studies of the activity of hen egg-white lysozyme. *Proc. Roy. Soc. (London)*, B(167):378–388, 1967.

[30] C. C. F. Blake, D. F. Koenig, G. A. Mair, A. C. T. North, D. C. Philips, and V. R. Sarma. Structure of hen egg-white lysozyme. *Nature*, (206):757–761, 1965.

[31] C. C. F. Blake, G. A. Mair, A. C. T. North, D. C. Philips, and V. R. Sarma. On the conformation of the hen egg-white lysozyme molecule. *Proc. Roy. Soc. (London)*, B(167):365–377, 1967.

[32] R. Boistelle and J. P. Astier. Crystallization mechanisms in solution. *J. Crystal Growth*, 90:14–30, 1988.

[33] J. M. Bolduc, D. H. Dyer, W. G. Scott, P. Singer, R. M. Sweet, D. E. Koshland Jr., and B. L. Stoddard. Mutagenesis and Laue structures of

enzyme intermediates: Isocitrate dehydrogenase. *Science*, 268:1312–1318, 1995.

[34] R. Bosch, P. Lautenschlager, L. Potthast, and J. Stapelmann. Experimental equipment for protein crystallization in μg facilities. *Journal of Crystal Growth*, 122:310–316, 1992.

[35] F. Boue, F. Lefaucheux, M. C. Robert, and I. Rosenman. Small-angle neutron-scattering study of lysozyme solutions. *J. Crystal Growth*, 3-4:246–254, 1993.

[36] D. Bourgeois, J. P. Moy, S. O. Svensson, and Å. Kvick. The point-spread function of X-ray image intensifiers/CCD-camera and imaging-plate systems in crystallography: assessment and consequences for dynamic range. *J. Appl. Cryst.*, 27:868–877, 1994.

[37] W. L. Bragg. The diffraction of short electromagnetic waves by a crystal. *Proc. Camb. Phil. Soc.*, 17:43–57, 1913.

[38] W. L. Bragg. Structure determination of rocksalt, iron pyrite and spinel. *Proc. Royal. Soc. Lond.*, A89:248–277, 1913.

[39] W. L. Bragg. General Survey. In W. H. Bragg and W. L. Bragg, editors, *The Crystalline State*, number I, page 27. 1949.

[40] W. L. Bragg. The Development of X-ray Analysis. G. Bell and Sons, London, 1975.

[41] R. C. Brammer, J. R. Helliwell, W. Lamb, A. Liljas, P. R. Moore, A. W. Thompson, and K. Rathbone. A new protein crystallography station on

the SRS wiggler beamline for very rapid Laue and rapidly tunable monochromatic experiments. 1. Design principles, ray tracing and heat calculations. *Nucl. Instrum. Methods A*, 271:678–687, 1988.

[42] B. A. Brice and M. Halwer. A differential refractometer. *J. Opt. Soc. Am.*, 41:1033–1037, 1951.

[43] A. T. Brünger. Free R value: a novel statistical quantity for assessing the accuracy of crystal structures. *Nature*, 355:472–475, 1992.

[44] A. T. Brünger. X-PLOR *Version 3.1 A System for X-ray Crystallography and NMR.* Yale University Press, New Haven and London, 1992.

[45] C. W. Bunn. Concentration gradients and the rates of growth of crystals. *Discussions of the Faraday Society*, 5:132–144, 1949.

[46] E. Cacioppo and M. L. Pusey. The solubility of the tetragonal form of hen egg white lysozyme from pH 4.0 to 5.4. *J. Crystal Growth*, 114:286–292, 1991.

[47] A. D. Cameron, S. J. Smerdon, A. J. Wilkinson, J. Habash, J. R. Helliwell, T. Li, and J. S. Olson. Distal pocket polarity in ligand binding to myoglobin: Deoxy and carbonmonoxy forms of a threonine^{68}(E11) mutant investigated by X-ray crystallography and infrared spectroscopy. *Biochemistry*, 32:13061–13070, 1993.

[48] J. W. Campbell. LAUEGEN, an X-windows-based program for the processing of Laue X-ray diffraction data. *J. Appl. Cryst.*, 28:228–236, 1995.

[49] J. W. Campbell, I. J. Clifton, T. J. Greenhough, J. Hajdu, S.C. Harrison, R.C. Liddington, and A.K. Shrive. Calcium binding sites in tomato bushy

stunt virus visualized by Laue crystallography. *J. Mol. Biol.*, 214:627–632, 1990.

[50] J. W. Campbell, A. Deacon, J. Habash, J. R. Helliwell, S. McSweeney, H. Quan, J. Raftery, and E. Snell. Electron density maps of lysozyme calculated using synchrotron Laue data comprising singles and deconvoluted multiples. *Bull. Mater. Sci.*, 17(1):1–18, 1994.

[51] J. W. Campbell and Q. Hao. Evaluation of reflection intensities for the components of multiple Laue diffraction spots. II. Using the wavelength normalisation curve. *Acta Cryst.*, A49:889–893, 1993.

[52] P. D. Carr, D. W. J. Cruickshank, and M. M. Harding. The determination of unit cell parameters from Laue diffraction patterns using their gnomonic projections. *J. Appl. Cryst.*, 25:294–308, 1992.

[53] P. D. Carr, I. M. Dodd, and M. M. Harding. The determination of unit-cell parameters from a Laue diffraction pattern. *J. Appl. Cryst.*, 26:384–387, 1993.

[54] C. W. Carter (Jr), E. T. Baldwin, and L. Frick. Statistical design of experiments for protein crystal growth and the use of a precrystallization assay. *J. Crystal Growth*, 90:60–73, 1988.

[55] C. W. Carter (Jr) and C. W. Carter. Protein crystallization using incomplete factorial experiments. *J. Biological Chemistry*, 254:12219–12223, 1979.

[56] C. W. Carter (Jr) and Y. Yin. Quantitative analysis in the characterization and optimization of protein crystal growth. *Acta Cryst.*, D50:572–590,

1994.

[57] A. Cassetta, A. Deacon, C. Emmerich, J. Habash, J. R. Helliwell, S. McSweeney, E. Snell, A. W. Thompson, and S. Weisgerber. The emergence of the synchrotron Laue method for rapid data collection from protein crystals. *Proc. R. Soc. Lond.*, A442:177–192, 1993.

[58] S. Chandrasekhar. Extinction in X-ray crystallography. *Adv. Phys.*, 9:363–386, 1960.

[59] N. E. Chayen, J. W. Radcliffe, and D. M. Blow. Control of the nucleation in the crystallization of lysozyme. *Protein Science*, 2:113–118, 1993.

[60] P. S. Chen, P. J. Shlichta, W. R. Wilcox, and R. A. Lefever. Convection phenomena during the growth of sodium chlorate crystals from solution. *J. Crystal Growth*, 47:43–60, 1979.

[61] I. J. Clifton, D. W. J. Cruickshank, G. Diakun, M. Elder, J. R. Helliwell, R. C. Liddington, P. A. Machin, J. Habash, and M. Z. Papiz. Synchrotron X-radiation protein crystallography: CEA film absorption factor as a function of wavelength $0.3 \leq \lambda \leq 2$ Å. *J. Appl. Cryst.*, 18:296–300, 1985.

[62] I. J. Clifton, M. Elder, and J. Hajdu. Experimental strategies in Laue crystallography. *J. Appl. Cryst.*, 24:267–277, 1991.

[63] I. J. Clifton, S. Wakatsuki, and J. Hajdu. New sources, newer detectors, old methods - The future of protein crystallography at synchrotrons. *Nuc. Ins. meth.*, B87:76–81, 1994.

[64] M. Colapietro, G. Cappuccio, C. Marciante, A. Pifferi, R. Spagna, and J. R. Helliwell. The X-ray diffraction station at the Adone wiggler facility:

Peliminary results (including crystal perfection). *J. Appl. Cryst.*, 25:192–194, 1992.

[65] Collaborative Computational Project Number 4. The CCP4 suite: Programs for protein crystallography. *Acta Cryst.*, D50:760–763, 1994.

[66] D. W. J. Cruickshank, J. R. Helliwell, and K. Moffat. Multiplicity distribution of reflections in Laue diffraction. *Acta Cryst.*, A43:656–674, 1987.

[67] D. W. J. Cruickshank, J. R. Helliwell, and K. Moffat. Angular distribution of reflections in Laue diffraction. *Acta Cryst.*, A47:352–373, 1991.

[68] C. G. Darwin. The reflection of X-rays from imperfect crystals. *Phil. Mag.*, 43(257):800–829, 1922.

[69] W. I. F. David. The probabilistic determination of intensities of completely overlapping reflections in powder diffraction patterns. *J. Appl. Cryst.*, (20):316–319, 1987.

[70] A. Deacon, J. Habash, S. J. Harrop, J. R. Helliwell, W. N. Hunter, G. A. Leonard, M. Peterson, A. Hadener, A. J. Kalb (Gilboa), N. M. Allinson, C. Castelli, K. Moon, S. McSweeney, A. Gonzalez, A. W. Thompson, S. Ealick, D. M. Szebenyi, and R. M. Walter. SR instrumentation for optimized anomalous scattering and high resolution structure studies of proteins and nucleic acids. *Rev. Sci. Instrum.*, 2:1287–1292, 1995.

[71] L. J. DeLucas, D. C. Carter, R. S. Snyder, A. McPherson, S. Koszelak, and C. E. Bugg. Microgravity protein crystal growth: Results and hardware development. *J. Crystal Growth*, 109:12–16, 1991.

[72] L. J. DeLucas, M. M. Long, W. M. Rosenblaum, T. L. Bray, C. Smith, M. Carson, S. V. L. Narayana, M. D. Harrington, D. C. Carter, A. D. Clark (Jr), R. G. Nanni, J. Ding, A. Jacobo-Molina, G. Kamer, S. H. Hughes, E. Arnold, H. M. Einspahr, L. L. Clancy, G. S. J. Rao, P. F. Cook, B. G. Harris, S. H. Munson, B. C. Finzel, A. McPherson, P. C. Weber, F. A. Lewandowski, T. L. Nagabhushan, P. P. Trotta, J. A. Thompson, R. N. Richards, K. D. Bowersox, C. J. Meade, E. S. Baker, S. P. Bishop, B. J. Dunbar, E. Trinh, J. Prahl, A. Sacco (Jr), and C. E. Bugg. Recent results and new hardware developments for protein crystal growth in microgravity. *J. Crystal Growth*, 135:183–195, 1994.

[73] L. J. DeLucas, K. M. Moore, T. L. Bray, W. M. Rosenblum, H. L. Einspahr, L. L. Clancy, G. S. J. Rao, B. G. Harris, S. H. Munson, B. C. Finzel, and C. E. Bugg. Protein crystal growth results from the United States Microgravity Laboratory-1 mission. *J. Phys. D: Appl. Phys.*, (26):B100–103, 1993.

[74] L. J. DeLucas, C. D. Smith, H. W. Smith, S. Vijay-Kumar, S. E. Senadhi, S. E. Ealick, D. C. Carter, R. S. Snyder, P. C. Weber, F. R. Salemme, D. H. Ohlendorf, H. M. Einspahr, L. L. Clancy, M. A. Navia, B. M. McKeever, T. L. Nagabhushan, G. Nelson, A. McPherson, S. Koszelak, G. Taylor, D. Stammers, K. Powell, G. Darby, and C. E. Bugg. Protein crystal growth in microgravity. *Science*, (246):651–654, 1989.

[75] L. J. DeLucas, W. Smith, S. Vijay-Kumar, S. E. Senadhi, S. E. Ealick, D. C. Carter, R. S. Snyder, P. C. Weber, F. R. Salemme, D. H. Ohlendorf, H. M. Einspahr, L. L. Clancy, A. McPherson, S. Koszelak, G. Taylor, D. Stammers, K. Powell, G. Darby, and C. E. Bugg. Protein crystal growth results

for shuttle flights STS-26 and STS-29. *J. Crystal Growth*, 110:302–311, 1991.

[76] L. J. DeLucas, F. L. Suddath, R. S. Snyder, R. Naumann, M. B. Broom, M. Pusey, V. Yost, B. Herren, D. Carter, B. Nelson, E. J. Meehan, A. McPherson, and C. E. Bugg. Preliminary investigations of protein crystal growth using the space shuttle. *J. Crystal Growth*, 76:681–693, 1986.

[77] R. Diamond. Real space refinement of the structure of hen egg-white lysozyme. *J. Mol. Biol.*, (82):371–391, 1974.

[78] I. M. Dodd, Q. Hao, M. M. Harding, and S. M. Prince. Structure determination with Laue diffraction data - Including refinement when anomalous scatterers are present. *Acta Cryst.*, B50:441–447, 1994.

[79] R. A. Duckett and A. R. Lang. The growth of nearly perfect hexamethylenetetramine crystals from solution. *J. Crystal Growth*, 18:135–142, 1973.

[80] E. M. H. Duke, A. Hadfield, S. Walters, S. Wakatsuki, R. K. Bryan, and L. N. Johnson. Time-resolved diffraction studies on glycogen phosphorylase. *Phil. Trans. R. Soc. Lond.*, A340:245–261, 1992.

[81] E. M. H. Duke, S. Wakatsuki, A. Hadfield, and L. N. Johnson. Laue and monochromatic diffraction studies on catalysis in phosphorylase b crystals. *Protein Science*, 3:1178–1196, 1994.

[82] S. D. Durbin and W. E. Carlson. Lysozyme crystal growth studied by atomic force microscopy. *J. Crystal Growth*, 122:71–79, 1992.

[83] S. D. Durbin, W. E. Carlson, and M. T. Saros. In situ studies of protein crystal growth by atomic force microscopy. *J. Phys. D: Appl. Phys.*, 26:B126–B132, 1993.

[84] S. D. Durbin and G. Feher. Crystal growth studies of lysozyme as a model for protein crystallization. *J. Crystal Growth*, 76:583–592, 1986.

[85] S. D. Durbin and G. Feher. Studies of crystal growth mechanisms of proteins by electron microscopy. *J. Mol. Biol.*, 212:763–774, 1990.

[86] S. D. Durbin and G. Feher. Simulation of lysozyme crystal growth by the Monte Carlo method. *J. Crystal Growth*, 110:41–51, 1991.

[87] M. Elder. Photographic science and microdensitometry in X-ray diffraction data collection. *Methods in Enzymology*, 114:199–211, 1985.

[88] S. H. Emara, B. R. Lawn, and A. R. Lang. Direct observation of dislocations in potash alum. *Phil. Mag.*, 19:7–12, 1969.

[89] V. A. Erdmann, C. Lippmann, C. Betzel, Z. Dauter, K. Wilson, R. Hilgenfeld, J. Hoven, A. Liesum, W. Saenger, C. W. Müller-Fahrnow, A. Hinrichs, M. Düvel, G. E. Schulz, C. W. Müller, H. G. Wittmann, A. Yonath, G. Weber, K Stegen, and A. Plaas-Link. Crystallization of proteins under microgravity. *FEBS Letters*, 259:194–198, 1989.

[90] ESRF. ESRF foundation phase report. European Synchrotron Radiation Facility, 1987.

[91] H. Euler, R. Gilles, and G. Will. The use of image plates for Laue diffraction with synchrotron radiation with olivine single-crystal studies as an example. *J. Appl. Cryst.*, 27:190–192, 1994.

[92] P. P. Ewald and numerous crystallographers, editors. *Fifty years of X-ray diffraction.* International Union of Crystallography, 1962.

[93] F. Ewing, E. Forsythe, and M. Pusey. Orthorhombic lysozyme solubility. *Acta Cryst.*, D50:424–428, 1994.

[94] G. K. Farber, P. Machin, S. C. Almo, G.A. Petsko, and J. Hajdu. X-ray Laue diffraction from crystals of xylose isomerase. *Proc. Natl. Acad. Sci. USA*, 85:112–115, 1988.

[95] G. Feher. Mechanisms of nucleation and growth of protein crystals. *J. Crystal Growth*, 76:545–546, 1986.

[96] G. Feher and Z. Kam. Nucleation and growth of protein crystals: General principles and assays. *Methods in Enzymology*, 114:77–112, 1985.

[97] R. W. Fiddis, R. A. Longman, and P. D. Calvert. Crystal growth kinetics of globular proteins lysozyme and insulin. *J. Chem. Soc. Faraday Trans.*, 75:2753–2761, 1978.

[98] A. Fleming. On a remarkable bacteriolytic element found in tissues and secretions. *Proc. Roy. Soc. Lond. B*, 39:306–317, 1922.

[99] E. Forsythe, F. Ewing, and M. Pusey. Studies on tetragonal lysozyme crystal growth rates. *Acta Cryst.*, D50:614–619, 1994.

[100] R. Fourme, A. Ducruix, M. Ries-Kautt, and B. Capelle. The perfection of protein crystals by direct recording of Bragg reflection profiles with a quasi-planar X-ray wave. *J. Synchrotron Rad.*, 2:136–142, 1995.

[101] M. Francqn. *Optical Interferometry.* Academic Press, 1966.

[102] M. Frey, S-C. Genovesio-Taverne, and J. C. Fontecilla-Camps. Molecular packing and morphology of protein crystals. *J. Phys D: Appl Phys*, 24:105–110, 1991.

[103] W. Friedrich, P. Knipping, and M. Laue. Interferenz-erscheinungen bei Röntgenstrahlen. *Sitzungsber. K. Bayer. Acad, d Wiss.*, pages 303–322, 1912.

[104] E. D. Getzoff, K. W. Jones, D. McRee, K. Moffat, K. Ng, M.L. Rivers, W. Schildkamp, P. T. Singer, P. Spanne, R. M. Sweet, T.-Y. Teng, and E. M. Westbrook. Laue diffraction protein crystallography at the national synchrotron light source. *Nucl. Instr. and Meth.*, B79:249–255, 1993.

[105] S. Gits-Leon, F. Lefaucheux, and M. C. Robert. Effects of stirring on crystalline quality of solution grown crystals - case of potash alum. *J. Crystal Growth*, 44:345–355, 1978.

[106] D. Gómez de Andérez, M. Helliwell, E. J. Habash, J. Dodson, J. R. Helliwell, P. D. Bailey, and R.E. Gammon. A comparison of Laue and monochromatic X-ray analyses of a small molecule crystal. *Acta Cryst.*, B45:428–488, 1989.

[107] Gómez de Andérez, D. *A study of the synchrotron Laue method for quantitative structure analysis.* Doctor of philosophy, York University, Physics Department, 1990.

[108] T. J. Greenhough and J. R. Helliwell. Oscillation camera data processing: Reflecting range and prediction of partiality. I. Conventional X-ray sources. *J. Appl. Cryst.*, 15:338–351, 1982.

[109] T. J. Greenhough and J. R. Helliwell. The uses of synchrotron X-radiation in the crystallography of molecular biology. *Progress in Biophysics and Molecular Biology*, 41:67–123, 1983.

[110] T. J. Greenhough and A. K. Shrive. Laue image analysis II. Variable radial elliptical masking and its application in studies involving streaked Laue exposures. *J. Appl. Cryst.*, 27:111–121, 1994.

[111] S. M. Gruner and S. E. Ealick. Charge coupled device X-ray detectors for macromolecular crystallography. *Structure*, 3:13–15, 1995.

[112] P. A. Guinier and J. Tennevin. Sur deux variantes de la méthode de laue et leurs applications. *Acta Cryst.*, 2:133–138, 1949.

[113] J. Hajdu and I. Andersson. Fast crystallography and time-resolved structures. *Annu. Rev. Biophys. Biomol. Struct.*, 22:467–498, 1993.

[114] J. Hajdu and L. N. Johnson. Progress with Laue diffraction studies on protein and virus crystals. *Biochemistry*, 29:1669–1678, 1990.

[115] J. Hajdu, P. Machin, J. W. Campbell, T. J. Greenhough, I. J. Clifton, S. Zurek, S. Gover, L. N. Johnson, and M. Elder. Millisecond X-ray diffraction and the first electron density map from Laue photographs of a protein crystal. *Nature*, 329:178–181, 1987.

[116] P. K. Hansma, V. B. Elings, O. Marti, and C. E. Bracker. Scanning tunneling microscopy and atomic force microscopy: application to biology and technology. *Science*, 243:209–216, 1988.

[117] Q. Hao, J. W. Campbell, M. M. Harding, and J. R. Helliwell. Evaluation of reflection intensities for the components of multiple Laue diffraction spots

by direct methods. *Acta Cryst.*, A49:528–531, 1993.

[118] Q. Hao, M. M. Harding, and J. W. Campbell. Determination of d_{min} and λ_{min} from the intensity distributions of Laue patterns. *J. Appl. Cryst.*, 28:447–450, 1995.

[119] M. M. Harding, S. J. Maginn, J. W. Campbell, I. Clifton, and P. Machin. Crystal structure of an organometallic compound from synchrotron radiation Laue diffraction photographs. *Acta Cryst.*, B44:142–146, 1988.

[120] D. Harker. The application of the three-dimensional Patterson method and the crystal structures of proustite, Ag_3AsS_3 and pyrargyrite, Ag_3SbS_3. *Journal of Chemical Physics*, 4:381–390, 1936.

[121] J. R. Helliwell. In R. B. Cundall and I. H. Munro, editors, *Applications of synchrotron radiation to the study of large molecules of chemical and biological interest*, number DL/SC1/R13 in Proceedings of the Daresbury Study Weekend, pages 1–6. Daresbury Laboratory, 1979.

[122] J. R. Helliwell. Synchrotron X-radiation protein crystallography - Instrumentation, methods and applications. *Reports on Progress in Physics*, 147(11):1403–1497, 1984.

[123] J. R. Helliwell. Protein crystallography with synchrotron radiation. *J. Molec. Struct.*, (130):63–91, 1985.

[124] J. R. Helliwell. Protein crystal perfection and the nature of radiation damage. *Journal of Crystal Growth*, (90):259–272, 1988.

[125] J. R. Helliwell. Macromolecular crystallography using synchrotron radiation: Progress on station 9.5 and a novel (toast-rack) detector scheme for

Laue diffraction. *Nucl. Instr. and Meth.*, A308:260–266, 1991.

[126] J. R. Helliwell. *Macromolecular Crystallography with Synchrotron Radiation.* Cambridge University Press, UK, 1992.

[127] J. R. Helliwell. Synchrotron X-ray crystallography techniques: Time-resolved aspects of data collection. *Phil. Trans. R. Soc. Lond. A*, (340):221–232, 1992.

[128] J. R. Helliwell, J. Habash, D. W. J. Cruickshank, M. M. Harding, T.J. Greenhough, J. W. Campbell, I. J. Clifton, M. Elder, P. A. Machin, M. Z. Papiz, and S. Zurek. The recording and analysis of synchrotron X-radiation Laue diffraction photographs. *J. Appl. Cryst.*, 22:483–497, 1989.

[129] J. R. Helliwell, S. Harrop, J. Habash, B. G. Magorrian, N. M. Allinson, D. Gómez de Andérez, M. Helliwell, Z. Derewenda, and D. W. J. Cruickshank. Instrumentation for Laue diffraction. *Rev. Sci. Instrum.*, pages 1531–1536, 1989.

[130] J. R. Helliwell, E. H. Snell, and S. Weisgerber. An investigation of the perfection of lysozyme protein crystals grown in microgravity (Spacehab-1 and IML-2) and on earth. In *Proceedings of the Berlin Microgravity Meeting.* Springer Verlag, 1995. In press.

[131] M. Helliwell, B Gallois, B. M. Kariuki, V. Kaucic, and J. R. Helliwell. A two wavelength crystallographic study of a new aluminophosphate containing nickel. *Acta Cryst.*, B49:420–428, 1993.

[132] M. Helliwell, D. Gómez de Andérez, J. Habash, J. R. Helliwell, and J. Vernon. A comparison of Laue and monochromatic X-ray analyses: The determination of the hydrogen atom positions of an organic small molecule crystal. *Acta Cryst.*, B45:591–596, 1989.

[133] G. Hilderbrandt. The discovery of the diffraction of X-rays in crystals - A historical review. *Cryst. Res. Technol.*, 28(6):747–766, 1993.

[134] R. Hilgenfeld, A. Liesum, R. Storm, and A. Plaas-Link. Crystallization of two bacterial enzymes on an unmanned space mission. *Journal of Crystal Growth*, (122):330–336, 1992.

[135] H. Hope. Cryocrystallography of biological macromolecules: A generally applicable method. *Acta Cryst.*, B44:22–26, 1988.

[136] S. B. Howard, P. J. Twigg, J. K. Baird, and E. J. Meehan. The solubility of hen egg-white lysozyme. *J. Crystal Growth*, 90:94–104, 1988.

[137] P. L. Howell, S. Almo, M. R. Parson, J. Hajdu, and G. A. Petsko. Structure determination of turkey egg-white lysozyme using Laue diffraction data. *Acta Cryst.*, B48:200–207, 1992.

[138] K. Hümmer, E. Weckert, and H. Bondza. Direct determination of triplet phases and enantiomorphs of non-centrosymmetric structures. II. Experimental results. *Acta Cryst.*, A45:182–187, 1989.

[139] S. Ikeno, H. Maruyama, and N. Kato. X-ray topographic studies of NaCl crystals grown from aqueous solutions with Mn ions. *J. Crystal Growth*, 3/4:683–693, 1968.

[140] J. Jollès, J. Jauregui-Adell, I. Bernier, and P. Jollès. La structure chimique du lysozyme de blanc d' oeuf de poule: Étude détaillée. *Biochim. Biophys. Acta*, 78:668–689, 1963.

[141] T. A. Jones. A graphics model building and refinement system for macromolecules. *J. Appl. Cryst.*, 11:268–272, 1978.

[142] T. A. Jones. Interactive computer graphics: FRODO. *Methods in Enzymology*, 115:157–171, 1985.

[143] T. A. Jones and L. Liljas. Crystallographic refinement of macromolecules having non-crystallographic symmetry. *Acta Cryst.*, A40:50–57, 1984.

[144] T. A. Jones, J. Y. Zou, S. W. Cowan, and M. Kjelgaard. Improved methods for building protein models in electron density maps and the location of errors in these models. *Acta Cryst.*, A(47):110–119, 1991.

[145] I. Kito and N. Kato. X-ray topographic studies of $NaClO_3$ crystals grown from aqueous solution. *J. Crystal Growth*, 24/25:544–548, 1974.

[146] G. S. Knapp and M. A. Beno. A new method to do time-resolved, X-ray diffraction studies: The rotating crystal Laue method. *Rev. Sc. Instrum.*, 63:1032–1034, 1992.

[147] S. Koszelak and A. McPherson. Time lapse microphotography of protein crystal growth using a colour VCR. *J. Crystal Growth*, 90:340–343, 1988.

[148] Å. Kvick and M. Wulff. The materials science and Laue diffraction beamlines at the European Synchrotron Radiation Facility. *Rev. Sc. Instrum.*, 63(1):1073–1076, 1992.

[149] A. R. Lang. A method for the examination of crystal sections using penetrating characteristic X radiation. *Acta Metallurgica*, 5:358–364, 1957.

[150] A. R. Lang. Direct observation of individual dislocations by X-ray diffraction. *J. Appl. Phys.*, 29:597–598, 1958.

[151] R. A. Laskowski, M. W. MacArthur, D. S. Moss, and J.M. Thornton. PROCHECK - a program to check the stereochemical quality of protein structures. *J. Appl. Cryst.*, 26:283–291, 1993.

[152] R. Lewis. Multiwire gas proportional counters: Decrepit antiques or classic performers ? *J. Synchrotron Rad.*, 1:43–53, 1994.

[153] K. Lim, J. X. Ho, B. S. Wright, P. D. Twigg, T. Y. Miller, J. Chapman, K. Keeling, and D. C. Carter. Analysis and crystallographic refinement of hen egg white lysozyme at 1.4 å from crystals produced in microgravity. *Protein Science*, submitted.

[154] M. Lindahl, A. Liljas, J. Habash, S. Harrop, and J. R. Helliwell. The sensitivity of the synchrotron Laue method to small structural changes: Binding studies of human carbonic anhydrase II (HCAII). *Acta Cryst.*, B(48):281–285, 1992.

[155] W. Littke and C. John. Protein single crystals grown under microgravity. *Science*, 225:203–204, 1984.

[156] W. Littke and C. John. Protein single crystal growth under microgravity. *J. Cryst Growth*, 76:663–672, 1986.

[157] S. J. Maginn, M. M. Harding, and J. W. Campbell. Structure determination of a complex pentamolybodisulphate from synchrotron radiation

Laue diffraction photographs: Derivation and application of a wavelength-dependent absorption correction. *Acta Cryst.*, B49:520–524, 1993.

[158] G. Margaritondo. A primer in synchrotron radiation: everything you wanted to know about SEX (synchrotron emission of X-rays) but were afraid to ask. *J. Synchrotron Rad.*, 2:148–154, 1995.

[159] B. W. Matthews. Solvent content of protein crystals. *J. Mol. Biol.*, 33:491–497, 1968.

[160] A. McPherson. Virus and protein crystal growth on earth and in microgravity. *J. Phys. D: Appl. Phys.*, 26:B104–B112, 1993.

[161] A. McPherson, A. J. Malkin, and Y. G. Kuznetsov. The science of macromolecular crystallization. *Structure*, 3(8):759–768, 1995.

[162] T. Y. Miller, X. He, and D. C. Carter. A comparison between protein crystals grown with vapour diffusion methods in microgravity and protein crystals using a gel liquid-liquid diffusion ground based method. *J. Crystal Growth*, 122:306–309, 1992.

[163] E. P. Mitchell and E. F. Garman. Flash freezing of protein crystals: Investigation of mosaic spread and diffraction limit with variation of cryoprotectant concentration. *J. Appl. Cryst.*, (27):1070–1074, 1994.

[164] J. Miyahara, K. Takahashi, Y. Amemiya, N. Namiya, and Y. Satow. A new type of X-ray area detector utilizing laser stimulated luminescence. *Nucl. Instr. and Meth.*, A246:572–578, 1986.

[165] K. Moffat, D. Bilderback, and W. Schildkamp. Workshop on PEP as a

synchrotron radiation source. Technical report, Stanford Synchrotron Radiation Laboratory, USA, 1987.

[166] K. Moffat, D. Bilderback, W. Schildkamp, and K. Volz. Laue diffraction from biological samples. *Nucl. Instr. and Meth.*, A246:627–635, 1986.

[167] K. Moffat, Y. Chen, K. Ng, D. McRee, and E. D. Getzoff. Time-resolved crystallography: principles, problems and practice. *Phil. Trans. R. Soc. Lond. A*, (340):175–190, 1992.

[168] K. Moffat and J. R. Helliwell. *The Laue Method and its use in Time-Resolved Crystallography*, volume 151 of *Topics in Current Chemistry*, pages 61–74. Springer-Verlag, Berlin, Heidleberg, 1989.

[169] K. Moffat, D. M. Szebenyi, and D. Bilderback. X-ray Laue diffraction from protein crystals. *Science*, 223:1423–1425, 1984.

[170] J. P. Moy. A 200 mm input field 5-80 keV detector based on an X-ray image intensifier and CCD camera. *Nucl. Instr. and Meth.*, A(348):641–644, 1994.

[171] J. P. Moy. Personal communication. 1995.

[172] J. P. Moy and S. Gibney. Low energy X-ray image intensifier development phase 1 report. Preliminary Report EXP/JGM/SG/92/91, ESRF, Grenoble, France, December 1992.

[173] A. Nadarajah, E. L. Forsythe, and M. L. Pusey. The averaged face growth rates of lysozyme crystals: the effect of temperature. *J. Crystal Growth*, 151:163–172, 1995.

[174] L. G. Napolitano. Marangoni convection in space microgravity enviroments. *Science*, 225:197–198, 1984.

[175] B. A. Nerad and P. J. Shlichta. Ground-based experiments on the minimization of convection during the growth of crystals from solution. *J. Crystal Growth*, 75:591–608, 1986.

[176] N. Niimura, Y. Minezaki, M. Ataka, and T. Katsura. Aggregation in supersaturated lysozyme solution studied by time-resolved small angle neutron scattering. *J. Crystal Growth*, 154:136–144, 1995.

[177] D. A. Noever. Size effects in models for mechanically-stressed protein crystals and aggregates. *J. Crystal Growth*, 122:120–135, 1992.

[178] T. A. Nyce and F. Rosenberger. Growth of protein crystals suspended in a closed loop thermosyphon. *J. Crystal Growth*, 110:52–59, 1991.

[179] K. Onuma, T. Kameyama, and K. Tsukamoto. In situ study of surface phenomena by real time phase shift interferometry. *J. Crystal Growth*, 137:610–622, 1994.

[180] K. Onuma, K. Tsukamoto, and S. Nakadate. Application of real time phase shift interferometer to the measurement of concentration field. *J. of Crystal Growth*, 129:706–718, 1993.

[181] K. Onuma, K. Tsukamoto, and I Sunagawa. Role of buoyancy driven convection in aqueous solution growth; A case study of $Ba(NO_3)_2$ crystal. *J. Crystal Growth*, 89:177–188, 1988.

[182] K. Onuma, K. Tsukamoto, and I Sunagawa. Measurements of surface supersaturations around a growing K-alum crystal in aqueous solution. *J. Crystal Growth*, 98:377–383, 1989.

[183] A. L. Patterson. A Fourier series method for the determination of the components of interatomic distances in crystals. *Phys. Rev.*, 46:372–376, 1934.

[184] A. L. Patterson. A direct method for the determination of the components of interatomic distances in crystals. *Z. Krist.*, 90:517–542, 1935.

[185] J. P. Priestle. RIBBON - a stereo cartoon drawing program for proteins. *J. Appl. Cryst.*, 22:572–576, 1988.

[186] K. Provost and M-C. Robert. Application of gel growth to hanging drop techniques. *J. Crystal Growth*, 110:258–264, 1991.

[187] M. Pusey and R. Naumann. Growth kinetics of tetragonal lysozyme crystals. *J. Crystal Growth*, 76:593–599, 1986.

[188] M. Pusey, W. Witherow, and R. Naumann. Preliminary investigations into solutal flow about growing tetragonal lysozyme crystals. *J. Crystal Growth*, 90:105–111, 1988.

[189] M. L. Pusey. Estimation of the initial equilibrium constants in the formation of tetragonal lysozyme crystals. *J. Crystal Growth*, 110:60–65, 1991.

[190] D. Rabinovich and B. Lourie. Use of the polychromatic Laue method for short-exposure X-ray diffraction data acquisition. *Acta Cryst.*, A43:774–780, 1987.

[191] N. Rajić, Dj. Stojaković, and V. Kaučič. Preparation of aluminophosphate molecular-sieves in the presence of nickel(II) and copper(II). *Zeolites*, (11):612–616, 1991.

[192] C. Ramakrishnan and G. N. Ramachandran. Stereochemical criteria for polypeptide and protein chain conformation. *Biophys. J.*, (5):909–933, 1965.

[193] I. I. Regel, A. A. Vedernikov, P. Queeckers, and J. C. Legros. Crystal separation from mother solution and conservation under microgravity conditions using inert liquid. In *Crystal Growth in Space and Related Optical Diagnostics*, volume 1557 of *SPIE Conference Proceedings*, pages 182–191. SPIE, 1991.

[194] Z. Ren and K. Moffat. Laue crystallography for analysing rapid reactions. *J. Synchrotron Rad.*, 1:18–82, 1994.

[195] Z. Ren and K. Moffat. Deconvolution of energy overlaps in Laue diffraction. *J. Appl. Cryst.*, (28):482–493, 1995.

[196] W-K. Rhim and S. K. Chung. Containerless protein crystal growth method. *J. Crystal Growth*, 110:293–301, 1991.

[197] D. Ringe, B.L. Stoddard, J. Bruhnke, P. Koenigs, and N. Porter. Can Laue catch Maxwell ?: Observation of short-lived species by Laue X-ray crystallography. *Phil. Trans. R. Soc. Lond.*, A340:273–284, 1992.

[198] M. C. Robert and F. Lefaucheux. Crystal growth in gels: Principle and applications. *J. Crystal Growth*, 90:358–367, 1988.

[199] W. C. Röntgen. On a new kind of rays. *Erste Mit. Sitzgsber. physik.-med. Ges Würzburg*, 137, 1895.

[200] W. C. Röntgen. On a new kind of rays. *Nature*, 53:274–276, 1896.

[201] G. Rosenbaum, K. C. Holmes, and J. Witz. Synchrotron radiation as a source for X-ray diffraction. *Nature*, 230:434, 1971.

[202] F. Rosenberger and E. J. Meehan. Control of nucleation and growth in protein crystal growth. *J. Crystal Growth*, 90:74–78, 1988.

[203] W. M. Rosenblum, J. P. Kennedy, and B. Bishop. Examination of protein crystals in the hanging drop using digital image capture techniques. *J. Crystal Growth*, 110:171–176, 1991.

[204] S. Sasaki. Numerical tables of anomalous scattering factors calculated by the Cromer and Liberman's method. Technical Report KEK/Photon Factory Report 88-14, National Laboratory for High Energy Physics, Tsukuba, Japan, 1988.

[205] K. Sato, Y. Fukuba, T. Mitsuda, K. Hirai, and K. Moriya. Observation of lattice defects in orthorhombic hen-egg white lysozyme crystals with laser scattering tomography. *J. Crystal Growth*, 122:87–94, 1992.

[206] D. Sayre. The squaring method: a new method for phase determination. *Acta Cryst.*, (5):60–65, 1952.

[207] A. J. Scheidig. Time-resolved crystallography on $p21^{H-ras}$. In *Time-resolved electron and X-ray diffraction*, volume 2521 of *SPIE Conference Proceedings*, pages 278–289. SPIE, 1995.

[208] A. J. Scheidig, E. F. Pai, I. Schlichting, J. Corrie, G. P. Reid, A. Wittinghofer, and R. S. Goody. Time-resolved crystallography on H-ras p21. *Phil. Trans. R. Soc. Lond.*, A340:263–272, 1992.

[209] A. J. Scheidig, A. Sanchez-Llorente, A. Lautwein, E. F. Pai, J. E. T. Corrie, G. P. Reid, A. Wittinghoffer, and R. S. Goody. Crystallographic studies on $p21^{H-ras}$ using the synchrotron Laue method: Improvement of crystal quality and monitoring of the GTPase reaction at different time points. *Acta Cryst.*, D50:512–520, 1994.

[210] I. Schlichting, S. C. Almo, G. Rapp, K. Wilson, K. Petratos, A. Lentfer, A. Wittinghofer, W. Kabsch, E. F. Pai, G. A. Petsko, and R. S. Goody. Time-resolved X-ray crystallographic study of the conformational change in Ha-ras p21 protein on hydrolysis. *Nature*, 345:309–315, 1990.

[211] G. M. Sheldrick. SHELXS-86 program for the solution of crystal structures, 1985. Program manual.

[212] G. M. Sheldrick. Phase annealing in SHELX-90: Direct methods for larger structures. *Acta Cryst.*, A46:467–473, 1990.

[213] G. M. Sheldrick. SHELXL-93 program for crystal structure refinement, 1992. Program manual.

[214] P. J. Shlichta. Feasibility of mapping solution properties during the growth of protein crystals. *J. Crystal Growth*, 76:656–662, 1986.

[215] A. K. Shrive, I. J. Clifton, J. Hajdu, and T. J. Greenhough. Laue film integration and deconvolution of spatially overlapping reflections. *J. Appl. Cryst.*, 23:169–174, 1990.

[216] L. C. Sieker. Microdialysis crystallization chamber. *J. Crystal Growth*, 90:349–357, 1988.

[217] L. Sjölin, A. Wlodawer, G. Bergquist, P. Holm, K. Loth, H. Malmström, J. Zaar, L. A. Svensson, and G. L. Gilliland. Protein crystal growth of ribonuclease A and pancreatic trypsin inhibitor aboard the MASER-3 rocket. *J. Cryst. Gorwth*, 110:322–332, 1991.

[218] M. Skouri, J-P. Munch, B. Lorber, R. Giegé, and S. Candau. Interactions between lysozyme molecules under precrystallization conditions studied by light scattering. *J. Cryst. Gorwth*, 122:14–20, 1992.

[219] E. Snell, J. Habash, M. Helliwell, J. R. Helliwell, J. Raftery, and V. Kaucic. Image-plate synchrotron Laue data collection and subsequent structural analysis of a small test crystal of a nickel-containing aluminophosphate. *J. Synchrotron Rad.*, 2:22–26, 1995.

[220] E. H. Snell, J. R. Helliwell, T. Boggon, P. Lautenschlager, and L. Potthast. First ground trials of a Mach-Zehnder interferometer for implementation into a microgravity protein crystallization facility - the APCF. *Acta Cryst D.*, 1995. Submitted.

[221] E. H. Snell, S. Weisgerber, J. R. Helliwell, E. Weckert, K. Hölzer, and K. Schroer. Improvements in lysozyme protein crystal perfection through microgravity growth. *Acta Cryst D.*, (51):1099–1102, 1995.

[222] R. S. Snyder, K. Fuhrmann, and H. U. Walter. Protein crystallization facilities for microgravity experiments. *Journal of Crystal Growth*, (110):333–338, 1991.

[223] M. Stanton, W.C. Phillips, Y. Li, and K. Kalta. Correcting spatial distortions and nonuniform response in area detectors. *J. Appl. Cryst.*, 25(5):549–558, 1992.

[224] W. H. Steel. *Interferometry.* Cambridge University Press, second edition, 1983.

[225] I. T. Steinberger, S. Bordas, and Z. H. Kalman. Microscopic structure studies of ZnS crystals using synchrotron radiation. *Philosophical Magazine*, 35:1257–1267, 1977.

[226] B. Stoddard, P. Koenigs, N. Porter, K. Petratos, G. Petsko, and D. Ringe. Observation of the light-triggered binding of pyrone to chymotrypsin by Laue X-ray crystallography. *Proc. Natl. Acad. Sci. USA*, 88:5503–5507, 1991.

[227] V. Stojanoff and D. P. Siddons. Unpublished, 1994.

[228] V. Stojanoff, E. H. Snell, D. P. Siddons, and J. R. Helliwell. Mosaic blocks and specimen handling damage in protein crystals imaged by synchrotron X-ray topography. In preparation.

[229] R. K. Strong, B. L. Stoddard, A. Arrott, and G. K. Farber. Long duration growth of protein crystals in microgravity aboard the MIR space station. *J. Crystal Growth*, 119:200–214, 1992.

[230] N. C. J. Strynadka and N. G. James. Lysozyme revisited: Crystallographic evidence for distortion of an N-acetylmuramic acid residue bound in site D. *J. Mol. Biol.*, 220:401–424, 1991.

[231] R. M. Sweet, P. T. Singer, and S. Smalås. Considerations in the choice of wavelength range for white beam Laue diffraction. *Acta Cryst. D*, (49):305–307, 1993.

[232] D. M. E. Szebenyi, D. H. Bilderback, A. LeGrand, K. Moffat, W. Schildkamp, B Smith Temple, and T-Y. Teng. Quantitative analysis of Laue diffraction patterns recorded with a 120 ps exposure from an X-ray undulator. *J. Appl. Cryst.*, 25:414–423, 1992.

[233] B. K. Tanner. *X-ray diffraction topography.* Pergamon Press, 1976.

[234] M. W. Tate, E. F. Eikenberry, S. L. Barna, M. E. Wall, J. L. Lowrance, and S. M. Gruner. A large format high-resolution area X-ray detector based on a fibre optically bonded charge-coupled-device CCD. *J. Appl. Cryst.*, 28:196–205, 1995.

[235] A. W. Thompson, J. Habash, S. Harrop, J. R. Helliwell, C. Nave, P. Atkinson, S. S. Hasnain, P. R. Moore, P. R. Harris, S. Kinder, and S. Buffey. A new macromolecular crystallography station (9.5) on the SRS wiggler beam line for very rapid Laue and rapidly tunable monochromatic measurements: Commissioning and first results. *Rev. Sci. Instrum.*, 63:1062–1063, 1992.

[236] S. D. Trakhanov, A. I. Grebenko, A. V. Gudkov, A. V. Egorov, I. N. Barmin, B. K. Vainstein, and A. S. Spirin. Crystallization of protein and ribosomal particles in microgravity. *J. Crystal Growth*, 110:317–321, 1991.

[237] K. Tsukamoto and K. Onuma. In-situ observation of crystal growth in microgravity by high resolution microscopies. In *Crystal growth in space and related optical diagnostics*, volume 1557 of *SPIE Conference Proceedings*, pages 112–123. SPIE, 1991.

[238] P. G. Vekilov, M. Ataka, and T. Katsura. Growth process of protein crystals revealed by laser Michelson interferometry investigation. *Acta Cryst.*, D51:207–219, 1995.

[239] F. M. D. Vellieux, J. Hajdu, C. L. M. J. Verlinde, H. Groendijk, R. J. Read, T. J. Greenhough, J. W. Campbell, K. H. Kalk, J. A. Littlechild, H. C. Watson, and W. G. J. Hol. Structure of glycosomal glyceraldehyde-3-phosphate dehydrogenase from Trypanosoma brucei determined from Laue data. *Proc. Natl. Acad. Sci. USA*, 90:2355–2359, 1993.

[240] C. S. Vikram, W. K. Witherow, and J. D. Trolinger. Determination of refractive properties of fluids for dual-wavelength interferometry. *Applied Optics*, 31:7249–7252, 1992.

[241] C. G. Vonk and A. P. Pijpers. The use of film methods in small-angle X-ray scattering. *J. Appl. Cryst.*, 14:8–16, 1981.

[242] G. Wagner and R. Linhardt. Liquid-liquid diffusion profiles in microgravity experiments and crystal growth of the membrane protein bacteriorhodopsin. *J. Crystal Growth*, 110:114–118, 1991.

[243] R. L. Walter, D. J. Thiel, S. L. Barna, M. W. Tate, M. E. Wall, E. F. Eikenberry, S. M. Gruner, and S. E. Ealick. High-resolution macromolecular structure determination using CCD detectors and synchrotron radiation. *Structure*, 3:835–844, 1995.

[244] E. Weckert. Personal communication. 1995.

[245] E. Weckert, W. Schwegle, and K. Hümmer. Direct phasing of molecular structures by three beam-diffraction. *Proc. R. Soc. Lond. A*, 442:33–46, 1993.

[246] S. Weisgerber. *Developments in Synchrotron Radiation Data Collection*

Techniques for Macromolecular Crystallography (Laue and LOT) and Application to Concanavalin A. PhD thesis, Manchester University, 1993.

[247] S. Weisgerber. Personal communication. 1993.

[248] S. Weisgerber and J. R. Helliwell. Chicken egg-white lysozyme crystals grown in microgravity and on earth for a comparison of their respective perfection. *Joint CCP4 and ESF-EACBM Newsletter on Protein Crystallography*, (29):10–13, Nov. 1993.

[249] S. Weisgerber and J. R. Helliwell. High-resolution crystallographic studies of native concanavalin A using rapid Laue data collection methods and the introduction of a monochromatic large-angle oscillation technique (LOT). *J. Chem. Soc. Faraday Trans.*, 89:2667–2675, 1993.

[250] W. R. Wilcox. Influence of convection on the growth of crystals from solution. *J. Crystal Growth*, 65:133–142, 1983.

[251] L. J. Wilson, L. D. Adcock, and M. L. Pusey. A dialysis technique for determining aggregate concentrations in crystallizing protein solutions. *Phys. D. Appl. Phys.*, 26:B113–B117, 1993.

[252] L. J. Wilson and M. L. Pusey. Determination of monomer concentrations in crystallizing lysozyme solutions. *J. Crystal Growth*, 122:8–13, 1992.

[253] I. G. Wood, P. Thompson, and J. C. Matthewman. A crystal structure refinement from Laue photographs taken with synchrotron radiation. *Acta Cryst.*, B39:543–547, 1983.

[254] W. A. Wooster. Microdensitometry applied to X-ray photographs. *Acta Cryst.*, (17):878–822, 1964.

[255] W. A. Wooster and J. A. L. Fasham. Studies in microdensitometry. *Journal of Scientific Instruments*, (35):153–156, 1957.

[256] M. Wulff, T. Ursby, D. Bourgeois, L. Goirand, and M. Sanchez del Rio. The realization of fast diffraction on BL3 of the ESRF. In *Time-resolved electron and X-ray diffraction*, volume 2521 of *SPIE Conference Proceedings*, pages 197–206. SPIE, 1995.

[257] W. Wycoff and D. Agard. Pseudo-rotation diffraction: The use of a convergent beam of X-rays to obtain diffraction patterns from protein crystals. In U. W. Arndt and A. J. Wonacott, editors, *The rotation method in crystallography: data collection from macromolecular crystals*, chapter 13, pages 187–206. Oxford: North Holland Publishing Co., Amsterdam, 1977.

[258] W. M. Zuk and K. B. Ward. Methods of analysis of protein crystal images. *J. Crystal Growth*, 110:148–155, 1991.

[259] S. Zurek, M. Z. Papiz, P. A. Machin, and J. R. Helliwell. Unscrambling of harmonic reflection intensities from spots on Laue patterns: results on pea lectin. *CCP4 Newsletter*, (16), 1985.

Publications

- "Image-Plate Synchrotron Laue Data Collection and Subsequent Structural Analysis of a Small Test Crystal of a Nickel-Containing Aluminophosphate". E. Snell, J. Habash, M. Helliwell, J.R. Helliwell, J. Raftery, V. Kaucic and J.W. Campbell. *Journal of Synchrotron Radiation* (1995) Vol. 2, Part 1, pages 22-26.

- "Improvements in lysozyme protein crystal perfection through microgravity growth". E.H. Snell, J.R. Helliwell, E. Weckert, K. Hölzer and K. Schroer. *Acta Crystallographica* (1995) Vol. D51, Part 6, pages 1099-1102.

J. Synchrotron Rad. (1995). **2**, 22–26

Image-Plate Synchrotron Laue Data Collection and Subsequent Structural Analysis of a Small Test Crystal of a Nickel-Containing Aluminophosphate

E. Snell,[a] J. Habash,[a] M. Helliwell,[a] J. R. Helliwell,[a]* J. Raftery,[a] V. Kaucic[b] and J. W. Campbell[c]

[a]*Department of Chemistry, University of Manchester, Manchester M13 9PL, UK,* [b]*National Institute of Chemistry and University of Ljubljana, 61000 Ljubljana, Slovenia, and* [c]*DRAL, Daresbury Laboratory, Warrington WA4 4AD, UK*

(*Received 24 May 1994; accepted 5 August 1994*)

Image plates have advantages over photographic films, which include wider dynamic range, higher detector quantum efficiency, reduced exposure time and large size. In this study, an on-line image-plate system has been used to record crystallographic data from a small crystal. In particular, synchrotron Laue data were recorded with λ_{min} = 0.455, λ_{max} = 1.180 Å, in 20 images 10° apart and with an exposure time of 0.3 s each from a crystal (0.02 × 0.05 × 0.25 mm) of a nickel-containing aluminophosphate, NiAPO. The Laue data were analyzed with the Daresbury Laue software, including the application of an absorption correction. The structure was solved by a combination of the Patterson method and successive difference Fourier calculations using *SHELXS*86 and *SHELXL*93; the final R value for 1934 unique reflections (all data) and 310 parameters was 7.90%. The structure agrees with that determined by monochromatic diffractometry using the same crystal and reported by Helliwell, Gallois, Kariuki, Kaucic & Helliwell [*Acta Cryst.* (1993), B**49**, 420–428] with an r.m.s. deviation of 0.03 Å. Hence, this study shows the image-plate device to be very effective for synchrotron data collection and subsequent structure analysis from small crystals, *i.e.* 0.02 × 0.05 × 0.25 mm, in chemical crystallography as well as providing further confirmation of the practicability of Laue data in structure solution and refinement.

Keywords: image plates; area detectors; synchrotron Laue method; pixel sampling.

1. Introduction

Image plates have had an important impact on X-ray crystallographic data collection from macromolecules, both at the synchrotron and in the home laboratory. Also, the advantageous speed of acquisition of area-detector data in chemical crystallography, compared with diffractometry, can be critical. For example, the number of reflections to be measured may be very large (*e.g.* 20 000 reflections), whether due to a larger than average unit cell, a low symmetry space group or an interest in very high resolution (*e.g.* 0.6 Å or better). Alternatively, a sample might be air sensitive and again speed of data collection may be critical.

At the synchrotron there is tremendous potential for data collection (*a*) from very small crystals (see, for example, Andrews, Papiz, McMeeking, Blake, Lowe, Franklin, Helliwell & Harding, 1988; Harding, 1990, 1991; Riekel, 1993; Bilderback, Thiel, Pahl & Brister, 1994), (*b*) involving the use of tunable wavelengths for anomalous-dispersion applications (Helliwell, Gallois, Kariuki, Kaucic & Helliwell, 1993) or (*c*) for perturbation studies. All these topics are reviewed by Coppens (1992).

The ease of data collection at the synchrotron, especially on time factors, can benefit from the use of a large versatile area detector like the image plate. Although photographic film has been used effectively in a number of synchrotron Laue studies of small molecules (*e.g.* Clucas, Harding & Maginn, 1988; Helliwell, Gomez de Anderez, Habash, Helliwell & Vernon, 1989; Harding, 1991), the use of film with smaller crystals is ultimately beset by the problem of very small or very narrow (streaked) spots for which the pixel sampling of the spot is too poor and/or the Wooster effect is a limitation. One aspect of this paper is to show that on-line image plates can readily be used with a small crystal to rapidly collect data with good pixel sampling of diffraction spots for structure determination and refinement. As a test case we have used the crystal structure of a nickel-containing aluminophosphate. This structure has been determined and reported recently using Cu $K\alpha$ and Mo $K\alpha$ diffractometry (Helliwell *et al.*, 1993). Attention has also been drawn to the use of image plates by Euler, Gilles & Will (1994), who reported on a synchrotron Laue study of olivine. Their initial impetus was clearly the same as our own. Our aim in this paper is the study of much smaller crystals than the 410 μm diameter olivine

* To whom correspondence should be addressed.

crystal case. Moreover, we go on to provide a full structural analysis. This paper, therefore, nicely complements that of Euler *et al.* (1994).

In the work of Andrews *et al.* (1988) with a very small, mosaic crystal of piperazine silicate, the Enraf–Nonius FAST television area-detector diffractometer was used with intense monochromatic synchrotron radiation. This detector is also an on-line system. Compared with the image plate it had fewer pixels and poorer resolution, but a faster duty cycle. A next generation of on-line detector beckons, combining a large aperture with fast duty cycle based on an array of CCDs (for a discussion, see Allinson, 1993) and without the need for an image intensifier (reviewed by Allinson, 1994).

For anomalous-dispersion studies, a particular wavelength is needed (*e.g.* Ni *K* edge 1.488 Å) and so the need for $d_{min} \leq 0.9$ Å in chemical crystallography implies $2\theta_{max}$ values of $\gtrsim 110°$ occur. Even longer wavelength absorption edges exacerbate this and a cylindrical geometry, *e.g.* realizing $2\theta_{max} = 180°$, is desired. Image plates can certainly be used in this geometry. An on-line cylindrical image-plate and reader design is described by Wilkinson (1994). Alternatively, the array concept of CCDs can be extended.

2. Experimental

A small needle-shaped crystal (0.02 × 0.05 × 0.25 mm) of NiAPO [$NiAl_3P_4O_{18}C_4H_{21}N_4$, $M_r = 676.77$, monoclinic, $P2_1/n$, $a = 10.02$, $b = 15.728\,(6)$, $c = 14.134\,(6)$ Å, $\beta = 101.313\,(14)°$, $V = 2184.16$ Å^3, $Z = 4$, $D_x = 2.06$ g cm^{-3}] elongated along [010] was used to collect Laue data on station 9.5 (Brammer, Helliwell, Lamb, Liljas, Moore, Thompson & Rathbone, 1988; Thompson, Habash, Harrop, Helliwell, Nave, Atkinson, Hasnain, Glover, Moore, Harris, Kinder & Buffey, 1992) at the synchrotron radiation source of the SRS at the Daresbury Laboratory. An image-plate system (Mar Research Scanner, diameter 180 mm) implemented at the station was used as the detector. The SRS operated at 2 GeV with a current of 195 mA and the wiggler at 5 T.

The illuminating white beam spectral range was $0.4 \leq \lambda \leq 2.0$ Å. The crystal-to-image-plate distance was 138 mm. 20 images were recorded at 10° intervals, each with an exposure time of 0.3 s and an overall duty cycle time of 2.5 min. The total collection time for all these images was less than 1 h. One example of a recorded image from the image plate is shown in Fig. 1(*a*) and the average spot profile of this data is shown in Fig. 1(*b*). The pixel size is 150 μm^2. It can be seen that the spots are circular with a FWHM of 350 μm (*i.e.* recorded over three square pixels). For comparison, Fig. 2(*a*) shows the Laue photograph for the same orientation of the crystal (crystal-to-film distance 80 mm). An average spot profile for this data is shown in Fig. 2(*b*). The pixel size is now 50 μm^2. The spot is now clearly seen to be sharply streaked with a FWHM of 120 μm in width and 350 μm in length; the spot shape and size is determined here by the size of the sample and its mosaic spread, since film has a negligible point-spread factor.

3. Data analysis

Laue reflections were processed up to 0.95 Å resolution using the wavelength range 0.36–1.50 Å. The Daresbury Laboratory Laue software package (Helliwell, Habash, Cruickshank, Harding, Greenhough, Campbell, Clifton, Elder, Machin, Papiz & Zurek, 1989) modified for image-

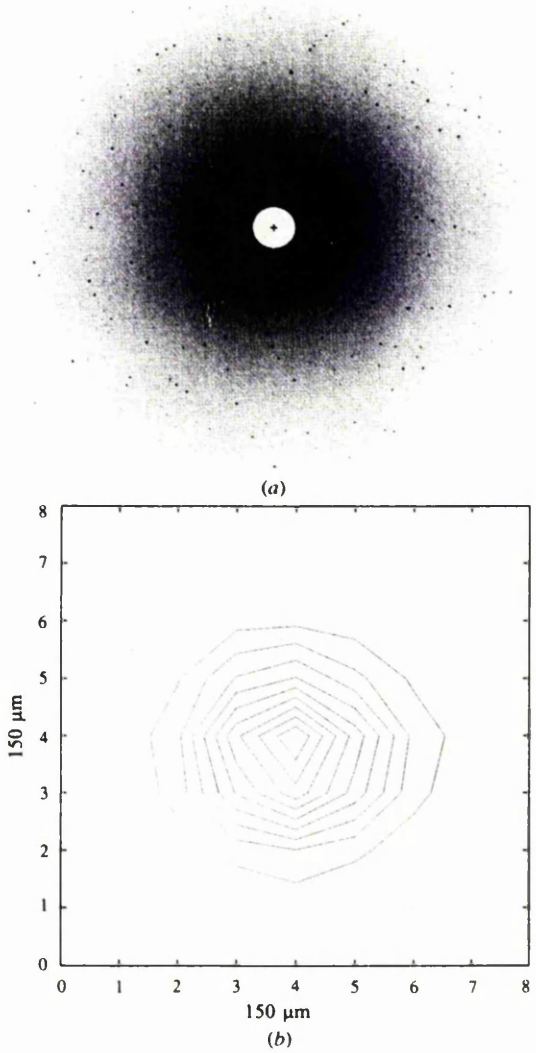

Figure 1
(*a*) Image-plate exposure from the NiAPO crystal. Crystal-to-plate distance 138 mm. The background is high due, in part, to the small crystal size, and also because the sample contains nickel; there is, of course, scope for improving the collimation and background control for such a sample. (*b*) Contour plot for the intensity of an average spot from the image in (*a*). The maximum value of 100 is arbitrarily chosen as the maximum intensity with contour intervals of 10. The pixel size is 150 μm.

plate data (J. W. Campbell, unpublished work) was used. There were no spatially overlapped spots. The unit-cell parameters and space group were available from the diffractometer study prior to data collection (Helliwell *et al.*, 1993). However, the unit-cell parameters were further refined (*i.e.* b and c, with a fixed) against the observed spot positions on each image. The r.m.s. deviation between observed and predicted spot positions was 0.031 (6) mm calculated over all the images. Table 1 compares the cell parameters for the three methods, Cu $K\alpha$, Mo $K\alpha$ and this Laue study.

LAUENORM was used for wavelength normalization. The wavelength range used was 0.455–1.180 Å and 6089 measured reflections were output. Fig. 3 shows the lambda curve for this image-plate data set. A unique set of data was produced by the programs *ROTAVATA/AGROVATA* (Collaborative Computing Project No. 4, 1994). The merging R factor (on I) was 10.6% for 6048 measurements (41 reflections rejected), giving 1896 unique data. The completeness of the data for ∞–d_{min}, ∞–$2d_{min}$ and $2d_{min}$–d_{min} was 67.6, 55.7 and 68.8%, respectively. The Ni-atom position was determined from the Patterson map using *SHELXS*86 (Sheldrick, 1985). The remaining atom positions were located by difference Fourier cycling.

With *SHELXL*93 (Sheldrick, 1992) and singlet data it is possible to make allowance for the f' and f'' variation with wavelength using the values of f' and f'' of Sasaki (1989). This was not necessary in this case because the variation for Ni in the wavelength range used is very small. Instead, the average value for Ni in this wavelength range was input.

Table 1
Cell parameters for the three data sets.

Data set	a (Å)	b (Å)	c (Å)	β (°)	V (Å^3)
Cu $K\alpha$	10.0209 (8)	15.661 (1)	14.0914 (8)	101.216 (5)	2169.3
Mo $K\alpha$	10.03 (2)	15.67 (2)	14.14 (2)	101.3 (1)	2180
Laue*	10.02	15.728 (6)	14.134 (6)	101.313 (14)	2184.16

*The refinement in *LAUEGEN* is displayed to two decimal places. The values given here are the averages over all 20 images and yield the values to three decimal places, and standard deviations, as shown. These average values have then been used for processing from *LAUEGEN* onwards. The a cell parameter was held fixed. As a test b and c were held fixed and a refined against five images. The value remained constant at 10.02 Å.

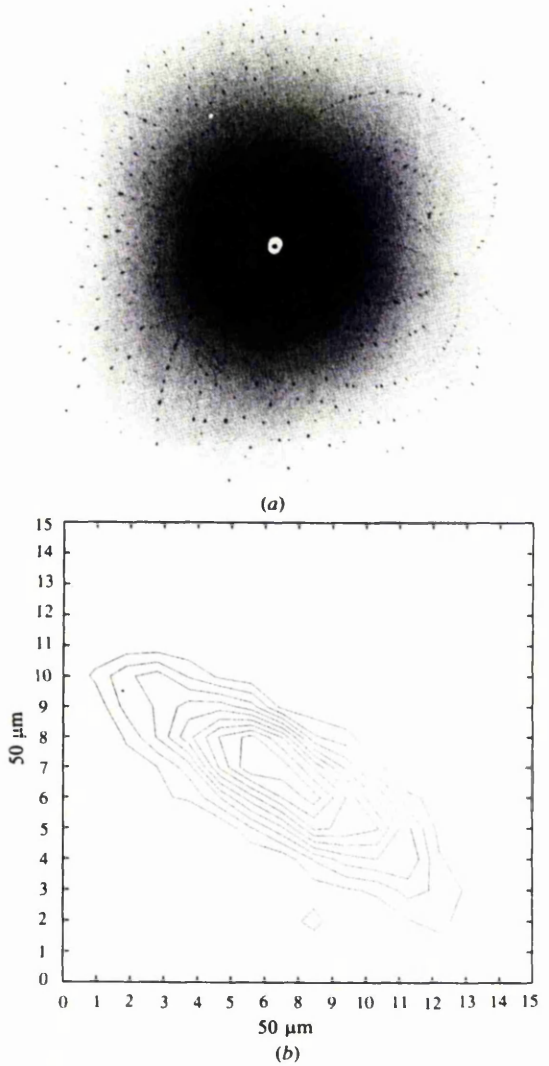

Figure 2
(*a*) Photographic film exposure from NiAPO. The same crystal is in the same orientation as used for the exposure in Fig. 1(*a*). Crystal-to-film distance 60 mm. (*b*) Contour plot for the intensity of an average spot from the photographic film exposure in (*a*). The maximum value of 100 is arbitrarily chosen as the maximum intensity with contour intervals of 10. The pixel size is 50 µm.

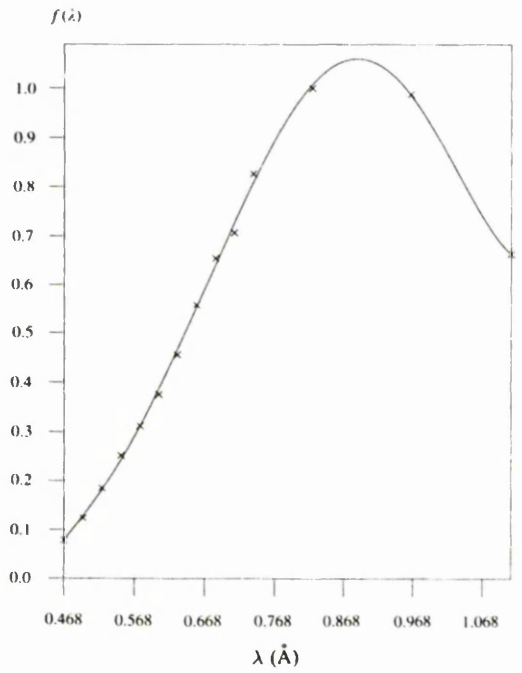

Figure 3
Lambda curve for the image-plate data set determined using *LAUENORM*. The wavelength values plotted on the abscissa are averages for each wavelength bin.

For the singlet data, the refinement (excluding H atoms) converged at an anisotropic R factor (on F) of 8.81% using all data.

In the refinement of the full structure (still excluding H atoms), the atomic displacement parameters of the atoms were low with a minority even being negative. An absorption correction procedure (Maginn, Harding & Campbell, 1993) was then applied to try to alleviate the problem. *SHELXL*93 produced a set of h, k, l and F_{calc} values from the best isotropic refinement. *LAUESCALE* used the F_{calc} values to apply an absorption surface to each original image. The absorption surface produced for the image in Fig. 1(*a*) is shown in Fig. 4. A new absorption-corrected final set of h, k, l, F, $\sigma(F)$ and λ values was then produced. The merging factor (on I) for *LAUESCALE*, now with 6472 singlet measurements (greater than *LAUENORM*'s 6089 measurements due to a slightly different acceptance procedure), was 10.9% producing 1979 unique measurements. The completeness of the data for ∞–d_{min}, ∞–$2d_{min}$ and $2d_{min}$–d_{min} was 70.6, 56.5 and 72.0%, respectively.

The final set of absorption-corrected data was then used with *SHELXL*93 and the structure refined again isotropically. All H atoms connected to the C and N atoms in the structure were then generated in their calculated positions. All atoms, with the exception of H atoms, were then refined anisotropically (310 parameters) with the refinement converging to a final R (on F) of 7.90% for 1934 unique measurements accepted by *SHELXL*93, 5.11% for $I > 3\sigma(I)$ (1397 measurements). Sensible values were then achieved for the atomic displacement parameters.*

* Lists of structure factors, anisotropic thermal parameters and the principal interatomic distances and angles have been deposited with the IUCr (Reference: HI0010). Copies may be obtained through The Managing Editor, International Union of Crystallography, 5 Abbey Square, Chester CH1 2HU, England.

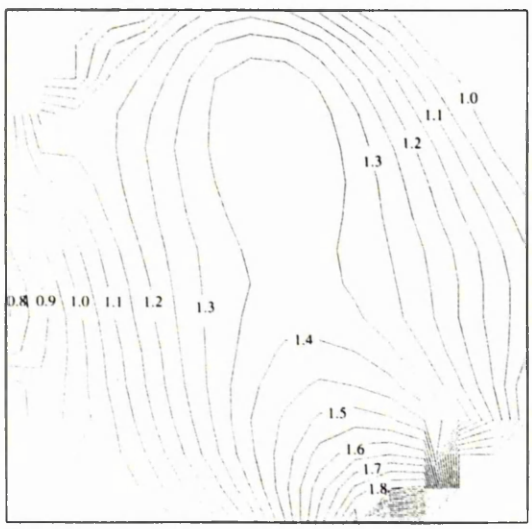

Figure 4
Absorption surface contour plot produced by *LAUESCALE* for the image-plate exposure shown in Fig. 1(*a*).

Table 2
Atomic coordinates ($\times 10^4$) and B_{eq} values for NiAPO derived from synchrotron Laue IP data.

Atom	x	y	z	B_{eq}† (Å^2)
Ni1	−8833 (1)	7711 (1)	1354 (1)	0.87 (4)
P1	−5496 (2)	7930 (1)	1425 (2)	0.61 (4)
P2	−23 (2)	7855 (1)	3402 (2)	0.61 (4)
P3	−2301 (2)	9938 (1)	4382 (2)	0.68 (4)
P4	−2725 (2)	9833 (1)	737 (2)	0.68 (4)
Al1	−2767 (2)	8781 (1)	2570 (2)	0.61 (4)
Al2	−5027 (2)	6233 (1)	365 (2)	0.61 (4)
Al3	−5010 (2)	8846 (1)	−491 (2)	0.65 (4)
O1	−6766 (5)	7998 (3)	1802 (4)	0.99 (8)
O2	−9169 (6)	8088 (3)	2700 (4)	0.91 (8)
O3	−9160 (6)	9028 (3)	1034 (4)	1.37 (8)
O4	−4291 (6)	8276 (3)	2154 (4)	1.06 (8)
O5	−5164 (6)	7000 (3)	1227 (4)	1.06 (8)
O6	−5596 (5)	8401 (3)	463 (4)	0.95 (8)
O7	−1535 (6)	8035 (3)	3053 (4)	0.99 (8)
O8	−3034 (5)	9517 (3)	3446 (4)	0.87 (8)
O9	−2201 (5)	9235 (3)	1593 (4)	1.14 (8)
O10	−4535 (5)	6664 (3)	−641 (4)	0.87 (4)
O11	−3887 (6)	5453 (3)	878 (4)	0.98 (8)
O12	−6655 (6)	5792 (3)	56 (4)	0.95 (4)
O13	−3203 (6)	10451 (3)	4846 (4)	1.14 (8)
O14	−6133 (6)	9628 (3)	−1012 (3)	1.14 (8)
O15	−4899 (6)	8102 (3)	−1377 (4)	0.95 (8)
O16	−3386 (6)	9276 (3)	−120 (4)	1.18 (8)
O17	−1574 (6)	10327 (4)	524 (4)	1.40 (8)
O18	−5322 (8)	5803 (5)	2836 (6)	2.77 (8)
N1	−8637 (9)	7483 (5)	−68 (7)	1.52 (8)
N2	−10906 (9)	7453 (4)	809 (7)	1.48 (8)
N3	−8238 (7)	6482 (4)	1874 (6)	1.40 (8)
N4	−7439 (8)	4601 (4)	1893 (6)	1.56 (8)
C1	−9953 (11)	7181 (8)	−629 (9)	2.20 (11)
C2	−11109 (12)	7557 (7)	−288 (10)	2.16 (15)
C3	−9128 (9)	5739 (5)	1791 (7)	1.41 (11)
C4	−8558 (11)	4959 (5)	2302 (8)	1.63 (11)

† $B_{eq} = (8\pi^2/3)\sum_i\sum_j U_{ij}a_i^*a_j^*\mathbf{a}_i.\mathbf{a}_j$.

All diagrams were produced using *TEXSAN* software (Molecular Structure Corporation, 1985). The atomic positional parameters are listed in Table 2, in a similar format to the table presented for the Cu $K\alpha$ and Mo $K\alpha$ results of Helliwell *et al.* (1993) to facilitate comparison.

4. Discussion

The refined structure obtained agrees well with that derived from earlier monochromatic studies (Helliwell *et al.*, 1993). The final R factors and data-to-parameter ratios for the Laue, Cu $K\alpha$ and Mo $K\alpha$ are 7.9%, 6.2; 5.7%, 11.32; 5.0%, 5.97, respectively. Fig. 5 shows one molecule of the structure. To illustrate the quality of the structure, the actual values of some of the bond distances from this study will now be given with the estimate from the earlier monochromatic Cu $K\alpha$ study given in square brackets. The average Ni—O bond distance is 2.102 (21) [2.097 (12) Å] and Ni—N bond distance is 2.103 (11) [2.111 (7) Å]. Two types of P—O bond distances exist: P—O linked to Al and P—O linked to Ni. Their average distances are 1.537 (7) [1.542 (9)] and 1.478 (1) [1.482 (1) Å], respectively. Further details of the structure and its chemistry can be found in

Rajic, Stojakovic & Kaucic (1991) and Helliwell *et al.* (1993) and references therein.

The refined structures from the Laue data and monochromatic data were overlapped with one another by a least-squares determination of a rotation matrix and a translation vector. This provides an overall idea of the structural accuracy. The r.m.s. deviation (Å) and maximum single atomic displacement (in parentheses) for the Laue:Cu $K\alpha$, Laue:Mo $K\alpha$ and Cu $K\alpha$:Mo $K\alpha$ cases (all atoms except H) were 0.030 (0.074), 0.034 (0.095) and 0.027 (0.060), respectively. The thermal parameters can be compared by taking the ratio $B_{\mathrm{Laue}}/B_{\mathrm{Cu}\,K\alpha}$, which has the value 0.64. This can be compared with the value $B_{\mathrm{Mo}\,K\alpha}:B_{\mathrm{Cu}\,K\alpha}$ of 0.86 (Helliwell *et al.*, 1993).

We can conclude that a good quality refinement has been realized for this structure using a small crystal. In particular, the use of the on-line image-plate device proved to be very effective for the synchrotron Laue data collection for this small crystal with data collection taking less than 1 h.

G. Leonard, Hao Quan, R. L. Beddoes, M. M. Harding and D. H. Bilderback are thanked for useful discussions.

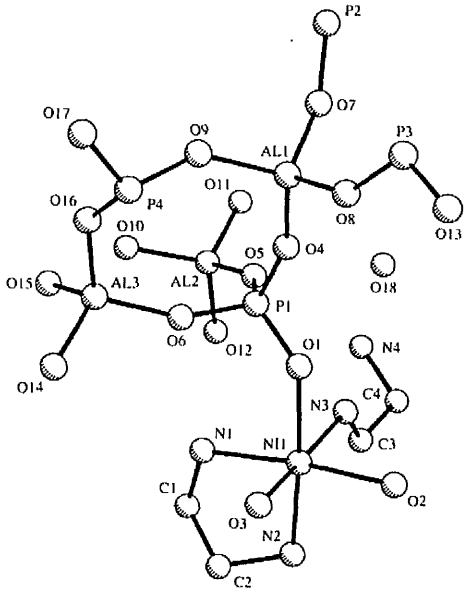

Figure 5
The asymmetric unit of NiAPO, with H atoms omitted.

We are grateful to G. M. Sheldrick for providing us with an advance copy of the *SHELXL*93 software and to S. McSweeney for assistance on station 9.5. The SERC (EPSRC) is thanked for grant support.

References

Allinson, N. M. (1993). *Synchrotron Rad. News*, **6**, 4–6.
Allinson, N. M. (1994). *J. Synchrotron Rad.* **1**, 54–62.
Andrews, S. J., Papiz, M. Z., McMeeking, R., Blake, A. J., Lowe, B. M., Franklin, K. R., Helliwell, J. R. & Harding, M. M. (1988). *Acta Cryst.* B**44**, 73–77.
Bilderback, D. H., Thiel, D. J., Pahl, R. & Brister, K. E. (1994). *J. Synchrotron Rad.* **1**, 37–42.
Brammer, R., Helliwell, J. R., Lamb, W., Liljas, A., Moore, P. R., Thompson, A. W. & Rathbone, K. (1988). *Nucl. Instrum. Methods*, A**271**, 678–687.
Collaborative Computing Project No. 4 (1994). *Acta Cryst.* D**50**, 760–763.
Clucas, J. A., Harding, M. M. & Maginn, S. J. (1988). *J. Chem. Soc. Chem. Commun.* pp. 185–187.
Coppens, P. (1992). *Synchrotron Radiation Crystallography*. New York: Academic Press.
Euler, H., Gilles, R. & Will, G. (1994). *J. Appl. Cryst.* **27**, 190–192.
Harding, M. M. (1990). *Chem. Br.* pp. 956–958.
Harding, M. M. (1991). *J. Phys. Chem. Solids*, **10**, 1293–1298.
Helliwell, J. R., Habash, J., Cruickshank, D. W. J., Harding, M. M., Greenhough, T. J., Campbell, J. W., Clifton, I. J., Elder, M., Machin, P. A., Papiz, M. Z. & Zurek, S. (1989). *J. Appl. Cryst.* **22**, 483–497.
Helliwell, M., Gallois, B., Kariuki, B. M., Kaucic, V. & Helliwell, J. R. (1993). *Acta Cryst.* B**49**, 420–428.
Helliwell, M., Gomez de Anderez, D., Habash, J., Helliwell, J. R & Vernon, J. (1989). *Acta Cryst.* B**45**, 591–596.
Maginn, S. J., Harding, M. M. & Campbell, J. W. (1993). *Acta Cryst.* B**49**, 520–524.
Molecular Structure Corporation (1985). *TEXSAN. TEXRAY Structure Analysis Package*. MSC, 3200 Research Forest Drive, The Woodlands, TX 77381, USA.
Rajic, N., Stojakovic, D. & Kaucic, V. (1991). *Zeolites*, **11**, 612–616.
Riekel, C. (1993). *ESRF Beamline Handbook*, pp. 53–56. ESRF, Grenoble, France.
Sasaki, S. (1989). KEK/Photon Factory Report 88–14. National Laboratory for High Energy Physics, Tsukuba, Japan.
Sheldrick, G. M. (1985). *SHELXS*86. *Program for the Solution of Crystal Structures*. Univ. of Göttingen, Germany.
Sheldrick, G. M. (1992) *SHELXL*93. *Program for Crystal Structure Refinement*. Univ. of Göttingen, Germany.
Thompson, A. W., Habash, J., Harrop, S., Helliwell, J. R., Nave, C., Atkinson, P., Hasnain, S. S., Glover, I. D., Moore, P. R., Harris, N., Kinder, S. & Buffey, S. (1992). *Rev. Sci. Instrum.* **63**(1), 1062–1064.
Wilkinson, C. (1994). *Biophys. Chem.* In the press.

Acta Cryst. (1995). D51, 000–000

Improvements in lysozyme protein crystal perfection through microgravity growth.

By E. H. SNELL, S. WEISGERBER, J. R. HELLIWELL,* E. WECKERT, K. HÖLZER and K. SCHROER, *Chemistry Department, University of Manchester, Manchester M13 9PL, England, and Institüt für Kristallographie, University of Karlsruhe (TH), Kaiserstrasse 12, Postfach 6980, D-76128 Karlsruhe, Germany*

(*Received* x xxx 1995; *accepted* 25 *August* 1995)

Abstract

Microgravity offers an environment for protein crystallization where there is an absence of convection and sedimentation. We have investigated the effect of microgravity conditions on the perfection of protein crystals. The quality of crystals for X-ray diffraction studies is characterized by a number of factors, namely size, mosaicity, and the resolution limit. By using tetragonal lysozyme crystals as a test case we show, with crystal growth in two separate Space Shuttle missions, that the mosaicity is improved by a factor of three to four over earth-grown ground control values. These microgravity-grown protein crystals are then essentially perfect diffraction gratings. As a result the peak to background of individual X-ray diffraction reflections is enhanced by a similar factor to the reduction in the mosaicity. This then offers a particularly important opportunity for improving the measurement of weak reflections such as occur at high diffraction resolution. These microgravity results set a benchmark for all future microgravity and earth-based protein crystallography procedures.

Introduction

The European Space Agency (ESA) have developed the Advanced Protein Crystallization Facility (APCF) (Snyder, Fuhrmann & Walter, 1991; Bosch, Lautenschlager, Potthast & Stapelmann, 1992) as a standard tool for microgravity crystallization experiments aboard the NASA Space Shuttle. We have utilized dialysis liquid diffusion for crystallization within the APCF. The dialysis reactors each consist of two quartz glass blocks containing two chambers separated by a dialysis membrane. The upper chamber contains the protein solution, the lower chamber the salt solution. The salt and protein solution are separated by a cylindrical quartz glass plug, which also contains salt solution. To activate the reactor this plug is rotated by 90°, once orbit is reached, so that all volumes then come into contact. Likewise the reactor is deactivated before descent to earth.

The perfection of a crystal refers to the precision with which each and every one of the 10^{15} or so unit cells in a crystal is aligned. Crystal perfection can be evaluated overall by measurement of the rocking width (Helliwell, 1988), Fig. 1. Measurements of rocking widths for weak reflections from protein crystals require an intense synchrotron X-ray source. The use of highly collimated synchrotron radiation is ideal for probing the mosaicity of crystals in the theoretical limit (Helliwell, 1988), rather than having it masked by the X-ray beam divergence and dispersion effects. Two methods of measurement have been utilized here; collection of polychromatic Laue data and collection of monochromatic data. To explore the fine mosaicity values expected, *i.e.* 0.0005° (Helliwell, 1988), the Laue method is used with a large crystal-to-detector distance and a tightly slitted down X-ray beam. The Laue method also allows a batch of crystals to be surveyed readily. Monochromatic data collection with a diffractometer allows specific regions of the diffraction pattern to be probed in detail. This work with such fine rocking widths requires a diffractometer with a small angular step width combined with a fine $\delta\lambda/\lambda$ monochromatic synchrotron beam, also of very low divergence.

Crystallization and X-ray analysis

Lysozyme was crystallized on two different NASA space shuttle missions, Spacehab-1 in 1993 and IML-2 in 1994.

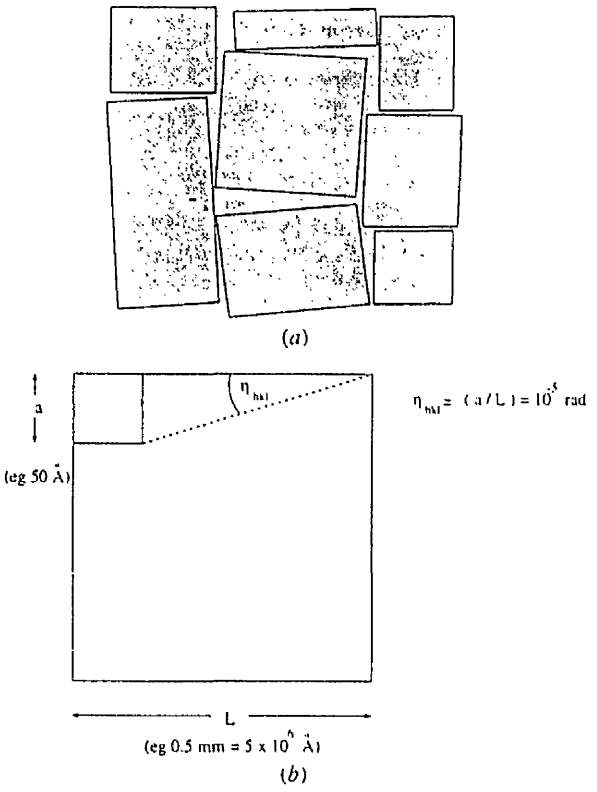

Fig. 1. The concepts of (*a*) an ideally imperfect crystal and (*b*) a perfect crystal. For case (*a*) a number of smaller perfect blocks make up the larger overall crystal; the overall misalignment of such blocks is the mosaicity or mosaic spread of an ideally imperfect crystal. For case (*b*) a simplified 'extinction free' calculation of the rocking width is shown based on a typical unit-cell size of 50 Å and a crystal of 0.5 mm, which quantifies the rocking width in the limit of a truly perfect crystal (see Helliwell, 1988, pages 260–263 for comparison with a dynamical theory estimate).

* To whom correspondence should be adressed.

ISSN 0907-4449 © 1995

Table 1. *Crystal mosaicities estimated from Laue spot sizes at the SRS (converted to FWHM i.e. 2.3σ values)*

For examples of the actual spots see Fig. 2 [space 3 is case (*a*) and earth 1 is case (*b*) *i.e.* the extremes observed]. Note also that the best observed here (space 3) is still larger than the theoretical limit (Helliwell, 1988) by a factor of 2 or so.

Crystal	Space 1	Space 2	Space 3	Earth 1	Earth 2
$\langle\eta\rangle$ (°)	0.0012	0.0022	0.0010	0.0062	0.0032
$\sigma(\langle\eta\rangle)$(°)	0.0002	0.0001	0.0001	0.0006	0.0001
Spots	3	14	7	7	7

Crystallization took place in the APCF at a constant temperature of 20 ± 0.1°C over periods of 7.5 and 12.5 d, respectively. The crystallization recipe consisted of 15.8 mg lysozyme dissolved in 188 µl of 0.04*M* acetate buffer (pH 4.7). The precipitant was altered slightly for each mission due to the different durations; 1.35*M* and 1.26*M* NaCl solutions for Spacehab-1 and IML-2, respectively. Spacehab-1 produced crystals of average size 0.7 mm, comparable with the ground control crystals grown in an identical APCF unit on earth. The longer IML-2 mission produced crystals of 1.8 mm average, compared with 0.8 mm for the ground control crystals.

The Spacehab-1 crystals were analyzed at the Daresbury Synchrotron Radiation Source (SRS) on station 9.5 (Brammer *et al.*, 1988) using the Laue method. The mosaicity, η, values were estimated for three microgravity-grown and two earth-grown crystals. Example Laue diffraction spots for microgravity-grown and earth-grown crystals are shown in Fig. 2, and a summary of the results for many spots over all the crystals surveyed is given in Table 1. The Laue diffraction spots from the microgravity-grown lysozyme crystals showed a factor of three reduction in mosaic spread over the earth-grown controls, reaching a value of 0.0010° (calculated at FWHM).

Crystals from the IML-2 mission were analyzed by monochromatic methods at the European Synchrotron Radiation Facility (ESRF) in Grenoble, France. By use of a diffractometer goniostat detailed exploration was possible of the diffraction patterns of one earth-grown control crystal and one microgravity-grown crystal. The earth-grown control crystal exhibited rocking widths ranging from 0.0067 to 0.0169° (0.0120° average), calculated at FWHM. The microgravity-grown crystal exhibited rocking widths ranging from 0.0017 to 0.0100°, averaging 0.0047°. For the microgravity-grown crystal, only single peaks were obtained (Fig. 3*a*), suggesting that essentially one mosaic block makes up the whole crystal, *i.e.* the angular misalignment of mosaic blocks was certainly smaller than the very fine instrument resolution function. In the case of most reflections from the earth-grown crystal a composite structure of the peak was resolved, Fig. 3(*b*). A prominent difference in peak intensities of reflections from the microgravity-grown crystal is seen compared with the identical earth-grown crystal reflections. Fig. 3(*c*) illustrates this whereby the peak intensity of reflections from the microgravity-grown crystal are a factor of eight greater than for the earth-grown. A factor of two of this is due to the increased volume of the microgravity-grown crystal sample bathed in the X-ray beam but the further factor of four in the enhancement of the peak is the effect of the narrow rocking width. The peak intensity enhancement will be particularly beneficial where the reflections are weak *e.g.* as at the diffraction resolution limit. Indeed the resolution limit of the microgravity-grown crystal was explored at high diffraction angle where it was readily possible to find evidence of diffraction to 1.2 Å, Fig. 4.

Discussion

The increased peak count, far greater than that expected from crystal volume considerations, is most startling. There are a number of reports of enhanced I/σ X-ray diffraction for microgravity-grown over earth-grown crystals (McPherson, 1993; DeLucas, *et al.*, 1989). There are also opposite conclusions drawn (Hilgenfeld, Liesum, Storm & Plaas-Link, 1992). Our results point to the physical basis of why I/σ for weak reflections can be improved with microgravity crystallization, that is that fewer, larger mosaic blocks are arranged more perfectly. Hence we can see that there is a direct link between the fine mosaicity and what might be achieved in terms of diffraction resolution. Moreover, for bigger, more perfect crystals and longer X-ray wavelengths extinction might be seen in the stronger intensities (Helliwell, 1992).

Comparing the two missions it seems that the shorter mission (Spacehab-1) has produced more perfect crystals, although smaller in size. In the absence of further diagnostics, such

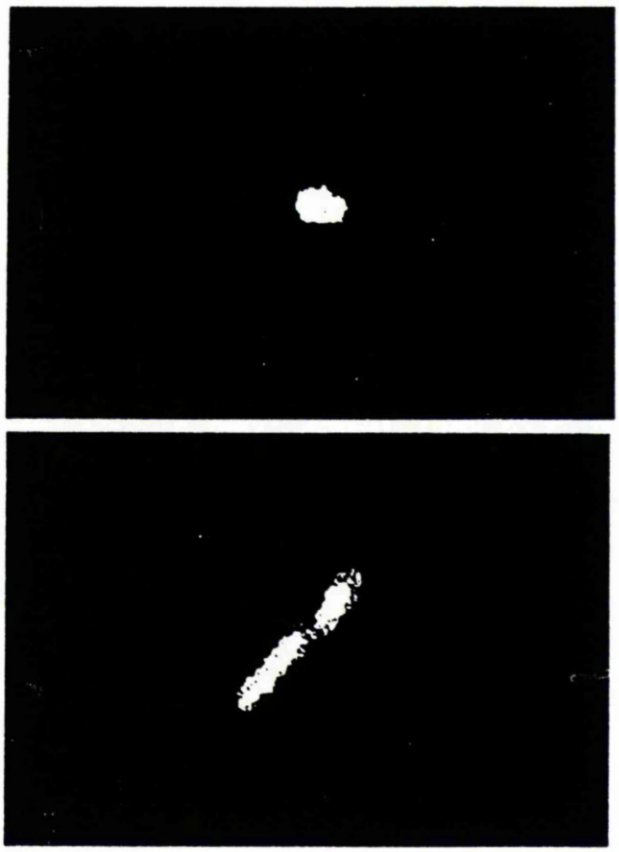

Fig. 2. Examples of Laue diffraction spots recorded on station 9.5 of the SRS Daresbury (Brammer *et al.*, 1988) at 2.4 m from the crystal on X-ray sensitive photographic film, (*a*) microgravity-grown crystal and (*b*) earth-grown crystal. The beam was trimmed down using slits to 20 × 10 µrad and a direct beam of 0.2 mm in size was used. This ensured that the direct beam 2.4 m from the sample had only increased in size by ~48 µm horizontally and ~24 µm vertically. Specifically then the spot sizes in the Laue method can be converted to mosaic spread values, η, according to the formula (Andrews, Hails, Harding & Cruickshank, 1987) $\Delta_{radial} = 2\eta D/\cos^2 2\theta$ where Δ_{radial} is the spot size, with the direct beam size at the film subtracted out. D is the crystal to detector distance, and θ the Bragg angle of a Laue spot.

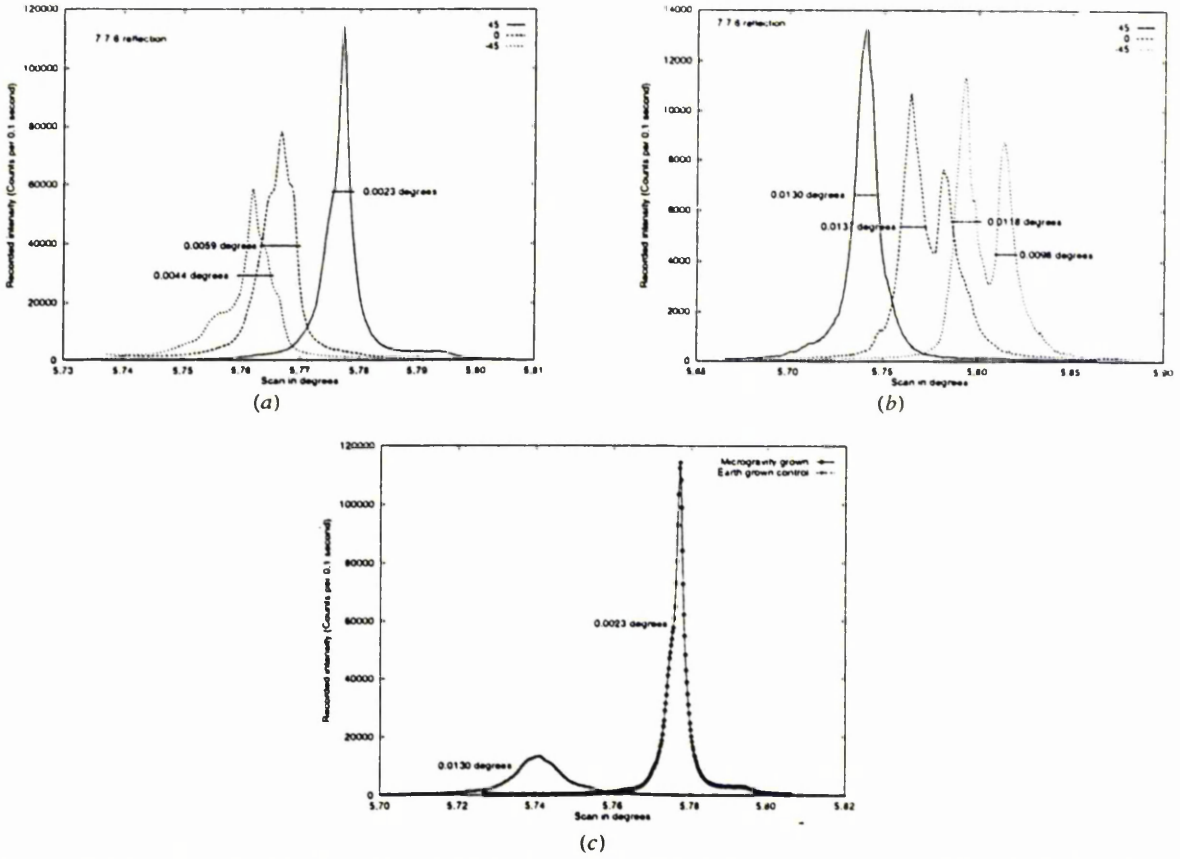

Fig. 3. ω scans of the reflection (7 7 6) at ψ angles of 45, 0 and −45°, respectively, (*a*) microgravity-grown crystal and (*b*) earth-grown crystal. The FWHM of each component of the reflection has been evaluated in each case where there is either no appreciable composite structure or the composite structure can be resolved separately from the main peak. These values are indicated in the figures by a short horizontal line with the instrument resolution function deconvoluted out. This deconvolution is given by $\eta = (\varphi_R^2 - IRF^2)^{1/2}$ where φ_R is the measured reflection rocking width and IRF is the instrument resolution function (Colapietro *et al.*, 1992). In (*c*) the ψ = 45° reflections for both the earth-grown control and the microgravity crystal are plotted on the same scale. The integrated intensity of the microgravity-grown crystal reflection is approximately double that of the earth-grown crystal reflection which corresponds to the microgravity-grown crystal being approximately double the volume of the earth-grown crystal. The peak intensity is eight times more for the microgravity crystal over the earth crystal. These crystal rocking widths were measured on station A of the ESRF Swiss–Norwegian beam line with a 1 Å wavelength incident monochromatic X-ray beam using a Huber ψ-circle diffractometer from the University of Karlsruhe. The station, at 45 m from the source, utilizes a double-crystal Si(111) monochromator and the beam is unfocused. The angular step size of the diffractometer is 0.000$\frac{1}{2}$° with an instrument resolution function (Colapietro *et al.*, 1992) of 0.00195°.

as interferometric monitoring, no rational basis exists in fact to terminate the crystal growth at any other moment in the microgravity mission than at the end. However, on the ground we have utilized a new Mach-Zehnder interferometer to monitor the lysozyme protein crystal growth process and find that the growth is essentially complete after 5 d (Snell, Helliwell, Lautenschlager & Potthast, 1995). Perhaps on the longer IML-2 flight the crystal growth should have been terminated before the end of the mission so as to realise the most perfect crystals possible.

In X-ray data collection, rapid freezing of crystals (Hope *et al.*, 1989) is routinely used to reduce X-ray radiation damage to the crystal. Unfortunately this also considerably increases mosaicity; for example, even with careful attention to the freezing mixture the minimum mosaic spread achieved is still about 0.25° (Mitchell & Garman, 1994). Its effects (blow up of the diffraction spots over distance) are circumvented by placing the detector close to the crystal (between tens of mm up to ~200 mm). Clearly, much larger distances (metres) can be contemplated with smaller mosaicity and hence great improvements in signal to noise could be obtained. It is interesting to wonder if, with better methods and apparatus, crystals could still be frozen in some way, to preserve their lifetime in the beam, whilst preserving their geometric perfection.

The precise attention to perfection in this way is relatively new (Helliwell, 1988, 1992; Colapietro *et al.*, 1992; Fourme, Ducruix, Ries-Kautt & Capelle, 1995) and should be applied more routinely. After all, it is not inconceivable that, on earth, procedures might be developed where more perfect crystals could be grown routinely so as to match the standard set by the microgravity-grown crystals. It could also be the case that a significant number of essentially perfect protein crystals do grow on earth. Indeed it can be noted that

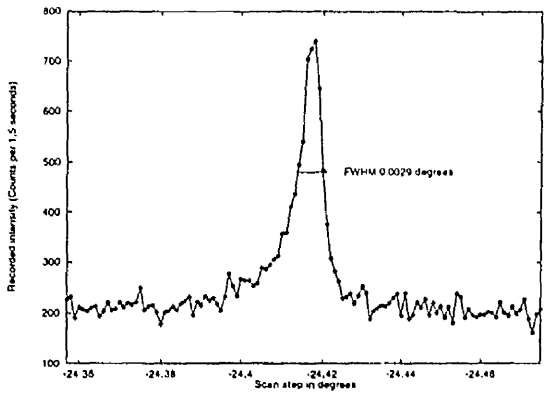

Fig. 4. Reflection (32 57 0) recorded at 1.2 Å resolution for a microgravity-grown crystal. The labelled FWHM value has the instrument resolution function value, IRF (0.00195°), deconvoluted out and, in addition, for a reflection of such a high diffraction resolution, the instrument $\delta\lambda/\lambda$ produces a $\delta\theta$ spread ($= \delta\lambda/2d_{hkl}\cos\theta_{hkl}$) of 0.00527°, which has also been deconvoluted out. Obviously if wide angular sampling had been used *e.g.* 0.25° or greater, as in standard X-ray crystallography data-collection methods, the peak counts would be swamped with background, thus eliminating the signal. Quite a high background is present here but with further optimization of the experiment this can be reduced by a factor of five.

all the microgravity-grown crystals investigated here are of comparable good quality (although not yet quite reaching the perfect limit (Helliwell, 1988) whereas only ~1 in 40 or so lysozyme crystals grown on earth are that good. Also if, by present crystallization knowledge and methods, only very small crystals could be grown (*e.g.* <20 μm), attention to mosaic block composition/angular rocking widths as a function of growth conditions might yield larger crystals in the end. This would also be useful in neutron crystallography if crystals were initially small (*e.g.* < 1 mm). All these techniques could become extremely valuable in structural research but require quite novel instrumentation, in terms of area detectors, diffractometer mechanical step sizes and data acquisition/processing computers, in addition to new radiation sources to exploit such crystal quality fully. In essence then, the use of microgravity has given profoundly new insights into protein crystallization methods, the nature of protein crystals and, indeed, how they might be exploited in future for structure determination.

We are grateful to the Daresbury SRS and ESRF Grenoble for the provision of synchrotron radiation and to ESA for flight opportunities on the NASA Space Shuttle. In particular we would like to express our thanks to the Swiss–Norwegian CRG (Dr Phil Pattinson and his colleagues) at the ESRF, Grenoble, for providing access to their beamline facilities. Dr Sean McSweeney at the Daresbury SRS is thanked for assistance on station 9.5. M. Masson and J. Zellner are thanked for their assistance during the experiments at the ESRF. We are extremely grateful to Robert Bosch, and Drs Luthor Potthast and Paul Lautenschlager at Dornier GmbH for allowing us the opportunity to use their Mach-Zehnder interferometer to monitor the process of ground-based lysozyme protein crystal growth. Finally, we are especially grateful to Drs H. U. Walter, K. Fuhrmann and O. Minster of ESA as well as Professor G. Wagner, University of Giessen (Chairman of ESA's protein crystallization working group) for their constant help and support with this research.

References

Andrews, S. J., Hails, J. E., Harding, M. M. & Cruickshank, D. W. J. (1987). *Acta Cryst.* A43, 70–73.

Bosch, R., Lautenschlager, P., Potthast, L. & Stapelmann, J. (1992). *J. Cryst. Growth*, **122**, 310–316.

Brammer, R. C., Helliwell, J. R., Lamb, W., Liljas, A., Moore, P. R., Thompson, A. W. & Rathbone, K. (1988). *Nucl. Instrum. Methods.* A271, 678–687.

Colapietro, M., Cappuccio, G., Marciante, C., Pifferi, A., Spagna, R. & Helliwell, J. R. (1992). *J. Appl. Cryst.* **25**, 192–194.

DeLucas, L. J., Smith, C. D., Smith, H. W., Vijay-Kumar, S., Senadhi, S. E., Ealick, S. E., Carter, D. C., Snyder, R. S., Weber, P. C., Salemme, F. R., Ohlendorf, D. H., Einspahr, H. M., Clancy, L. L., Navia, M. A., McKeever, B. M., Nagabhushan, T. L., Nelson, G., McPherson, A., Koszelak, S., Taylor, G., Stammers, D., Powell, K., Darby, G. & Bugg, C. E. (1989). *Science*, **246**, 651–654.

Fourme, R., Ducruix, A., Ries-Kautt, M. & Capelle, B. (1995). *J. Synchrotron Rad.* **2**, 136–142.

Helliwell, J. R. (1988). *J. Cryst. Growth*, **90**, 259–272.

Helliwell, J. R. (1992). *Macromolecular Crystallography with Synchrotron Radiation*, ch. 2, pp. 24–26. Cambridge Univ. Press.

Hilgenfeld, R., Liesum, A., Storm, R. & Plaas-Link, A. (1992). *J. Cryst. Growth*, **122**, 330–336.

Hope, H., Frolow, F., von Bohlen, K., Makowski, I., Kratky, C., Halfon, Y., Danz, H., Webster, P., Bartels, K. S., Wittmann, H. G. & Yonath, A. (1989). *Acta Cryst.* B45, 190–199.

McPherson, A. (1993). *J. Phys. D*, **26**, B104–B112.

Mitchell, E. P. & Garman, E. F. (1994). *J. Appl. Cryst.* **27**, 1070–1074.

Snell, E. H., Helliwell, J. R., Lautenschlager, P. & Potthast, L. (1995). *Acta Cryst.* D51. Submitted.

Snyder, R. S., Fuhrmann, K. & Walter, H. U. (1991). *J. Cryst. Growth*, **110**, 333–338.